
UNIVERSITÄT ZU LÜBECK
INSTITUTE OF MEDICAL ENGINEERING

**From the Institute of Medical Engineering**
**of the University of Lübeck**
**Director: Prof. Dr. rer. nat. Thorsten M. Buzug**

# INSPECT
# (In-situ Magnetic Particle Spectrometer)

Dissertation
for Fulfilment of
Requirements
for the Doctoral Degree
of the University of Lübeck

from the Department of Computer Sciences and Engineering

Submitted by

Ankit Malhotra
from Delhi, India

Lübeck 2022

First referee: Prof. Dr. rer. nat. Thorsten M. Buzug
Second referee:
Date of oral examination:
Approved for printing. Lübeck,

# Acknowledgement

Words cannot express my gratefulness to Prof. Dr. Thorsten M. Buzug for his invaluable support, patience, and feedback. Prof. Thorsten M. Buzug not only generously provided knowledge and guidance but also provided an environment (IMT) that made everything feasible regarding my research. I am also thankful to the defense committee for Prof. Dr. Philipp Rostalski and Prof. Dr. Alfred Mertins for their invaluable feedback and support towards the completion of the thesis.

I am deeply indebted to Dr. Kerstin Lüdtke-Buzug for her immense unending support throughout my thesis. I am grateful to her for providing valuable knowledge in the field of chemistry and being patient in the early days of my work in her lab. This endeavor would not have been possible without all my co-workers at IMT. I am extremely grateful to them for their expert views, knowledge, and moral support throughout my tenure at IMT. I cherish the time spent together in the lab, and in social settings. Special thanks to the MPI team consisting of Matthias Gräser, Ksenija Gräfe, Alexander Neumann, Mandy Ahlborg, Christina Debbeler, André Behrends, Thomas Friedrich, Jonas Schumacher, Eric Aderhold, Pascal Stagge, Huimin Wei, Xin Chen, Anselm von Gladiß, Gael Bringout, and Corinna Stegelmeier. A special thanks to the technical staff consisting of Dirk Steinhagen and Maren Bobek, without your help and expertise this journey would never have been completed.

Lastly, I would like to thank my parents and family, for providing the air below my wings and keeping my spirit and motivation high throughout the journey. A special shout out to my friends in Germany and back home, because of you guys I cry a little less and smile a lot more.

# Abstract

MPS (magnetic particle spectrometry) is an investigative modality for characterizing magnetic properties of nanoparticles and was instigated with the initiation of MPI (magnetic particle imaging). MPI is an imaging modality providing quantitative information on the spatial distribution of magnetic nanoparticles such as SPIONs (superparamagnetic iron oxide nanoparticles). As SPIONs are one of the most integral parts of MPI affecting the image resolution, therefore immense research is being done for improving the magnetic properties of the synthesized SPIONs. Moreover, due to MPI, various newer applications came into existence such as MFH (magnetic fluid hyperthermia), magnetic manipulation, drug delivery, etc. This lead to an immense demand for specifically tailored SPIONs not just for attaining better image resolution with minimum dosage but also for implementing therapeutic scenarios in combination with the imaging modality. This leads to the development of various MPS systems capable of characterizing SPIONs in terms of their magnetic properties at excitation frequencies used in MPI scanners. MPS is a measurement technique to determine the magnetic properties of SPIONs in an oscillating magnetic field. State of the art MPS devices are solely capable of measuring the magnetization response of small volume SPIONs to an oscillatory magnetic excitation after the completion of the synthesis process. Therefore, no information regarding the nucleation and growth of these SPIONs can be observed.

The first part of this thesis is dedicated to the design and development of a novel in-situ magnetic particle spectrometer (INSPECT), which can be used to monitor the entire synthesis process from particle genesis via growth to the stable colloidal suspension of the nanoparticles in real-time. INSPECT has a field strength of 10 mT with an excitation frequency of 23 kHz. The time required for a single measurement is approximately 1 s with 10 periods and 2300 averages. The measurement time can be further reduced to 46 µs by just measuring one single period. The device is suitable for use in a biochemistry environment. It has a chamber size of 72 mm allowing the usage of a standard reaction flask for synthesis. For alkaline-based precipitation, the change of magnetic properties of SPIONs during the nucleation and growth phase of the synthesis is demonstrated. The

device can record the changes in the amplitude and phase spectra, and, in turn, the hysteresis. Hence, it is a powerful tool for an in-depth understanding of the nanoparticles formation dynamics during the synthesis process. Other real-time devices such as in-situ TEM and X-ray diffraction requires a special in-situ chamber for analyzing nucleation and growth. Moreover, these devices are high on engineering complexity and require higher user expertise. In comparison, INSPECT is fully automatic, modular, and there is no need for special in-situ chambers for experimentation which makes the device suitable for tracking the nucleation and growth of the SPIONs in everyday research quiet convenient.

The second part of the thesis is dedicated to the various syntheses performed via INSPECT. In these sections, the usage of INSPECT is demonstrated to track the nucleation and growth of SPIONs undergoing synthesis based on an alkaline co-precipitation process. Two syntheses are shown in details followed by various experiments to show the effects of different parameters like flow rate, the effect of different types of coating material, the quantity of dextran, absence of coating material and the effects of initial cooling on the change in the magnetic moment versus time. This idea is further carried by showing the effects of certain external parameters such as reaction temperature and external magnetic fields (static and sinusoidal) on the final magnetic properties of SPIONs. These measurements are carried out without INSPECT but via a 1-D MPS.

The thesis also deals with another important module present in the receive chain of MPI/MPS called LNA (low noise amplifier). An LNA's paramount task is to amplify the received signal while keeping the noise induced by its own circuitry minimum. In the current research, design and development of four different LNAs with a primary focus on the low input noise and the best NF (noise figure) is described. For mitigating the input noise all the LNA's are based on the summing configuration also known as parallelization. Two of the LNAs are single ended with different noise characteristics and different degree of parallelization. Followed by a VGA (variable gain amplifier) and an FDA (fully differential amplifier) for different MPI/MPS based applications. One of the single-ended LNA with 16 Op-amps in parallel has approximately 653 pV/ $\sqrt{\text{Hz}}$ of input noise with an NF (noise figure) of 3.32 dB with a 50 Ω termination. The other single-ended LNA with 4 Op-amps in parallel has an input noise of 1.1 nV/ $\sqrt{\text{Hz}}$ of input noise with an NF of 7.87 dB with the same termination. Followed by a low noise VGA consisting of 8 Op-amps in parallel has an input noise of 868 pV/ $\sqrt{\text{Hz}}$ with an NF of 1.86 dB with 50 Ω termination. The gain of the VGA can be varied from -11 dB to 30 dB. Finally, a low noise FDA with in-built protection circuitry to prevent damage to the acquisition card due to high voltages. The FDA has approximately 1.76 nV/ $\sqrt{\text{Hz}}$ of input noise with an NF

of 11.93 dB with a 50 Ω termination.

Most importantly, this thesis constitutes the first steps required for tracking and manipulating the nucleation and growth of SPIONs by sensing real-time changes in the magnetic moment and then manipulating internal and external parameters for synthesis of SPIONs suited for various diagnostic and therapeutic applications of MPI. Specifically adapting the SPIONs for the various application scenarios leverages the potential of this imaging technique.

# Kurzfassung

MPS (Magnetpartikelspektrometrie) ist eine Untersuchungsmodalität zur Charakterisie
-rung magnetischer Eigenschaften von Nanopartikeln und wurde mit der Initiierung des MPI (Magnetic Particle Imaging; deutsch: Magnetpartikelbildgebung) ins Leben gerufen. Das MPI ist eine Bildgebungsmodalität, die quantitative Informationen über die räumliche Verteilung von magnetischen Nanopartikeln wie SPIONs (Superparamagnetic Iron Oxide Nanoparticles; deutsch: superparamagnetische Eisenoxid-Nanopartikel) liefert. Da SPIONs einer der integralen Bestandteile des MPI sind, die die Bildauflösung beeinflussen, wird daher intensive Forschung zur Verbesserung der magnetischen Eigenschaften der synthetisierten SPIONs betrieben. Darüber hinaus sind durch MPI verschiedene neuere Anwendungen entstanden, wie MFH (Magnetic Fluid Hyperthermia; deutsch: Magnetflüssigkeits-Hyperthermie), magnetische Manipulation, Medikamentenverabreichung über Nanopartikel usw. Daraus ergibt sich ein immenser Bedarf an spezifisch zugeschnittenen SPIONs, nicht nur zur Erzielung einer besseren Bildauflösung bei minimaler Dosis, sondern auch zur Realisierung therapeutischer Szenarien in Kombination mit der Bildgebungsmodalität. Dies führte zur Entwicklung verschiedener MPS-Systeme, die in der Lage sind, SPIONs hinsichtlich ihrer magnetischen Eigenschaften bei den in MPI-Scannern verwendeten Anregungsfrequenzen zu charakterisieren. Die MPS ist ein Messverfahren zur Bestimmung der magnetischen Eigenschaften von SPIONs in einem oszillierenden Magnetfeld. Aktuell MPS-Geräte sind meist nur in der Lage, die Magnetisierungsantwort der SPIONs auf eine oszillierende magnetische Anregung rückwirkend zu messen. Der Syntheseprozess wird dabei unbeobachtet gelassen.

Der erste Teil dieser Arbeit ist dem Design und der Entwicklung eines neuartigen Insitu-Magnetpartikel-Spektrometers (INSPECT) gewidmet, mit dem der gesamte Syntheseprozess von der Partikelgenese über das Wachstum bis hin zur stabilen kolloidalen Suspension der Nanopartikel in Echtzeit überwacht werden kann. INSPECT hat eine Feldstärke von 10 mT mit einer Anregungsfrequenz von 23 kHz. Die für eine Einzelmessung benötigte Zeit beträgt ca. 1 s bei 10 Perioden und 2300 Mittelwerten. Durch die Messung einer einzigen Periode kann die Messzeit auf 46 µs reduziert werden. Das Gerät ist für

den Einsatz in einer biochemischen Laborumgebung geeignet. Es hat eine Kammergröße von 72 mm, was die Verwendung eines Standard-Reaktionskolbens für die Synthese ermöglicht. Für die Fällung auf alkalischer Basis wird die Änderung der magnetischen Eigenschaften von SPIONs während der Keimbildungs- und Wachstumsphase der Synthese demonstriert. Das Gerät kann die Änderungen in den Amplituden- und Phasenspektren und damit die Hysterese aufzeichnen. Damit ist es ein leistungsfähiges Werkzeug für ein vertieftes Verständnis der Bildungsdynamik von Nanopartikeln während des Syntheseprozesses. Im Vergleich zu anderen Echtzeitgeräten wie In-situ-TEM (Transmissionselektronenmikroskopie) und Röntgendiffraktometrie, die immer eine spezielle In-situ-Kammer und -Umgebung für die Analyse erfordern, gibt es bei INSPECT keine solchen Anforderungen. Darüber hinaus sind diese Geräte technisch sehr komplex und erfordern höhere Anwenderkenntnisse. INSPECT ist vollautomatisch, modular, kosteneffektiv und es besteht keine Notwendigkeit für die spezielle Umgebung oder spezielle In-situ-Kammern für Experimente, wodurch sich das Gerät für die Verfolgung der Keimbildung und des Wachstums der SPIONs in der täglichen Forschung eignet.

Der zweite Teil der Arbeit ist den verschiedenen Synthesen gewidmet, die in INSPECT durchgeführt wurden. Hier wird die Anwendung von INSPECT demonstriert, um die Keimbildung und das Wachstum von SPIONs zu verfolgen, die auf der Grundlage eines alkalischen Kopräzipitationsprozesses synthetisiert werden. Zwei Synthesen werden im Detail gezeigt, gefolgt von verschiedenen Experimenten, um die Auswirkungen von Parametern wie Durchflussrate, die Wirkung unterschiedlicher Arten von Beschichtungsmaterial, die Menge an Dextran, das Fehlen von Beschichtungsmaterial und die Auswir -kungen der anfänglichen Kühlung auf die Änderung des magnetischen Moments über die Zeit zu zeigen. Diese Idee wird durch das Aufzeigen der Auswirkungen bestimmter externer Parameter wie Reaktionstemperatur und externe Magnetfelder (statisch und sinusförmig) auf die resultierenden magnetischen Eigenschaften von SPIONs weitergeführt. Die Messungen wurden nicht in INSPECT, sondern in einem 1-D-MPS durchgeführt.

Die Arbeit befasst sich auch mit einem weiteren wichtigen Modul, welches in der Empfangskette von MPI/MPS vorhanden ist und LNA (Low Noise Amplifier; deutsch: rausch -armer Verstärker) genannt wird. Die vorrangige Aufgabe eines LNA besteht darin, das empfangene Signal zu verstärken und gleichzeitig das durch die eigene Schaltung induzierte Rauschen minimal zu halten. In der aktuellen Forschung wird das Design und die Entwicklung von vier verschiedenen LNAs mit primärem Fokus auf das niedrige Eingangsrauschen und die beste NF (Noise Figure; deutsch:Rauschzahl) beschrieben. Zur Minderung des Eingangsrauschens basieren alle LNAs auf der Summenkonfigura-

tion, die auch als Parallelisierung bekannt ist. Zwei der LNAs sind Single-Ended-LNAs mit unterschiedlichen Rauscheigenschaften und unterschiedlichem Parallelisierungsgrad. Daran schließen sich ein VGA (Variable Gain Amplifier; deutsch Verstärker mit variabler Verstärkung) und ein FDA (Fully Differential Amplifier; deutsch: volldifferenzieller Verstärker) für verschiedene MPI/MPS-basierte Anwendungen an. Einer der Single-Ended-LNAs mit 16 parallel geschalteten Operationsverstärkern hat ein Eingangsrauschen von ca. 653 pV/ $\sqrt{\text{Hz}}$ bei einem NF (Noise Figure) von 3,32 dB mit einer 50 Ω-Terminierung. Der andere Single-Ended-LNA mit 4 parallel geschalteten Operationsverstärkern hat ein Eingangsrauschen von 1,1 nV/ $\sqrt{\text{Hz}}$ mit einem NF von 7,87 dB bei gleicher Terminierung. Darauf folgt ein rauscharmer VGA mit 8 parallel geschalteten Operationsverstärkern, der ein Eingangsrauschen von 868 pV/ $\sqrt{\text{Hz}}$ und einer NF von 1,86 dB bei 50 Ω-Terminierung aufweist. Die Verstärkung des VGA kann von -11 dB bis 30 dB variiert werden. Abschließend wird ein rauscharmer FDA mit eingebauter Schutzschaltung zur Vermeidung von Schäden an der Erfassungskarte durch hohe Spannungen beschrieben. Der FDA hat ein Eingangsrauschen von ca. 1,76 nV/ $\sqrt{\text{Hz}}$ mit einer NF von 11,93 dB bei einer Terminierung von 50 Ω.

Der wichtigste Beitrag dieser Arbeit im Kontext der aktuellen Forschung ist, dass hier die ersten Schritte dargestellt werden, die für die Beobachtung und Manipulation der Keimbildung und des Wachstums von SPIONs erforderlich sind, indem Änderungen des magnetischen Moments in Echtzeit erfasst und dann interne und externe Parameter für die Synthese von SPIONs manipuliert werden. Diese sind für verschiedene diagnostische und therapeutische Anwendungen von MPI geeignet und ihre gezielte Anpassung für diverse Anwendungsszenarien erhöht die Möglichkeiten dieser Bildgebungstechnik.

# Contents

# List of Figures

# List of Tables

# 1

# Introduction and motivation

## Contents



Over the last few years, magnetic nanoparticles are being widely used for different industrial and research applications, including medicine. The extent of usage in medicine relies on the physical properties of the nanoparticles, biocompatibility in moderate doses and well known iron metabolism pathways. Moreover, the magnetic nanoparticles can be synthesized in different shapes and sizes with high biofunctionalization potential which makes it stand out in comparison to other nanotechnology-based therapeutic and diagnostic approaches. Magnetic nanoparticles have improved the existing imaging modalities such as MRI (magnetic resonance imaging) for immunological diseases, cancer, and even cerebrovascular pathologies. Due to their size and physical properties, magnetic nanoparticles can serve as a cell tracking system for cell-based therapies as well for therapeutic applications such as hyperthermia for tumor cells. One more imaging modality where magnetic nanoparticles have found a niche is MPI (magnetic particle imaging). MPI is an emerging imaging modality for quantitative analysis regarding the spatial distribution

of the magnetic nanoparticles inside a tissue. The first images using an MPI scanner were published in 2005. MPI relies on the superparamagnetism of the magnetic nanoparticles which is widely seen in ferromagnetic or ferrimagnetic nanoparticles. The magnetic nanoparticles used in MPI are often called as SPIONs (superparamagnetic iron oxide nanoparticles). As the overall quality of the image is highly dependent on the SPIONs, the magnetic and physical properties of the SPIONs become highly important. There are a number of devices to characterize the magnetic properties of the SPIONs such as MPS (magnetic particle spectrometer) and VSM (vibrating sample magnetometer). However, both of these devices are designed to be used on synthesized particles and hence the synthesis process is left completely unobserved and there is no information regarding the nucleation and growth of the SPIONs. There are other techniques available to study the nucleation and growth of the SPIONs such as real-time TEM (transmission electron microscopy) and X-ray scattering. Unfortunately, all these devices require special synthesis chambers as well as user experience to get useful results. Moreover, these devices are exorbitant in price and are technically complex. Hence, there is a need for better and efficient technique therefore, this work mainly focuses on a novel device called INSPECT (in-situ magnetic particle spectrometer) for real-time analysis of the complete synthesis process. With INSPECT, tracking the nucleation and growth of the SPIONs is very easy as the synthesis can be carried out in a normal glass flask used in a chemistry laboratory. Furthermore, in another part of the thesis the focus is on the LNA (low noise amplifiers) which amplifies the received signals from the excited SPIONs to the dynamic range of the acquisition device. Usually, LNAs are an integral part of conventional MPI/MPS device.

## 1.1 Outline

This work mainly focuses on the design, development, and evaluation of the INSPECT. The physical principle of the INSPECT and an MPS are quiet similar but INSPECT comprises of lesser modules in comparison to a conventional MPS device. This makes INSPECT low-cost, portable and user-friendly for tracking the nucleation and growth of the SPIONs. To evaluate the performance of the INSPECT, the nucleation and growth of the synthesis process based on the alkaline co-precipitation are performed. Change in the magnetic moment with time is shown for two different experiments (with and without coating material). The measurements from the INSPECT comprises of the amplitude and the phase spectra. Moreover, the dynamic magnetization curves for every measurement are also plotted. Furthermore, four different LNAs based on the summing configuration are designed and developed. The performance of the LNAs is evaluated according to

their noise characteristics.

## 1.2 Originality of the thesis

The originality of the work can be summarized as follows:

- Design and development of a novel magnetic particle spectrometer called INSPECT to study the nucleation and growth of SPIONs.
- Tracking the nucleation and growth of SPIONs during the synthesis process with and without coating material.
- Illustrating the effects of the quantity of coating material (dextran), flow rate, ultrasound frequency and temperature on the nucleation and growth of the SPIONs.
- Illustrating the effects of steering or manipulating the nucleation and growth of the SPIONs with external parameters such as AC and DC magnetic fields.
- Providing a road-map to steer and manipulate the growth of the SPIONs with different hardware scenarios.
- Design, development, and evaluation of application-based LNAs for different MPI and MPS systems.

## 1.3 Published work

During the course of the research, the author published research work on the design of different LNAs for MPI and MPS [O1][O2] and [O3]. Some research work was also published dealing with the synthesis of the SPIONs [O4][O5][O6]. Research work related to INSPECT as well as for tracking the nucleation and growth of the SPIONs is published in [O7] and in two patent applications [O8] and [O9]. Other collaborated articles published are [O10][O11] [O12].

## 1.4 Thesis organization

Chapter 1 goes through with the main aim and scope of the research work.

Chapter 2 deals with the basic physical and chemical principles used throughout this work. The basic idea behind MPI, comprising from signal generation to reconstruction

is explained. This chapter also provides a brief introduction to the synthesis technique used for evaluating INSPECT as well as fundamentals of nucleation and growth of the SPIONs. Moreover, fundamentals regarding the Op-amps (operational amplifiers) and FDA (fully differential amplifiers) are also explained. Furthermore, a brief introduction to the noise in different electrical and electronic circuits is explained. As well as evaluation and calculation of noise in Op-amps and FDA are introduced.

Chapter 3 deals with the technical considerations of an MPS device in general. A brief introduction is given regarding the different signal chains (send and receive chain) required for an MPS device followed by an explanation of different modules present in an MPS device.

Chapter 4 exclusively deals with the design and development of different LNAs, which is one of the most important modules for any MPI or MPS device. This chapter mainly covers different LNAs with single ended fixed gains, VGA (variable gain amplifier) and FDA (fully differential amplifier). Evaluation of the noise characteristics comprises of input noise, output noise, and noise figure (NF). Moreover, it also illustrates a protection circuit for protecting the acquisition card from high voltage and currents which are quite common in MPI and MPS hardware.

Chapter 5 deals with the design and development of INSPECT. In this chapter, all the different modules needed for INSPECT are explained, starting from the signal generation to acquisition.

Chapter 6 explains the measurements pertaining to nucleation and growth of the SPIONs obtained through the INSPECT. Two complete synthesis processes (in the presence of coating material and without the coating material) based on alkaline co-precipitation method are explained. Moreover, this chapter also explains the effects of some of the key parameters such as flow rate and amount of dextran on the nucleation and growth of the SPIONs.

Chapter 7 deals with steering or manipulating the nucleation and growth of SPIONs by external factors such as the presence of alternating current (AC), direct current (DC) magnetic fields, ultrasound frequency, synthesis temperature, etc. In this chapter different syntheses are performed and compared.

Chapter 8 gives a brief conclusion regarding the complete research followed by chapter 9 dealing with the summary and future outlook. Chapter 9 also gives a roadmap for construction of different hardware setups for manipulating nucleation and growth of SPIONs by addition of external magnetic fields to the synthesis process.

# 2 Basics

## Contents



In this chapter, the underlying physical and chemical principles regarding the current research are explained. Section 2.1 consists of the physical principles which are being exploited for MPI, starting with the signal generation to the acquisition of the signals

from SPIONs followed by a short description of MPS in Section 2.2. Section 2.4 gives a brief introduction regarding the different physical properties of the SPIONs which play an essential role for the MPI and MPS. Section 2.5 deals with the different chemical techniques which can be used for the synthesis of the SPIONs. Followed by Section 2.6, that deals with the fundamentals of the nucleation and growth of the SPIONs in general. From Section 2.7 to Section 2.10, the focus is laid on the theory regarding the evaluation of noise in Op-amps and FDAs.

## 2.1 Magnetic particle imaging

MPI is an imaging modality providing quantitative information regarding the spatial distribution of the magnetic structures such as SPIONs (superparamagnetic iron oxide nanoparticles) in a specified region which is also termed as FOV (field of view). MPI was first introduced in 2005 by Gleich and Weizenecker and relies on the non-linear behaviour of the SPIONs for acquiring images. The technique allows the acquisition of high contrast three-dimensional images of the SPIONs distribution in the FOV with very high temporal and spatial resolution. The physics behind the visualization is due to special properties of the SPIONs that they can be magnetically saturated providing a characteristic response consisting of harmonics. It is one of the techniques in which the SPIONs are the source of the signal and hence playing an essential role in determining the resolution of the acquired images. As the strength of the acquired signal from the SPIONs is dependent on the concentration as well as the physical properties of SPIONs, therefore, immense research is undertaken for the development and characterization of these SPIONs. The spatial resolution can be less than 1 mm and the images can be acquired with high speeds of more than 40 volumes per second [13][14]. With further advancement in the development of SPIONs, the acquisition can become much faster with better temporal and spatial resolution while administering lower dosage. In this section, a basic concept for the generation of the excitation signal, acquiring the SPIONs characteristic response as well as the principle of spatial encoding in MPI is explained.

### 2.1.1 Signal generation and acquisition

For the generation of the signals, the SPIONs are excited with a varying magnetic field at a specific frequency $f_0$ with a high amplitude A. This applied field is known as an excitation field and the primary function is to change the direction of the magnetization of the SPIONs. This induces a voltage signal in the receive coil and as the response of the

SPIONs is non-linear, the Fourier transform of the magnetization over time M(t) consists of the excitation frequency as well as the subsequent higher harmonics. The number of harmonics, as well as the amplitude of these harmonics, are dependent on the sensitivity of the scanner as well as the physical characteristics of the SPIONs. The relationship between the particle concentration and the induced voltage in the receiving coil is assumed to be linear [13]. Moreover, further investigation has been done from different research groups to validate this hypothesis [15][16][17]. As the excitation frequency is known, hence it is very easy to separate the excitation signal and the characteristic response from the SPIONs. The response of the SPIONs is acquired with the help of an electromagnetic receiving coil. This is based on the principles of mutual inductance and induces a voltage in the receiving coil which attributes to the characteristic response of SPIONs. Figure 2.1 shows the basic concept of MPI. In the non-saturated region, due to the behaviour of the SPIONs, a voltage is induced in the receiving coil. The signal spectrum consists of the excitation frequency $f_0$ and the subsequent higher harmonics which is attributed to the characteristic SPIONs' response. The excitation signal could be order of magnitudes higher in amplitude in comparison to the SPION's response and hence must be attenuated. There are different ways to achieve attenuation such as using analog filters (e.g. bandstop filters) or compensation coils or a combination of both the techniques [18]. A comparison of these techniques is well explained by Graeser *et al.* [19]. There are other techniques which can also be used for attenuating the excitation signal such as cancellation unit [20] and perpendicular sensing [21]. In the saturated region, the amplitude of the induced signal in the receiving coil is negligible. Hence, the signal spectrum is free from the characteristic SPIONs response. In Figure 2.1, M is the magnetization of the SPIONs, H is the strength of the magnetic field, $H_D$ is the field strength of the excitation field, t is the time, u is the induced voltage signal in the receiving coil and $\hat{u}$ is the Fourier transform of the voltage signal u [22].

### 2.1.2 Spatial encoding in MPI

All the particles present in the magnetic field get excited and lead to the generation of the signal, this could be referred to as a zero-dimensional MPI. But for imaging in a three-dimensional volume, only a small volume of particles must get excited in a defined region called FFR (field free region). One way of achieving this is to superimpose the excitation field with a static magnetic or an offset magnetic field so that the other particles in the vicinity remain saturated. This is shown in Figure 2.1 in the unsaturated region. In the saturated region, the change in magnetization over time becomes smaller and hence no voltage signal is induced in the receiving coil leading to no or a negligible particle

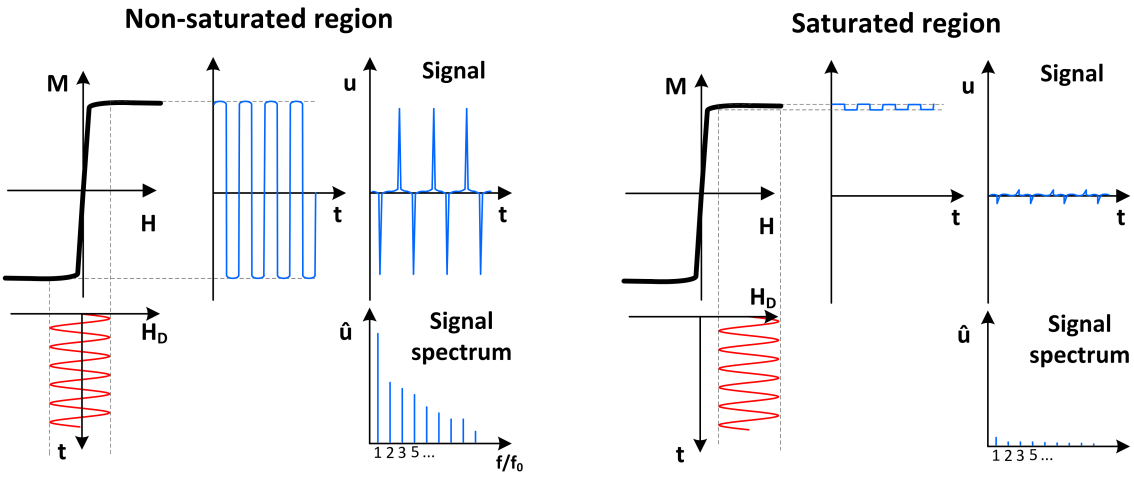


Figure 2.1: Basic concept of MPI: The non-saturated region consisting of the SPIONs response in the Fourier domain as can be seen in the signal spectrum. The first harmonic is generated due to the excitation frequency as well as the SPION response but the subsequent higher harmonics are only generated due to the response of the SPIONs. The SPIONs present in or near the non-saturated region produce the characteristic signal. On the other hand, the saturated region produces no or a negligible SPIONs response. In the figure, M is the magnetization of the SPIONs'; H is strength of the magnetic field; $H_D$ is the field strength in the saturated region; t is the time; u is the induced voltage signal in the receiving coil; û is the Fourier transform of the voltage signal u [22]

.

spectrum. The size of the FFR and the achievable resolution is strongly dependent on the gradient of the generated magnetic field in x, y, and z-direction. Such a field can be referred to as a selection field and can be generated by using Maxwell-coil pairs. This leads to the generation of an FFP (field free point). With an FFP, only the particles which are in or at close vicinity to the FFP generates the characteristic response and other regions become saturated. In other words, most of the MPI signal is generated from the position where the magnetic flux density is in the range of a few millitesla. Instead of an FFP, an alternative encoding concept called field free line (FFL) can be used. The only difference between an FFP and an FFL is the change in the shape of the region which produces the MPI signal. FFL promises increased sensitivity of the imaging system [23][24][25]. Figure 2.2 shows an illustration of a generated FFP and FFL.

For the acquisition of the signal in a larger FOV, it is important to move the FFP or FFL throughout the region. To achieve this movement another magnetic field called drive field is used. The drive field can be generated predominately by two methods. In the first method either a mechanical shift of the object in the FOV or by using another set of coils to move the FFP or FFL electromagnetically can be applied. The first method is being

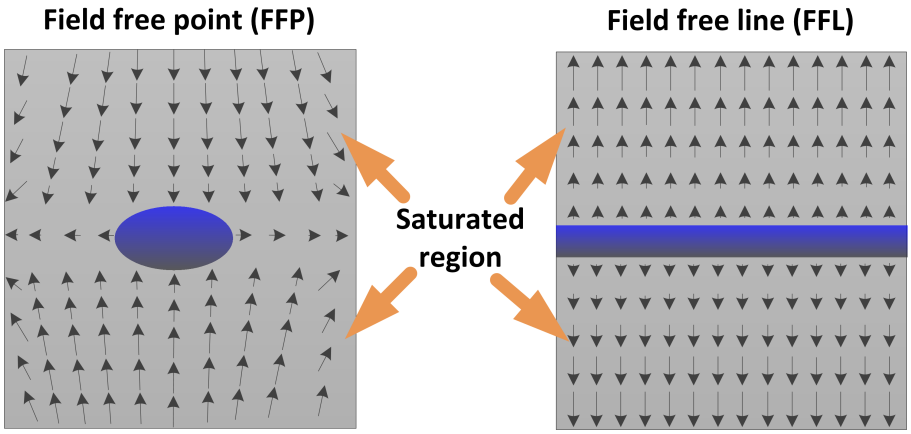


Figure 2.2: An illustration of FFP and FFL in an imaging device. The SPIONs in and near the vicinity of the FFP or FFL respond to the excitation signal, hence producing MPI signals. On the other hand, SPIONs outside FFP or FFL are magnetically saturated and hence do not contribute to the MPI signal. This provides a spatial encoding of the SPIONs in the three-dimensional space.

used by scanners from Berkeley group [26][27][28][29].

In the second method, different trajectories are used in a reasonable time frame to achieve the movement of the FFP or FFL in the complete FOV. For example, Lissajous trajectory which is being used in various imaging scanners [30]. Lissajous trajectory provides a fast movement and good coverage of the FOV by moving the FFP or FFL electromagnetically with the help of the drive and focus fields. Another possible way of achieving spatial encoding is by using traveling wave MPI. In traveling wave MPI the gradient of the saturating particles is not static but moves electromagnetically in one direction by a set of coils covering the complete FOV [31].

### 2.1.3 Reconstruction

There are different approaches to reconstruct the spatial distribution of the SPION concentration from the received voltage signal [32][33][34]. All these approaches are evaluated according to their computational effort and reconstruction time while gaining sufficient image quality. For the existing imaging devices, the reconstruction is carried out primarily by two different methods. The first method is called system matrix-based reconstruction [14][33][32]. In this method, a known SPION sample (calibration sample) is moved in the FOV and the response of the SPIONs is recorded to acquire a system matrix [15][35]. Usually, this movement is achieved with the help of a robot and depending on the size of FOV the whole process can be time-consuming. Moreover, the

size of the calibration sample and the volume of SPIONs inside the sample influences the resolution of the constructed image. According to Knopp *et al.*, the size of the calibration sample influences the SNR (signal to noise ratio) of the measured system matrix and the spatial discretization affecting the image quality [36]. In the second method, a direct reconstruction is performed by a mathematical approach with certain idealized assumptions [37][38]. In this approach, the system matrix is simulated with maximum SNR and arbitrary discretization, but still more research is needed as realistic particle models are absent. There is another method called x-space reconstruction which is also based on direct reconstruction with some idealized mathematical assumptions, the details of this method can be found in [34].

A system matrix represents a complete calibration of an MPI system as it includes the response of the SPIONs at every position inside the scanner. With the help of the system matrix, it is possible to differentiate the signal of all the SPIONs encoded inside the received signal according to their spatial position. Therefore, the relationship between the system matrix **S**, received signal **u** and the particle concentration **c**, can be defined by Equation 2.1.

$$\mathbf{Sc} = \mathbf{u} \tag{2.1}$$

To solve the minimization problem through this system of equations, ideally, an iterative solver combined with regularization techniques is used. Moreover regularization techniques are important as it is an ill-posed inverse problem and can be represented by Equation 2.2.

$$\| \mathbf{Sc\text{-}u} \|_{\mathbf{w}}^2 + \lambda \| \mathbf{c} \|_2^2 \xrightarrow{\mathbf{c}} min \tag{2.2}$$

Where $\lambda$ denotes the regularization parameter to control the influence of the regularization on the reconstructed image. **w** corresponds to the weighted matrix to suppress the measurements with a bad SNR. SNR has a strong influence on the resolution of the reconstructed image in this particular method. One drawback of the system matrix approach is the time needed to measure the calibration matrix. This is because the calibration sample has to be dimensionally moved throughout the imaging region of the scanner in discrete steps. Currently, the system matrix-based approach provides the best accuracy as the matrix contains the imperfections of the magnetic fields as well as the complex particle response. So far a lot of reconstruction results have been published based on system matrix-based approach [14][39][40][41]. Another approach to decrease the time needed to measure the system matrix is by using a hybrid system matrix approach [42].

In the hybrid system matrix approach, the response of the SPIONs is measured in an MPS device which is capable of emulating the imaging system's field geometry [43][44][45]. Due to this approach, there is no need to move the calibration sample mechanically and hence reducing the acquisition time drastically. As stated earlier another possibility is the reconstruction based on an x-space reconstruction [34]. The method is based on the assumptions regarding the homogeneity of the applied field and the particle's behaviour in the applied field. A simplified equation describing the x-space method is given by Goodwill *et al.* in [34].

$$c(x) = \frac{u(x)}{v_{FFP}(x)} \tag{2.3}$$

When all the assumptions are fulfilled, Equation 2.3 can be used for determining the SPION concentration $c(x)$. In the Equation 2.3, $u(x)$ is the voltage signal acquired at position $x$ with the corresponding FFP velocity $v_{FFP}(x)$ [46]. But the resulting images are blurry due to the relaxation effects and have to be post-processed using a deconvolution kernel hence making it a two-step process. When comparing it with the system matrix approach the computation effort and time consumed are relatively lower. Some of the reconstruction procedures and the obtained reconstructed images based on x-space reconstruction are shown in [46][26].

## 2.2 Magnetic particle spectroscopy

Magnetic particle spectroscopy is also known as zero-dimensional MPI and conceptually very similar to an MPI scanner. Instead of scanning an image, MPS provides an overview regarding the physical properties of SPIONs used for MPI. MPS is a characterization tool for different SPIONs providing information regarding the magnetic properties of the nanoparticles. The measurements usually consist of amplitude and phase spectra of the nanoparticles. The amplitude spectra contain both the even and odd harmonics, odd harmonics consists of the characteristic particle response and even harmonics are due to earth magnetic field or offsets present inside the field generator. Furthermore, it also provides information regarding the magnetization curve as well as geometrical properties such as the diameter of the SPIONs [20] and hydrodynamic diameter [47]. Moreover, it is a powerful tool to study the effects of different parameters on the response of SPIONs such as temperature [48] and binding status [49]. As it is a powerful tool for analyzing different magnetic nanoparticles, therefore different variants of MPS are present or under research for various applications which help in understanding the physics behind the nanoparticles

and helps in the synthesis of new SPIONs for various imaging and therapeutic applications. Contrary to imaging scanners, the MPS device does not need spatial encoding and the sample volume is usually not more than 20 µL. This provides a characterization device which is low cost, smaller in size and with lower instrumentation complexity. For performing a measurement in an MPS a time-varying magnetic field is applied to SPIONs and the particle response is recorded. The amplitude of the particle response corresponds directly to the concentration of the SPIONs contained in the measured sample. This can also provide information regarding the SPIONs uptake in the specific cell lines, tissues or lymph nodes and hence providing information regarding the efficacy of functionalized SPIONs.

In recent times, a lot of advances have been made to improve the sensitivity and signal purity of MPS devices [19][50]. Different variants of MPS both in commercial and research field are already present. All these MPS devices are designed for specific applications such as zero-dimensional MPS without offset field and with different excitation frequencies [51][20]. A two-dimensional MPS for simulating a Lissajous trajectory and analyzing the response of the SPIONs in both x and y-direction is also available [18]. A three-dimensional MPS can emulate magnetic fields inside an MPI scanner and can be used for constructing a hybrid matrix at a much faster rate compared to scanner-based approaches [42]. For image reconstruction, the inverse problem can be solved by using a system matrix. System matrix defines the relationship between the measured signals and the spatial position of the SPIONs as mentioned in the previous section. The hybrid approach is much faster than the conventional measurement-based method. In the measurement-based method, a known SPION sample (calibration sample) is measured in a FOV at different spatial locations by mechanically moving the calibration sample with a robot. In the hybrid method, the magnetic fields of the scanners are emulated in the three-dimensional MPS. Removing the need to mechanically move the calibration sample and hence reducing the acquisition time [43][44][45].

This research work deals with a new variant of a one-dimensional MPS with an application focus on tracking the nucleation and growth of SPIONs undergoing synthesis. Throughout the thesis, this device will be referred to as INSPECT (in-situ magnetic particle spectrometer). INSPECT provides an overview of different parameters which affects the nucleation and growth of the SPIONs in a synthesis environment. Further details regarding the construction, calibration and the obtained measurements results will be discussed in Chapter 5 and Chapter 6, respectively.

## 2.3 Nanoparticles

There are different ways of classifying nanoparticles depending upon their shape, size, morphology, physical, and chemical characteristics. Figure 2.3 shows different types of nanoparticles due to their different chemical compositions. According to their chemical composition, the nanoparticles can be ceramic, carbon-based, metallic, polymeric, lipid-based, and semiconductor nanoparticles. Figure 2.3 provide an overview of different nanoparticles based on the above classification. Further details of these nanoparticles can be found in the research published by Lu *et al.* [52], Puri *et al.* [53], and other research papers cited therein. The target group for this thesis is magnetic nanoparticles and the focus is on nanoparticles made up of superparamagnetic iron-oxide cores. These nanoparticles are widely known as SPIONs.

## 2.4 Superparamagnetic iron oxide nanoparticles (SPIONs)

In the last two decades, magnetic nanoparticles have attracted much interest because of their magnetic and electrical properties in bulk phases. Nanoparticles are extensively used in several biomedical applications such as drug delivery [54], MRI [55][56], cell labeling and sorting [57] as well as in therapeutic applications such as hyperthermia or AC magnetic field-assisted cancer therapy [58][59][60]. These SPIONs also take the center stage in MPI, as the whole imaging modality is based on the SPION response to generated fields in the scanner. All the physical properties such as shape, size, magnetic properties, etc. play an essential role in the final reconstructed image, but there are two characteristic properties which make them well suited to MPI. Firstly, the SPIONs are superparamagnetic and hence do not show any remanent magnetization in the absence of an excitation field. This effect is due to Brownian and Néel relaxation, which causes a change in the magnetization direction even at room temperature, thereby helping in localization of the SPIONs in a region of interest. Secondly, SPIONs exhibit a nonlinear magnetization which is also responsible for generation of harmonics and therefore can be magnetically saturated. This provides a method to separate the SPION response from the excitation or the drive-field signal hence, pinpointing their exact location in the FOV i.e. spatial encoding. Besides the magnetic properties, the spatial resolution and sensitivity are also influenced by the other properties of SPIONs such as the concentration of iron oxide, core diameter, hydrodynamic diameter, as well as shape. Figure 2.4 illustrates a schematic model of a single SPION. A single SPION consists of an iron-oxide

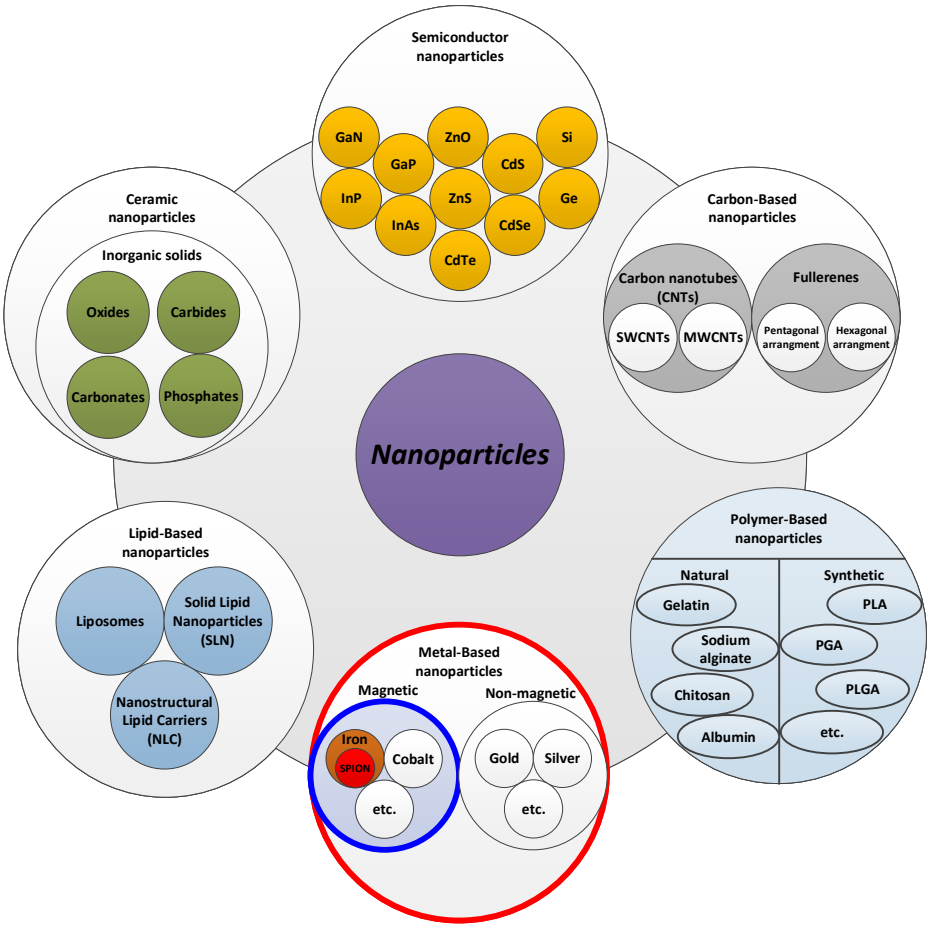


Figure 2.3: Classification of nanoparticles based on their chemical composition. The nanoparticles can be ceramic, carbon-based, metal nanoparticles, polymeric nanoparticles, lipid-based nanoparticles, and semiconductor nanoparticles. In this thesis, the focus will be on the magnetic nanoparticles consisting of an iron-oxide core with superparamagnetic behaviour called SPIONs. In the figure, SWCNT: single-walled carbon nanotubes; MWCNT: multi-walled carbon nanotubes; PLA: Polylactides; PGA: Polyglycolides; PLGA: Poly(lactide co-glycolides) [52][53].

core surrounded with a coating material but multi-core particles have at least two cores surrounded by the coating material. The diameter of the core is known as core diameter ($d_c$) and the diameter including the coating material is known as hydrodynamic diameter ($d_h$). Diverse applications require different coating materials. Some of the coating materials which are widely used are dextran, silica, starch, PEG (polyethylene glycol), PEI (polyethyleneimine), amino acids, etc [61][62][52].

Spatial resolution and sensitivity are largely influenced by the characteristic properties of the SPIONs. When focusing on the magnetic properties of the SPIONs, the di-

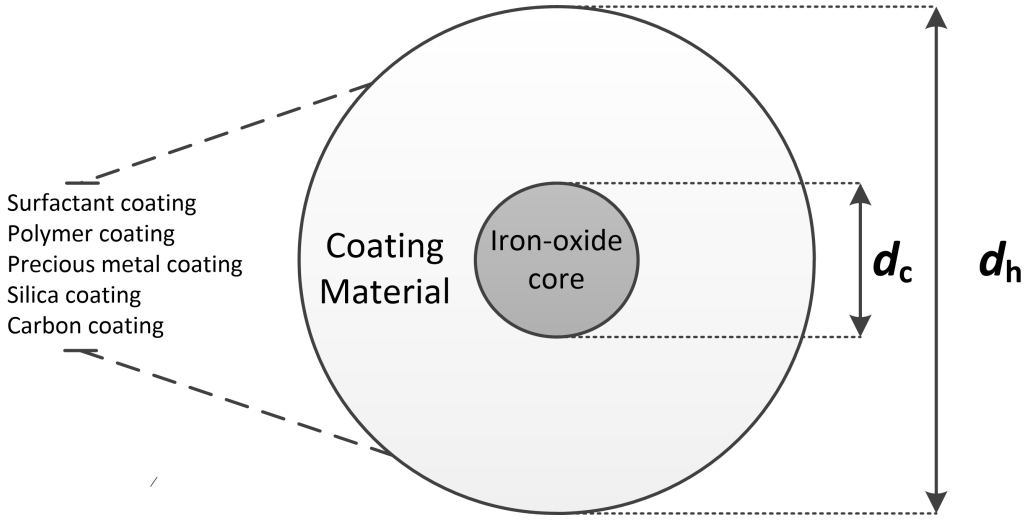


Figure 2.4: Schematic model of a single SPION consisting of an iron-oxide core ($d_c$) with a hydrodynamic diameter ($d_h$). The iron-oxide core usually consists of magnetite or hematite. The coating material ranges from polymers to silica coating and is widely dependent on the application area. One of the widely used coating material for MPI is different variants of a polysaccharide called dextran. Dextran provides the needed biocompatibility and contains branches of $\alpha$-1,3 which could be used for further functionalization.

ameter of the iron-oxide core ($d_c$) plays an essential role in determining the resolution of the SPIONs in an imaging device. The magnetic moment of the SPIONs directly affects the sensitivity and in turn, is affected by the core diameter. An increase in the core diameter leads to an increase in the strength of the received signal, thus affecting the magnetic moment [63]. Besides the strength of the gradient field, the spatial resolution mainly relies on the slope of the SPIONs magnetization curve. A high steepness in the slope of the magnetization curve leads to an increase in the spatial resolution as the received signal can be resolved from even smaller areas [35][64].

Some of the general properties which are essential to ensure that the SPIONs are useful for MPI are:

- narrow size distribution or uniform size [65][66]
- high and uniform superparamagnetic moment [65][66][67]
- high colloidal stability [67]
- high biocompatibility and low toxicity [67]

### 2.4.1 Size

After the magnetic properties, the size of the SPIONs is unarguably the most important parameter for MPI. There is an informal classification for nomenclature depending on the size range. The particles between 50 and 180 nm are called SPIONs (superparamagnetic iron oxide nanoparticles); between 10 and 50 nm, USPIONs (ultra-small superparamagnetic iron oxide nanoparticles); and below 10 nm, VSPIONs (very small superparamagnetic iron oxide nanoparticles) [62]. The size of the SPIONs significantly affects the dynamics of the magnetic moment and is also vital for the detection, internalization and eventual fate of SPIONs inside mammalians. From the biological point of view, all these particles can easily travel through the circulatory system as the smallest capillaries are approximately 4 µm to 6 µm wide [68]. But for quick endocytosis, the size should not exceed 35 nm [62] and for tumor penetration, the size should be around 4 nm [69]. The size directly affects the relaxation time which is discussed in the subsequent section.

#### 2.4.1.1 Relaxation mechanisms of SPIONs

In a bulk ferromagnet tries to minimize its internal energy by splitting into magnetic domains [70]. But there comes a point where the required energy to form domains is not sufficient and therefore, magnetostatic energy competes with one another, favoring single domain particles [71][72]. These single-domain particles stay superparamagnetic and bear relaxations because the torque rotates between the crystallographic property axes. However, the time-averaged bulk magnetization continues to be zero. For single-domain particle, the magnetization vector can be defined by Equation 2.4[72].

$$M = VM_0\hat{n} \tag{2.4}$$

Where $V$ is the magnetic volume of the particle with diameter $d_c$ and is given by Equation 2.5. $M_0$ is the saturation magnetization and $\hat{n}$ is a unit vector pointing in the direction of magnetization.

$$V = \frac{\pi d_c^3}{6} \tag{2.5}$$

The magnetic energy for the uniaxial anisotropy is given by Equation 2.6.

$$E = VK\sin^2\theta \tag{2.6}$$

Where $K$ defines the anisotropy constant and $\theta$ is the angle between the direction of

uniaxial anisotropy and unit vector $\hat{n}$. Therefore due to thermal fluctuations, a magnetic reversal can take place inside the particle by overcoming the energy barrier represented by Equation 2.6. This switching and reversal time is known as Néel relaxation time $\tau_N$ and is described by Equation 2.7, where $k_B$ is the Boltzmann constant, $T$ is the temperature and $\tau_0$ represents the attempt period or attempt time and is material dependent and typically ranges between $10^{-9}$ to $10^{-10}$ seconds [71].

$$\tau_N = \tau_0 e^{\frac{VK}{k_B T}} \tag{2.7}$$

The other mechanism for relaxation is called Brownian relaxation and is due to the physical rotation of the particle within the suspending medium due to thermal fluctuations. Usually, for biomedical applications, the particles are suspended in a fluid, but when occurring in solid-state, the Brownian relaxation is canceled or mitigated. The Brownian relaxation time $\tau_B$ is given by Equation 2.8. [72]

$$\tau_B = \frac{\pi \eta d_h^3}{2 k_B T} \tag{2.8}$$

Where $d_h$ is the hydrodynamic diameter and $\eta$ is the dynamic viscosity of the carrier medium in which the nanoparticles are suspended. As it can be inferred from Equation 2.7 and Equation 2.8, both relaxation times depend on the size of the particles whether its core diameter or the hydrodynamic diameter. While Néel relaxation time $\tau_N$ increases exponentially, Brownian relaxation time $\tau_B$ increases with a power of three with the increase in nanoparticle dimensions. As both $\tau_N$ and $\tau_B$ play an essential role in determining the overall particle response, the combined effective relaxation time ($\tau_e$) can be given by Equation 2.9.

$$\tau_e = \frac{1}{\tau_N} + \frac{1}{\tau_B} = \frac{\tau_N + \tau_B}{\tau_N \tau_B} \tag{2.9}$$

In other words, Néel relaxation represents the internal switching of the magnetization due to thermal fluctuations and Brownian relaxation is the physical rotation of the particles in the medium. For SPIONs in MPI, the dominating relaxation mechanism is the Néel relaxation [22]. Therefore, Brownian and Néel relaxation time ($\tau_B$ and $\tau_N$ respectively) determines the particle response to the time-varying field and is a key parameter for the sensitivity and spatial resolution. Hence, it is desirable to have SPIONs with bigger core diameter but it should not exceed the critical diameter as the particles lose their superparamagnetism. There has been immense research and development for the synthesis of SPIONs useful in MPI and furthermore, a parallel development of MPS devices to char-

acterize these SPIONs [73]. It has been found that the particles with a core diameter of 20 nm and a hydrodynamic diameter of 30 nm showed the best MPI performance [74].

### 2.4.2 Shape

The shape of the core of the nanoparticles also effects the magnetic properties of the SPIONs. Moreover, the shape of the nanoparticles are distorted ellipsoids leading to a change in the energy of magnetic anisotropy. Usually, the overall magnetization of the SPIONs is zero but at the surface of the nanoparticles, there are free poles which generate a demagnetizing field $H_{\text{demag}}$. $H_{\text{demag}}$ works opposite to the external excitation field $H_{\text{ext}}$ and is heavily dependent on the shape of the SPIONs. This leads to change in the effective excitation field $H_{\text{eff}}$ and for spherical nanoparticles, it could be given by Equation 2.10. Where $M$ represents the magnetization of the particles and $N$ corresponds to the so-called demagnetization factor. For spherical nanoparticles $N = 1$ as there is even distribution of the free poles on the surface of SPIONs. [75]

$$H_{\text{eff}} = H_{\text{ext}} - H_{\text{demag}} \tag{2.10}$$

$$H_{\text{demag}} = N \cdot M \tag{2.11}$$

For distorted ellipsoids, the anisotropy can be given by Equation 2.12. Where $\mu_0$ is the permeability of the free space, $M_s$ is the saturation magnetization, $N_x$ and $N_z$ are the demagnetization factors arising due to the difference in the aspect ratio or the shape of the SPIONs.

$$E_{\text{shape}} = \frac{2}{\mu_0 M_s^2 (N_x - N_z)} \tag{2.12}$$

On the biological side, the shape and the aspect ratio of SPIONs determine the extent of interaction with membrane receptors and hence the degree of internalization. For example, SPIONs with increasing aspect ratio and decreasing particle sizes produce more favorable conditions for endocytosis [76]. Finally, the fate of the administered SPIONs in any living organism is determined by the shape of these particles [68].

## 2.5 Synthesis technique for SPIONs

There are several approaches to synthesize SPIONs for different biomedical applications. The three most investigated processes for synthesizing SPIONs are alkaline co-precipitation in water, water-in-oil micro-emulsions and thermal decomposition of organo-metallic iron in organic solvents [70]. In the current research, the focus is on SPIONs useful for MPI and its applications such as hyperthermia. The alkaline co-precipitation process is used for the validation of INSPECT and will be discussed in detail. It is one of the simple and common methods to synthesize SPIONs in large quantities but can lead to a broad core-size distribution [77][65]. A stoichiometric mixture of ferric and ferrous salts in an aqueous medium is used for the preparation of SPIONs, which could be either magnetite ($Fe_3O_4$) or maghemite ($\gamma Fe_2O_3$). It is difficult to structurally differentiate between magnetite and maghemite but both have different magnetic properties. The difference lies in the spinal structure of a crystal (smallest block of atoms); magnetite occupies positions in the octahedral and tetrahedral lattices of these crystals [78]. Contrarily, maghemite has cationic vacancies in the octahedral position [78]. This difference in the crystal structure results in the difference of the net spontaneous magnetization. According to Corot *et al.* at 300 °K, the magnetite has a net spontaneous magnetization of 92 emu/g and maghemite has 78 emu/g [79]. As the magnetic moment of magnetite is higher than maghemite, it is more suitable for MPI and its associated applications, as higher amplitude signal at the receiving coil can be obtained by using the same concentration of iron. The SPIONs are prepared with a specific ratio (2:1) of iron salts, i.e. $Fe^{2+}$ and $Fe^{3+}$ in a pH range of 8 to 14. Jolivet *et al.* conducted a compressive study regarding the effects of the ratio of $Fe^{2+}/Fe^{3+}$ on magnetic properties, size, and shape [80]. Other pieces of literature also confirmed that the ratio between 0.4 to 0.6 produce the most monodisperse particles and correspond to the magnetite stoichiometry [80][81][82].

The chemical reaction is a two-step process and the corresponding chemical equations are shown in Equation 2.13 and Equation 2.14.

$$2Fe^{3+} + Fe^{2+} + 8OH^- \longrightarrow Fe(OH)_2 + 2Fe(OH)_3 \tag{2.13}$$

$$Fe(OH)_2 + 2Fe(OH)_3 \longrightarrow Fe_3O_4 + 4H_2O \tag{2.14}$$

For the synthesis, a mixture of iron salts ($Fe^{2+}$ & $Fe^{3+}$) and dextran $[H(C_6H_{10}O_5) \times OH]_n$; used as a coating material are dissolved in demineralized water and placed in an ice bath. The whole synthesis process is carried out under ultrasonic control. Followed by precipitating this aqueous solution with a base such as ammonia ($NH_3$), methylamine ($CH_3NH_2$),

sodium hydroxide (NaOH), etc. [83]. A detailed explanation of the various steps involved in the synthesis process, as well as the quantity of the solvents, solutes and the base used, is mentioned with the appropriate experiment in Chapter 6 and Chapter 7.

## 2.6 Fundamentals for nucleation and growth

Nucleation and growth of nanoparticles is a very complex and multi-step process. But for understanding, the complete process can be divided in two-steps; the first step consists of a short burst of nucleation followed by the second step consisting of a coherent growth. In this section, a simplified model of the nucleation and growth is explained. Nucleation and growth are driven by the change in Gibb's free energy of a defined volume $\Delta G_{\mathrm{V}}$ which in turn depends on the concentration of the solute in the solvent and can be described by Equation 2.15.

$$\Delta G_{\mathrm{V}} = -\frac{k_{\mathrm{B}}T}{\Omega}\ln\frac{c}{c_0} = -\frac{k_{\mathrm{B}}T}{\Omega}\ln(1+\sigma) \tag{2.15}$$

Where $c_0$ is the equilibrium concentration or solubility, $c$ is the concentration of the solute, $\Omega$ is the atomic volume of the solid phase and $\sigma$ is the supersaturation (when the solution contains a higher amount of the solute which can be dissolved in a solvent) defined by $(c - c_0)/c_0$. Therefore, for nucleation to commence the solution must be supersaturated. Supersaturation is generally achieved by adding reactants in higher quantities or by dissolving the required solute at a higher temperature [84]. Therefore, when there is no supersaturation (i.e. $\sigma = 0$) then nucleation will also not commence. For the formation of the nucleus, the total change in the chemical potential $\Delta G$ is also dependent on the changes happening in the volume energy $\Delta\mu_{\mathrm{V}}$ and the surface energy $\Delta\mu_{\mathrm{S}}$ of the formed nucleus. Volume energy can be calculated by assuming the spherical structure of the formed nucleus with a radius $r$ in Equation 2.16.

$$\Delta\mu_{\mathrm{V}} = \frac{4}{3}\pi r^3 \Delta G_{\mathrm{V}} \tag{2.16}$$

This change in the volume energy is compensated by the surface energy due to the formation of a new phase. The surface energy is described by Equation 2.17, where $\gamma$ is the surface energy per unit area.

$$\Delta\mu_S = 4\pi r^2 \gamma \tag{2.17}$$

The total change in the chemical potential is given by Equation 2.18. Figure 2.5 shows

the relationship between the volume energy $\Delta\mu_V$, surface energy $\Delta\mu_S$, total free energy $\Delta G$ to the radius of the nucleus. As it can be easily inferred from the Figure 2.5, the nucleus is only stable when the radius exceeds a critical size known as $r^*$. A nucleus bigger than the critical size keeps on growing and on the other hand, the nucleus which is not able to attain $r^*$ would eventually dissolve back into the solute decreasing overall energy.

$$\Delta G = \Delta\mu_S + \Delta\mu_V = \frac{4}{3}\pi r^3 \Delta G_V + 4\pi r^2 \gamma \tag{2.18}$$

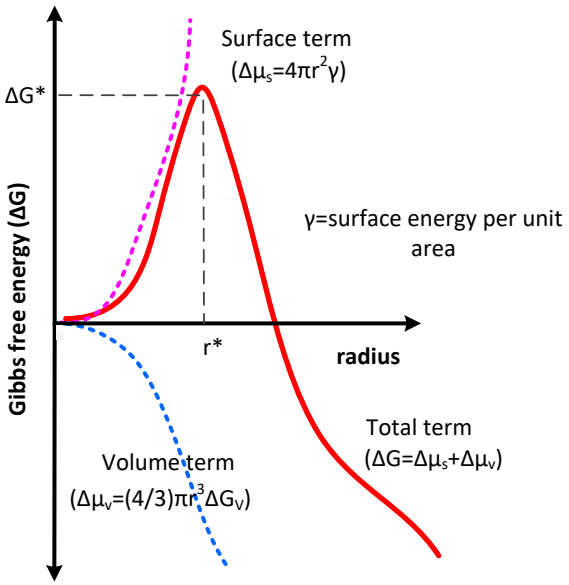


Figure 2.5: Schematics describing the relationship between the volume energy $\Delta\mu_V$, surface energy $\Delta\mu_S$, total free energy $\Delta G$ to the radius of the nucleus. Critical size $r^*$ is needed for achieving the required growth of the nanoparticles. [85]

Following the assumption r = $r^*$ then $d\Delta G/dr = 0$, then the critical size $r^*$ and critical energy barrier $\Delta G^*$ can be defined by Equation 2.19 and Equation 2.20.

$$r^* = \frac{-2\gamma}{\Delta G_V} \tag{2.19}$$

$$\Delta G^* = \frac{16\pi\gamma}{3(\Delta G_V^2)} \tag{2.20}$$

Therefore, to synthesize smaller nanoparticles there is a necessity to reduce $r^*$ and to overcome the energy barrier $\Delta G^*$. This could be achieved by increasing the Gibbs free energy $\Delta G$ and reducing the surface energy of the new phase $\gamma$. One method could

be increasing the supersaturation $\sigma$ as described in Equation 2.18. For reducing the surface energy $\gamma$, there are several possibilities like incorporating some specific impurities in solid-phase or adding some additives to decrease the surface tension of the solution. Hence, change in supersaturation $\sigma$ is an easy parameter for achieving the nucleation and can lead to homogeneous growth. Figure 2.6 schematically illustrates the process of nucleation and growth versus time due to an increase in the concentration of the solute. For nucleation to commence, the supersaturation reaches a certain value of solubility, which corresponds to overcoming the energy barrier described in Equation 2.20. After the formation of initial nuclei, the supersaturation will decrease and theoretically, no new nuclei should form and the growth should proceed until the concentration of growth species reaches the solubility level or the equilibrium concentration.

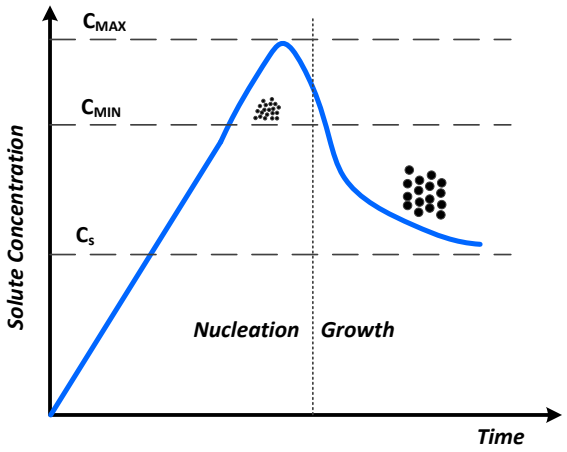


Figure 2.6: Schematics describing the process of nucleation and growth with time, due to an increase in the concentration of solute. Initially, the concentration of the solute increases until it reaches the supersaturation level. At this point of time, the formation of nuclei takes place and the concentration of solute decreases paving way for further growth. [85]

To conclude, for achieving ideal nucleation and growth while synthesizing nanoparticles with a uniform size distribution, all nuclei must be formed at the same point of time and with the same size leading to subsequent homogeneous growth. But in reality, this is difficult to achieve, as in most of the synthesis processes nucleation is a never-ending process and leads to the formation of different nuclei with varying sizes undergoing different growth patterns. There are other mechanisms to achieve uniform size distribution in the growth phase but is it depends on the kinetics of the chemical reaction. Some of these mechanisms are well explained by Den Ouden *et al.* [86][87], Morales *et al.* [88] and Ocana *et al.* [89].

It is very difficult to measure the change in the Gibbs free energy or to track the nucleation

and growth of the nanoparticles. In the last two decades, immense research has been initiated to track the nucleation and growth of nanoparticles to understand the effect of various chemical and physical parameters on the final properties of the nanoparticles. This real-time monitoring has been accomplished with the help of devices like in-situ TEM or with the help of X-ray diffraction [90][91]. In-situ TEM is a very advanced tool providing structural and optical information in the nanometer to sub-Angstrom scale. X-ray diffraction lacks the optical details provided by in-situ TEM, but provides a direct window to infer the change in the crystal structure of the developing nanoparticles. The hardware setup of these devices is very complex and usually, they require special in-situ chambers for experimentation. In this research, we introduce a novel principle to track the nucleation and growth of the magnetic nanoparticles by observing the change in magnetization of in-situ particles. This is achieved with the help of a new device called **INSPECT (In-Situ Magnetic Particle Spectrometer)**. The hardware realization for INSPECT and the obtained measurement results are explained in Chapter 6 and Chapter 7 respectively. In the next subsections fundamentals related to low noise amplifiers will be introduced.

## 2.7 Noise

Any unwanted disturbance in an electrical signal is called noise. Noise generated in any electrical or electronic system can vary, as it could be produced by several different effects. In early 1928, noise was first described by J.B. Johnson as "Statistical fluctuations".

*Statistical fluctuation of electric charge exists in all conductors, producing a random variation of potential between the ends of the conductor. The electric charges in a conductor are found to be in a state of thermal agitation, in thermodynamic equilibrium with the heat motion of the atoms of the conductor. The manifestation of the phenomenon is a fluctuation of the potential difference between the terminals of the conductor.* [92]

Johnson showed that electric noise is a major setback for designing sensitive amplifiers. The source of noise in any electrical circuit can arise from external as well as internal factors. Different types of noise sources which can affect a signal are shown in Figure 2.7. In the case of an LNA, the focus will be on the intrinsic noise namely noise within the receiver. As all the prototyped LNAs in this research are Op-amp based circuits and are free from burst and avalanche noise. The other noise sources are just mentioned for the completeness but will not be considered in the noise analysis and the prime focus will be

on the thermal noise and achieving better NF (noise figure).

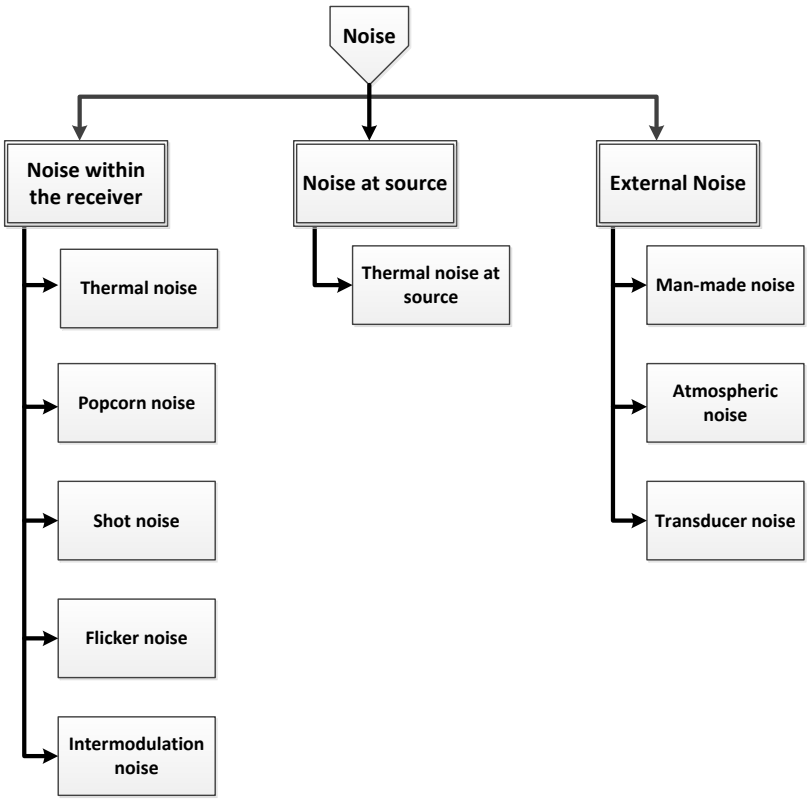


Figure 2.7: Different sources of noise in an electrical or electronic system.

### 2.7.1 Shot noise

Current flow across a potential barrier (for example p-n junction) is responsible for the shot noise. This noise is widely present in the semiconductors and arises due to random diffusion of carriers through the base of a transistor or due to recombination of hole electron pairs. The power density of shot noise is constant with frequency and the amplitude has a Gaussian distribution [93]. The mean-square variation of the shot noise $\overline{i_n^2}$ can be defined by Equation 2.21.

$$\overline{i_n^2} = \overline{(i - i_D)^2} = \int 2qi_D \, df \tag{2.21}$$

Where, $i_D$ is the average of the generated current pulses, $q$ is the electron charge approximately $1.6021 \times 10^{-19}$ $C$ and df is differential frequency.

### 2.7.2 Thermal noise

Thermal noise arises due to the thermal agitation of the electrons or holes present in the conductor. Thermal noise is also referred to as Johnson noise or resistance noise. Thermal noise is present in all the passive components whether resistors or capacitors. Just like shot noise, thermal noise also has a uniform spectral density and is independent of the frequency but dependent on the temperature. Thermal noise can be modeled as current (placed parallel) or voltage noise (placed in series) in accordance with a noiseless resistor. The average mean-square value of the thermal noise can be defined by Equation 2.22.

$$\overline{e^2} = \int 4k_{\mathrm{B}}TR \ \mathrm{df} \ or \ \overline{i^2} = \int \frac{4k_{\mathrm{B}}T}{R} \ \mathrm{df} \tag{2.22}$$

Where $\mathrm{k_B}$ is the Boltzmann constant ($\mathrm{k_B} = 1.38 \times 10^{-23}$ J/K), $T$ is the absolute temperature in Kelvin (K), $R$ is the resistance of the conductor in ohms ($\Omega$) and df is the differential frequency.

### 2.7.3 Flicker noise

Flicker noise is also known as $1/f$ noise. The main reason behind flicker noise is dc current in the circuit or can be traced back to the properties of the semiconductor material specially at the surface of the conductor between electrical contacts. As the name suggests the power density of the flicker noise decreases with frequency. The average mean-square value of the flicker noise can be defined according to Equation 2.23. If the amount of current is lower in the circuit then the flicker noise is not predominant. Moreover, the flicker noise is inversely proportional to the frequency. Therefore, MPI devices operating at an excitation frequency of few kHz is nearly independent of the current noise.

$$\overline{e^2} = \int (K_{\mathrm{e}}^2/f) \ \mathrm{df} \ or \ \overline{i^2} = \int (K_{\mathrm{i}}^2/f) \ \mathrm{df} \tag{2.23}$$

Where $K_{\mathrm{e}}^2/f$ and $K_{\mathrm{i}}^2/f$ are voltage and current power densities given in $\mathrm{V}/\sqrt{\mathrm{Hz}}$ and $\mathrm{A}/\sqrt{\mathrm{Hz}}$.

### 2.7.4 Burst noise

The burst noise is widely known as popcorn noise. It is generally due to manufacturing defects in a semiconductor junction in the form of metallic impurities. The noise occurs

in bursts and can cause discrete changes in power and amplitude level of the signal. The power noise density of the burst noise is inversely proportional to the frequency and thus also related to the current in the electrical circuit. This noise is particularly observed in the audio range from 20 Hz to 20 kHz. As most of the MPI devices are working in a frequency range higher than 20 kHz therefore, this noise does not cause any adverse effects. Moreover, due to the overall improvement in the manufacturing processes of semiconductors, the noise is mitigated to a large extent.

### 2.7.5 Avalanche noise

Avalanche noise occurs when a p-n junction is operated near its breakdown voltage. This noise is evident in all types of diodes when operated in reverse breakdown such as the Zener diode. One application where avalanche noise can cause adverse effects to an MPI/MPS system is in the protection circuit for the acquisition cards. The protection circuit can be constructed by reverse biasing the diodes in the electrical circuit. Therefore, due to an increase in the voltage beyond a certain limit causes an avalanche breakdown leading to the clamping of the signal. As all the prototyped LNAs discussed in this work have no operating component based on diodes, the system is free from avalanche noise. Moreover, the protection circuit used with INSPECT is also Op-amp based and hence is free from diodes, therefore, no avalanche noise can be present in the system.

## 2.8 Operational amplifier (Op-amp)

Operational amplifiers (Op-amp) are the building block of analog electronics and are widely being used for numerous applications in the field of analog and digital electronics. It is a DC-coupled voltage amplifier with a differential input and usually a single-ended output. Op-amps are so popular because the voltage gain can be controlled with additional external passive components when operating with feedback. Therefore, a normal Op-amp can be configured in different modes for different applications such as inverting amplifier, non-inverting amplifier, adder, differential amplifiers, etc. For this particular research, the focus will be on noise analysis in both non-inverting and differential amplifiers.

The basic pin configuration of a single-ended Op-amp and FDA is shown in Figure 2.8. Usually an Op-amp consists of two differential inputs consisting of an inverting input $V_{\mathrm{IN-}}$ and a non-inverting input $V_{\mathrm{IN+}}$, ideally, an Op-amp just amplifies the difference between the voltages present at those pins. The output voltage for a single-ended Op-amp is

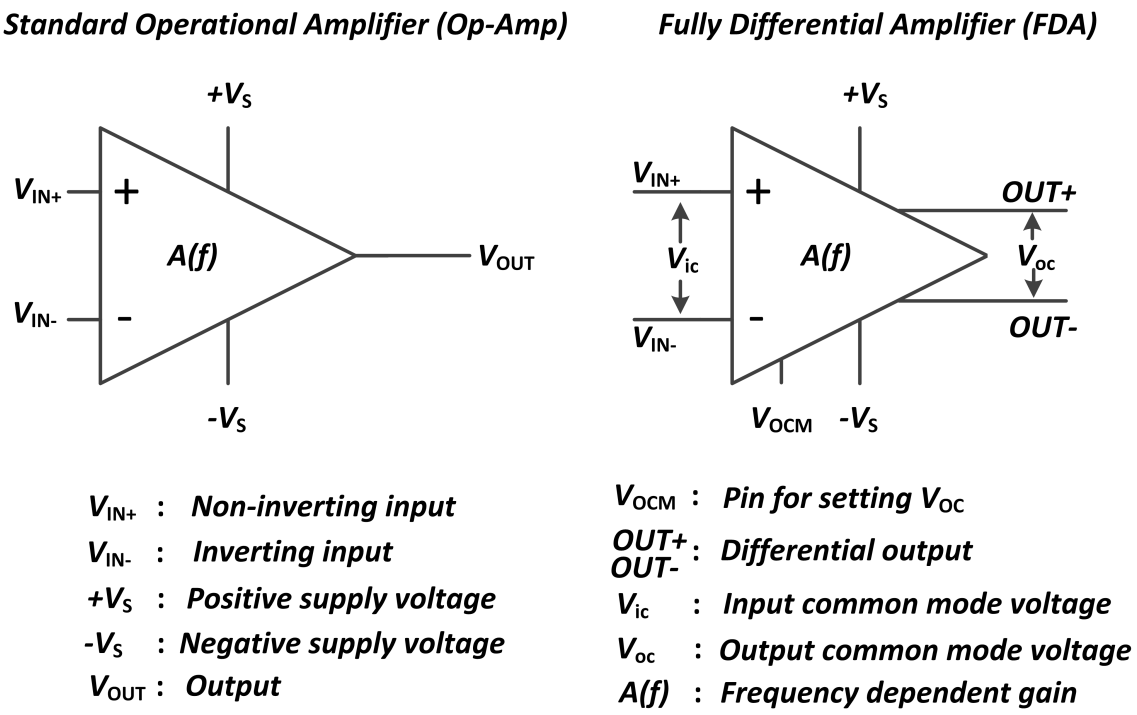


Figure 2.8: Pin configuration of single-ended Op-amp and fully differential amplifier (FDA).

explained in Equation 2.24.

$$V_{\mathrm{OUT}} = A_{\mathrm{OL}} \left(V_{\mathrm{IN+}} - V_{\mathrm{IN-}}\right) \tag{2.24}$$

Where $A_{\mathrm{OL}}$ is the open-loop gain of the Op-amp. But typically for an integrated circuit, the $A_{\mathrm{OL}}$ is in the magnitude of 10000 or more. Therefore, in a typical Op-amp based application, there is always negative feedback to control the gain of the Op-amp so that the saturation of the output voltage can be prevented. In negative feedback, a portion of the output signal $V_{\mathrm{OUT}}$ is fed back to the inverting input $V_{\mathrm{IN-}}$ which drastically reduces the overall output gain and this gain is referred to as closed-loop gain. The closed-loop gain can be easily controlled with the help of passive components present in series to the input pins and in the feedback loop. For a typical FDA, the voltage definitions are a bit different. The input differential voltage $V_{\mathrm{id}}$ is the voltage difference between the input pins $V_{\mathrm{IN+}}$ and $V_{\mathrm{IN-}}$. The average of these voltages is referred as input common-mode voltage $V_{\mathrm{ic}}$. At the output, the difference between the voltages $OUT+$ and $OUT-$ is referred to as output differential voltage $V_{\mathrm{od}}$. The averaged output of the two differential voltages is referred to as output common-mode voltage $V_{\mathrm{oc}}$ and can be controlled with the help of pin $V_{\mathrm{OCM}}$. The mathematical representation of all the voltage definitions is

shown in Equation 2.25 and Equation 2.26. [94]

$$V_{\text{id}} = (V_{\text{IN+}}) - (V_{\text{IN-}}); V_{\text{ic}} = \frac{(V_{\text{IN+}}) + (V_{\text{IN-}})}{2} \tag{2.25}$$

$$V_{\text{od}} = (V_{\text{OUT+}}) - (V_{\text{OUT-}}); V_{\text{oc}} = \frac{(V_{\text{OUT+}}) + (V_{\text{OUT-}})}{2} \tag{2.26}$$

When *A(f)* is the frequency-dependent gain of the differential amplifier, then the transfer function is given by Equation 2.27 and the output common-mode voltage is given in Equation 2.28. [94]

$$V_{\text{od}} = V_{\text{id}}\, A(f) \tag{2.27}$$

$$V_{\text{oc}} = V_{\text{OCM}} \tag{2.28}$$

In the next section, the closed-loop gain and the noise characteristics for the single-ended output Op-amps (non-inverting mode) and the FDA will be discussed.

## 2.9 Noise in single ended Op-amp

For analyzing the noise characteristics of an Op-amp, noise sources have to be isolated using principles of superposition. After calculating the noise generated by each source, all these noise-producing sources are added according to the rules of adding independent noise sources. Figure 2.9 shows all the independent noise sources for an Op-amp in the non-inverting configuration. For explanation purpose, we fix the gain of the amplifier to 21 by using feedback resistors $R_1$ equal to 3 kΩ and $R_2$ equal to 150 Ω shown in Equation 2.29. In Figure 2.9, $e_{\text{n}}$ denotes the voltage noise, $i_{\text{n-}}$ denotes the current noise at the inverting input and $e_{\text{r}}$ denotes the thermal noise generated by passive components such as $R_1$ and $R_2$.

$$G = \frac{R_1}{R_2} + 1 \tag{2.29}$$

The thermal noise $e_{\text{r}}$ generated by the resistors can be calculated by using Equation 2.30. According to Equation 2.30, thermal noise generated by $R_1$ and $R_2$ is approximately 7.12 nV/ $\sqrt{\text{Hz}}$ and 1.59 nV/ $\sqrt{\text{Hz}}$ respectively.

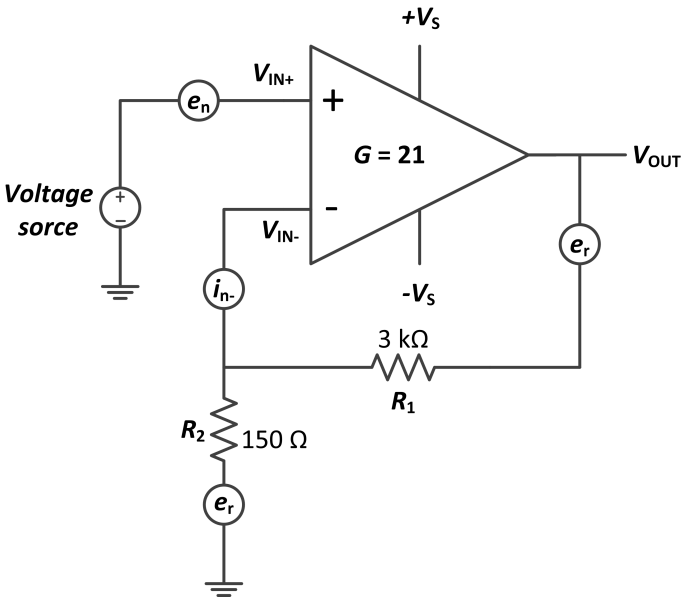


Figure 2.9: Noise model for non-inverting Op-amp with different noise sources. The gain of the amplifier is fixed to 21 with the help of $R_1$ and $R_2$. In the figure, $e_n$ denotes the voltage noise, $i_{n-}$ denotes the current noise at the inverting input and $e_r$ denotes the thermal noise generated by passive components.

$$e_r = \sqrt{4k_B T R \Delta f} \approx 0.13\sqrt{R} \text{ nV}/\sqrt{\text{Hz}} \tag{2.30}$$

Where $k_B$ is the Boltzmann constant in joules per Kelvin, $T$ is the resistor's absolute temperature in Kelvin and $R$ is the resistor value in Ohms (Ω). As the Op-amp is in non-inverting configuration and the resistor $R_2$ is connected to the inverting pin, the noise from this particular resistor is calculated in Equation 2.31.

$$e_r(R_2) = G \times 1.59 \text{ nV}/\sqrt{\text{Hz}} \approx 31.8 \text{ nV}/\sqrt{\text{Hz}} \tag{2.31}$$

Current noise $i_{n-}$ and voltage noise $e_n$ depends on the specified values given in the datasheet of the particular Op-amp. In the datasheet, the values are specified as noise current density $i_d$ and noise voltage density $e_d$. For this particular example, $i_d$ is assumed to be 2.6 pA/ $\sqrt{\text{Hz}}$ and $e_d$ is assumed to be 0.69 nV/ $\sqrt{\text{Hz}}$. The total current noise and the total voltage noise can be calculated by using Equation 2.32.

$$i_{n-} = i_d \times G \times R_{\text{equivalent}}(R_1 \parallel R_2) = 7.42 \text{ nV}/\sqrt{\text{Hz}} \tag{2.32}$$

Similarly, $e_n$ can be calculated by using the Equation 2.33.

$$e_{\mathrm{n}} = e_{\mathrm{d}} \times G = 13.8\ \mathrm{nV}/\sqrt{\mathrm{Hz}} \tag{2.33}$$

The total output noise can be easily calculated by adding all the noise sources mentioned in Equation 2.30 to Equation 2.33 and is illustrated in Equation 2.34.

$$Total\ output\ noise = \sqrt{(e_{\mathrm{r}})^2 + (i_{\mathrm{n-}})^2 + (e_{\mathrm{n}})^2} \approx 36.15\ \mathrm{nV}/\sqrt{\mathrm{Hz}} \tag{2.34}$$

The total input noise can be calculated by dividing the total output noise by the gain $G$ of the amplifier and is given by Equation 2.35.

$$Total\ input\ noise = \frac{\sqrt{(e_{\mathrm{r}})^2 + (i_{\mathrm{n-}})^2 + (e_{\mathrm{n}})^2}}{G} \approx 1.80\ \mathrm{nV}/\sqrt{\mathrm{Hz}} \tag{2.35}$$

Therefore, the resistor $R_2$ and the equivalent circuit formed due to the combination of the resistors play a vital role in the total output noise. A wise selection of these parameters helps in reducing the noise induced in the Op-amp. Choosing smaller resistor values reduces the overall noise but can make the Op-amp instable. This is a simplified method for calculating noise in a single-ended Op-amp in the non-inverting configuration. The same principle of addition of different noise sources is applicable for all the Op-amp configurations. The equations become more complicated depending upon the circuit and due to various passive components present in the circuit.

## 2.10 Noise in fully differential amplifier (FDA)

An FDA provides increased noise immunity to the circuits as the coupled noise are attributed to common-mode noise which is rejected due to the differential signal pathways. Another advantage with an FDA is the doubling of the output voltage swing in comparison to the single-ended counterpart. This is due to the phase change between the differential outputs. FDA also has reduced even-order harmonic distortion due to symmetry in the feedback loops. While expanding the transfer function of the differential circuit into the power series as shown in Equation 2.36 and Equation 2.37, where, $k_1$, $k_2$, and $k_3$ are constants. The cubic terms are responsible for the even-order harmonic distortions and the quadratic terms lead to odd-order harmonic distortion.

$$OUT+ = k_1 V_{\mathrm{IN}} + k_2 (V_{\mathrm{IN}})^2 + k_3 (V_{\mathrm{IN}})^3 + k_4 (V_{\mathrm{IN}})^4 + .... \tag{2.36}$$

$$OUT- = k_1 (-V_{\mathrm{IN}}) + k_2 (-V_{\mathrm{IN}})^2 + k_3 (-V_{\mathrm{IN}})^3 + k_4 (-V_{\mathrm{IN}})^4 + ... \tag{2.37}$$

Taking the differential output, the power series in Equation 2.36 and Equation 2.37 can be modified as the odd-order terms retain their polarity, even-order terms are positive, hence the power series can be simplified to Equation 2.38.

$$V_{OC} = 2k_1(V_{IN}) + 2k_3(V_{IN})^3 + .... \tag{2.38}$$

This reduces the even harmonic distortions in the signal. To calculate the induced noise in the FDA, all the possible noise sources for a typical FDA are marked in Figure 2.10. As in the noise calculations for the non-inverting Op-amp configuration, the total output noise is root square sum of all the noise sources associated with the model. In most differential applications the inverting and non-inverting sides of the FDA are symmetrical. Therefore, $R_1 = R_3$ and $R_2 = R_4$. $e_n$ is the input-referred RMS noise voltage of the amplifier modeled as a differential input at the input. $i_{n+}$ and $i_{n-}$ are the input-referred RMS noise currents. As the inverting and non-inverting sides are symmetrical, they are considered equal. These noise currents develop proportional voltages depending upon the parallel combination of the gain setting resistors, shown in Equation 2.39.

$$R_{eq1} = \frac{R_1\,R_2}{R_1 + R_2} \text{ and } R_{eq2} = \frac{R_3\,R_4}{R_3 + R_4} \tag{2.39}$$

$e_{r1}$ and $e_{r2}$ is the thermal noise generated by the resistors present in the circuit and can be calculated by using Equation 2.30. $e_{cm}$ denotes the RMS voltage noise related to the pin $V_{OCM}$. A proper bypassing of this pin with capacitors reduces the effective bandwidth and hence this noise is negligible. $E_D$ is the differential RMS output noise which can be calculated by multiplying the gain ($A$) of the amplifier with the independent single-input noise source ($E_I$). The half magnitude of the $E_D$ is due to the positive output ($\frac{+E_D}{2}$) and the other half is attributed to negative output ($\frac{-E_D}{2}$). As due to symmetry in the inverting and non-inverting feedbacks the noise sources are correlated, they can be directly added as shown in Equation 2.40.

$$E_D = A(E_I) = (\frac{+E_D}{2}) - (\frac{-E_D}{2}) \tag{2.40}$$

For the addition of all the non-correlated noise sources, the sum of square technique is used, which means total RMS voltage squared is equal to the square of individual RMS voltages together. Considering this the value of $E_D$ by just considering $e_n$ can be given by Equation 2.41.

$$E_D = A[(e_n) - (\frac{+E_D}{2})\,\beta_1 + (\frac{-E_D}{2})\,\beta_2] \tag{2.41}$$

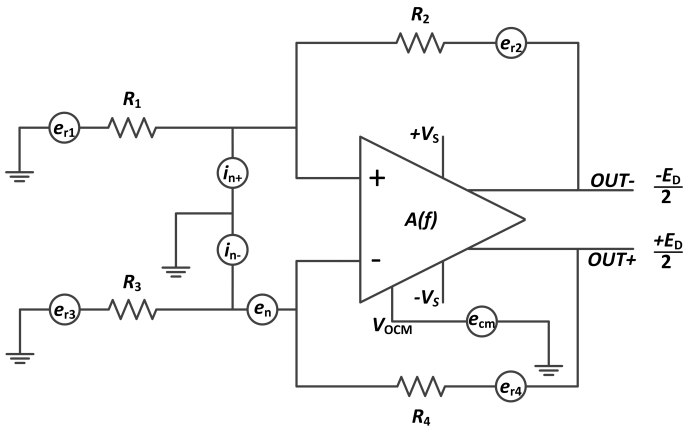


Figure 2.10: Noise model for FDA with different noise sources. The gain of the amplifier is given by $A(f)$ and can be set with resistors from $R_1$ to $R_4$. In the figure, $e_\mathrm{n}$ denotes the voltage noise, $i_{\mathrm{n}-}$ denotes the current noise at the inverting input, $i_{\mathrm{n}+}$ denotes the current noise at the non-inverting input and $e_\mathrm{ri}$ denotes the thermal noise generated by passive components.

Where, $\beta_1 = \dfrac{R_3}{R_3 + R_4}$ and $\beta_2 = \dfrac{R_1}{R_1 + R_2}$. Assuming that the feedback for FDA is symmetrical ($\beta_1 = \beta_2$), hence the Equation 2.41 can be reduced to Equation 2.42.

$$E_\mathrm{D} = \frac{e_\mathrm{n}}{\beta} \tag{2.42}$$

Similarly, by considering the same assumption for symmetry the noise-induced due to $i_{\mathrm{n}+}$ and $i_{\mathrm{n}-}$ can be calculated by the Equation 2.43.

$$i_{\mathrm{n}+} = \frac{2i_\mathrm{n} \times R_\mathrm{eq1}}{\beta_1 + \beta_2} \text{ and } i_{\mathrm{n}-} = \frac{2i_\mathrm{n} \times R_\mathrm{eq2}}{\beta_1 + \beta_2} \tag{2.43}$$

The noise-induced through the pin $V_\mathrm{OCM}$ is attributed to the common-mode noise source as $e_\mathrm{cm}$. As this pin is connected internally to the inputs of the FDA through the feedback paths $\beta_1$ and $\beta_2$, it is amplified and can be seen at the output as a differential noise source and is given by the Equation 2.44.

$$\text{Total } e_\mathrm{cm} = \frac{2e_\mathrm{cm}(\beta_1 - \beta_2)}{\beta_1 + \beta_2} \tag{2.44}$$

The resistors $R_1$ and $R_3$ are connected to the non-inverting and inverting pins of the FDA respectively, therefore the feedback resistors, as well as the gain of the FDA, play a vital role. The noise contribution from these two resistors can be given by Equation 2.45. The noise from the resistors $R_2$ and $R_4$ are directly contributed to the total output noise without

any amplification and can be attributed to $e_{r2}$ and $e_{r4}$ respectively.

$$R_1 = \frac{2e_{r1}(1-\beta_2)}{\beta_1+\beta_2} \; and \; R_3 = \frac{2e_{r3}(1-\beta_1)}{\beta_1+\beta_2} \tag{2.45}$$

Adding all the individual noise sources gives the total output RMS noise and is shown in Equation 2.46.

$$\begin{aligned}(E_d)^2 = & \frac{(2e_n)^2 + (2i_n \times R_{eq1})^2 + (2i_n \times R_{eq2})^2 + (2e_{r1}(1-\beta_2))^2 + (2e_{r3}(1-\beta_1)^2)}{(\beta_1+\beta_2)^2} \\ & + \frac{(2e_{cm}(\beta_1-\beta_2))^2}{(\beta_1+\beta_2)^2} + \frac{(e_{r2})^2+(e_{r4})^2}{(\beta_1+\beta_2)^2}\end{aligned} \tag{2.46}$$

Due to symmetry in the feedback loops, the equation can be reduced further as $\beta_1 = \beta_2 = \beta$, which leads to the noise at the pin $V_{OCM}$ equal to zero. Therefore, a careful planning of the PCB (printed circuit board) layout is essential for the noise reduction in an FDA. It is highly recommended that the length of the differential traces on the PCB are equal. This increases the symmetry and reduces the noise in the FDA. Moreover, the passive components with minimum tolerance should be used to reduce asymmetry in the feedback loops. Due to symmetry, the gain of the amplifier is equal to Equation 2.47.

$$A = \frac{2}{\beta_1+\beta_2} = \frac{1}{\beta} = 1 + \frac{R_f}{R_g} \tag{2.47}$$

## 2.11 Reduction of noise due to parallelization

An LNA not only amplifies the input signal but also amplifies the noise in the input signal as well as the inherent noise produced by the various passive and active components present in the LNA itself. By using the parallelization technique, the input signal (correlated signal) is amplified by a factor of $N$, but the uncorrelated noise (LNA noise) increases just by a factor of $\sqrt{N}$, where $N$ is the number of amplifiers in the summing configuration [95].

Mathematically, one can assume an amplifier with an input signal $S_{In}$. However, the final input also contains the noise generated at the input by the system $N_{In}$. Therefore, the final input of the amplifier is given by equation 2.48.

$$Input_{\text{Single Op-amp}} = S_{In} + N_{In} \tag{2.48}$$

The output of the amplifier contains the output signal $S_{\text{Out}}$ plus the total output noise $N_{\text{Out}}$. The output noise contains the input noise $N_{\text{In}}$ as well as the noise generated by the Op-amp $N_{\text{Amp}}$ itself.

$$Output_{\text{SingleOp-amp}} = S_{\text{Out}} + N_{\text{Out}} \tag{2.49}$$

When $G$ is the gain of the Op-amp, then $S_{\text{Out}} = S_{\text{In}} \cdot G$ and $N_{\text{Out}} = N_{\text{In}} \cdot G + N_{\text{Amp}}$. The SNR is calculated by dividing the output RMS signal power by the output RMS noise power by using equation 2.50

$$(\text{SNR})^2 = \frac{(S_{\text{Out}})^2}{(N_{\text{Out}})^2} = \frac{(S_{\text{In}} \cdot G)^2}{((N_{\text{In}} \cdot G)^2 + (N_{\text{Amp}})^2)} \tag{2.50}$$

For simplicity, the input noise generated by the system (if it is below the level of the SPIONs response) is neglected and thus the equation becomes:

$$(\text{SNR})^2 \approx \frac{(S_{\text{Out}})^2}{(N_{\text{Out}})^2} \approx \frac{(S_{\text{In}} \cdot G)^2}{(N_{\text{Amp}})^2} \tag{2.51}$$

As stated earlier, by connecting the second amplifier in parallel, there is an increase in the power of the RMS signal by two times, but the increase in the RMS noise is $\sqrt{2}$ as the amplifiers in parallel add uncorrelated noise. The SNR calculation for two amplifiers considering the above assumptions can be calculated by equation 2.52.

$$(\text{SNR})^2_{\text{Two Op-amps}} = \frac{(2S_{\text{In}} \cdot G)^2}{0.5 \cdot (N_{\text{Amp}})^2} \tag{2.52}$$

Therefore, in theory, by increasing the value of N, we can mitigate the inherent noise generated by LNA. But parallelization can increase the input capacitance of the LNA forming a resonance circuit with the receive coil [96]. However, appropriate layout of the LNA, as well as the selection of the Op-amps used in LNA, play a significant role. To deduce the merit of the LNA, foremost criteria is noise density. The noise density is specified as voltage noise density in $\text{nV}/\sqrt{\text{Hz}}$ and the current noise density in $\text{pA}/\sqrt{\text{Hz}}$. For simplicity, these values are always referred to its input noise density thus making it independent of the set gain of the LNA. A spectrum analyzer can be used to measure the average spectral noise density from which the output noise of the LNA can be calculated. Noise density is the power spectral density of noise or in other words the noise power per unit of bandwidth. The values obtained in dBm/Hz can be easily converted in term of power (P) dBW by equation 2.53 and the P in dBW can be obtained by using the set of equations mentioned from 2.54 to 2.56.

$$1000 \text{ mW} = 1 \text{ W}; +30 \text{ dBm} = 0 \text{ dBW}; -30 \text{ dBm} = -60 \text{ dBW} \tag{2.53}$$

$$\text{P [dBW]} = Averagenoisedensity \text{ [dBm/Hz]} - 30 \tag{2.54}$$

$$\text{P [W]} = 10^{\frac{\text{dBW}}{10}} \tag{2.55}$$

$$N_{Out} = \sqrt{Resistance \times \text{P [W]}} \tag{2.56}$$

By using output noise $N_{Out}$, the input noise $N_{In}$ can be easily calculated by dividing the output noise by the gain $G$ of the Op-amp using equation 2.57.

$$N_{In} = \frac{N_{Out}}{G} \tag{2.57}$$

One more significant parameter is the NF, it is defined as a degradation of the SNR as it passes through a device, for example, a spectrum analyzer operating at a specific input noise. NF can be easily defined by the noise factor (F) which is given by equation 2.58.

$$\text{F} = \frac{S_{\text{In}}/N_{\text{In}}}{S_{\text{Out}}/N_{\text{Out}}} = \frac{S_{\text{In}}/k_B TB}{S_{\text{In}} \cdot G/N_{\text{Out}}} = \frac{N_{\text{Out}}}{GTBk_B} \tag{2.58}$$

Where $N_{\text{Out}}$ is the power of the noise output, $G$ is device gain, $k_{\text{B}}$ is Boltzmann constant, $T$ is Temperature in Kelvin, $B$ is Bandwidth and F is noise factor. By using equation 2.59 NF can be obtained.

$$\text{NF} = 10 \log_{10} (\text{F}GTBk_{\text{B}}) - 10 \log_{10} (G) - 10 \log_{10} (TBk_{\text{B}}) \tag{2.59}$$

It is necessary to accommodate the bandwidth of the spectrum analyzer as the noise is proportional to the bandwidth. Therefore, the above formula can be written for the bandwidth of 1 Hz as:

$$\text{NF} = 10 \log_{10} (\text{F}GTBk_{\text{B}}) - 10 \log_{10} (G) - 174 \text{ dB} \tag{2.60}$$

In a real-world application, it is preferable to measure the noise directly. As the calculated noise does not take into account the EMI (electromagnetic interference) induced in the PCBs. Therefore, Chapter 4 is dedicated to the design and development of four different LNAs. Two of the LNAs are single-ended for the MPS, followed by VGA (variable gain amplifier) which is also in single-ended configuration and in the end, an FDA is

also developed for an imaging system under development. The noise in these LNAs is measured with the help of a spectrum analyzer with two different terminations (50 Ω and a receiving coil which is designed for INSPECT). In the next chapter, the focus will be on other electrical modules that are essential for an MPS system.

# 3

# Technical considerations for MPS systems

## Contents



## 3.1 Introduction

As stated in Section 2.2, an MPS device is a powerful tool for the characterization of SPIONs used in MPI and various other MPI based applications. In this chapter, a conventional MPS system consisting of different components used for the send and receive chain will be explained. Most of the components in an MPS device consist of inductors and capacitors. Therefore, it is essential to discuss their electrical behaviour.

### 3.1.1 Inductance

A magnetic field is created around a conductor when an electric current flows through it. Any change in the current leads to a change in the generated magnetic field, the surface integral of which is known as magnetic flux. According to Faraday's law of induction, a change in the magnetic flux through a current-carrying conductor induces a voltage EMF (electromotive force), across the conductor. This phenomenon is known as electromagnetic induction. Inductance $L$ is defined as a ratio between the induced voltage $v$ and the rate of change of current $i(t)$ and is given in Equation 3.1 [97].

$$L = -v\left(\frac{\mathrm{d}i}{\mathrm{d}t}\right)^{-1} \tag{3.1}$$

When the EMF is induced in the same conductor which is carrying a current, it is known as self-inductance. And when the EMF is induced into an adjacent conductor, then the induced EMF is known as mutual-inductance. Inductance can also be defined in terms of the induced voltage $v$ and magnetic flux $\Phi$ and is given in Equation 3.2.

$$v(t) = -\frac{\mathrm{d}}{\mathrm{d}t}\,\Phi(t) \tag{3.2}$$

#### 3.1.1.1 Power in an inductor

Due to the flow of charges in the conductor, there is a loss of potential energy. This loss of energy is stored in the form of an increasing magnetic field around the conductor. Rate of change of the stored energy $U$ is the product of the voltage $v(t)$ and the current $i(t)$ at any given point of time. The power $p(t)$ flowing into the magnetic field can be calculated by using Equation 3.3 and signifies a change in the stored energy $U$.

$$p(t) = \frac{\mathrm{d}U}{\mathrm{d}t} = v(t)\,i(t) \tag{3.3}$$

Using Equation 3.1, Equation 3.3 can be written as:

$$\frac{\mathrm{d}U}{\mathrm{d}t} = L(i)\,i\,\frac{\mathrm{d}i}{\mathrm{d}t} \tag{3.4}$$

Solving further, the change in the stored energy is given in Equation 3.5:

$$\mathrm{d}U = L(i)\,i\,\mathrm{d}i \tag{3.5}$$

#### 3.1.1.2 Inductance reactance

The opposition of an inductor to an AC (alternating current) is known as inductance reactance. The excitation field generated either in the MPI or MPS is usually achieved with the help of power amplifiers using AC with a specific frequency. When the current through the inductance is $i(t) = I_p \sin(\omega t)$, then the induced voltage or EMF can be calculated by using Equation 3.1 and is given by:

$$\begin{aligned} v(t) &= L\frac{di}{dt} = L\frac{d}{dt}(I_p \sin(\omega t)) \\ &= \omega L I_p cos(\omega t) = \omega L I_p sin(\omega t + \frac{\pi}{2}) \end{aligned} \tag{3.6}$$

Where $L$ is the inductance, $I_p$ is the peak value of the sinusoidal current, $\omega = 2\pi f$ is the angular frequency in hertz (Hz). According to Equation 3.6, in an ideal conductor, the current lags voltage by a phase angle 90°. The peak voltage across the inductance is given in Equation 3.7.

$$V_P = \omega L I_P = 2\pi f L I_P \tag{3.7}$$

Inductive reactance can be defined analogously to the electrical resistance as a ratio of the peak voltage to the peak current with units in ohms (Ω) and is given by [98]:

$$X_L = \frac{V_P}{I_P} = 2\pi f L \tag{3.8}$$

Equation 3.1 to Equation 3.7 describes the inductance of an ideal conductor but in a real-world scenario, a coil is made up of a winded wire. Each coil comprises of a series resistance $R_S$ and a series inductance $L_S$. Due to multiple turns in the coil, there are stray capacities in close proximity. Hence, an overall parallel capacitance $C_P$ is also included in the model. This capacitance generates a self-resonance in the coil, above the resonant frequency the coil acts as a pure capacitance. Figure 3.1 shows an equivalent circuit of the coil.

### 3.1.2 Capacitance

As a passive component, any capacitance can store energy in the form of electrical charge across the two or more parallel plates producing a potential difference. These plates are either separated with air or may contain a dielectric material such as mica, ceramic,

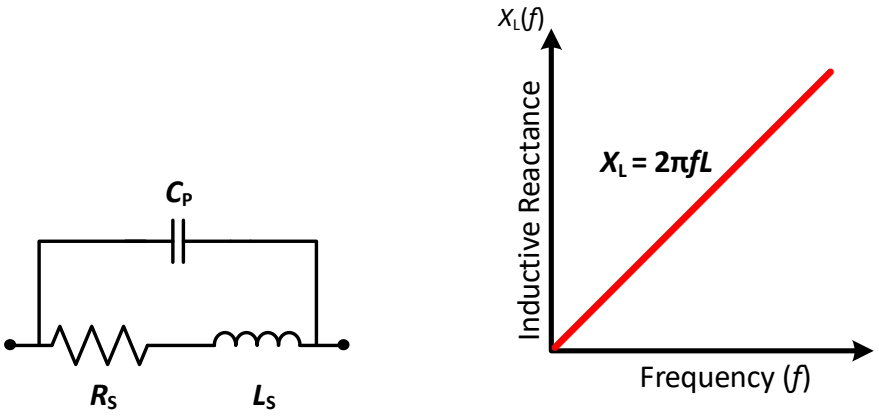


Figure 3.1: The equivalent electrical model of a real-world coil consisting of series resistance $R_S$ and series inductance $L_S$. The capacitance in parallel $C_P$ corresponds to the stray capacities due to turns in the coil.

plastic, etc. functioning as an insulator. The capacitor's (with vacuum as a dielectric) has ability $C$ to store charge $Q$ is proportional to the applied voltage $V$ and is given in Equation 3.9.

$$C = \varepsilon_0 \frac{Q}{V} \tag{3.9}$$

For the capacitors with different dielectrics, it is calculated according to Equation 3.10. Where ε is the permittivity or dielectric constant.ε is material dependent property.

$$C = \varepsilon_r \, \varepsilon_0 \frac{Q}{V} \tag{3.10}$$

Due to the presence of a dielectric material between the plates of the capacitor, there is no flow of the electrical current. But due to charging and discharging of two plates because of the applied voltage, a similar effect showing a flow of current is visible. As the applied voltage $V$ across the two plates increases or decreases with time, therefore both the voltage $v(t)$ and current $i(t)$ are functions of time. The relationship between the current and the voltage for a capacitance is given in Equation 3.11.

$$i(t) = C \frac{\mathrm{d}V}{\mathrm{d}t} \tag{3.11}$$

#### 3.1.2.1 Energy stored in capacitance

Due to an applied voltage, an electrostatic field is produced between the two plates that stores energy. The amount of energy ($W$, measured in Joules) produced is proportional

to the energy which voltage exerts to maintain the charge $Q$ on the plates and is given by Equation 3.12.

$$W = \frac{1}{2} C V^2 \tag{3.12}$$

#### 3.1.2.2 Capacitive reactance

DC signals are blocked by the capacitors but there is a flow of current for the AC signals. The capacitive reactance $X_C$ is the resistance to the flow of current in a purely capacitive circuit. This resistive value is dependent on the frequency of the signal and is given in Equation 3.13.

$$X_C = -\frac{1}{2\pi f C} = -\frac{1}{\omega C} \tag{3.13}$$

The equivalent circuit for a capacitor as well as the relationship between the capacitive reactance with frequency is shown in Figure 3.2. The equivalent model consists of internal resistance $R_S$ in series as well as a series inductance $L_S$ due to connectors present on the capacitance (it is also known as stray inductance). Moreover, the resistance of the dielectric is also taken into account by a parallel resistance $R_P$ [98]. Due to the presence of stray inductance, the capacitors also resonate at a certain frequency. At resonance, the capacitors behave like a short circuit and above the resonance, it shows a pure inductive behaviour.

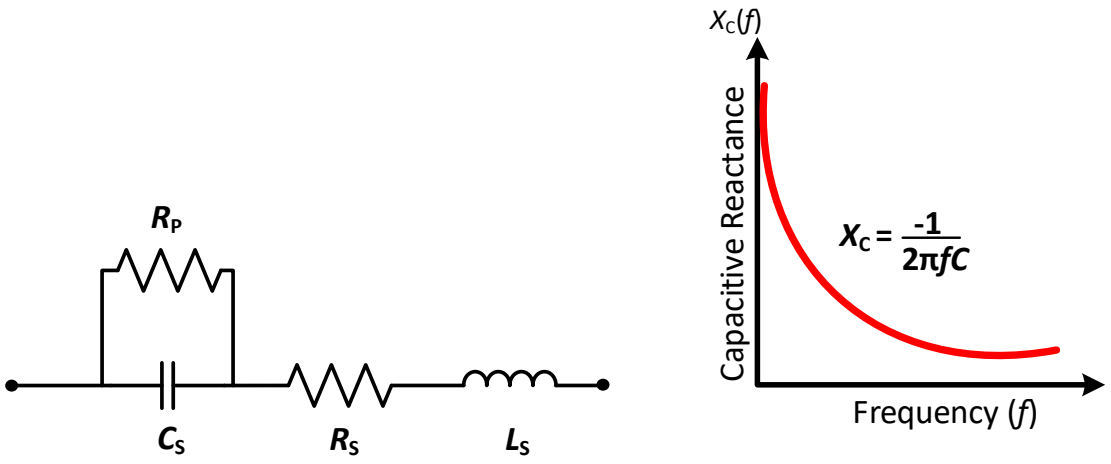


Figure 3.2: The equivalent electrical model of a real-world capacitor consisting of series resistance $R_S$ and stray inductance $L_S$. The resistance in parallel $R_P$ is due to the resistance of the dielectric material used for manufacturing the capacitor.

### 3.1.3 Electrical resonance

Resonance is defined as a condition when the magnitude of the inductive reactance is equal to capacitive reactance. This causes electrical energy to oscillate between the magnetic field of the inductor and the electric field of the capacitor. Electrical resonance is a frequency-dependent phenomenon and occurs at a particular frequency called resonant frequency $f_r$. At the resonant frequency, the admittances and impedances cancel out each other. Due to frequency dependence, resonance circuits are widely used for designing filters and for tunning devices like radio receivers. On the other hand, unwanted resonance can lead to noise and signal distortions causing permanent damage to the circuit. As the inductive reactance is equal to capacitive reactance, the resonant frequency can be defined by Equation 3.14 to Equation 3.15.

$$\omega L = -\frac{1}{\omega C} \tag{3.14}$$

$$f_r = \frac{1}{2\pi\sqrt{L C}} \tag{3.15}$$

The quality factor $Q$ determines the bandwidth and is dependent on the passive components present in a circuit such as an RLC network.

#### 3.1.3.1 Series resonance

According to the inductive reactance, as described in Equation 3.8, the relationship between the frequency $f$ and $X_L$ is linearly proportional. Contrarily, the relationship between the capacitive reactance $X_C$ is inversely proportional as shown in Figure 3.2. Figure 3.3 shown the series RLC circuit and the relationship between $X_L$ and $X_C$ in a series resonance circuit.

When $X_L = X_C$, the resonant frequency ($f_r$) can be calculated by using Equation 3.15. At $f_r$, the two reactances cancel out each other, due to this the LC combination acts as a short circuit. Therefore, the total impedance of an RLC circuit is just dependent on the resistance $R$ and no imaginary part of the impedance is present i.e. $Z = R$. Moreover, at resonance, there is no phase lag between the voltage and the current signal. The $Q$ (Quality factor) can be easily calculated by using Equation 3.16. s

$$Q = \frac{1}{R}\sqrt{\frac{L}{C}} \tag{3.16}$$

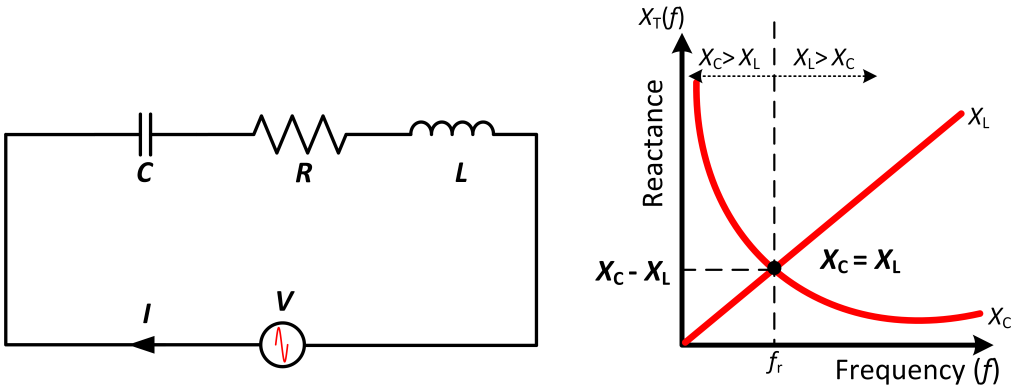


Figure 3.3: The equivalent series resonance circuit and the relationship between the $X_L$ and $X_C$. When $X_L > X_C$, then it is an inductive circuit and when $X_C > X_L$, then its a capacitive circuit.

### 3.1.3.2 Parallel resonance

Parallel resonance is similar to the series resonance but is influenced by the current present in the parallel LC branch. Figure 3.4 shows an equivalent RLC parallel resonance circuit. In parallel resonance, there is a continuous transfer of energy between the electric field of the capacitor $C$ and the magnetic field of the inductor $L$. In parallel resonance, the total current $I$ is the vector sum of the current through all the passive components and is given by Equation 3.17.

$$I = \sqrt{I_R^2 + (I_L + I_C)^2} \tag{3.17}$$

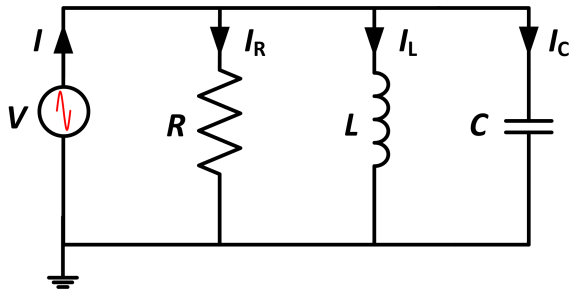


Figure 3.4: The equivalent parallel resonance circuit consisting of the resistor $R$, inductance $L$, and capacitor $C$. The current through the different passive components ($I_R$, $I_L$, $I_C$) is a vector sum of the total current $I$ present in the circuit.

Resonance occurs when $X_L = X_C$, hence the resonant frequency $f_r$ can be given by Equation 3.15. As the formula for $f_r$ is same as for the inductive resonance, therefore the impedance at resonance just consists of the real part and is therefore directly equal to the

value of the resistor $R$ used in the parallel resonance circuit. By changing the value of the resistance $R$, the current flowing through the inductor $L$ and capacitor $C$ changes and the impedance of the circuit can be given as $Z = R_{\mathrm{MAX}}$ and is known as dynamic resonance. Moreover, at resonance the currents $I_{\mathrm{L}}$ and $I_{\mathrm{C}}$ are equal and get canceled, therefore, the current in the circuit can be described by Equation 3.18.

$$I \;=\; \sqrt{I_{\mathrm{R}}^2 + (I_{\mathrm{L}} + I_{\mathrm{C}})^2} = \;\sqrt{I_{\mathrm{R}}^2 + (0)^2} \;=\; I_{\mathrm{R}} \tag{3.18}$$

The Q-factor of the parallel resonance circuit is defined by Equation 3.19 and is inversely proportional to the series resonance circuit. Therefore, Q-factor in the series resonance circuits defines the voltage amplification and on the other hand in the parallel resonance circuits signifies the current amplification.

$$Q \;=\; R\sqrt{\frac{C}{L}} \tag{3.19}$$

Inductors and capacitors are widely used in MPI/MPS systems for the development of various modules such as for the construction of band-pass filters in the transmitting chain and band-stop filters in the receiving chain. Furthermore, the parallel resonance circuit is used for matching impedance between the power amplifier and the transmit coil to avoid excessive heating in the power amplifier leading to power loss.

## 3.2 Modules in a magnetic particle spectrometer (MPS)

An MPS requires different components for the generation as well as for the acquisition of the SPION's response. All the modules can be primarily divided into two signal chains: the transmit chain (marked in red) and the receive chain (marked in blue). Figure 3.5 shows a block diagram of different modules present in an MPS device and the measurement data obtained after every module in the form of the frequency spectrum. The signal acquired by the receive coil is a voltage signal but for better visualization of the SPIONs characteristic response, the amplitude spectrum of this voltage signal is used. For explanation purpose, only an MPS device capable of producing an excitation in the x-direction is described.

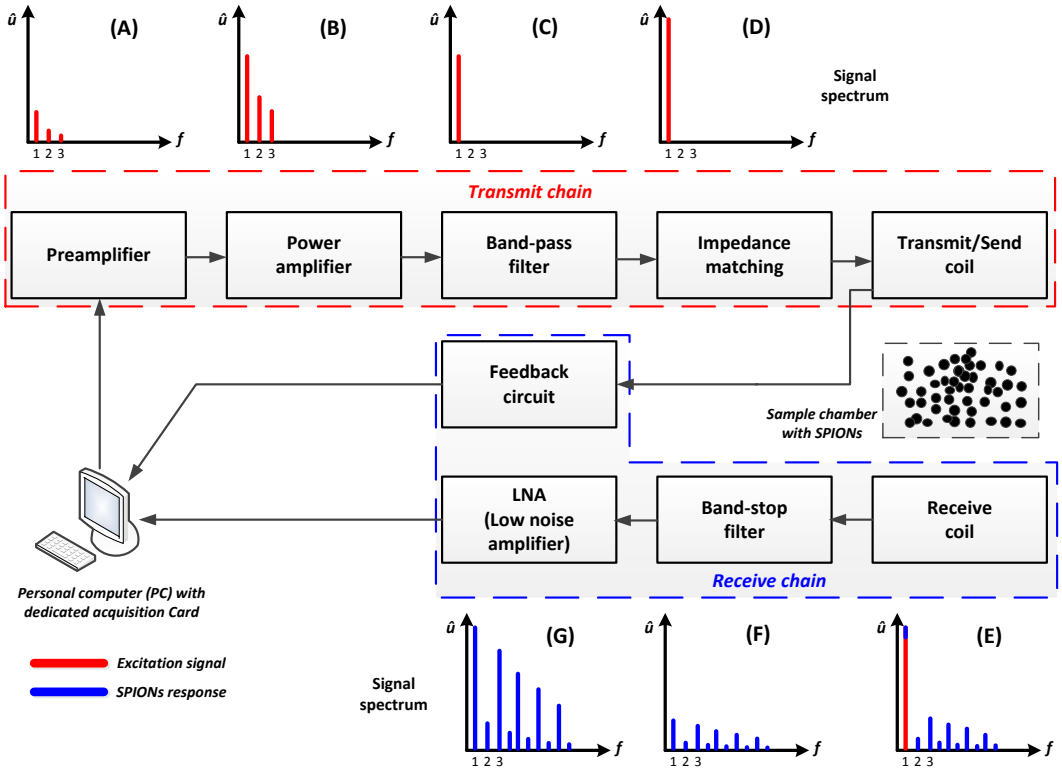


Figure 3.5: Block diagram of a conventional MPS system consisting of different modules in transmitting and receiving chain. A personal computer (PC) with a dedicated acquisition card is used for generation of the excitation signal and for acquisition of the SPION's characteristic response. Images marked **(A)** to **(E)** shows the output in terms of the frequency spectrum at the output of each module present in an MPS device.

### 3.2.1 Signal generation and acquisition

For the generation of the excitation signal at a fixed frequency, a high-resolution DAC (digital to analog converter) present in a dedicated acquisition card is used. Similarly, ADC (analog to digital converter) present in the acquisition card is used for acquiring the SPION response. A PC is used for displaying the acquired data in the form of amplitude and phase spectrum, which in turn can be used to calculate the magnetization curve. For the excitation signal generation, it is essential that the DAC has sufficiently high discretization capabilities and can produce the excitation signal with low distortions. The DAC present in the acquisition card has a limited output in terms of voltage and current, which is not enough to produce the required excitation field. Therefore, it is essential to amplify the excitation signal with minimum distortions. The distortions present in the excitation signal at a particular frequency is further amplified by the subsequent modules and can hamper the overall noise characteristics of the MPS device. Similarly, the re-

ceiving signal carrying the characteristic response of the SPIONs needs to be digitized, this is achieved with an ADC at the same sample rate or higher as compared to the DAC. The input-referred noise of the ADC should be as low as possible. There is also a need to synchronize the excitation and the received signal. This is usually achieved by using the same clock to trigger the ADC and DAC channels of the acquisition card. For a three dimensional MPS device, a dedicated external timing card is required to synchronize different transmitting and receiving signals. Synchronization of the excitation signal and the receiving signal is also important to carry out averaging to reduce the noise and to improve the resolution of the acquired signal. For explanation purpose, we assume that the excitation signal produced by the acquisition card is sinusoidal of 25 kHz with almost zero distortions. The frequency response of such a signal is just a single harmonic present at the desired frequency i.e. 25 kHz ($f_0$). In an ideal case, the frequency spectrum of the excitation signal should only consist of a single harmonic at $f_0$. If there are further harmonics or distortions present then this is due to the distortions produced by the DAC in the acquisition card and by the power amplifier.

## 3.3 Transmit chain

The main aim of the transmit chain is to produce the required magnetic field in the transmit coil for excitation of the SPIONs. There are different modules present in the transmit chain to produce the required field strength as well as to remove the unwanted distortions present in the excitation signal.

### 3.3.1 Preamplifier

Sometimes, due to the limited output response of the acquisition card used for the generation of the excitation signal, there is a need for a certain amplification before the power amplifier. Therefore, this stage may or may not be present in a conventional MPI/MPS system. This can be easily achieved by using a preamplifier at the DAC output of the acquisition card. Depending upon the maximum input voltage of the acquisition card and the output of the power amplifier the gain is determined. One of the most important parameters for designing a preamplifier is the impedance matching between the preamplifier and the DAC of the acquisition card. As an impedance mismatch can lead to a decrease in the amplitude of the transmitting signal leading to a decrease in the field strength of the excitation field. Other parameters which could play an essential role are the input voltage noise, input current noise as well as the total harmonic distortions pro-

duced by the preamplifier. The input voltage noise is measured in nV/ $\sqrt{\text{Hz}}$ and the input current noise is measured in pA/ $\sqrt{\text{Hz}}$. The total harmonic distortion (THD) is given as HD2 ($2^{\text{nd}}$ order distortion) and HD3 ($3^{\text{rd}}$ order distortion) and is measured in dBm or dBc. All these parameters are well stated in the datasheet of the Op-amp used for designing the preamplifier stage. The frequency spectrum of the excitation signal generated by the acquisition card is further amplified by the preamplifier is shown in Figure 3.5(**A**). As there is no ideal amplifier, it leads to the production of $2^{\text{nd}}$ order and $3^{\text{rd}}$ order distortions which can be seen in the frequency spectrum marked as **(A)** in Figure 3.5. This output signal from the preamplifier becomes the input signal to the next stage consisting of the power amplifier.

### 3.3.2 Power amplifier

Primarily, the function of the power amplifier is to further increase the magnitude of the signal generated by the preamplifier. This amplification is needed to produce the required magnetic field to excite the SPIONs. The power amplifier forms the most essential part of the system as the design of the subsequent modules is heavily dependent on the performance of the power amplifier i.e. the design of the filters. The most important parameter is the THD. For better signal fidelity, power amplifier should have low THD values. The power amplifier should have a tolerance for both the inductive and capacitive loads as at resonance there could be a shifting between the inductive and capacitive loads due to heating. Moreover, it is recommended to use switching power amplifiers with switching frequencies above a few MHz to avoid mixing frequencies in the signal bandwidth. The frequency response at the output of the power amplifier is marked as **(B)** in Figure 3.5. The higher harmonics present are due to the THD produced by the power amplifier.

### 3.3.3 Band-pass filter

The THD produced by the acquisition card, preamplifier, and power amplifier needs to be removed or attenuated before it is fed to the transmit coil for producing the required magnetic field. Depending on the required field strength to excite the SPIONs, the amplitude of the signal at the output of the power amplifier could be in a range of few volts. Therefore an active filtration is difficult to implement, hence passive T or $\pi$-filters are used based on resonance circuit as discussed in Section 3.1.3. The foremost important parameter for designing such a filter is input impedance. A mismatch can not only attenuate the overall signal but can also produce distortions. The transfer function for such a filter should be as narrow as possible to remove the distortions produced by the power

amplifier and to transfer the pure excitation signal to the transmit coil.

Therefore, band-pass filters of higher-order and with high Q factor are favorable for such an application. The order of the filter is decided depending on the magnitude of the distortions. For distortions of higher magnitude, it is essential to design a filter with higher-order to achieve maximum attenuation of the unwanted distortions. Figure 3.5 (**C**) shows the spectral response of the output of a band-pass filter. When comparing to Figure 3.5 (**B**), it can be seen that in the ideal conditions the 2$^{nd}$ order and 3$^{rd}$ order distortions are completely removed from the excitation signal, increasing the fidelity of the excitation signal generated by the DAC of the acquisition card. Figure 3.6 shows an example of such an RLC band-pass filter with its transfer function. The cut-off frequency for such a filter should be close to the $f_0$.

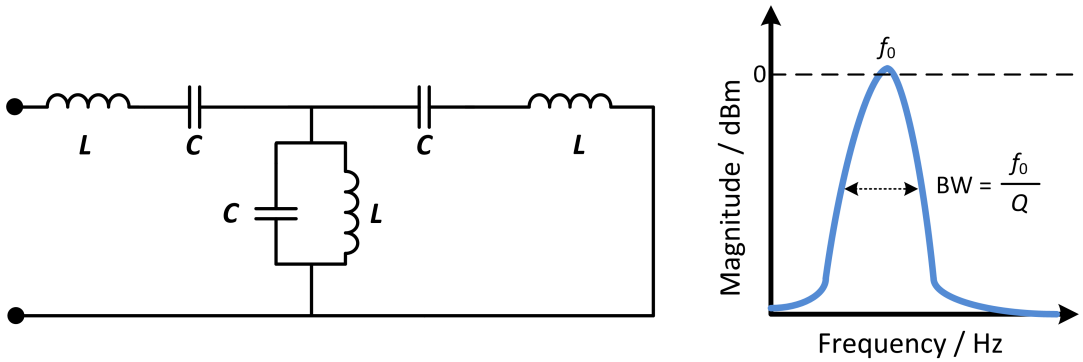


Figure 3.6: An example of an RLC band-pass filter used in the transmit chain of an MPS/MPI system. The second schematics shows the transfer function for such a filter. The filter is designed in such a way that it passes the excitation frequency $f_0$ and attenuates all the other frequencies thus removing the unwanted harmonic distortions present in the signal chain. The steepness of the transfer function is determined by the Q-factor of the designed band-pass filter.

### 3.3.4 Impedance matching

To achieve the maximum power transfer and to reduce reflected power, an impedance matching is needed between the transmit coil to the output of the power amplifier. Most of the power amplifiers can only operate for a specific range of loads. When there is a mismatch in impedance, the power amplifier is forced to operate at its voltage or current limits. Depending upon the degree of mismatch, the output of the power amplifier is reduced and can lead to an increase in the reflected power hence causing heating effects or even can cause a complete shutdown of the power amplifier. The field generator comprises of coils and thus functions as an inductive load. Therefore, it is necessary to match

the impedances between the two modules. Primarily, this can be achieved by either capacitive impedance matching or by inductive impedance matching (using transformers with specific turn ratio). Moreover, due to resonance, the excitation signal is further amplified as shown in Figure 3.5 (**D**). An example of the capacitative and inductive impedance matching is shown in Figure 3.7.

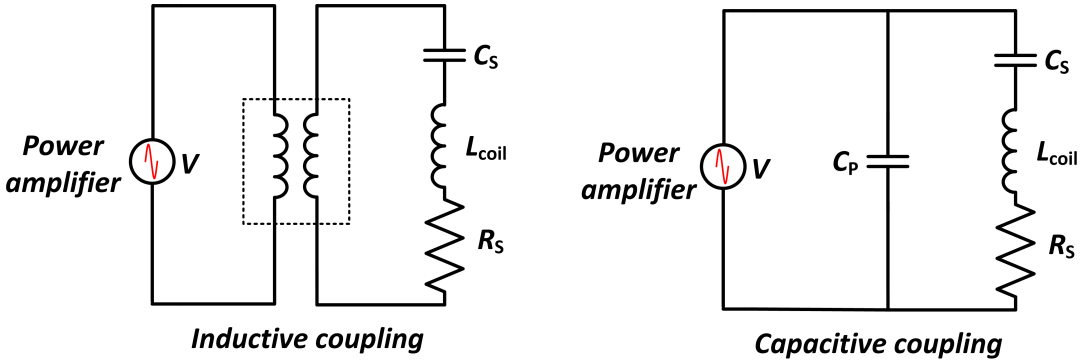


Figure 3.7: Inductive impedance consisting of a transformer in parallel to the transmit coil ($L_{coil}$). The voltage can be controlled by the ratio of the turns in the primary and secondary coil of the transformer. Capacitive impedance matching consisting of a parallel capacitor ($C_P$) and a series capacitor ($C_S$). $R_S$ is the internal resistance of the transmit coil.

Impedance matching is the last electrical module before the excitation signal is fed to the transmit coil. In the next section, the focus will be on the field generator of an MPS system comprising of the transmitting and receiving coil.

## 3.4 Field generator

Field generator consists of the transmit coil used for generating the required magnetic field for excitation of the SPIONs. A receive coil is used for acquiring the characteristic response of the SPIONs due to mutual inductance. For a zero-dimensional MPS system, both the receive coil and transmit coil consists of multiple turns of copper wire forming a solenoid. Other configurations are also possible, for example for generating excitation fields in y and z-direction other configurations such as flat circular, crossed flat circular or saddle coils can be used [42]. In most of the systems, the center of the transmit coil and the receive coil are concentric, i.e. the receive coil spatially lies inside the transmit coil. As the field generator relies on the principle of induction, the response of the SPIONs is induced in the receiving coil as a voltage signal. For the transmit coil it is important to generate the required magnetic field for exciting SPIONs. The Biot-Savart law and Ampere's law can be used to calculate the magnetic field strength of the solenoid. The axial

magnetic field density near the center of the solenoid can be described by Equation 3.20.

$$\mathrm{B} = \frac{\mu_0 \, N \, I}{L} = \mu_0 \, n \, I \; , \; n = \frac{N}{L} \tag{3.20}$$

Where $L$ is the length of the solenoid, $N$ is the number of windings, $I$ is the applied current, $\mu_0$ is the permeability of vacuum and $n$ is the density of turns (turns per meter length of the solenoid). The Reciprocity principle for magnetic recording can be used to calculate the induced voltage $u(t)$ in a receiving coil due to a temporal change in the particle magnetization $\boldsymbol{M}(\boldsymbol{x}, t)$ and is given in Equation 3.21 [99].

$$u(t) = -\mu_0 \int_v \boldsymbol{p_0}(\boldsymbol{x}) \frac{\partial}{\partial t} \boldsymbol{M}(\boldsymbol{x}, t) \, \mathrm{d}V \tag{3.21}$$

Where $\boldsymbol{p_0}$ is the spatial sensitivity of the coil, $V$ is the sample volume and $\boldsymbol{x}$ denotes the x-direction of the magnetic field. For simplicity, only a homogeneous generated magnetic field is considered. The average coil sensitivity $\boldsymbol{p_0}$ is given in Equation 3.22 [20].

$$\boldsymbol{p_0} = \int_v \boldsymbol{p_0}(\boldsymbol{x}) \cdot e_x \, \mathrm{d}V \tag{3.22}$$

where $\boldsymbol{p_0}(\boldsymbol{x}) = \boldsymbol{H_r}(\boldsymbol{x})/i_0$ and $\boldsymbol{H_r}(\boldsymbol{x})$ is the magnetic field generated by the receiving coil due to current $i_0$. Using the above equation, the frequency spectrum of the magnetization $\widehat{m}(f)$ is defined in Equation 3.23.

$$\widehat{m}(f) = \frac{j}{2\pi f} \frac{1}{\mu_0 p_0} \int_0^T u(t) e^{-j2\pi f t} \, \mathrm{d}t \tag{3.23}$$

where $f$ the frequency, $T = 1/f_0$ and $f_0$ the excitation frequency.

In the induced signal, the fundamental frequency $f_0$ has to be attenuated as the amplitude of the excitation frequency is orders of magnitude higher than the signal induced due to the SPIONs. There are several approaches to attenuate the fundamental frequency. Some of the methods which are frequently used in the MPI/MPS system are passive filters, compensation unit, and gradiometer coils.

## 3.5 Receive chain

As mentioned earlier the magnitude of the excitation frequency is way higher in amplitude than the signal induced by the SPIONs. The primary task of the receive chain is to attenuate the excitation frequency and then to amplify the SPIONs response with

minimum addition of noise and distortions. The amplification is necessary to match the SPIONs response to the dynamic range of the ADC present in the acquisition card to achieve the highest possible resolution. The dynamic range of the ADC can be defined as the ratio between the maximum voltage to the minimum voltage that the ADC can convert. The specified maximum input level and the noise floor determines the dynamic resolution of the ADC present on the acquisition system. In this section, we will discuss different possible modules for designing the receive chain of an MPS system. Figure 3.5 shows a possible configuration of the complete receive chain (marked in blue).

### 3.5.1 Band-stop filter

To attenuate the excitation frequency band-stop filters can be used. The required order of the filter and the attenuation heavily depends on the magnitude of the received voltage. One of the possible equivalent circuit for a band-stop RLC filter is shown in Figure 3.8 with the stimulated and measured transfer function.

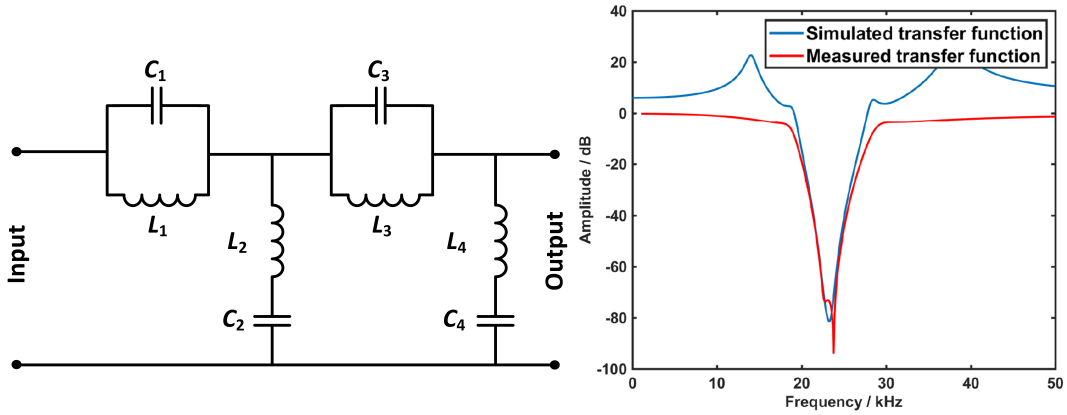


Figure 3.8: Design of a band-stop filter for attenuating the excitation frequency. The filter is a $4^{th}$ order resonance RLC circuit consisting of four inductors ($L_1$ to $L_4$) and four capacitors ($C_1$ to $C_4$). The second figure shows the simulated and measured transfer function for such a filter.

In Figure 3.8, the described filter is a $4^{th}$ order resonance RLC circuit. All the stages have almost the same cut-off frequency and other subsequent stages are just cascaded achieving further attenuation. The second stage generates zero potential due to the low impedance at the fundamental frequency. This creates a high current in the first stage, therefore it is essential to design inductors in such a way that they do not get saturated leading to distortions in the received signal. For higher frequencies than the fundamental frequency the capacitors in the filter act as a short circuit. The transfer function shown in Figure 3.8 consists of simulated as well as recorded transfer function for a band-stop

filter principally based on the equivalent circuit. The attenuation achieved by this filter is approx -80 dB for the fundamental frequency of 25 kHz. The tolerances of the used passive components play a vital role in determining the cut-off frequency. As can be seen in Figure 3.8, the cutoff frequencies are slightly shifted due to the mismatch of the simulated and the measured passive components. Therefore, there is always a need to tune the capacitors and inductances to achieve the desired attenuation at the required bandwidth.

### 3.5.2 Low noise amplifier (LNA)

Due to the presence of the band-stop filter, the excitation frequency is almost attenuated and the overall magnitude of the received signal decreases considerably. Therefore, there is a need to amplify the signal to match the dynamic range of the acquisition card. This task is performed with the help of an LNA by keeping the noise due to internal circuitry minimum. Most important specification for an LNA is to provide good SNR and NF at high gains. An LNA increases the power of both the particle signal as well as the noise present at the input of the LNA plus adding noise due to its own circuitry consisting of passive and active components. The bandwidth of the LNA is also significant because the higher harmonics in MPS can reach up to 2 MHz. Hence, amplifiers with a higher gain-bandwidth product are preferable. The other important characteristics are the input resistance, input capacitance, input voltage noise density and input current noise density. There are several techniques for designing LNA by using CMOS [100], MOSFETS [101], and Op-amps [102]. Figure 3.5 (**F**) shows the amplitude spectrum at the output of the band-stop filter, as it can be seen, only the characteristic response of the SPIONs is present. With the help of an LNA, this signal is amplified to the dynamic range of the ADC for recording and displaying the characteristic SPION's response. Op-amp based LNAs designed in the current research will be further described in Chapter 4 with their measured noise characteristics.

# 4

# Materials: Low noise amplifier and protection circuit

## Contents



## 4.1 Introduction

LNA plays a vital role in an MPI/MPS device. The signal induced in the receive coil can be in a range lower than 1 μV (- 110 dBm) compared to the excitation signal depending upon the physical properties and concentration of the nanoparticles. The paramount func-

tion of the LNA is to amplify the characteristic SPIONs response to the dynamic range of the data acquisition card without changing the signal integrity and keeping the inherent noise added by its own circuitry as low as possible. Therefore, the LNA needs to have good noise characteristics which include minimum input noise followed by an appropriate SNR or NF. There are several techniques and configurations for producing LNA which relies on CMOS [100], MOSFETS [101], and Op-amps [102]. This research focuses on LNA based on the parallelization technique (also known as summing configuration), to decrease the internal noise produced by its circuitry. To demonstrate the noise characteristics of the prototyped LNA the induced input noise, output noise, spectral density, spectral power, and NF are calculated. In the next section, the design, development, and the measurement setup for different prototyped LNAs will be explained. Different types of LNA are prototyped for different applications such as single-ended fixed gain amplifiers consisting of two different LNA based on LMH6629 (Texas Instruments, USA) and LT6232 (Linear Technology Corporation, USA). Followed by a VGA based on AD603 (Analog Devices, USA) for INSPECT to continuously adapt to the changing magnitude signals produced by the SPIONs undergoing nucleation and growth. At last an FDA based on LMH6553 (Texas Instruments, USA) for an FFL cylindrical scanner based on two Halbach cylinders is presented [103].

## 4.2 LNA based on LMH6629

For the design of this particular LNA, the first stage consists of the LMH6629 (Texas Instruments, USA) an ultra-low noise, high-speed Op-amp which is used in the non-inverting configuration. The specified input voltage noise for LMH6629 is 0.69 nV/ $\sqrt{\text{Hz}}$ and the input current noise is 2.6 pA/ $\sqrt{\text{Hz}}$ [104]. The final design also consists of a second stage consisting of the LT6232 (Linear Technology, USA), a rail to rail Op-amp with the input noise voltage of 1 nV/ $\sqrt{\text{Hz}}$ [105]. The advantage of this particular Op-amp is its availability in SSOP (shrink small outline package) package. Therefore, a total of four Op-amps in a single Integrated Circuit (IC), which makes the layout easier and efficient. In the initial design and development, the second stage is added to achieve an extra gain when required. In the current research, the second stage is not used. The block diagram of the prototyped LNA is shown in Figure 4.1. For this design, the first stage of amplification consists of four Op-amps (LMH6629) in parallel followed by four OP-amps (LT6232) in the second stage. The simulations are performed with the LTspice (Linear Technology, USA).

Various tools from OrCAD PCB design suites (Cadence Design Systems, USA) are used

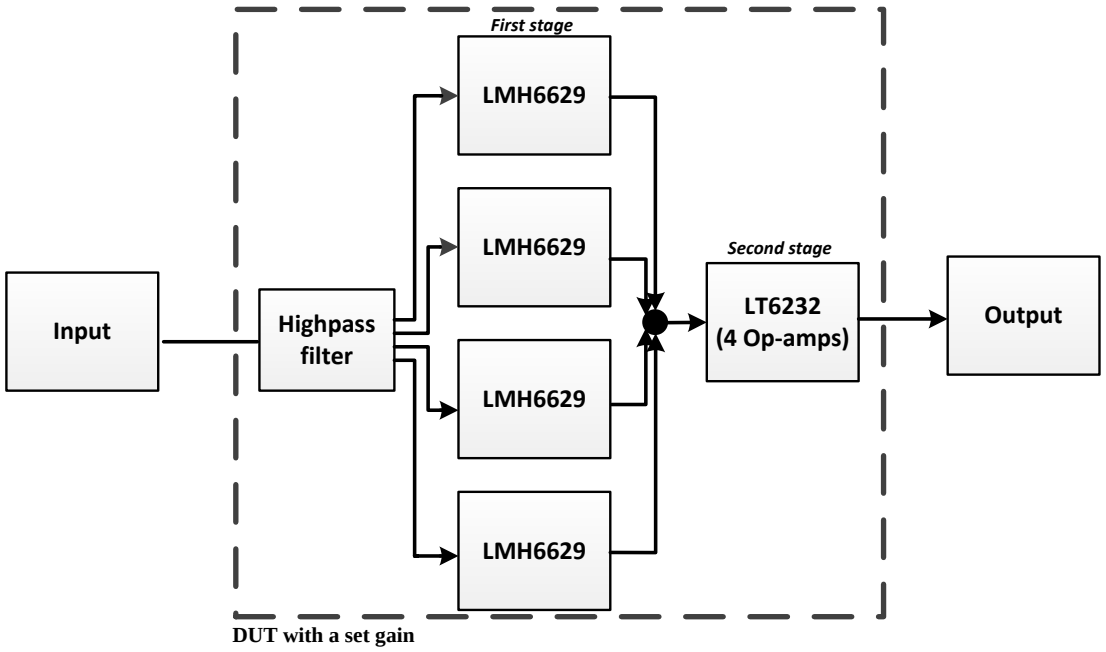


Figure 4.1: Block Diagram of the prototyped LNA based on LMH6629 operating at a fixed gain with four Op-amps in parallel. The second stage consists of another Op-amp LT6232 for additional gain.

for the layout and the design of the prototyped LNA. PCB consists of four layers and is 65 mm × 53 mm with 114 components in total. Some of the resistor footprints were initially added to deal with the instability of the Op-amp, or to make a low pass or high pass filter at the input or output of the LNA to remove unwanted frequencies. Figure 4.2 shows an image of the realized PCB without housing and cables. A comparison of the inherent noise produced by the prototyped LNA based on LMH6629 is carried with a commercially available low-noise voltage preamplifier SR560 (Stanford Research Systems, USA) [106].

### 4.2.1 Measurement setup

According to the datasheet, the SR560 has an input-referred noise of 4 nV/ $\sqrt{\text{Hz}}$ at 1 kHz with 25 pF as input capacitance and a bandwidth of -3 dB at 1.2 MHz [106]. For noise measurement, an EXA-N9010A signal analyzer (Keysight, USA) is used. As the noise level of the SR560 falls below the noise level of the spectrum analyzer, therefore the second stage with a fixed gain of 10 is employed, to raise the level of the signal. Figure 4.3 shows the noise level of the spectrum analyzer and the SR560 (with a gain of 5) at RBW (resolution bandwidth) of 10 kHz. As it could be inferred, the noise level of SR560

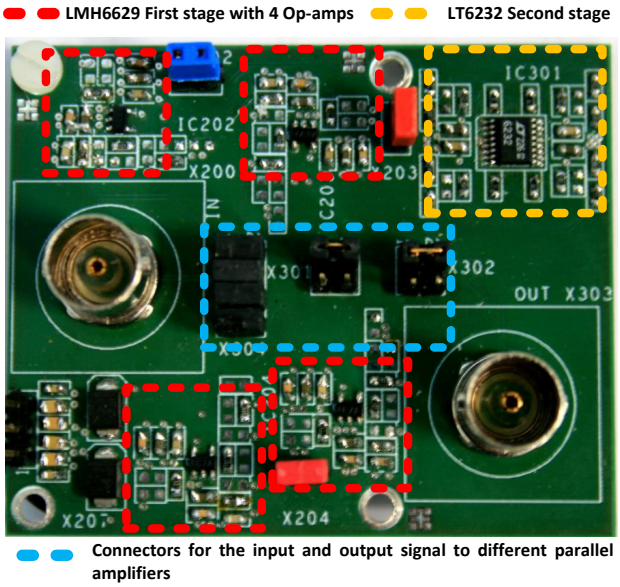


Figure 4.2: The finished PCB showing the connectors and the different stages of the LNA. The input and output signals are connected to the signal chain via BNC connectors. The PCB consists of four different layers with 114 components. The second stage is present for further amplification of the received signal but for the current noise analysis, the second stage is neglected by bypassing the output.

is very close to the noise floor of the spectrum analyzer. Hence there is a need to increase the gain as well as to decrease the RBW for proper and precise noise analysis.

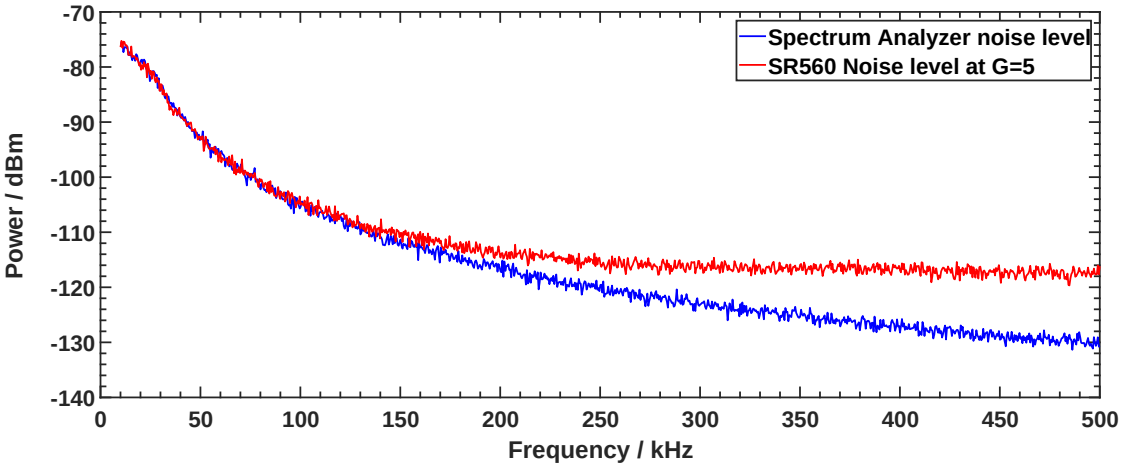


Figure 4.3: The noise level of the commercially available preamplifier SR560 with a gain of 5 in comparison to the noise level of the spectrum analyzer used for noise analysis.

For the measurement of noise characteristics the prototyped LNA based on LMH6629 is connected with the SR560 (G = 10) in a cascade mode with a fixed gain. The block

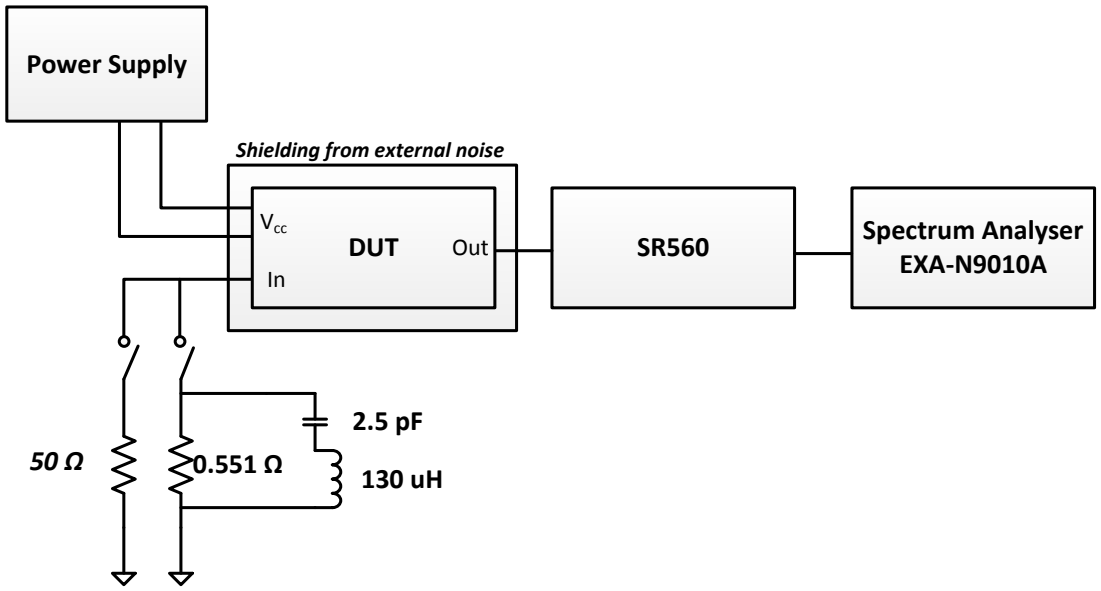


Figure 4.4: The measurement setup for the comparison of the prototyped LNA with the commercially available preamplifier (SR560). The first stage consists of the DUT (Device Under Test) followed by a gain stage (SR560). In the first test, the input of the DUT is terminated with a 50 Ω resistor and in the second test, the DUT is connected to a receiving coil with an internal resistance of 0.551 Ω and inductance of 130 μH.

diagram of the measurement setup is shown in Figure 4.4. In Figure 4.4 DUT is referred to the device under test and in a real setup its the prototyped LNA based on LMH6629. For comparison to SR560, the DUT is replaced with SR560 with a gain of 20. In the first test, the gain of both LNAs is set to 20 and the inputs are terminated with a 50 Ω resistor. All the measurements are performed with an RBW of 1 Hz with 100 averages in the spectrum analyzer. In the second test, the LNAs are connected with a receive coil with an internal resistance of a 0.551 mΩ, an inductance of 130 μH and a self-capacitance of 2.5 pF. For this particular measurement, the gain of the amplifiers is increased to 200 and the spectrum analyzer's RBW is set to 10 Hz with 100 averages.

### 4.2.2 Results

The prototyped LNA based on LMH6629 and SR560 is measured according to the procedure described in the previous section. Figure 4.5 shows the noise power of the LNA prototype based on the LMH6629 in comparison to the commercially available SR560 with a gain of 20. The measurements are done at a resolution bandwidth of 1 kHz with 100 averages. From this data, using an inbuilt function of the spectrum analyzer, the spectral

density in dBm/Hz is calculated. The output noise, the input noise, and the noise figure are calculated according to the equation 2.56 and equation 2.59. The results are shown in Table 4.1.

Table 4.1: The spectral density in dBm/Hz, input noise and NF of the prototyped LNA (LMH6629) and the commercially available SR560 with a gain of 200 terminated with a 50 Ω resistor and a receiving coil. The output noise can be calculated by multiplying the input noise with the gain.

| | **Spectral density (dBm/Hz)** | **Input noise (nV/ $\sqrt{\text{Hz}}$)** | **NF (dB)** |
|---|---|---|---|
| **Prototyped LNA (50 Ω)** | -120.13 | 1.10 | 7.87 |
| **SR560 (50 Ω)** | -98.21 | 13.73 | 29.76 |
| **Prototyped LNA (coil)** | -106.40 | 0.561 | 11.57 |
| **SR560 (coil)** | -92.85 | 2.67 | 25.12 |

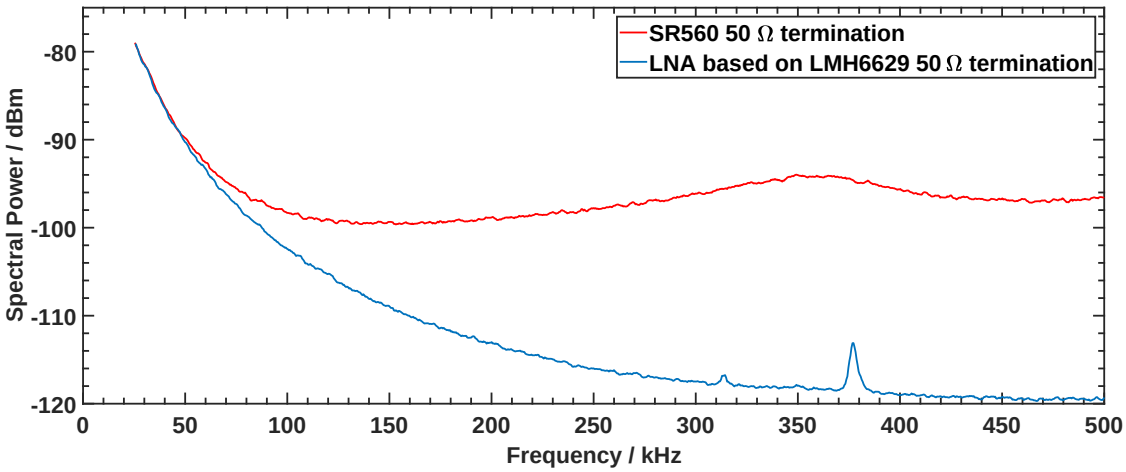


Figure 4.5: The noise spectrum of the prototyped LNA based on LMH6629 compared to commercially available preamplifier (SR560) when connected with a 50 Ω resistor.

A further comparison is made by connecting a receiving coil to the input of the prototyped LNA based on LMH6629 and the commercially available preamplifier SR560. The RBW of the spectrum analyzer is set to 10 Hz with 100 averages. The measurement bandwidth for calculating the spectral density is set to 300 kHz starting from 100 kHz to 400 kHz.

Figure 4.6 shows the noise power of the prototyped LNA in comparison to SR560 with a receiving coil connected at the input. The results are shown in Table 4.1. In comparison to the commercially available amplifier (SR560), the prototyped LNA has around 4.78 times less input noise, when connected with the receiving coil with just 4 stages in parallel. The noise can be further reduced by increasing the number of Op-amps in parallel. The input

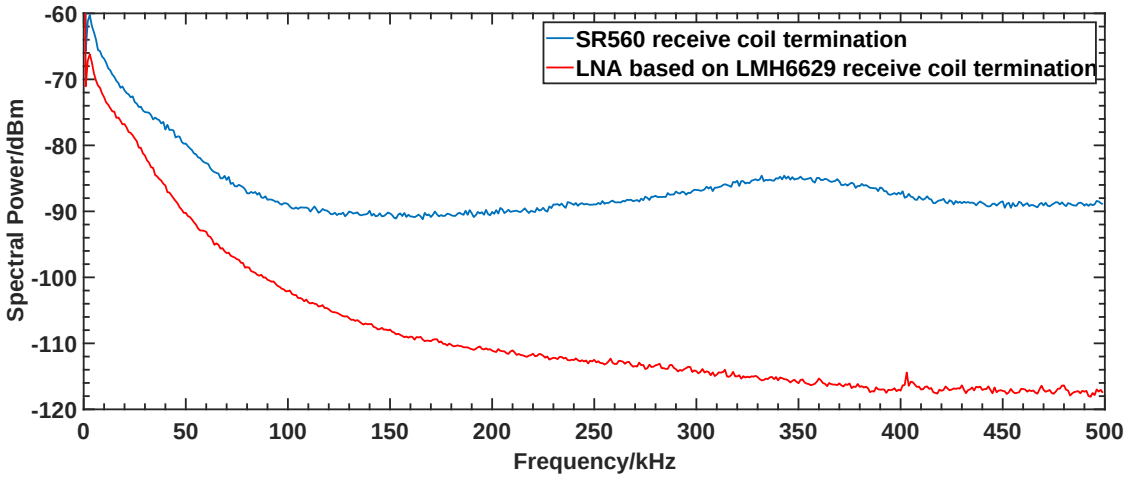


Figure 4.6: The noise spectrum of the prototyped LNA based on LMH6629 compared to a commercially available preamplifier (SR560) when connected with a receive coil.

noise of the LNA based on LMH6629 for 50 Ω termination is 1.1 nV/ $\sqrt{\text{Hz}}$ and with the receive coil termination it is 561 pV/ $\sqrt{\text{Hz}}$.

## 4.3 LNA based on LT6232

The design is based on the LT6232 (the Linear Technology, USA), a rail to rail Op-amp with an input noise voltage of 1.1 nV/ $\sqrt{\text{Hz}}$ and an input noise current of 1 pA/ $\sqrt{\text{Hz}}$ [105]. Besides the low noise characteristics of the Op-amp, another advantage is its availability in SSOP (shrink small outline package) package. Therefore, a total of four Op-amps in a single IC are present, which makes the layout easier and efficient. Other specifications include a gain-bandwidth product of 215 MHz and an input bias current of 5 μA. The operating supply voltage for the particular design is set to ± 5 V. This Op-amp is operated in the non-inverting configuration. The block diagram and the measurement setup of the prototyped LNA based on LT6232 are shown in Figure 4.7.

The LNA is divided into two stages and both stages consist of an LT6232. The first stage has 16 Op-amps and the second stage has 8 Op-amps in parallel. All the Op-amps have a non-inverting configuration. For this particular research, only the first stage is used. The second stage is just added to get some extra gain if required. There are jumpers present on the PCB to configure the usage of different stages depending upon the magnitude of the received signal from the SPIONs. The input power supply to the PCB is 5 V DC with 500 mA, 2.5 W from a power adapter (MPU 31-102 from Dehner Eletronik GmBH). This 5 V DC is converted to ± 5 V DC with the help of LT8582 (Linear Technologies) which

is a DC/DC converter with fault correction and a switching frequency of 2.5 MHz. The switching frequency near the excitation frequency in MPS/MPI devices can cause noise due to the varying magnetic fields generated by the components causes physical vibration at higher frequencies. The PCB consists of four layers with separate ground and power plane with over 200 components. The jumpers are used for bypassing the second stage and hence connecting the first stage directly to the output. The image of the manufactured PCB is shown in Figure 4.8.

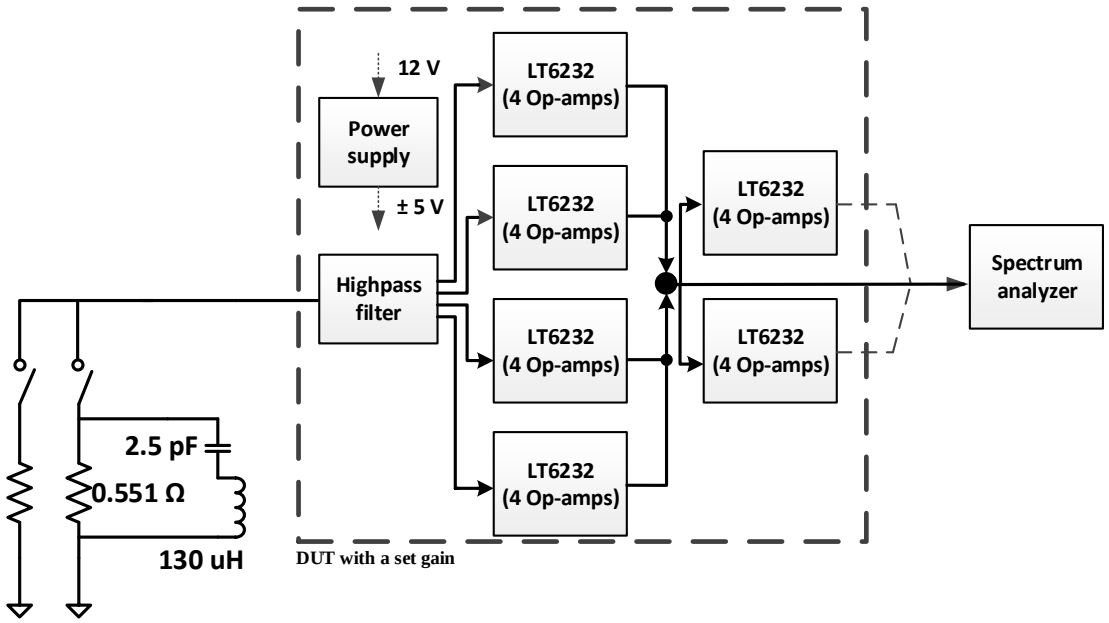


Figure 4.7: Block diagram of the prototyped LNA based on LT6232 and the measurement setup for noise analysis. The LNA also consists of two different stages, in the first stage there are 16 Op-amps in parallel and the second stage consists of four Op-amps in parallel. The second stage is not accounted for noise analysis and can be easily bypassed by using jumpers located on the PCB. DUT is referred to the prototyped LNA based on LT6232 as its the device under test. For comparison of the noise parameters, the DUT is replaced with the commercial preamplifier SR560.

### 4.3.1 Measurement setup

For the measurements, the LNA is directly connected to the spectrum analyzer EXA-N9010A (Keysight, USA) as described in Figure 4.4. For testing and calculating the input voltage noise, the measurements are done in two setups, with an input termination of a 50 Ω resistor and in the other case with a receive coil. The gain is also varied for the two setups to see the variance in noise at low and high gains. Therefore, two gains are

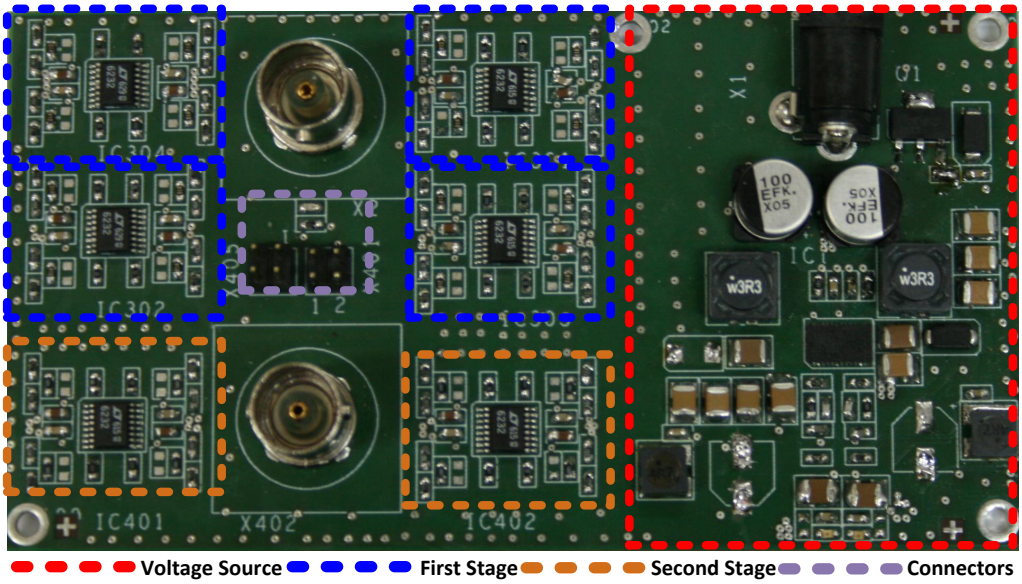


Figure 4.8: Manufactured PCB of the LNA based on LT6232 with all the modules. The PCB is symmetrically designed to avoid voltage drop over the traces in the PCB. The PCB consists of four layers with over 200 components. The voltage source (marked in red) converts the input voltage of 5 V to ± 5 V. The connectors (marked in purple) can be used to bypass the second stage of the prototyped LNA based on LT6232.

used, 105 and 500, respectively. The spectral density is measured from 1 kHz to 1 MHz. The RBW (resolution bandwidth) and VBW (video bandwidth) of the spectrum analyzer are set to 1 kHz and 100 Hz, respectively. RBW is the frequency span of the final filter that is applied to the input signal. Small values of RBW leads to finer frequency resolution and makes differentiation possible when the input signal's frequencies are closer together. VBW is the frequency span of a time-domain low-pass filter, mathematically equivalent to the mean or average. VBW does not affect the measurement results as its just applied before the screen of spectrum analyser displays the trace. Reduced VBW makes small signals much more clear in the display. Each measurement constituted of 100 averages with 500 points. By using the in-built function of the spectrum analyzer, the spectral noise power is calculated at 600 kHz by keeping the BW at 1 Hz. BW is the range of frequencies used for the measurement of the input signal. Furthermore, the prototyped LNA is compared with the commercially available preamplifier SR560 (Stanford Research Systems). The results will be presented in the next section.

### 4.3.2 Results

In this section, all the measurements, as well as the calculated values regarding the noise analysis, will be described. For measurement of the noise power, all the measurements are performed by the measurement setup described in the previous Section 4.3.1. For comparison purpose, the device under test (DUT) is switched between the prototyped LNA and the commercially available LNA SR560. For simplification purposes, not all the measurements are shown in graphs but the calculated values such as input noise, output noise, and NF are shown in Table 4.2. Figure 4.9 shows the noise performance of the prototyped LNA with gains of 105 and 500, with input termination with a 50 Ω resistor. Similarly, Figure 4.10 shows the performance of the LNA with input termination with a receive coil. The receive coil has an internal resistance of 0.551 mΩ, a self-capacitance of 2.5 pF and inductance of 130 µH. From the above data, an in-built function present in the spectrum analyzer for calculating the spectral noise density in dBm/ $\sqrt{\text{Hz}}$ is used. For further comparison, these values are also measured with the commercially available LNA SR560. And the equation 2.56 to equation 2.59 are used for calculating input noise, output noise as well as corresponding NF. These values are stated in Table 4.2.

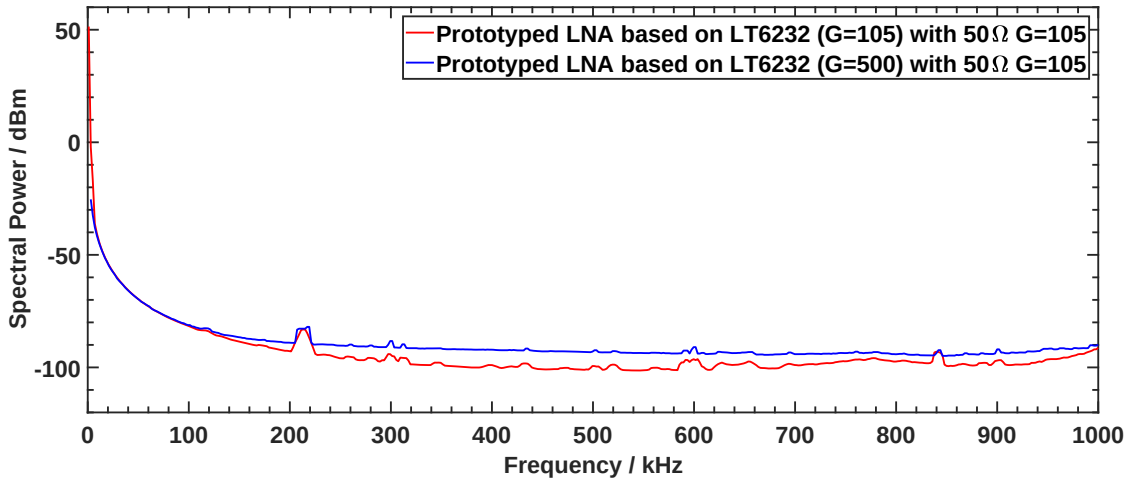


Figure 4.9: The noise spectrum of the prototyped LNA based on LT6232 connected with a 50 Ω resistor at the input with two different gains of G = 105 and G = 500.

In the current research, a prototyped LNA is designed and manufactured for MPS. Moreover, the prototyped LNA is compared with a commercially available LNA. The prototyped LNA has an input noise of 546 pV/ $\sqrt{\text{Hz}}$ and NF of 1.35 dB with a receive coil at the input. The NF is approximately 25 times lower than the NF of the commercially available LNA in the same testing conditions.

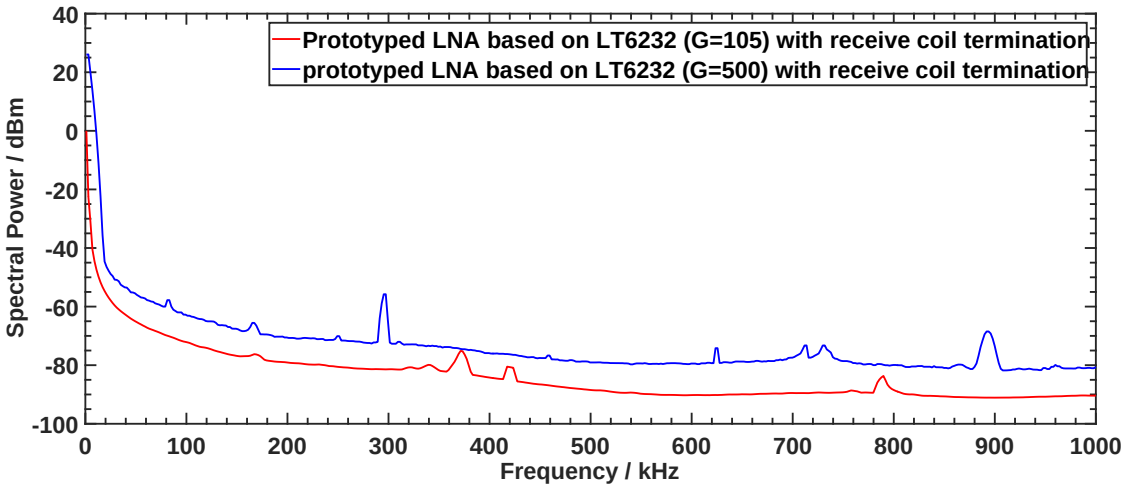


Figure 4.10: The noise spectrum of the prototyped LNA based on LT6232 connected with a receive coil with an internal resistance of 0.551 mΩ and a self-capacitance of 2.5 pF at two different gains of G = 105 and G = 500.

Table 4.2: The spectral density in dBm/Hz, input noise and NF of the prototyped LNA based on LT6232 and the commercially available SR560 with a gain of 105 and 500 with 50 Ω resistor and a receiving coil. The output noise can be calculated by multiplying the input noise with the gain.

| | **Input** | **G** | **Spectral density (dBm/ $\sqrt{\text{Hz}}$)** | **Input noise (nV/ $\sqrt{\text{Hz}}$)** | **Output noise (μV/ $\sqrt{\text{Hz}}$)** | **NF (dB)** |
|---|---|---|---|---|---|---|
| **Prototyped LNA (LT6232)** | **50 Ω** | **105** | -128.549 | 0.795 | 0.083 | 5.30 |
| | | **500** | -116.712 | 0.653 | 0.326 | 3.32 |
| | **Receive coil** | **105** | -120.419 | 0.223 | 0.022 | 13.58 |
| | | **500** | -118.670 | 0.546 | 0.273 | 1.35 |
| **Preamplifier SR560** | **50 Ω** | **105** | -108.430 | 8.421 | 0.840 | 25.57 |
| | | **500** | -93.65 | 9.2 | 4.64 | 26.37 |
| | **Receive coil** | **105** | -107.266 | 1.01 | 0.10 | 26.73 |
| | | **500** | -92.900 | 1.06 | 0.53 | 27.11 |

## 4.4 Variable gain amplifier (VGA)

In the synthesis process of SPIONs, specifically at the initialization of the nucleation and growth, the magnetic response of the particles is weak and with the passage of the synthesis, this magnetic response increases depending on the growth of the SPIONs. Therefore, it is sometimes necessary to attenuate the signals produced by the SPIONs so that other modules in the signal path does not get saturated. Therefore, for the SPIONs

undergoing nucleation and growth, it is necessary to have high gain at the initialization and maybe attenuation at the final steps of the growth. Therefore, a variable gain amplifier based on AD603 (Analog Devices, USA) is designed. AD603 is a low noise, a voltage-controlled amplifier with pin selectable gains from -10 dB to +30 dB with a bandwidth of 9 MHz. The input-referred noise of the LNA is 1.3 nV/ $\sqrt{\text{Hz}}$ with a load impedance as low as 100 Ω with THD of -60 dBc[1] for a ± 1 V sinusoidal output at 10 MHz [107].

### 4.4.1 Block diagram and measurement setup

Figure 4.11 shows the block diagram and the noise measurement setup of the VGA based on AD603. For the measurement, the VGA is directly connected to the spectrum analyzer EXA-N9010A (Keysight, USA) as described in Figure 4.11. For testing and calculating the input voltage noise, the measurements are done in two setups, with an input termination of a 50 Ω resistor and in the other case with a receive coil. The noise measurements are done at the maximum gain of 31 dB. The designed PCB of the VGA is shown in Figure 4.12 with all the connectors needed for the desired operation. All measurements are performed in a frequency range of 1 kHz to 1 MHz with 100 averages. The RBW for the measurement is set to 10 Hz and VBW to 30 Hz.

### 4.4.2 Results

The measured transient response (for all the gains ranging from -11 dB to 31 dB) and the frequency response (over the maximum gain), as well as the phase response of the designed PCB, is shown in Figure 4.13. The measurement of the output voltage over time is carried out with an oscilloscope (HDO6104-MS from Teledyne LeCroy, USA). The input signal is generated with the help of a function generator producing 25 kHz at 170 mV. The results obtained differ from the simulated values by only a few millivolts. For the measurement of the gain and the frequency response, a network Analyzer (E5061B from Keysight Technologies, USA) is used. It is important to check the gain as well as the phase change of the signal as it is a frequency-dependent process. The measurement is carried over a frequency range of 1 kHz to 1 MHz. The results are shown in Figure 4.13. The gain of the system is 29.37 dB slightly lower than mentioned in the datasheet and with a variation of only 0.1 % and is very stable. The change in the phase till 1 MHz is about 5 degrees or 1.4 % which could be easily corrected with the help of its transfer

[1] dBc is an unconventional unit defining the power of the fundamental frequency of the signal used for testing. Therefore, dBc value should be converted to dBm for each of the harmonic values before calculating their power level in watts.

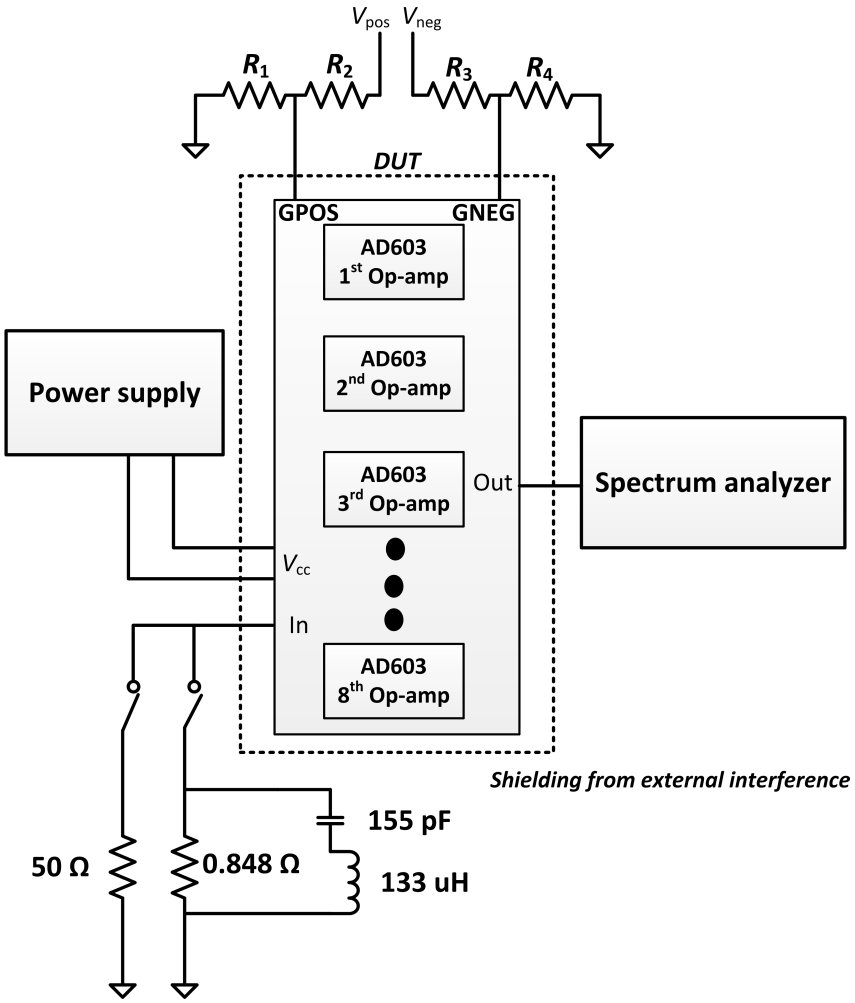


Figure 4.11: The block diagram and the noise measurement setup for the prototyped VGA based on AD603.

function.

To assess the noise level of the LNA, two different measurements are made as described in the previous section. First measurement with a 50 Ω resistor and another measurement with a coil at the input of the circuit. The input noise versus frequency response of the VGA is shown in Figure 4.15 for single AD603 with parallelization as well as with two to eight AD603 in parallel.

In the next measurement, a receive coil is used with a resistance of 848 mΩ, a capacitance of 155 pF and an inductance of 133 μH. The results with the coil are better than the noise analysis with 50 Ω resistance, but at higher frequency range the values are quite similar. Figure 4.16 represents the input noise obtained with a receive coil termination. Table 4.3 shows the NF obtained with VGA for single AD603 to eight in parallel for both the 50 Ω

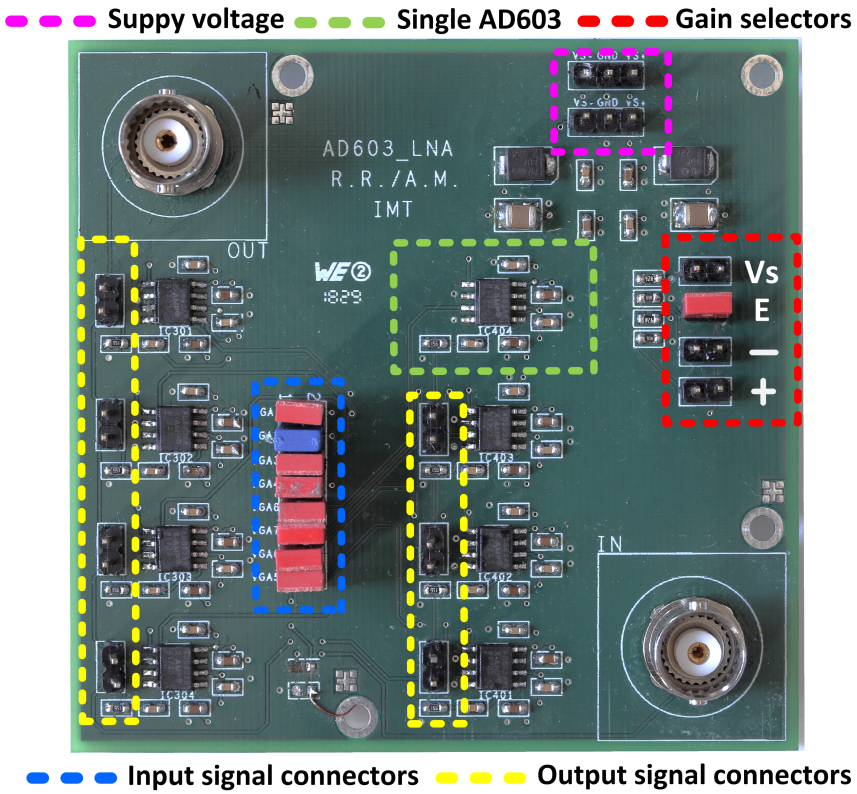


Figure 4.12: Manufactured PCB of the prototyped VGA with all eight AD603 parallel at maximum gain. The pins in the red rectangle are used to set the desired gain. '+' Stands for the maximum gain '-' stands for the minimum gain. Both pins get their voltage through a voltage divider ratio from the supply voltage. Via 'E' will connect to one variable voltage applied to 'Vs'. The pins in the pink rectangle serve as pins for the supply voltage. In the blue area are the pins for connecting the input signal to the inputs of each amplifier. So that different numbers of Op-amps can be connected in parallel. Analogous to the inputs in the blue box are all pin connections in the yellow boxes to connect the output pins to the overall output of the circuit. Only the Op-amp on the top left is always connected to the output. In the green rectangle is a single Op-amp block with all its associated passive components required for its operation.

resistance and the receive coil at the input.

## 4.5 Fully differential amplifier (FDA)

As stated earlier in Section 2.10, an FDA has more advantages as it provides an increased noise immunity in comparison to a normal operational amplifier. In this section, a fully differential amplifier based on LMH6553 (Texas Instruments, USA) is presented. The bandwidth of the LMH6553 is 900 MHz and has an integrated output clamping circuit

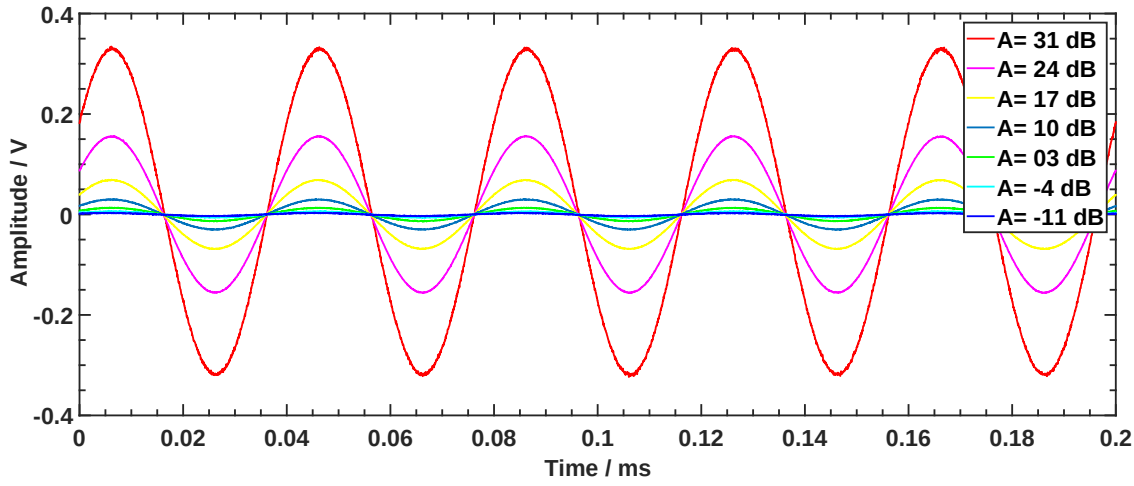


Figure 4.13: The transient response of the designed VGA based on AD603. The input signal for measuring the transient response is 10 mV. The graph shows the output with different gains: -11 dB (blue), -04 dB (cyan), 03 dB (green), 10 dB (black), 17 dB (yellow), 24 dB (pink) and 31 dB (red).

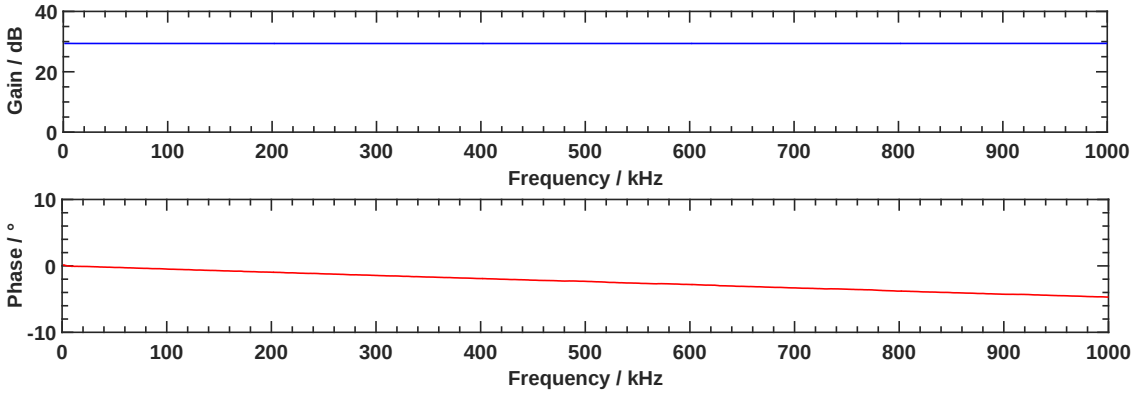


Figure 4.14: The gain and phase response of the designed VGA based on AD603.

Table 4.3: NF of the designed VGA with different parallel units as well as with two different input termination i.e. 50 Ω resistor and a receive coil (resistance = 848 mΩ, capacitance = 155 pF, inductance = 133 μH).

| **Parallel Stages** | **NF with 50 Ω (dB)** | **NF with receive coil (dB)** |
|---|---|---|
| 1 | 6.24 | 5.92 |
| 2 | 4.59 | 4.08 |
| 4 | 3.57 | 2.83 |
| 8 | 1.86 | 1.91 |

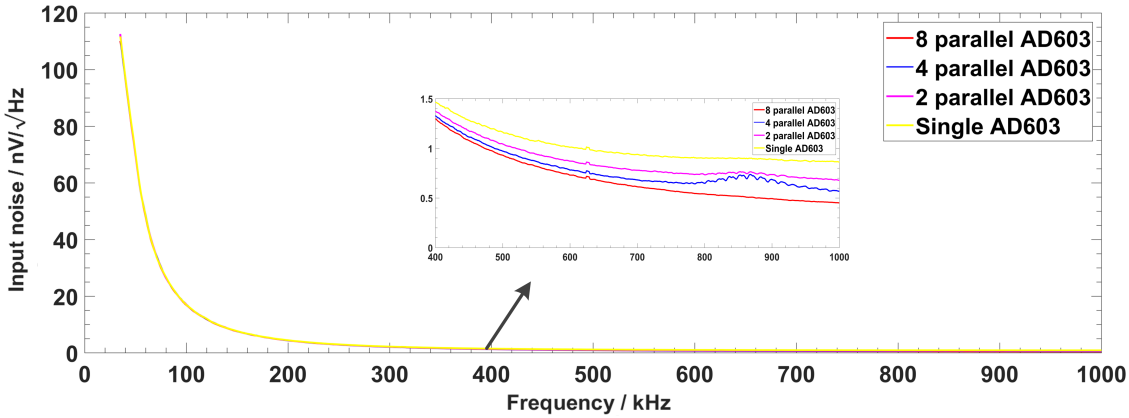


Figure 4.15: Input noise calculated from the measured data from the signal analyzer with 50 Ω resistance. As the noise level of individual parallel AD603 is difficult to visualize. Therefore, an enlarged image from 400 kHz to 1 MHz is also displayed.

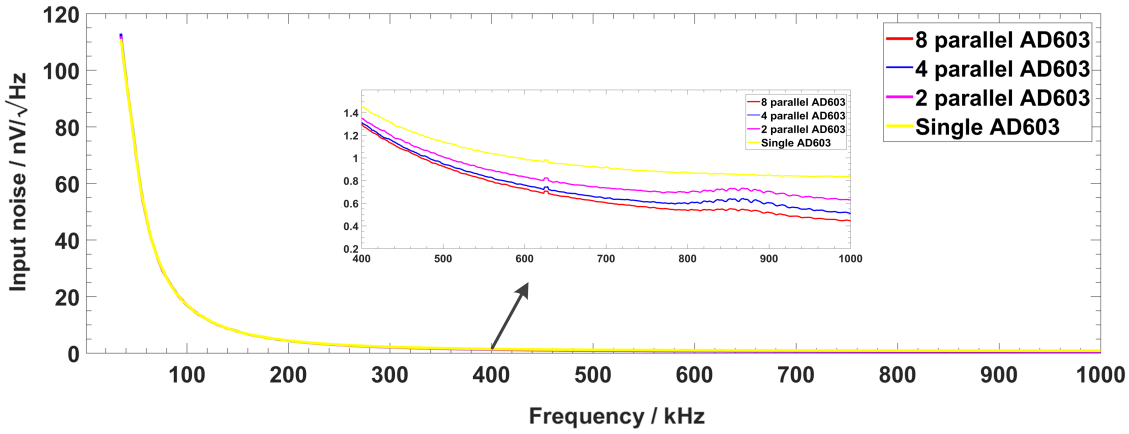


Figure 4.16: Input noise calculated from the measured data from the signal analyzer with receive coil with a resistance of 848 mΩ, a capacitance of 155 pF and an inductance of 133 µH. As the noise level of individual parallel AD603 is difficult to visualize. Therefore, an enlarged image from 400 kHz to 1 MHz is also displayed.

to provide transient over voltage protection to the ADC present in the signal chain of an MPI/MPS device. Therefore, eliminating the need for external protection circuit and leading to reduction of noise in the overall signal chain. As LMH6553 is a fully differential amplifier, it can also be connected to a single-ended device and produce a differential output for ADC driver. According to the datasheet the input noise voltage and input current voltage at 100 kHz is 1.2 nV/ $\sqrt{\text{Hz}}$ and 13.6 pA/ $\sqrt{\text{Hz}}$ with second harmonic distortion (HD2) at -79 dBc [108]. The input voltage noise can be further reduced by parallelization as the input capacitance in differential mode is just 0.5 pF [108]. The block diagram and the noise measurement setup of the manufactured FDA based on LMH6553 is shown in

Figure 4.17. In the block diagram the -IN is grounded but in the original design, there is a connector which makes the usability in sense of differential signals possible. The gain of the amplifier can be set by using the feedback resistors shown in Section 2.10. The FDA is operated with a power supply of ± 5 V. The $V_{CM}$ pin is grounded to achieve the output reference at 0 V leading to symmetrical signals without any offsets. Moreover, it is very important to drive $V_{CM}$ with low impedance source and a bypass capacitor of 0.1 µF, as any unwanted signal which couples to this pin will be passed along the outputs reducing the noise performance of the amplifier. For setting the gain of the amplifier it is very important to achieve maximum matching between the positive and negative feedback. As asymmetry, adversely effects the CMRR (common-mode rejection ratio), DC offset, and the output balance of the LMH6553. Therefore, resistors with 0.1 % should be used. The next useful feature of the FDA is the $V_{CLAMP}$ pin which allows the control of the output swing of the FDA to protect the ADC from high voltages as well as to achieve fast recovery from transients, which could saturate the signal path. To achieve the proper operation of the clamping voltage the value of $V_{CM} < V_{CLAMP} < V_{CM} + 2$ V for the lower ended output voltage and the upper ended output voltage is set according to the voltage set at $V_{CM}$. The voltage of $V_{CM}$ could be easily set with the help of a voltage divider consisting of resistors $R_1$ and $R_2$ connected to the power supply of the FDA, depending upon the maximum input voltage allowed for the ADC.

The designed PCB is shown in Figure 4.18. The size of the PCB is 125.47 mm × 25.45 mm consisting of 160 components. The PCB consists of four layers with a separate ground and power plane. Special care was taken to maintain the symmetry of the differential signal paths as small amounts of asymmetry could contribute to distortions. In Figure 4.18 a small window shows the ground plane consisting of the signal path using differential pair layout technique in which the length matching is done for both the input signal as well as the output signal to achieve maximum symmetry. Moreover, to get the maximum symmetry from any differential amplifier it is essential to use precision resistors with 0.1% tolerance at the input pins, feedback resistors as well as the output matching resistors.

### 4.5.1 Measurement setup

Figure 4.17 also shows the measurement setup for the noise characterization of the FDA. A spectrum analyzer EXA-N9010A (Keysight Technologies, USA) is used to measure the power spectrum of the FDA which is in turn used to calculate the output noise, input noise and NF of the FDA. The same measurement principle is followed for the measurement of the FDA as shown with previous LNAs. Two measurements are performed, first with an input termination of a 50 Ω resistor and second with a receiving coil with an internal

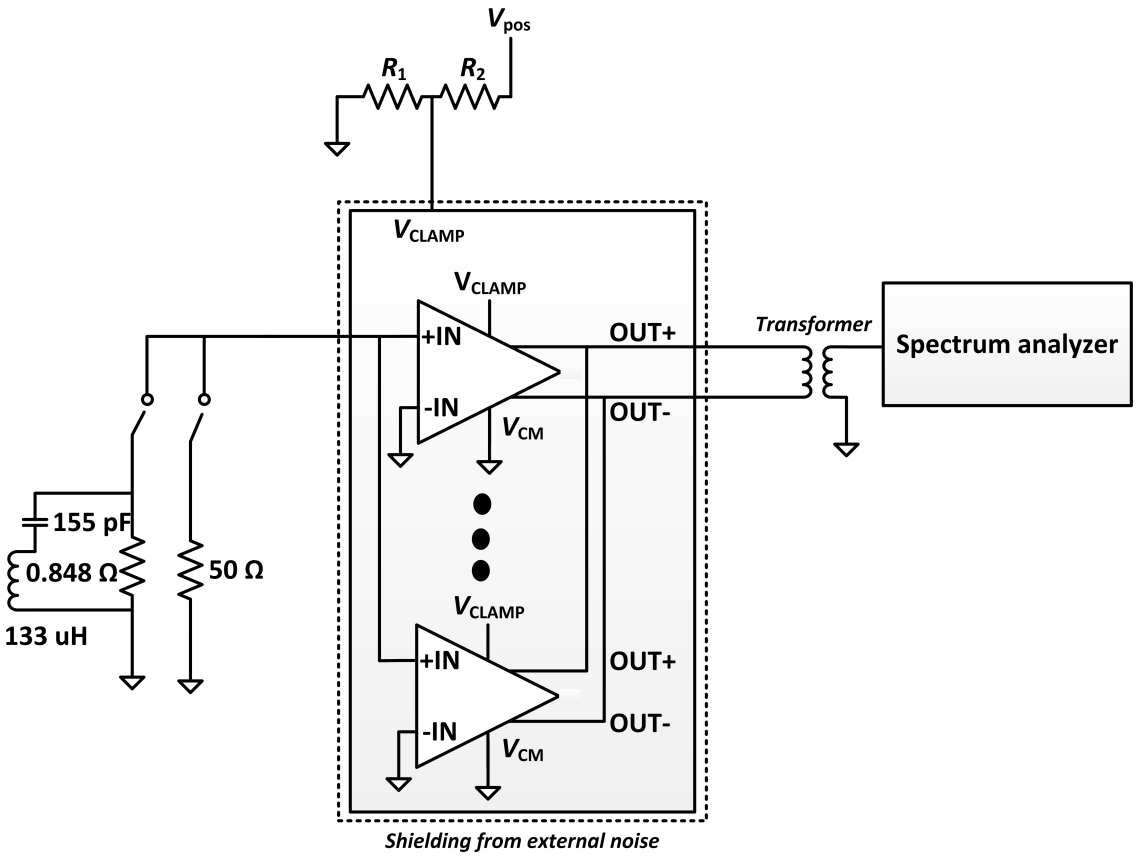


Figure 4.17: Block diagram of the designed FDA consisting of four LMH6553 in parallel. Resistors $R_1$ and $R_2$ is used to set the clamping voltage for protection circuit. Pin -IN is grounded just to operate it in single-ended input configuration but the FDA is also capable of handling differential input.

resistance of 848 mΩ, a capacitance of 155 pF and an inductance of 133 µH as shown in Figure 4.17. As the spectrum analyzer is a single-ended device, the differential output of the designed FDA is converted to single-ended with the help of a transformer (Würth Elektronik, Germany) with a turn ratio of 1:1. The measured noise also contains a noise factor generated through the transformer but it is assumed that the noise produced by such a transformer is negligible. The results obtained will be shown in the next section.

### 4.5.2 Results

Figure 4.19 shows the transient and frequency response of the designed FDA. The transient response is measured with the help of an oscilloscope (LeCroy HDO402A-MS from Teledyne Lecroy, USA) and the frequency response is measured with an audio amplifier (APx500 from Audio precision Inc., USA). The transient response displays the output

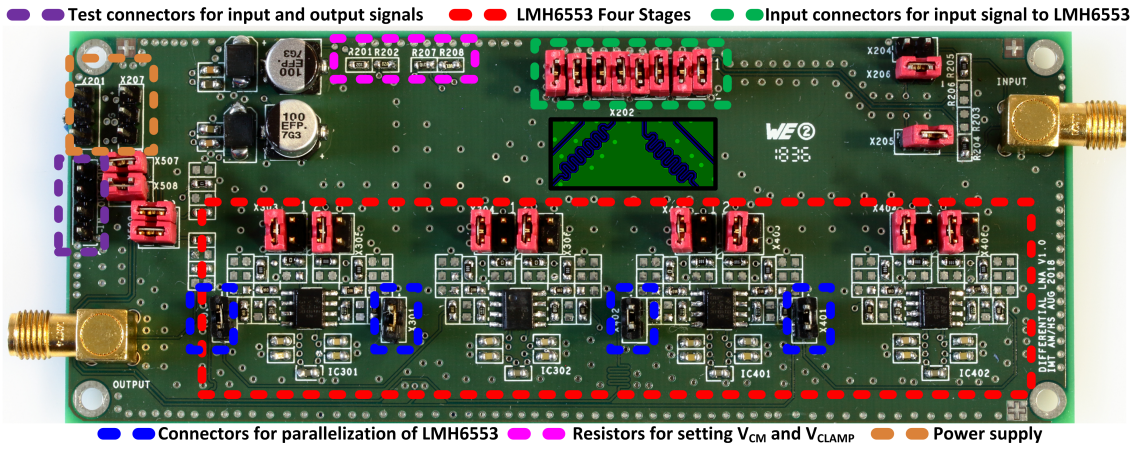


Figure 4.18: Manufactured PCB of the prototyped FDA based on LMH6553 consisting of four layers. The PCB consists of four LMH6553 with the feedback resistors for controlling the gain (marked in red). The PCB consist of various connectors (marked in green) for feeding the input signals to the LMH6553 as well connectors (marked in blue) for parallelization of the four LMH6553. The connectors (marked in purple) are test pins for visualizing the differential input as well as output to the LMH6553. SMA connectors are used at the input and output to connect the FDA to the signal chain of an MPI/MPS device. A small window in black shows the ground layer consisting of traces carrying differential signals maintaining the same length to conserve the symmetry between the two differential signals.

signal from the Out+ (marked in blue), Out- (marked in black) pins and the differential voltage (marked in red). The voltage difference between the signal from Out+ and Out- is less than 0.01 % displaying the signal symmetry. According to the datasheet, the harmonic distortion should be around -79 dBm and the values measured are completely in the range. But the value of HD3 is higher than estimated by the datasheet. This is due to the stray capacities in the designed PCB. Nevertheless, HD3 is approx -69 dBm which should not hamper the signal integrity.

The clamping voltage can be set by supplying a DC voltage to the $V_{\mathrm{CLAMP}}$ pin. This is achieved with the help of a voltage divider and by using the supply voltage to the FDA itself. Figure 4.20 shows the transient response of the FDA when operated below the set clamping voltage as well as the transient response when the output voltage exceeds the set clamping voltage. $V_{\mathrm{CLAMP}}$ is set to approximately 2 V as it can be seen from the upper graph in Figure 4.20 when the output voltage is below 2 V the signal is passed without any clamping but as soon as the voltage exceeds 2 V then the clamping occurs safeguarding the ADC for high voltages which can cause damage to the internal circuitry of the ADC. Figure 4.21 shows the spectral response of the fully differential signal marked in orange in Figure 4.20. In Figure 4.21 the upper graph (marked in blue) constitutes the

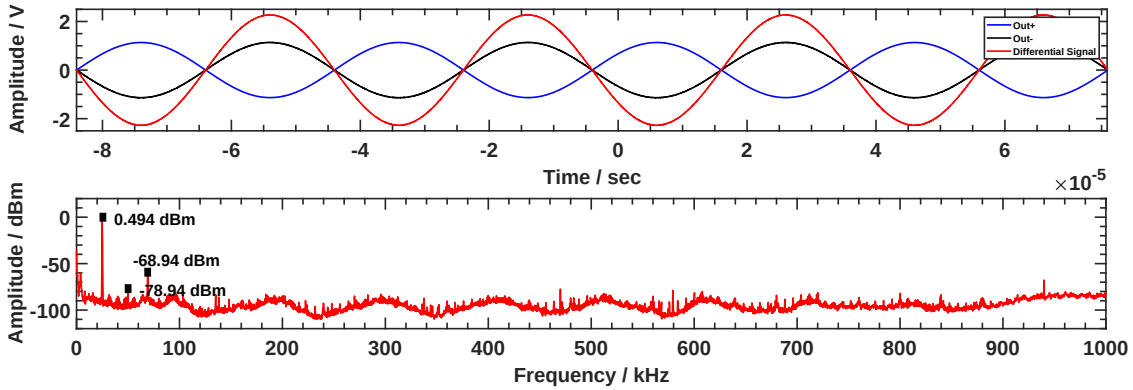


Figure 4.19: Upper graph shows the transient response of the designed FDA consisting of the Out+, Out- and the fully differential signal ((Out+)+(Out-)). The lower graph shows the spectral response of the designed FDA with $f_0$ = 25 kHz at 0.494 dBm and the HD2 at -78.94 dBm and HD3 at -68.94 dBm respectively.

frequency response of a signal operating in the limits of the clamping voltage followed by the frequency response of the clipped signal (shown in red) when the output voltage exceeds the clamping voltage. The signal marked in red is saturated due to the presence of additional harmonics caused by clamping.

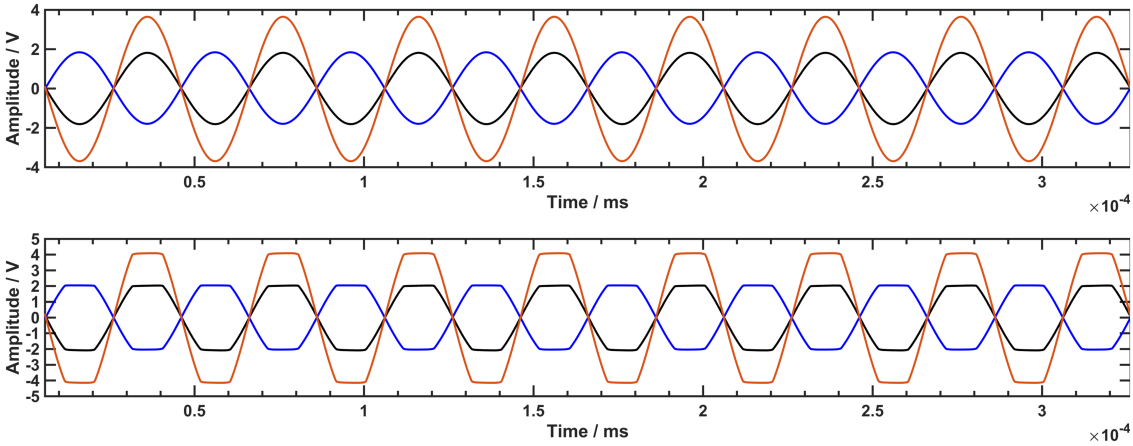


Figure 4.20: Upper graph shows the transient response of the designed FDA when no clamping takes place as the voltage does not exceed the set voltage at pin $V_{CLAMP}$ and the lower graph shows the clipped signal as it exceeds the set voltage at $V_{CLAMP}$.

The spectral noise is measured with the help of a spectrum analyzer EXA-9010A (Keysight technologies, USA). The block diagram for the measurements is shown in Figure 4.17. Two measurements are performed, first with an input termination of a 50 Ω resistor and second with a receive coil with an internal resistance of 848 mΩ, a capacitance of 155 pF and an inductance of 133 µH. A transformer WE 510348 (Würth Elektronik eiSos GmbH

& Co. KG, Germany) with 1:1 winding ratio is used to convert the differential signal to signal ended for the measurement with the spectrum analyzer.

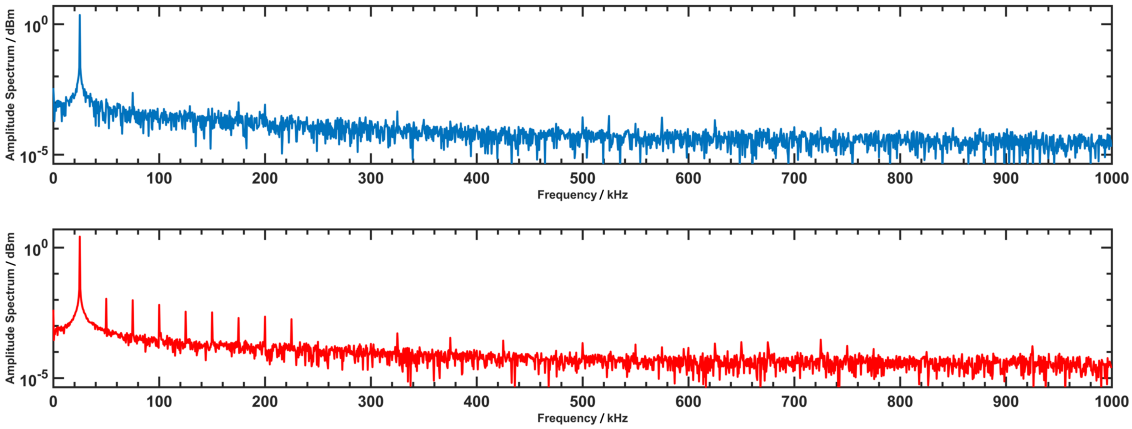


Figure 4.21: Upper graph shows the frequency response of the designed FDA when no clamping takes place as the voltage does not exceed the set voltage at pin $V_{CLAMP}$ and the lower graph shows the frequency response of the clipped signal as it exceeds the set voltage at $V_{CLAMP}$.

Figure 4.22 shows the spectral power of the FDA at a gain of 41 dB. The FDA is planned to operate with an FFL cylindrical scanner based on two Halbach cylinders [103]. The bandwidth range of this scanner is 600 kHz. Therefore the noise analysis is carried out in this particular bandwidth. Two measurements are conducted one with a 50 Ω resistance (marked in red) and with a receiving coil (marked in blue) with an internal resistance of approx. 0.848 mΩ and a self-capacitance of 155 pF. The black curve shows the noise floor of the spectrum analyzer. Table 4.4 shows the calculated output noise, input noise and the NF of the designed FDA using measurements shown in Figure 4.22. Unfortunately, the prototyped FDA cannot be compared to a commercially available preamplifier SR560 as it is a differential amplifier at the input but the output is single-ended. Hence, it would be not favorable to compare a FDA to a single-ended amplifier. The input noise parameters of the FDA are quite impressive, especially with the receive coil termination. The input noise of the FDA in the bandwidth of 200-600 kHz with the receiving coil at the input is around 299 pV/ $\sqrt{\text{Hz}}$ and with a 50 Ω resistance at the input is around 1.76 nV/ $\sqrt{\text{Hz}}$. The difference between the input noise between the two measurements can be attributed to the higher resistance of the 50 Ω resistor in comparison to the receiving coil. But it is important to measure the noise with the 50 Ω resistor as it could be considered as a standard measurement as the noise in the receive coil heavily depends on the dimension of the receiving coil as well as it is more prone to environmental noise. The NF of the FDA with a 50 Ω resistor is around 11.93 dB and with the receiving coil, it is around

14.05 dB. The NF calculated is higher in comparison to all the LNAs discussed in this chapter but its still satisfactory as a typical commercially radio receivers usually have an NF of about 15 dB.

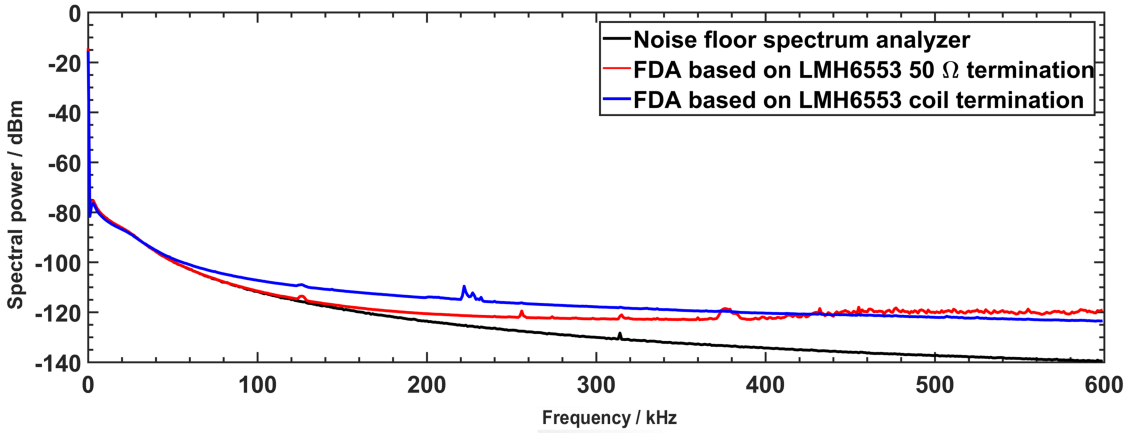


Figure 4.22: The noise spectrum of the designed FDA based on LMH6553 connected with a receiving coil (marked in blue) with an internal resistance of 0.848 mΩ and a self-capacitance of 155 pF and a 50 Ω resistance (marked in red) at a gain of G = 110.60. The curve in black is the noise floor of the spectrum analyzer.

Table 4.4: The spectral density in dBm/Hz, input noise and NF of the designed FDA based on LMH6553 with a gain of G = 110.60 with 50 Ω resistor and a receiving coil. The input noise can be calculated by dividing the output noise with the gain.

| | **Input** | **Bandwidth (kHz)** | **Spectral density (dBm/ $\sqrt{\text{Hz}}$)** | **Input noise (nV/ $\sqrt{\text{Hz}}$)** | **Output noise (nV/ $\sqrt{\text{Hz}}$)** | **NF (dB)** |
|---|---|---|---|---|---|---|
| **Designed FDA (LMH6553)** | **50 Ω** | **200-400** | -122.127 | 1.58 | 175 | 10.99 |
| | | **200-600** | -121.189 | 1.76 | 195 | 11.93 |
| | **Receive coil** | **200-400** | -117.200 | 0.36 | 40.19 | 15.92 |
| | | **200-600** | -118.875 | 0.30 | 33.14 | 14.05 |

## 4.6 Protection Circuit

As mentioned earlier, it is of importance to protect the acquisition unit containing ADC from transient high voltages and currents. These transient high voltages and currents could be produced due to several factors such as sparks in the filtering stages, bad soldering joint or even through the human errors of setting a higher gain in the LNA. This

could lead to irreversible damage to the acquisition unit. The FDA mentioned in the above section has an inbuilt clamping unit but this is not the same for the other LNAs discussed in this chapter. Therefore, it is necessary to manufacture a protection module to protect the acquisition unit from these unwanted signals. There are several ways to design a protection circuit based on both passive components such as diodes as well as with active components such as amplifiers. For passive diodes, Schottky diodes and Zener diodes are ideal and makes sure that voltages higher above the power supply + 0.7 V (0.3 V for germanium based diodes) are rectified. With Zener diode, this is more simple as they are available with Zener breakdown voltages ranging from 2.4 V to 33 V and even higher. But the inherent problem with the passive components is that they fail to provide a hard rectification to the signal leading to the passage of higher current and voltages to the acquisition unit. This rectified signal still can damage sensitive acquisition unit. To overcome this problem a protection circuit is designed with Op-amps based on OPA698 (Texas Instruments, USA). OPA698 is a unity stable, wide-band voltage limiting amplifier with a gain-bandwidth product of 250 MHz with a gain ($G \geq 5$) and a slew rate of 1100 V/µs. The limiting voltage can have a maximum offset error of a maximum of ± 10 mV. The protection circuit is operated with a voltage supply of ± 5 V which is the same supply voltage to all the LNAs described in this chapter. Figure 4.23 shows the image of the designed PCB. The PCB consists of two channels consisting of two different Op-amps (OPA698) and BNC connectors for an easy connection with the receive chain. Two channels are designed, one channel needed for the receive signal carrying the characteristic response of SPIONs and the other channel functions as a feedback signal to monitor the magnetic flux generated by the field generator. For protection against the high current, a 100 mA fuse is used which could be adjusted depending upon the maximum current allowed to the acquisition board. The PCB has four different layers with separate ground and power planes and the total size of the PCB is 56.64 mm × 62.99 mm. The PCB can be easily configured to be used as a unity gain amplifier or with a desired gain depending on the magnitude of the received signal.

### 4.6.1 Results

The cutoff voltage for the protection of the acquisition unit can be easily set with a voltage divider circuit connected to two pins of OPA698. The positive cutoff can be set by supplying the required voltage at pin $V_H$ and the negative voltage can be set at pin $V_L$. This provides the freedom to set different voltages for the positive as well as the negative signals. For estimating the performance of the protection circuit a sinusoidal signal with the frequency of 10 kHz with a $V_{pp}$ of 1.9 V is generated with the help of a function

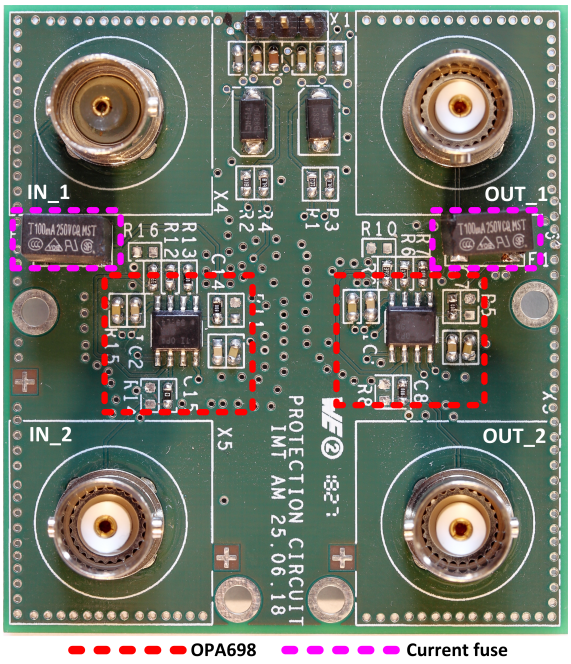


Figure 4.23: The designed PCB of the protection circuit consisting of two channels with separate OPA698 (marked in red) for voltage overload protection and current fuse (marked in pink) for overload current protection. The inputs and outputs can be connected with the help of BNC connectors.

generator (DG1022, from RIGOL Technologies USA, Inc.) and fed to the input of the protection circuit. The cutoff voltage at the $V_{\mathrm{H}}$ and $V_{\mathrm{L}}$ is set to 2.3 V. Therefore, when the input signal exceeds 2.3 V then the clamping circuit should get activated.

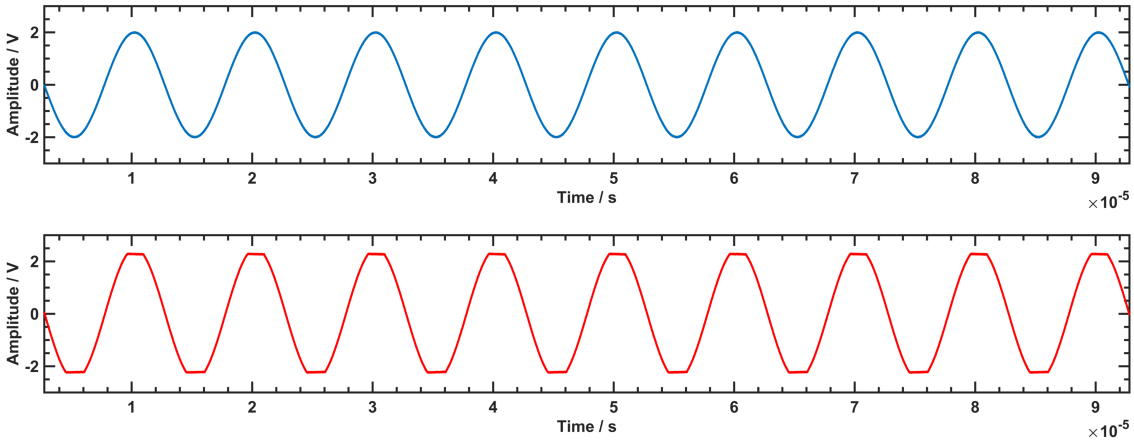


Figure 4.24: Transient response of the protection circuit in normal mode and the overload mode when the output signal exceeds the cutoff voltage.

The upper graph in Figure 4.24 shows the transient response of the protection circuit in

non-clipping mode and Figure 4.25 shows the frequency response of the same signal. Overall the fidelity of the signal looks good but there are some HD2 and HD3 distortions present in the frequency response of the signal.

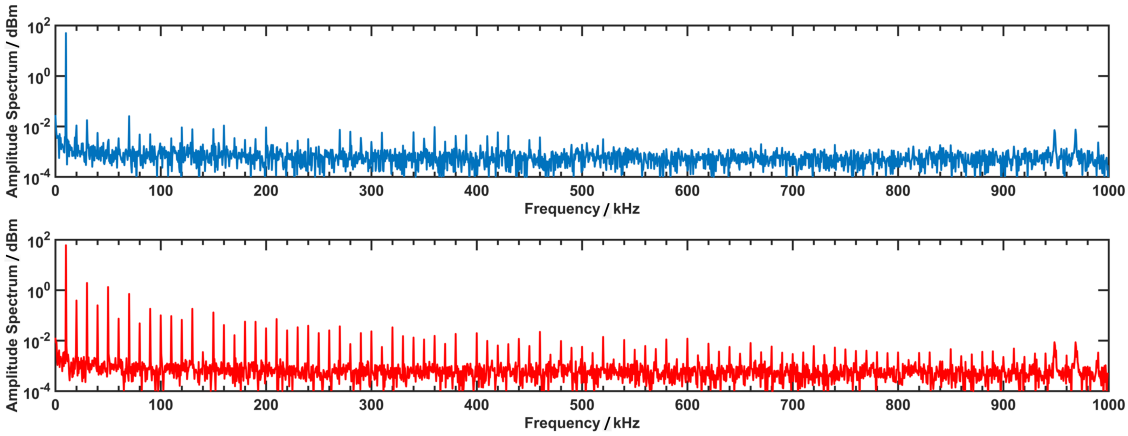


Figure 4.25: The frequency response of the protection circuit in the normal mode and the overload mode when the output signal exceeds the cutoff voltage.

The amplitude of HD2 and HD3 is 66.3 dBm and 62.5 dBm respectively. These harmonic distortions are negligible and hence can be neglected. As soon as the amplitude of the input signal exceeds 2.3 V the clamping takes place. This can be easily seen in the transient response of the protection circuit (lower graphs) of Figure 4.24 and in the frequency response (lower graphs) in Figure 4.25. For this experiment, the supplied input signal to the protection circuit has an amplitude of 2.5 V at the same frequency of 10 kHz. The clipping of the signal is quite evident from the lower graph in Figure 4.24 followed by the ringing effect seen in the frequency response of the protection circuit in Figure 4.24 (lower graph). The protection circuit provides a hard-clipping even when the input signal is increased to 5 V the output of the protection circuit is limited to 2.3 V. The disadvantage with the protection circuit is the addition of further noise to the receiving signal, but it provides the needed overload protection to the expensive modules like the acquisition board. According to the datasheet the amplifier has a voltage noise of 5.6 nV/ $\sqrt{\text{Hz}}$ and current noise of 2.2 pA/ $\sqrt{\text{Hz}}$.

## 4.7 Conclusion

All the LNAs discussed in this chapter are based on the parallelization technique to mitigate the inherent noise produced by various components present in the LNA itself. Different LNAs were designed such as two single-ended LNAs, an VGA and an FDA. These

LNAs can be used in different MPI/MPS devices with minor changes regarding the operational gain which in turn would determine the operational bandwidth depending upon the gain-bandwidth product.

# 5

# In-situ magnetic particle spectrometer (INSPECT)

## Contents



## 5.1 Introduction

An MPS is a device used for characterizing SPIONs for their performance in an MPI scanner. The anisotropy and size distribution of the SPIONs (used as a tracer material) play a vital role in the quality of the MPI images [109]. The nanoparticles used for the first experiments in MPI were predominantly developed for MRI and are of limited use in the excitation fields of an MPI scanner. Not only for imaging techniques such as MRI or MPI, SPIONs have also been used for therapeutic applications such as MFH (magnetic fluid hyperthermia) [110]. In MFH, the SPIONs serve as a medium for the deposition of energy to a specific area using their hysteresis losses [111]. Therefore, another significant

property for such an application is the magnetization curve of the SPIONs. For MFH, the hysteresis curve area should be large enough to cause cell ablation due to the deposition of the required energy through a process called magnetostriction. Moreover, the larger the size of the SPIONs, the steeper would be the rise in the magnetization curve leading to measurements of higher harmonics. But as the size increases, the field strength of the excitation field must be increased as bigger SPIONs require more energy to get magnetized directly affecting the power consumption of an MPI scanner. The size of the particles also directly affects the Brownian and Néel relaxation time, as the Brownian and Néel relaxation time increases with increasing size [72][71]. In addition to this, the geometrical properties such as shape and size plays an essential role in the biodistribution and biocompatibility inside a living biological system [112][113][114].

Furthermore, SPIONs can also be used for targeted drug delivery at a specific location such as tumor cells [115]. Therefore, there is an immense need for tailored SPIONs with specific properties which could be used for many applications. Fortunately, there is immense research and development being performed to produce SPIONs that are well suited for MPI and MFH based therapy [116][117]. The most important properties of SPIONs are defined magnetic properties (e.g., saturation magnetization, steepness of magnetization curves, anisotropy) and geometrical properties (core diameter, hydrodynamic diameter distribution in suspension) to show optimal results in any magnetism based application. Previously, a lot of commercially as well as research-based SPIONs have been characterized and compared based on of their magnetic properties in an MPS device [73]. In earlier studies, it was found that the SPIONs with a core diameter of 20 nm and hydrodynamic diameter of 30 nm showed the best performance for MPI [74].

There are different techniques used for determining the magnetic properties of the SPIONs. One of the well-known devices is VSM (vibrating-sample magnetometer) which provides information regarding the magnetic susceptibility by measuring the static magnetization curve. But a VSM is not able to measure the spectral magnetic moment of the SPIONs at a desired frequency and field strength used in MPI scanners. This is achieved with the help of an MPS device which can operate at different field strength at various frequencies to provide information regarding the magnetic properties of SPIONs. The measurements obtained with an an MPS device usually consists of amplitude and phase spectra. The amplitude spectrum consists of both the even and odd harmonics. The SPIONs response just consists of the odd harmonics and even harmonics can be attributed to the presence of DC offset of the produced magnetic field. By using the information from the amplitude and phase spectra, dynamic magnetization curves can also be calculated giving information regarding the energy stored in the SPIONs as well as the saturation

characteristics. These measurements could further be used for estimating the core diameters of the SPIONs [51]. Therefore, there had been immense hardware development in the field of MPS. Currently, there are different variants of MPS devices available with specific applications. For instance, one-dimensional MPS without offset and with various excitation frequency followed by two-dimensional MPS which can measure the SPIONs response with different trajectories (such as Lissajous, spiral, circular trajectories, etc.) used in MPI scanners [20][18]. Two more variants which are worth mentioning are the arbitrary-waveform generator and the three-dimensional MPS system [118][42]. The arbitrary-waveform generator is the first untuned MPS with 400 kHz of excitation bandwidth and hence is capable to capture the response of SPIONs at different excitation frequencies [118]. The three-dimensional spectrometer can emulate a complete MPI scanner. This not only provides the response of the SPIONs in a three-dimensional field but also helps in measuring system matrices which are needed for image reconstruction. The conventional method for measuring the system matrices in an MPI scanner comprises of mechanical movement of a point sample through the FOV. The conventional method is time-consuming and lacks the required sensitivity. The three-dimensional MPS can perform the measurements much faster and with higher sensitivity [118][42]. One of the inherent problems with all the mentioned MPS devices is that the sample chamber is very small and can fit maximum 100 µL of SPIONs which is not enough to carry the synthesis process. But the small chamber size is justified as the measurements are performed on synthesized SPIONs. Therefore, the synthesis process is left completely unobserved and there is no information regarding the nucleation and growth of the SPIONs. The current research deals with another variant of the MPS called INSPECT (in-situ magnetic particle spectrometer). This device can track the nucleation and growth of the SPIONs undergoing a synthesis process in real-time by measuring the change in the magnetic moment of the SPIONs undergoing synthesis.

Other methods exist to track the nucleation and growth of SPIONs, such as X-ray diffraction and real-time TEM (Transmission electron microscopy, also known as in-situ TEM) [90][91]. TEM is an advanced tool and provides optical and structural information in the sub-Angstrom scale of the nanoparticles undergoing synthesis. X-ray diffraction technique lacks the optical information but provides direct information regarding the crystal structure, chemical composition and the physical parameters for nanoparticles undergoing nucleation and growth. Moreover, by using X-ray diffraction techniques nanoparticles can also be observed at a higher temperature and pressure conditions, therefore it is widely used for studying mechanochemical reactions [119][120]. But for both techniques there are requirements for specifically designed in-situ chambers for carrying out chemical reactions. Moreover, these devices have a very tedious setup with high hardware complex-

ities and cannot be used in a normal chemistry laboratory [121][122][123][124][125]. They also require user experience for not only experimenting but for analyzing the measurement results. The device proposed in this work, does not require any special sample chambers or experimentation setup to conduct chemical reactions. Moreover, the measurement chamber is big enough for a 100 ml flask so that conventional chemical reactions can be easily performed as in a normal chemistry laboratory. INSPECT is a low-cost device with low instrumentation complexity as compared to X-ray diffraction and in-situ TEM. With low or negligible user expertise it is still possible to carry out a chemical synthesis process in INSPECT and the device can autonomously track the nucleation and growth of the SPIONs. INSPECT gives direct access to the change in the magnetic moment, a parameter which is important for magnetic imaging (e.g. MPI) and magnetic thermo-therapeutic scenarios such as MFH. One limitation of INSPECT is that the physical principle relies on the change of magnetization of the growing nanoparticles, therefore, it can only be used for tracking the nucleation and growth of those nanoparticles which are magnetic in nature. In this chapter, the hardware and software realization of INSPECT will be described. The measurements obtained through INSPECT will be explained in the next chapter.

## 5.2 Materials and method

In this section, the different modules present in the INSPECT will be described. The diameter of the measurement chamber of INSPECT is approximately 72 mm and can easily fit a reaction flask of 100 ml. The complexity of the hardware modules in comparison to the previously described MPS systems is kept as modest as possible taking into consideration the usage and application of the device [20][18][118][42]. SPION synthesis is a chemical process and the safety of the chemists is very important. Therefore, the device is designed in such a way that only the field generator is located inside the fume hood and the other modules can be located outside. Figure 5.1 shows the block diagram of the INSPECT with all the modules. As can be seen from Figure 5.1, INSPECT does not have any filters either in the transmit or the receive chain.

### 5.2.1 Signal generation and acquisition

The excitation signal ($T_X$) is generated with the help of a dedicated acquisition card connected to a PC. The acquisition card is also used for acquiring the characteristic SPION's response ($R_X$) and displaying it to the user. For this research, an X3-25M (Innovative

Integration, USA) is used as an acquisition card [126]. The X3-25M comprises of two 16-bit ADC channels and two 16-bit DAC channels with a bandwidth of 75 MHz. Moreover, the ADC has programmable input ranges so the input voltage can be configured depending upon the magnitude of the received signal ($R_X$).

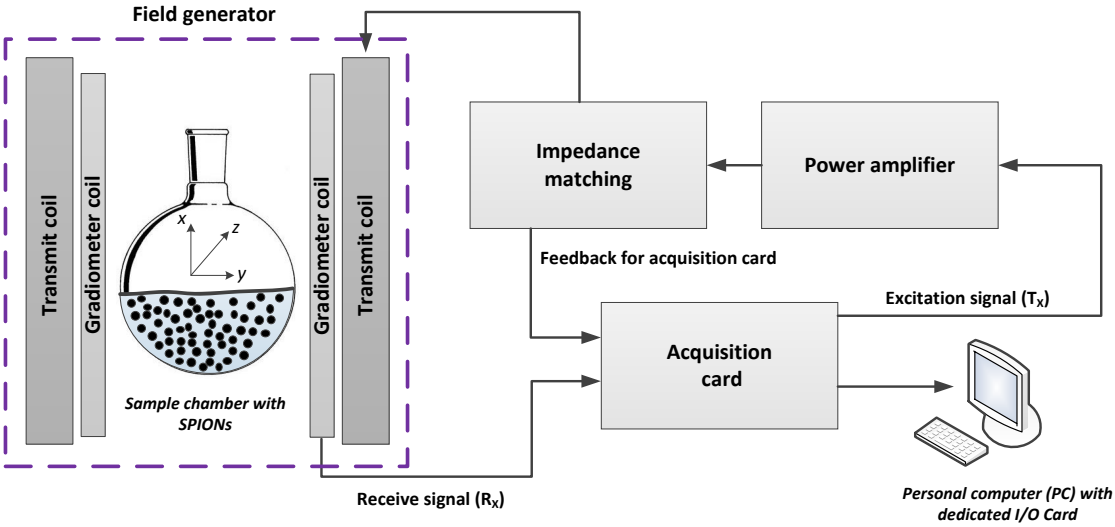


Figure 5.1: Block diagram of in-situ magnetic particle spectrometer (INSPECT) with different modules. Personal computer with a dedicated acquisition card is used for generating the excitation frequency as well as for acquiring the SPION's characteristic response. INSPECT device has no filters as well as low noise amplifier as compared to other MPS systems.

One of the DAC channels is used for generating the excitation signal ($T_X$) and has an output of $\pm$ 2$V$. $T_X$ is a sinusoidal signal with a frequency of 23 kHz with a sampling frequency of 5.06 MSPS (mega samples per second) ensuring a high signal quality. One of the ADC channels of the X3-25M is used for acquiring the receive signal ($R_X$). $R_X$ is also acquired with the same sampling rate of 5.06 MSPS. The other ADC input is used for the feedback signal from a Rogowski coil at the same sampling frequency. A Rogowski coil functions as an electrical sensor for measuring AC or current pulses. It consists of a helical coil which could be wrapped around a straight conductor for current measurements. The feedback signal is used for estimating the produced magnetic field generated by the transmit coil. All the signals are synchronized with the help of a timing unit present in the X3-25M. The total measurement time for one measurement is approximately 1 s with 10 periods and 2300 averages. These measurement parameters are used for analyzing the sensitivity of the INSPECT as well as monitoring the nucleation and growth of the SPIONs in Chapter 6. For faster acquisition, the measurement time for one single measurement can be further reduced to 42.9 µs comprising of one single period

making the system real-time.

### 5.2.2 AC power amplifier

The generated $T_X$ has to be amplified to achieve the required field strength of 10 mT to excite the SPIONs. This is achieved with the help of a power amplifier called AE Techron 2105 (AE Techron, USA) [127]. The power amplifier has a bandwidth of up to 400 kHz and can be operated in both current-controlled and voltage-controlled modes. The slew rate of the power amplifier is 75 V/µs and for impedance matching the prescribed load can be between 0.1 Ω to 8 Ω [127]. For INSPECT, the power amplifier is operated in voltage-controlled mode with a gain of 20. The power amplifier has a very low THD of less than 0.1 % at the excitation frequency of 23 kHz. This reduces the need for a band-pass filter, which is used in conventional MPS systems as described in Chapter 3. Figure 5.2 shows the electrical block diagram of the system with all the electrical modules from the power amplifier to the field generator. The field generator comprises of the transmit coil **(1)** and gradiometer coil **(2)** (cancellation coil and receiving coil). Impedance matching **(3)** consists of two capacitors $C_S$ and $C_P$. The Rogowski coil **(4)** is used for the feedback channel to measure the changes in the magnetic flux density.

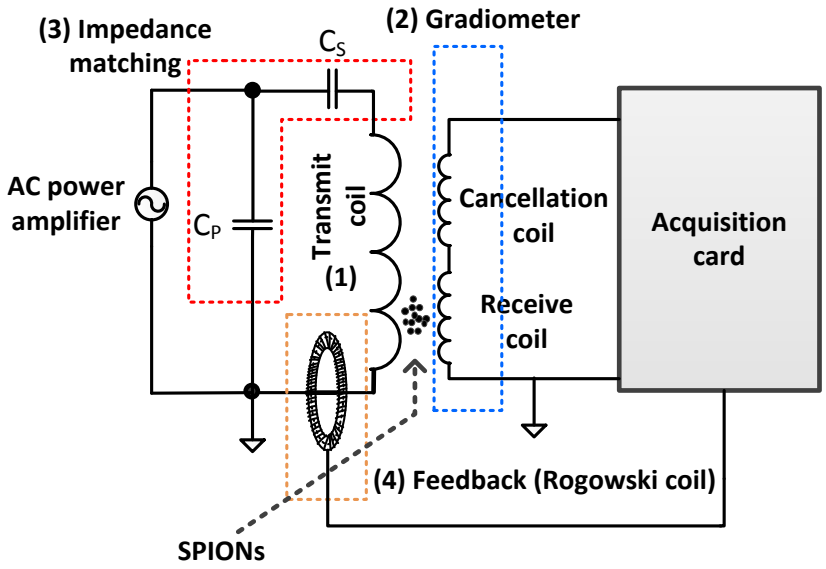


Figure 5.2: Electrical block diagram of INSPECT with different modules: transmit coil **(1)**, gradiometer coil **(2)**, impedance matching **(3)** and Rogowski coil **(4)**.

### 5.2.3 Impedance matching

The function of the impedance matching is to transfer the maximum power from the power amplifier to the transmit coil while reducing the reflected power. For INSPECT capacitive impedance matching is used. Capacitive impedance matching comprises of two capacitors namely, $C_P$ connected in parallel to the transmit coil and $C_S$ connected in series to the transmit coil as shown in Figure 5.2. As the $C_S$ is connected in series, the voltage rating of these capacitors should be very high. This voltage rating can also be achieved by forming a bank of capacitors consisting of series and parallel capacitors to reduce the amount of current flowing through them. Figure 5.3 shows the designed and manufactured impedance unit for INSPECT. For constructing the impedance matching unit, different capacitors with voltage rating from 1000 V DC to 3000 V DC from KEMET Electronics Corporation are used.

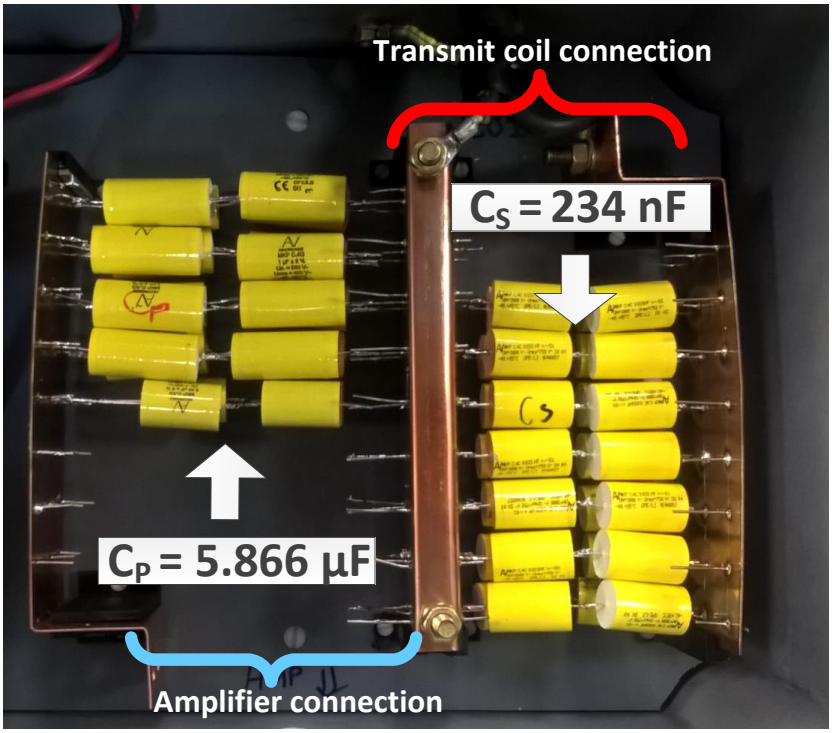


Figure 5.3: The impedance matching unit for INSPECT, connecting the transmit coil to the power amplifier. The impedance matching is done with the help of capacitor banks to achieve the right voltage and current rating for the used capacitors.

Figure 5.4 shows the transfer function of the impedance matching unit connected to the transmit coil used in INSPECT. The black curve shows the impedance (Z) measured in Ohms (Ω) and the blue curve denotes the corresponding phase angle measured in degree (°). The impedance is matched to the excitation frequency of 23 kHz at a load

of 3.05 Ω with a slightly negative phase of −1.05° for making the impedance matching capacitive. The temperature of the transmit coils during the measurement periods must be kept constant as due to heating the internal resistance of the coil will change leading to impedance mismatch. As can be seen from Figure 5.4 due to the slope of the curve a slight change in the value of capacitors (in ranges of nH) can lead to impedance mismatch. To match the impedance between the transmit coil and the power amplifier the values of the capacitors bank, $C_P$ = 5.866 µF and $C_S$ = 234 nF is chosen.

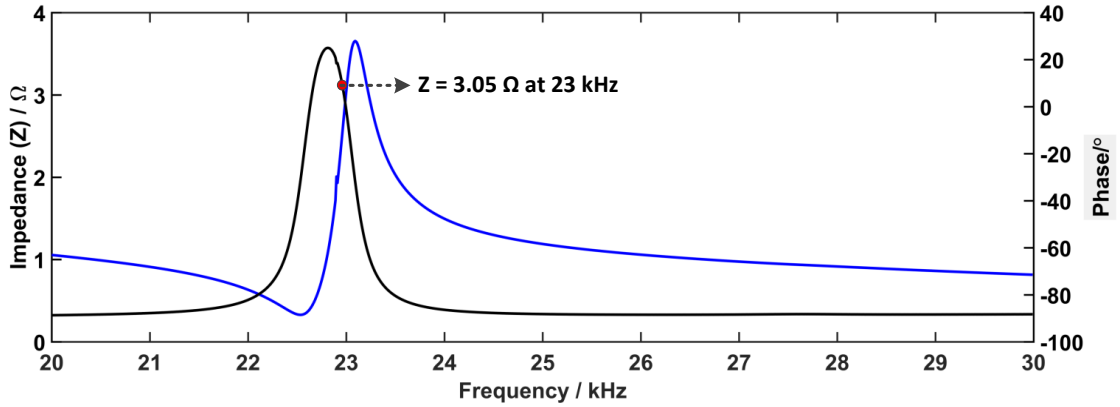


Figure 5.4: Impedance matching curve for transfer of maximum power between the power amplifier and the transmit coil. Impedance is matched to a load of 3.05 Ω with a slightly negative phase of −1.05°. Two capacitor banks used for impedance matching have $C_P$ = 5.866 µF and $C_S$ = 234 nF.

### 5.2.4 Field generator

The field generator comprises of a transmit coil and a gradiometer coil. The transmit coil is responsible for the generation of the required field for exciting the SPIONs. The gradiometer coil comprises of two different coils i.e. the cancellation coil and the receiving coil connected in series and wound up in reverse directions. The gradiometer coils perform two different tasks simultaneously, firstly canceling the transmit signal and secondly acquiring the SPION's characteristic response. Figure 5.5 and Figure 5.6 shows the complete field generator with the housing. The housing is 3D-printed and includes the transmit coil, the gradiometric coil and air channels for cooling both the coils. The housing is manufactured with ProJet 3510 HDPlus 3D printer (3D Systems, USA). The printed material can withstand temperatures up to 80 °C, with this temperature the alkaline co-precipitation synthesis could be easily performed. For chemical reactions requiring higher temperatures such as organic synthesis, there is a need to manufacture housing

with resins which can withstand higher temperatures in the range of 250 °C. One such resin material is available from Formlabs (Formlabs Inc., USA) called High Temp Resin (FLHTAM02) offering HDT (heat deflection temperature) of 238 °C at 0.45 MPa [128]. The transmit coil and the gradiometer coils are cooled with the help of pressurized air flowing through the cooling channels.

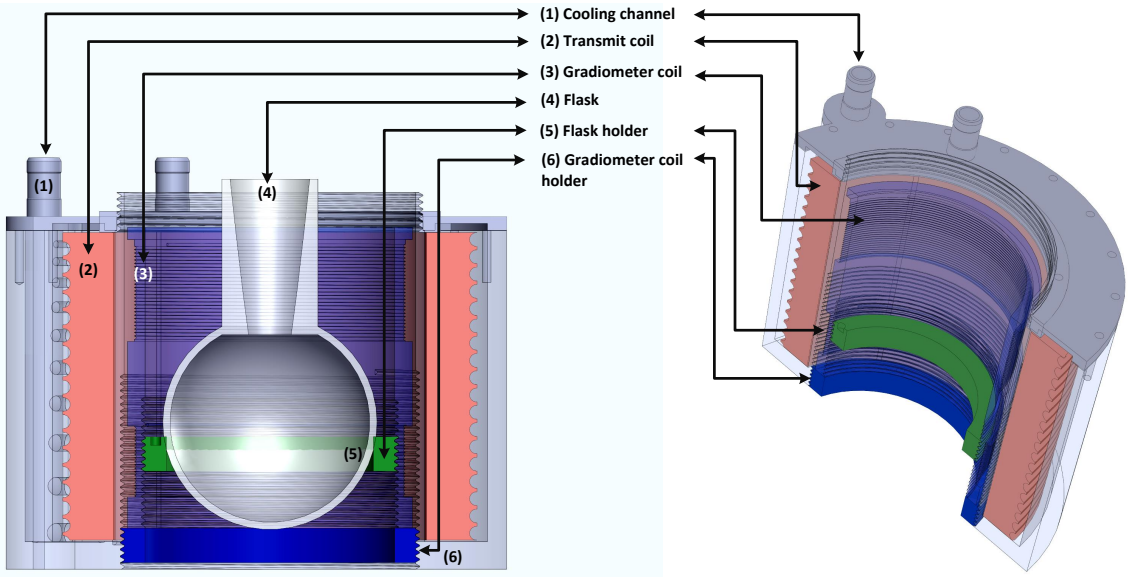


Figure 5.5: Field generator comprising of transmit coil, gradiometer coil and the housing for cooling the transmit coil and gradiometer coil. Pressurized air is used as a cooling medium which can be easily channeled through the housing. The housing also contains the flask holder and the gradiometer holder to provide flexibility regarding the attenuation of the excitation frequency.

#### 5.2.4.1 Transmit coil

Transmit coil is designed as a solenoid with an outer diameter of 121 mm and the inner diameter of 92 mm. The height of the transmit coil is approximately 93.75 mm and is housed in a 3-D printed enclosure. The transmitting coil consists of 40×4 turns realized with 2000×50 µm litz wire with the inductance of approximately 229 µH. To generate a required field of 10 mT in such a large area, there is a high consumption of power which leads to heating of the transmit coil. This produced heat can cause a change in the resistance of the coil and can lead to impedance mismatching between the power amplifier and the transmit coil. These thermal effects can decrease the field strength and increase the reflected power back to the power amplifier causing permanent damage. The transmit coil can generate a field strength of 10 mT in the x-direction for exciting the SPIONs.

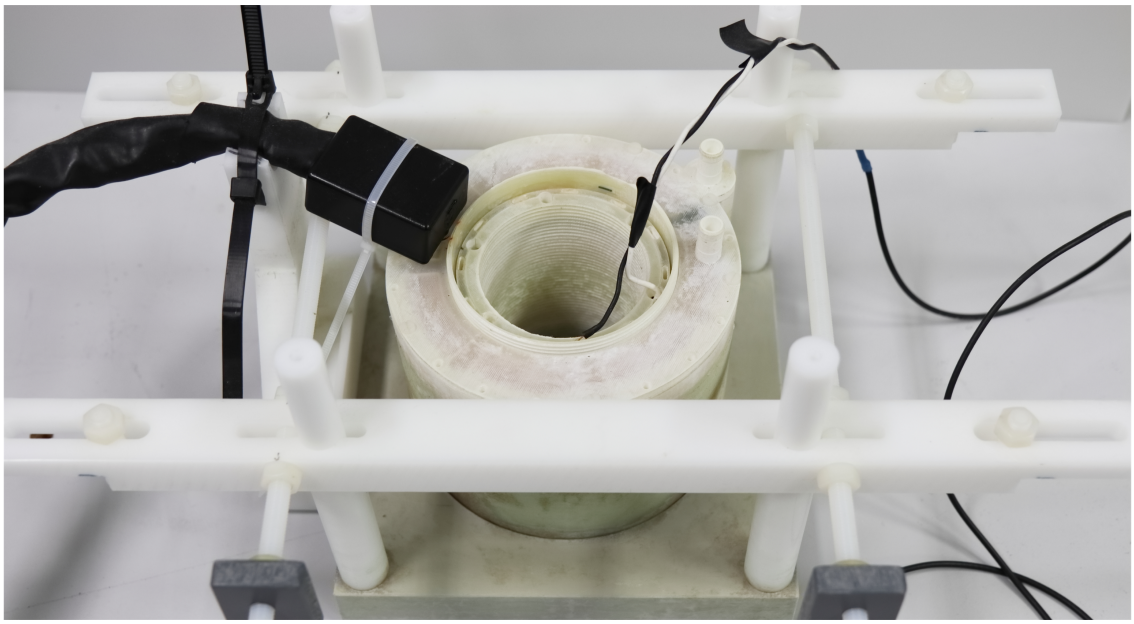

Figure 5.6: 3-D printed field generator housing comprising of transmit coil, gradiometer coil and the housing for cooling the transmit coil and gradiometer coil.

Figure 5.7 shows the front view **(A)**, the top view **(B)** of the manufactured transmit coil and the assembly drawing **(C)** of the transmit coil with the housing. As the transmit coil carries a huge amount of current and voltage and is used for water-based chemical synthesis, it is very important to secure the transmit coil inside the housing for electrical safety. To achieve this, proper fixture groves (marked in Figure 5.7 **(C)**) were made in the housing so the transmit coil does not move inside the housing. The transmit coil is cooled with the help of pressurized air. As shown in Figure 5.7 **(C)** the housing also contains cooling channels for the flow of pressurized air around the transmit coil. For uniform cooling of the complete transmit coil small air channels are present for the flow of the pressurized air throughout the height of the transmit coil. This ensures that the pressurized air uniformly flows in and around the transmit coil.

#### 5.2.4.2 Receive coil

After the excitation of the SPIONs, the characteristic particle response is captured with the help of the receive coil. For INSPECT, instead of a dedicated receive coil, a gradiometer coil is used. The gradiometer coil consists of a receiving part and a cancellation part wound in the opposite direction. Gradiometer coils have already been employed in different research fields such as in medical science [129], in geology [130] as well as for the construction of magnetometers [131]. The gradiometer coil is located inside the

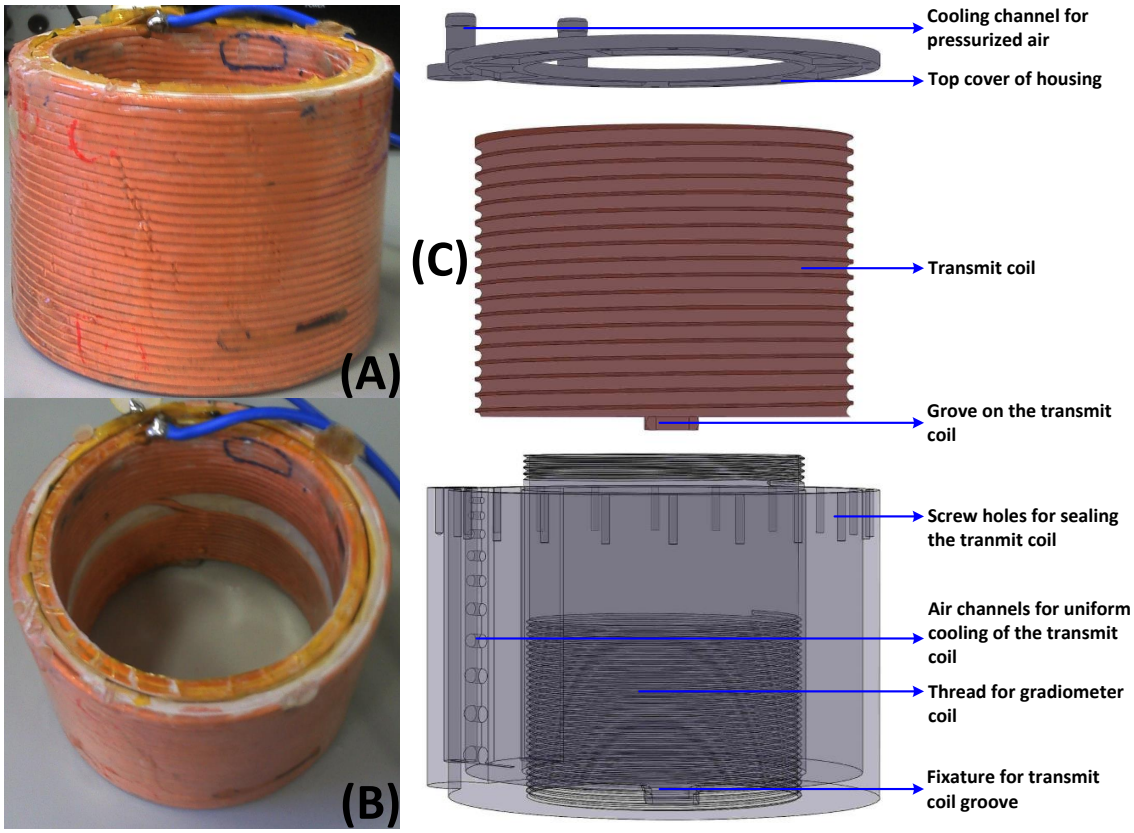


Figure 5.7: The manufactured transmit coil **(A)** front view **(B)** top view. The assembly drawing **(C)** of the transmit coil with its housing.

transmitting coil, which leads to higher mutual inductance causing direct feed-through of the excitation signal to both the receiving coil as well as the cancellation coil. As the cancellation coil is wound up in the reverse direction hence there is a cancellation of the excitation signal due to the reverse polarity of the current. Most of the state of the art MPS devices relay on bandstop filters or compensation coils to dampen the excitation signal [18]. It is essential to dampen the excitation signal as the magnitude of the excitation frequency is way higher in magnitude than the SPION's response. In the past, other techniques have also been employed such as dedicated cancellation units [20] and perpendicular sensing [21]. Graeser et al. did a comprehensive comparison between some of the different techniques [19]. Figure 5.9 shows the front view of the manufactured gradiometer coil and the assembly of the gradiometer coil with the flask holder and the gradiometer coil holder. All the parts are designed in SolidWorks (Dassault Systémes, France) and 3D printed with ProJet 3510 HDPlus 3D printer (3D Systems, USA).

For determining the number of turns for the receive part and the cancellation part the field profile of the transmit coil is measured. For this measurement, a test coil is used

which is vertically moved throughout the length of the transmit coil and the induced voltage is recorded. The test solenoid coil consists of five turns with an outer diameter of 18 mm. The copper wire used for winding has a diameter of 0.4 mm. Figure 5.8 shows the response of the test coil. These measurements can also be made with the help of a Hall probe. These measurements help in determining the vertical location as well as the number of turns needed for the cancellation as well as the receive coil. The principle behind the measurement is to attain a near-zero magnitude of the recorded response by dimensionally placing the winding of the cancellation and receive part inside the transmit coil. Moreover, it also helps in determining the gap between the cancellation and receive part of the gradiometer coil so the dimensions of the measurement chamber can be defined. With the help of this measurement, pure copper wire with a diameter of 0.5 mm is used for manufacturing the gradiometer coil. The receiving part of the gradiometer coil consists of 30 turns and the cancellation coil has approximately 28 turns. The inner diameter of the gradiometer coil is 74 mm and can easily fit up to a 100 ml glass flask for synthesis and for tracking the nucleation and growth of SPIONs.

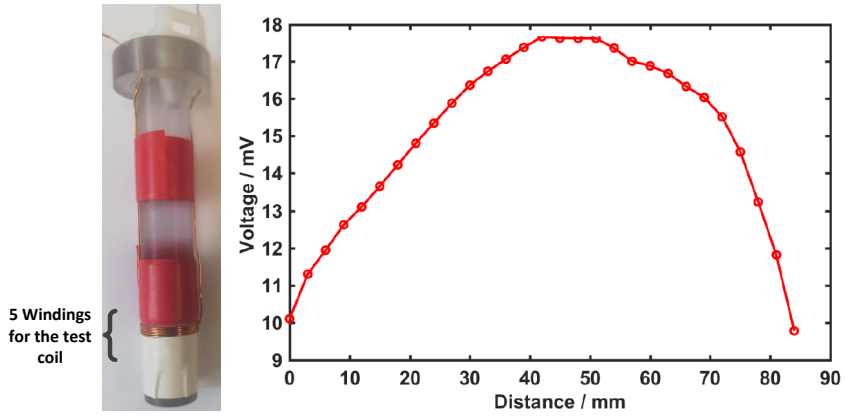


Figure 5.8: Left: the test coil consisting of five turns with an outer diameter of 18 mm. Right: the field profile of the transmit coil along the centre and covering the complete length of the transmit coil. Maximum amplitude is obtained at the centre of the coil and decreases towards the periphery. This measurement helps in determining the number of turns in the cancellation part and the receiving part as well as the physical gap between the cancellation and receive part of the gradiometer coil.

Figure 5.9 also shows the gradiometer coil holder and the flask holder. The gradiometer coil holder provides the flexibility to move the gradiometer coil inside the transmit coil to attain maximum attenuation of the excitation frequency. The gradiometer coil holder is vertically movable along the tread for the gradiometer coil as shown in Figure 5.7. The flask holder is also vertically movable inside the gradiometer coil and works as the sample chamber. This dimensional tuning helps to acquire the characteristic response of the

SPIONs with maximum amplitude. A synthesis flask with a volume of 25 ml to 100 ml can easily fit in the gradiometer coil for determining the change in the magnetic moment with time as the synthesis proceeds, providing a direct analysis of the nucleation and growth of the SPIONs in-situ. The combination of the gradiometer coil holder and flask holder helps us to achieve appropriate attenuation of the excitation signal and attaining maximum SPION's response. Therefore, there is no need for other modules such as band-stop filters or compensation units for attenuation. Moreover, the magnetic response of the SPIONs can also be adjusted by vertically moving the flask holder.

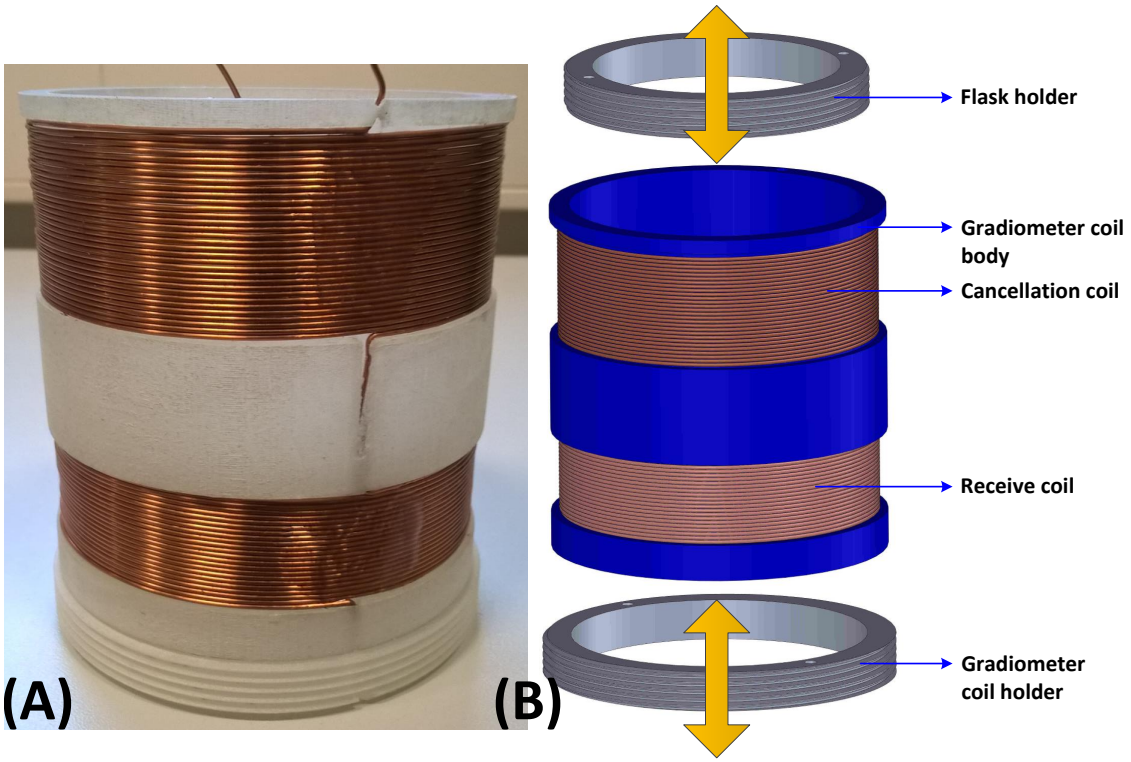


Figure 5.9: The front view of the manufactured gradiometer coil shown in **(A)** is printed with a 3-D printer. The assembly drawing of the gradiometer coil with the flask holder and gradiometer coil holder shown in **(B)**. The gradiometer coil holder is vertically movable inside the transmit coil via the treads shown in Figure 5.7 to attain maximum attenuation of the excitation signal. The flask holder is also vertically movable inside the gradiometer coil to attain maximum amplitude response from the SPIONs under test.

### 5.2.5 Current monitoring

For current monitoring, a Rogowski coil is used for measuring an alternating current by wrapping it around a current-carrying conductor. In INSPECT a self-made Rogowski

coil is used for measuring the alternating current supplied to the transmit coil. This is done to measure the excitation field strength produced by the transmit coil and forms a feedback between the transmit coil and the acquisition card. Depending on the inductance of the Rogowski coil very fast-changing currents down to several nanoseconds can be measured easily. Due to the absence of an iron core the response of the Rogowski coil is highly linear. Depending on the number of turns, the Rogowski coil could be used for determining different magnitudes of currents. For INSPECT a dedicated Rogowski coil is manufactured with the help of a 3D printer and pure copper wire is used for making the required winding. The geometry and number of turns are in such a way that it can measure currents in the range of 1-30 A with a maximum output below 1 V, which is the input dynamic range of the acquisition card. Figure 5.10 shows the designed Rogowski coil printed with a ProJet 3510 HDPlus 3D printer (3D Systems, USA). Figure 5.10 also shows the manufactured Rogowski coil that can be easily connected to the transmit coil.

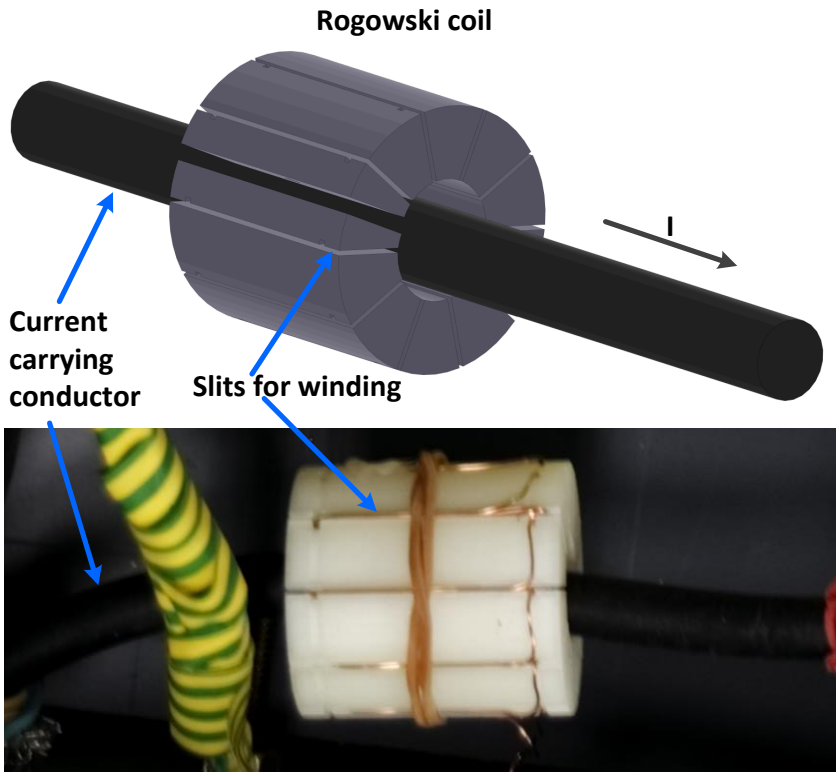


Figure 5.10: 3-D designed Rogowski coil showing the body for winding the coil as well as a current-carrying conductor. The outer diameter of the coil is 31 mm and the inner diameter is approximately 13 mm. The coil is designed to measure the amplitude of the current being supplied to the transmit coil.

The outer diameter of the Rogowski coil is 31 mm and the inner diameter is 13 mm. The Rogowski coil is made up of total 10 slits with 10 turns on each slit. The total

resistance of the coil is approximately 480 mΩ with an inductance of 12 μH. Figure 5.11 shows the calibration curve for the manufactured Rogowski coil. The induced voltage in the Rogowski coil is shown on the y-axis and the measured current in the x-axis. The calibration curve is obtained with the help of a commercially available current clamp MA200 MiniFlex (Chauvin Arnoux - Metrix, France).

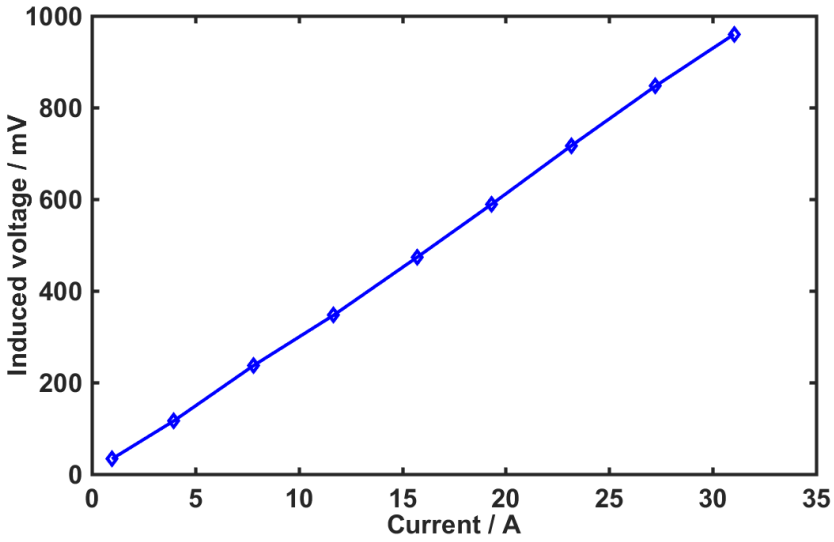


Figure 5.11: The calibration curve for the manufactured Rogowski coil showing the linear behavior from 1 A to 31 A. The calibration curve is obtained with the help of a commercially available current sensor MA200 MiniFlex (Chauvin Arnoux - Metrix from France).

### 5.2.6 Protection circuit

Due to the mutual inductance between the transmit coil and the gradiometer coil, there is a possibility that a very high voltage and current can be induced in the receiving coil which is connected directly to the acquisition card. The acquisition cards usually have a maximum input voltage in the range of 2-10 V, therefore there is a need for protection. These high voltages can also be produced due to sparks in the impedance matching or due to the various soldering joints for connecting wires. This could lead to irreversible damages to the ADC present on the acquisition card. The protection circuit makes sure that these high voltages and currents are not passed to the acquisition card. To overcome this problem a protection circuit is designed based on Op-amps using OPA698 (Texas Instruments Incorporated, USA). The details of the manufactured PCB based on OPA698 as well as the clamping capabilities are explained in Chapter 4 in Section 4.6.

## 5.3 Calibration of INSPECT

Due to the presence of different modules in the receiving chain or the transmitting chain, the excitation signal, as well as the signal induced in the gradiometer coil, can lose its fidelity. Therefore, it is very important to calibrate the device so that an appropriate response from the SPIONs could be obtained. INSPECT does not contain any kind of filters or the amplifiers in either the transmit chain or the receive chain except the power amplifier, therefore the transfer function is quite constant throughout the measurement bandwidth. Due to the absence of additional filters and amplifiers in the receiving chain and the transmitting chain, INSPECT is almost free from heating effects caused due to various passive and active components usually used in a conventional MPS device. To determine the transfer function two calibration coils are designed namely, the transmitting calibration coil ($u_{Tcal}$) and the receiving chain calibration coil ($u_{Rcal}$). For acquiring the transfer function these coils are fed a signal from an external source and the induced signal is acquired with the help of a network analyzer E5061B (Keysight Technologies, USA).

### 5.3.1 Transmit chain calibration

The transmitting calibration coil ($u_{Tcal}$) consists of a voltage divider and a coil in the form of a solenoid made up of copper wire. The coil is mounted on a cylinder of 51 mm in diameter and consists of 21 turns of 0.40 mm copper wire. The transmitting calibration coil ($u_{Tcal}$) detects the magnetic field generated by the transmit coil. Due to the known geometry as well as the induced voltage in the $u_{Tcal}$, the generated magnetic field can be easily calculated by using Faraday's law of induction. The generated field can be calculated by Equation 5.1.

$$B_{Tx}(t) = -\frac{u_{Tcal}}{f_0 \cdot A \cdot N} \tag{5.1}$$

Where $B_{Tx}(t)$ is the generated magnetic flux density, $f_0$ is the fundamental frequency of 23 kHz, N is the number of turns in the transmitting calibration coil, and A is the cross-section area. Using Equation 5.1 the field strength of the INSPECT is calibrated to 10 mT.

### 5.3.2 Receive chain calibration

Generally, the passive and active components present in filters and amplifiers can modify the signals detected at the receive chain in terms of amplitude and phase. Therefore, it is

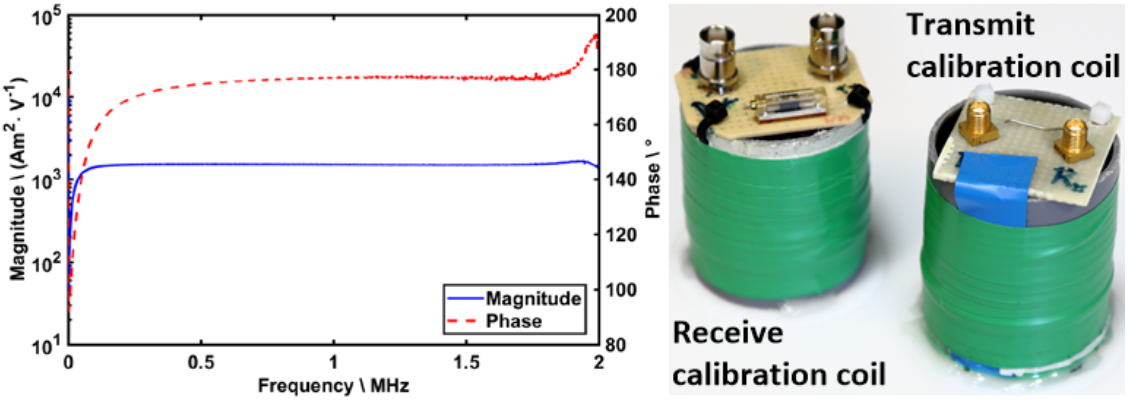


Figure 5.12: The transfer function of the receive chain showing the phase and magnitude in a wide frequency range. Due to the absence of filters and amplifiers, the response is quite straight in the complete measurement range. The visible peak around 2 MHz is the self-resonance peak of the gradiometer coil. The image on the right shows the designed and constructed receiving calibration coil and transmitting calibration coil.

essential to detect these changes and then to correct the measurements with the help of the measured transfer function. For measuring the transfer function of the receive chain a receiving calibration coil ($u_{Rcal}$) is designed and manufactured. The diameter of the $u_{Rcal}$ is approximately 20 mm consisting of 5 turns made up of pure copper wire of 0.5 mm thickness. The coil is connected to a 500 Ω series resistance to measure the induced current in the $u_{Rcal}$. Figure 5.12 shows the obtained magnitude and phase of the receive chain. Due to the absence of band-stop filters for attenuating the excitation frequency and LNA to amplify to the SPIONs response, the transfer function is constant in a wide frequency range.

Transmit chain and receive chain calibration is the last step before using INSPECT for tracking the nucleation and growth of the SPIONs. The obtained transfer functions are used to correct the subsequent measurements. Figure 5.13 shows the complete INSPECT comprising of three parts the power amplifier, the impedance matching unit (the box also contains the protection unit as well as the Rogowski coil) and the field generator. The measurements obtained with the help of INSPECT will be shown in the next Chapter 6. This chapter is dedicated to tracking the nucleation and growth of SPIONs in two different experiments: with and without the coating material. Furthermore, the sensitivity of the device is also shown and a few other experiments to show the effects of different parameters on the nucleation and growth of the SPIONs.

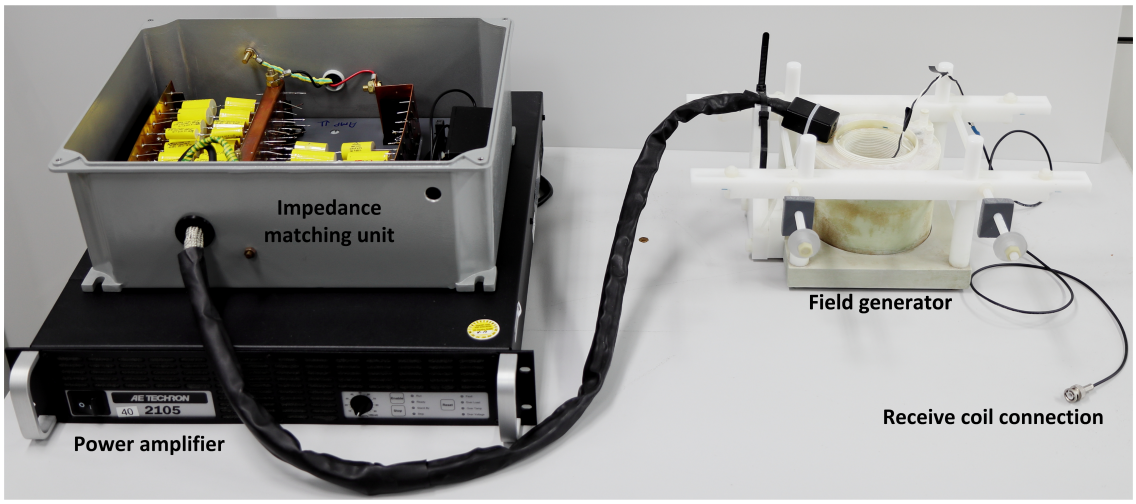


Figure 5.13: Complete setup of INSPECT comprising of three main components, the power amplifier, impedance matching unit (including the Rogowski coil) and the field generator containing the transmit and gradiometer coil. The receive coil can be connected to the protection unit followed by the acquisition card.

# 6

# Nucleation and growth of SPIONs in INSPECT

## Contents

## 6.1 Introduction

In this section, the results relating to nucleation and growth of SPIONs undergoing synthesis are discussed. For demonstrating the usefulness of INSPECT, for monitoring the nucleation and growth, various syntheses are performed based on the alkaline co-precipitation method. Therefore, it is essential to understand the process followed for synthesizing SPIONs using the alkaline co-precipitation method. Different steps followed by our research groups are explained in Section 6.3. To demonstrate the sensitivity of the INSPECT, a reference measurement with a very small quantity of iron concentration is shown with a commercially available SPION solution. Two example measurements consisting of the synthesis process with and without coating material is also explained in details. Furthermore, some measurements comparing the effect of vital parameters such as the amount of dextran and flow rate of the base are also shown. The measurements consist of both the amplitude spectra and the phase spectra obtained at different stages of the synthesis process. The magnetization curves are calculated with the help of amplitude and phase spectra at various timestamps. Magnetization curves are calculated by measuring the magnetization of the SPIONs depending on the dynamic excitation field. The dynamic excitation field is monitored by using a Rogowski coil which is explained in Section 5.2.5. For INSPECT, the total measurement time consisting of 2300 averages is less than 1 s.

## 6.2 Reference measurement for INSPECT

The measurement chamber of INSPECT can hold a 100 ml glask flask for synthesis, but it is also crucial that the INSPECT can also detect a small concentration of SPIONs. At the time of nucleation, the size of the SPIONs is very small, hence the change in magnetization has a very low amplitude and the detection becomes a challenging task. In this section, the results of an experiment are presented to demonstrate the lowest concentration of SPIONs detectable by INSPECT. For this particular experiment, Resovist (Bayer, Germany), a commercially available SPIONs is placed at the centre of the receiving part of the gradiometer coil. Resovist is a multi-core particle with an iron oxide core consisting of many single-core particles with approximately 4.2 nm as mean diameter [132]. Figure 6.1 shows the empty measurement together with the amplitude spectrum of 10 µL Resovist sample (containing 0.28 mg of iron). INSPECT is easily able to detect the first

six odd harmonics till the frequency of 253 kHz. This measurement ensures that INSPECT is sensitive enough to detect smaller quantities of SPIONs and hence can detect the changes in magnetization even in the nucleation phase.

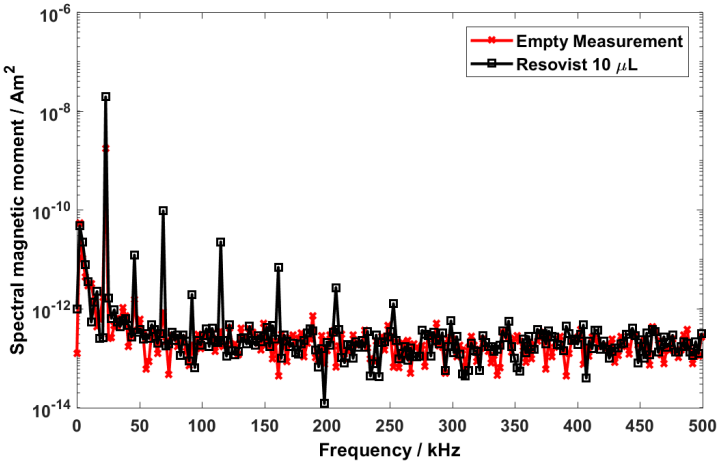


Figure 6.1: Reference measurement of INSPECT using commercially available SPIONs called Resovist. The empty measurement is shown in red and the spectral magnetic moment of a 10 µL Resovist sample is shown in black. INSPECT is easily able to detect the first six odd harmonics up to the frequency of 253 kHz.

## 6.3 Synthesis process and measurement protocol

In this section, all the protocols related to the chemical, technical as well as measurement protocol needed for experimenting are explained. The chemical protocol deals with the requirements for the synthesis of the SPIONs and the technical protocol deals with setting up the INSPECT to track the nucleation and growth of the SPIONs under the synthesis process. The chemical protocols are heavily influenced by the synthesis techniques used in the alkaline co-precipitation method. But depending on different synthesis processes the chemical protocols could change. All the experiments conducted for this research are based on the synthesis process explained by Lüdtke-Buzug [83]. Therefore, all the experiments in this research are conducted under ultrasonic control with the help of a commercially available ultrasound bath. Before starting the synthesis process, the INSPECT is placed in the commercially available ultrasound bath by using the designed holder for INSPECT. The INSPECT holder is flexible and can be readjusted for different commercially available ultrasound baths. The INSPECT holder makes sure that the INSPECT is located at the center of the ultrasound bath. This is necessary as the inductance of the transmission coils can change due to the shielding effects caused by the metal

body of the ultrasound bath. This change in inductance can lead to impedance mismatch leading to overheating of the system. Hence, if there is a need to change the ultrasound bath it is essential to check the impedance matching followed by recalibration of the INSPECT. For conducting successful experiments in INSPECT, the protocol can be divided into three steps which will be explained in the next subsections.

### 6.3.1 Preparation steps

The first step is to place the INSPECT holder and the INSPECT inside the ultrasound bath. Then the ultrasound bath is filled with a mixture of water and ice. The level of the water and ice mixture should at least cover 70% - 80% of the height of INSPECT. Meanwhile, a mixture of iron salts ($Fe^{2+}$ and $Fe^{3+}$) and a coating material (for example dextran) is prepared by dissolving them in a glass flask containing demineralized water. The required quantity of the base is added at a constant flow rate with the help of a syringe pump. Before initiating the measurements it is important that the ultrasound bath is turned on and INSPECT is connected to the pressurized air for cooling.

### 6.3.2 Initializing measurement

In the next step, by using the graphic user interface, the subsequent time for the measurements is set. For most of the experiments, this time is set between 3-5 minutes. The minimum measurement time possible is the length of the one period of the excitation frequency (23 kHz), which is approximately equal to 42.9 µs. In the second step, an empty measurement is taken which is subtracted from all the subsequent measurements. After these two steps, the graphical user interface waits for an input from the user. This means that the INSPECT is ready for monitoring the nucleation and growth of the SPIONs undergoing the synthesis process. This time gap is provided to set the final steps needed for the synthesis process for example for placing the flask in INSPECT followed by starting the syringe pump.

### 6.3.3 Initializing the synthesis process

For initializing the synthesis process, the flask containing a homogeneous mixture of iron salts, coating material (for example dextran) and water is placed in INSPECT. The syringe pump is connected to add the base for the co-precipitation of iron salts. After this point the system becomes autonomous and all other subsequent measurements are taken according to the time period set in the Section 6.3.2. After the addition of the

required base with the help of the syringe pump, the mixture is slowly heated to the desired temperature for 60-100 minutes. Depending upon the duration of the synthesis process the INSPECT acquires the change in magnetization of the SPIONs until it is manually stopped by the user.

All these steps are followed for every synthesis shown in this research. If a new protocol is used, then it is stated with the appropriate experiment. In the next sections, various experiments performed in the INSPECT are explained.

## 6.4 In-situ magnetic particle measurements during synthesis with coating material

For this particular synthesis the iron salts, iron (III) (1.32 g of $FeCl_3 \cdot 6H_2O$, $\geq$ 99 % obtained, Carl Roth GmbH Karlsruhe, Germany) and iron (II) (0.50 g of $FeCl_2 \cdot 4H_2O$, $\geq$ 99 % obtained, Merck kGaA, Darmstadt, Germany) plus Dextran T70 (1.32 g, AppliChem GmbH, Darmstadt, Germany) are dissolved in demineralized water and placed in a round bottle flask inside INSPECT and ammonia as a base is dropped into the solution. The flow rate of the base is controlled with an infusion pump (PERFUSOR secura FT, B.Braun, Germany), which is set to 20 ml/h. After the addition of the base, the mixture is slowly heated to a temperature around 80 °C under ultrasonic control [83], where the growth of SPIONs takes place. Figure 6.2 shows the change of magnetic properties in the colloidal solution (for third to ninth odd harmonics) versus time for the entire synthesis process. For simplification and without loss of generalization, the discussion of the results is limited to the temporal change of the magnetic moment in the third harmonic as the third harmonic has the maximum power in comparison to subsequent odd harmonics. According to Figure 6.2, the whole synthesis can be divided into three different intervals. In the first interval, nucleation of the SPIONs takes place. In this time interval, there is no or negligible formation of the SPIONs. This interval ends with the initial particle formation but with a weak magnetic moment. In the second interval, a sudden increase in the magnetic moment is observed pointing towards the growth of the SPIONs due to supersaturation as well as the thermal energy due to the heating of the colloidal solution. In a span of 30 minutes the magnetic moment increases from $5.32 \times 10^{-7}$ Am$^2$ to $1.99 \times 10^{-5}$ Am$^2$, which is approximately a factor of 37.4. This also points to the increase in the core diameter of the SPIONs. In the last interval, there is a slow and steady growth of the SPIONs. The change in the magnetic moment from the previous interval is just a factor of 1.45. At this point, the synthesis process is stopped as no further changes in the magnetic moment occur. The total duration of the synthesis process is approximately

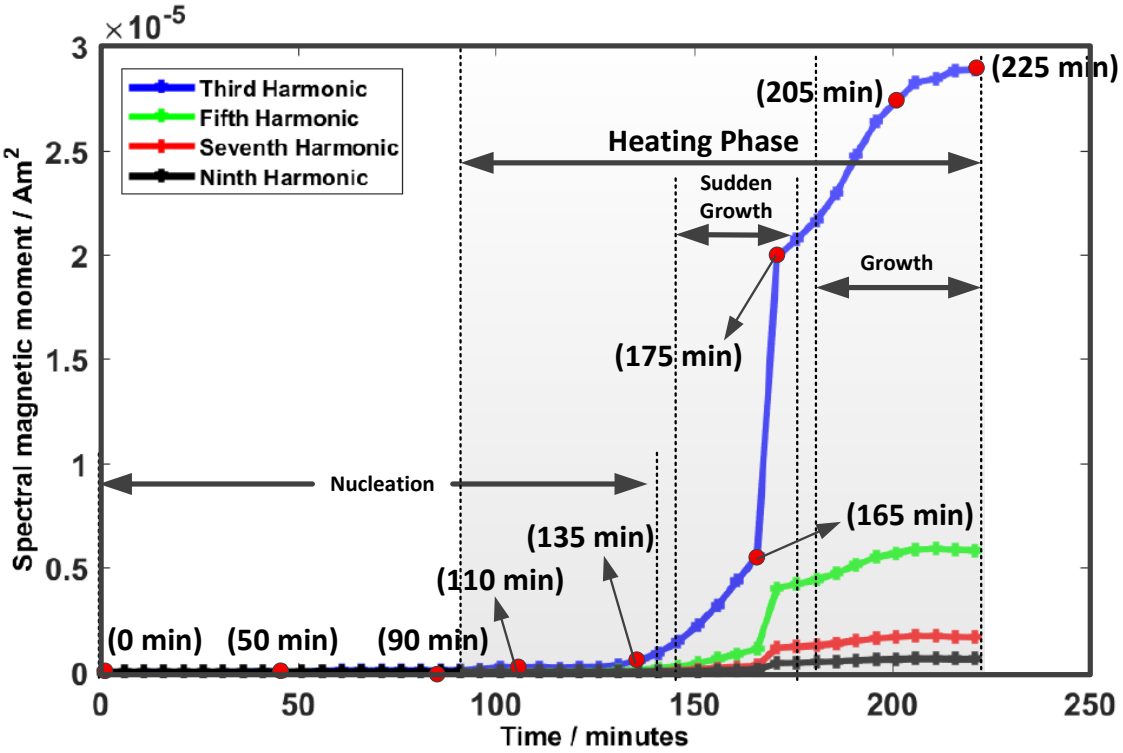


Figure 6.2: The change in the magnetic moment of the third, fifth, seventh and ninth harmonics versus time for the entire synthesis process. The synthesis process can be divided into three different intervals. The first interval is the nucleation phase, where the magnetic moment changes very slowly throughout the interval. This is followed by a sudden growth, where the magnetic moment changes drastically in a period of 30 minutes. The last interval is the growth phase, where a slow particle growth takes place until it converges to a static behaviour. At this point, the synthesis process is stopped. The measurements marked with the red points will be further discussed in the next section in details. The heating phase is also indicated in the figure. This is a time point where the addition of the base to the solution is stopped and the solution is further heated to 80 °C for homogeneous growth.

230 minutes and consisted of 46 measurements. In Figure 6.2 some measurement points are marked in red, these measurement points will be further discussed in the subsequent sub-sections.

### 6.4.1 Nucleation phase

In the nucleation phase, there is a slow change in the magnetic moment of the SPIONs undergoing the synthesis process as it takes some time to reach the supersaturation state. Nucleation only occurs when the supersaturation reaches a certain value above the sol-

ubility. The addition of the base is a slow process, therefore, it takes approximately 80 minutes for complete addition of the base to the solution. Theoretically, there should be no nucleus formation, but the characteristic SPION response can be acquired just after passage of few seconds. This is because supersaturation occurs in localized spaces when the base comes in contact to the mixture of iron salts and dextran. This leads to the formation of nuclei which produces a weak magnetic moment. However, after a few seconds of ultrasonic stirring, the base is mixed into the solution. The kinetics of the reaction is very fast. To slow down the process, the addition of the base is carried out at 4 °C to 5 °C. The slow addition of the base is important, as a sudden increase in the concentration can lead to broad size distribution of the nuclei. Some of the measurements taken during the nucleation phase are shown in Figure 6.3. The measurements consist of the amplitude and the phase spectra as well as the calculated dynamic magnetization curves for each measurement. The measurement timestamps are marked in Figure 6.2 with red dots. The first measurement in Figure 6.3 at 0 min consists of an empty measurement marked in blue and then another measurement is acquired with the flask containing all the reagents i.e. iron salts, dextran, and water. The diamagnetic behaviour of the water can also be seen in the magnetization curve at timestamp 0 min [133]. At 0 min there is a negligible change in the amplitude spectrum but there is a prominent change in the phase and magnetization curve till timestamp 50 min. This process continues for the next 90 min, leading to changes in the phase spectra and shifting of the magnetization curve. Moreover, there is an increase in the amplitude of the third harmonic for the measurement at 90 min proving an increase in the concentration of the nuclei in the colloidal solution. In the nucleation phase, the detection of the SPIONs is challenging as the magnetic moment of the particles is small.

### 6.4.2 Sudden growth phase

After the addition of the required quantity of the base to the solution, the heating process is started. This leads to a decrease in the change of the volume Gibbs free energy and the concentration of the growth species. Ideally, this should prohibit the formation of any nuclei and a coherent growth process should continue until the concentration of the growth species reaches the equilibrium concentration [85]. Figure 6.4 shows the measurements in the sudden growth phase. All these measurements are acquired at timestamps of 135 min, 165 min, and 174 min. The measurement at timestamp 135 min is acquired before the sudden growth happens. At this point, the SPIONs have already acquired the critical size required for the initialization of the growth process. This can be visualized by the amplitude spectrum at timestamp 135 min, as the higher harmonics start appearing,

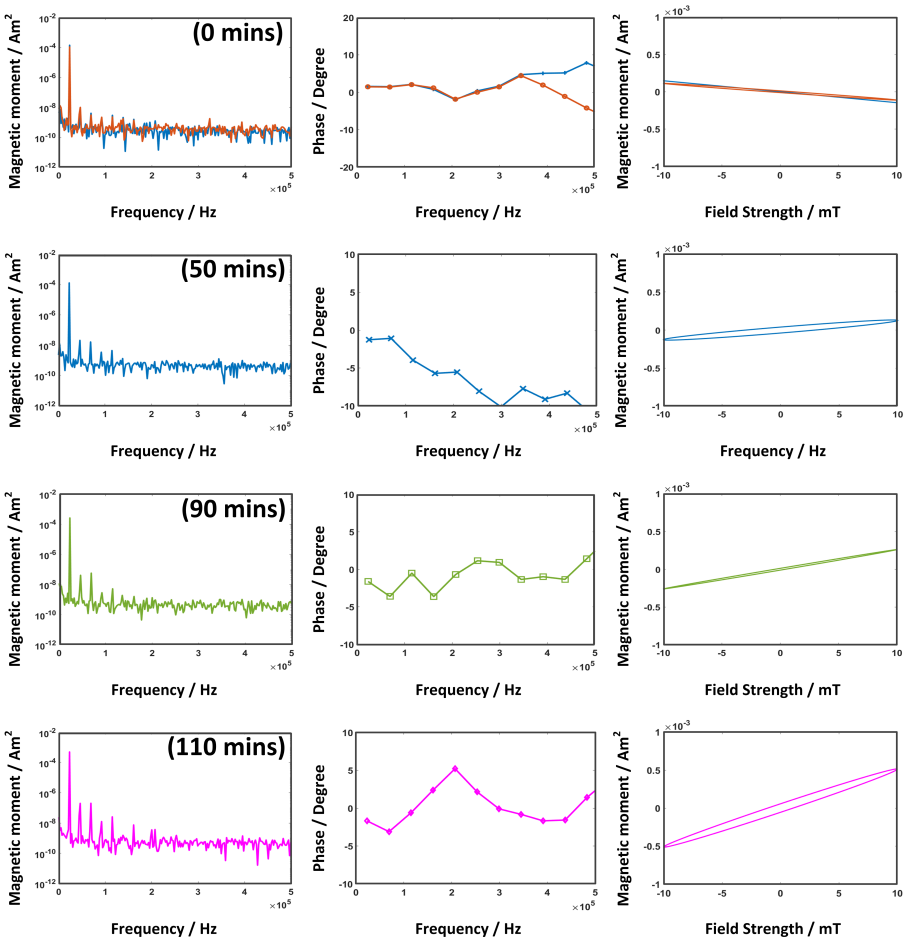


Figure 6.3: Measurements are acquired in the nucleation interval. The rows comprise of the amplitude and phase spectra, and the magnetization curves at different time intervals. The first row, acquired at timestamp 0 min, includes two measurements, one is the empty measurement (marked in blue color) and the other one is with the glass flask containing the reagents (iron salts, dextran) and water inside the measurement chamber (marked in red color). The other measurements are performed at timestamp 50 min, 90 min, and 110 min, respectively. As all the above measurements have been acquired in the nucleation phase of the synthesis process, for the amplitude spectrum there are no significant changes till 90 min but at 110 min the fourth odd harmonic appears. There are significant changes in the phase spectra, and, in turn, in the resulting magnetization curves. However, the area under the magnetization curve is maximum for the measurement at timestamp 110 min. Due to small amplitudes, the phase measurements can be inaccurate and may fluctuate.

which is a prerequisite for a good resolution for MPI [134]. At 165 min, in the amplitude spectrum, the first nine odd harmonics can be observed. The phase also shows linearity until 500 kHz. But the magnetization curves do not show any saturation effects at a field strength of 10 mT. But this situation changes in the next 10 min, at the measurement ac-

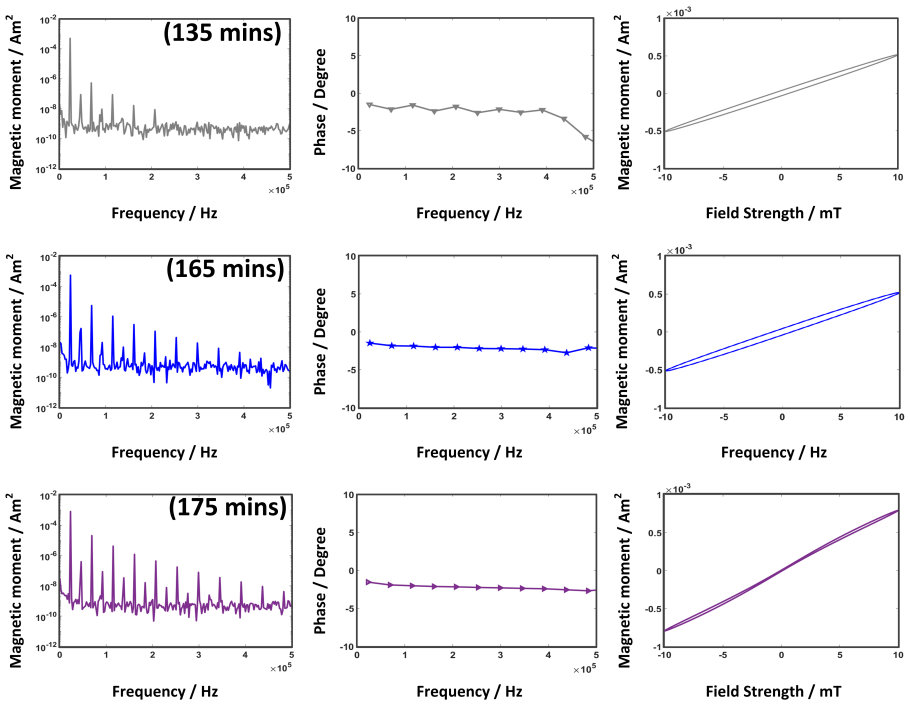


Figure 6.4: Sudden growth phase. The measurements comprise of the amplitude and phase spectra, and the magnetization curve, respectively. The first row is acquired when the growth is initiated at the timestamp at 135 min. In comparison to the measurements in Figure 6.3, there is a significant increase in the amplitude of the odd harmonics. This directly implies that there is further growth in the particles, which are formed in the nucleation phase. The measurements at the timestamp 165 min and 175 min show harmonics up to 500 kHz in the amplitude spectra, which confirms the particle growth. At timestamp 175 min, the magnetization curve indicates the beginning of the saturation effect. Furthermore, with the progression of the synthesis, the phase becomes much more stable, as it can be seen by comparing the phase spectra at timestamp 135 min to the timestamp at 175 min.

quired at 175 min. At timestamp 175 min the magnetization curve shows the saturation effect indicating the superparamagnetic behaviour. But there is no change in the phase spectrum from the previous measurements.

### 6.4.3 Growth phase

The third interval is the growth phase, where the SPIONs show a incremental growth with time behaviour. The measurements are shown in Figure 6.5. Over time there is an increase in the area of the magnetization curve. The measurements have been acquired at 205 min and 225 min after the synthesis initiation. The measurement at the timestamp 225 min marks the termination of the synthesis process as no significant change in the

magnetic properties over time can be observed.

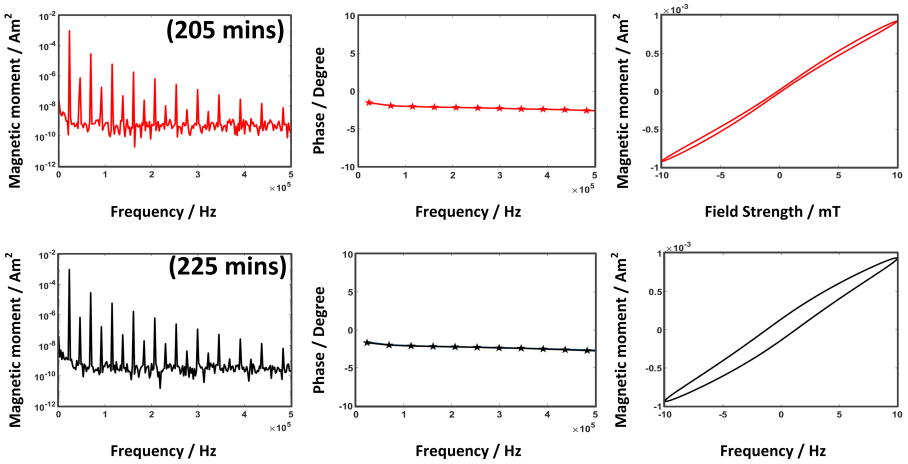


Figure 6.5: Measurements are acquired in the growth interval for the synthesis process with the coating material. The measurements at the timestamp 205 min and 225 min show harmonics up to 500 kHz in the spectral magnetic moments. There are no further changes in the magnetic moment with time, therefore, the synthesis process is stopped.

## 6.5 In-situ magnetic particle measurements during synthesis without coating material

For this particular synthesis the iron salts, iron (III) (1.32 g of $FeCl_3 \cdot 6H_2O$, ≥ 99 % obtained, Carl Roth GmbH Karlsruhe, Germany) and iron (II) (0.50 g of $FeCl_2 \cdot 4H_2O$, ≥ 99 % obtained, Merck kGaA, Darmstadt, Germany) are placed in a round bottle flask inside INSPECT and ammonia ($NH_3$) as a base is dropped into the solution. The flow rate of the base is controlled with an infusion pump (PERFUSOR secura FT, B.Braun), which is set to 50 ml/h. After the addition of the base, the mixture is slowly heated to a temperature around 80 °C under ultrasonic control [83], where the growth of SPIONs takes place. Figure 6.6 shows the change in the magnetic moment versus time for the third, fifth, seventh and ninth harmonics. For simplification and without loss of generalization only third harmonic is discussed. The complete synthesis process can be divided into three intervals: nucleation phase, growth phase, and agglomeration phase. In this particular experiment, there is no coating material; hence the SPIONs can not only undergo excessive growth but can also agglomerate. As there is no coating material, the particles are physically closer to each other in the colloidal solution promoting further agglomeration. In the nucleation phase, there is not much change in the magnitude of the amplitude spectra. For the first 25 minutes, ammonia is dropped in the solution and then

the solution is heated to 80 °C for further growth. Figure 6.6 shows some timestamps (marked in red) which will be further discussed in detail in the following subsections.

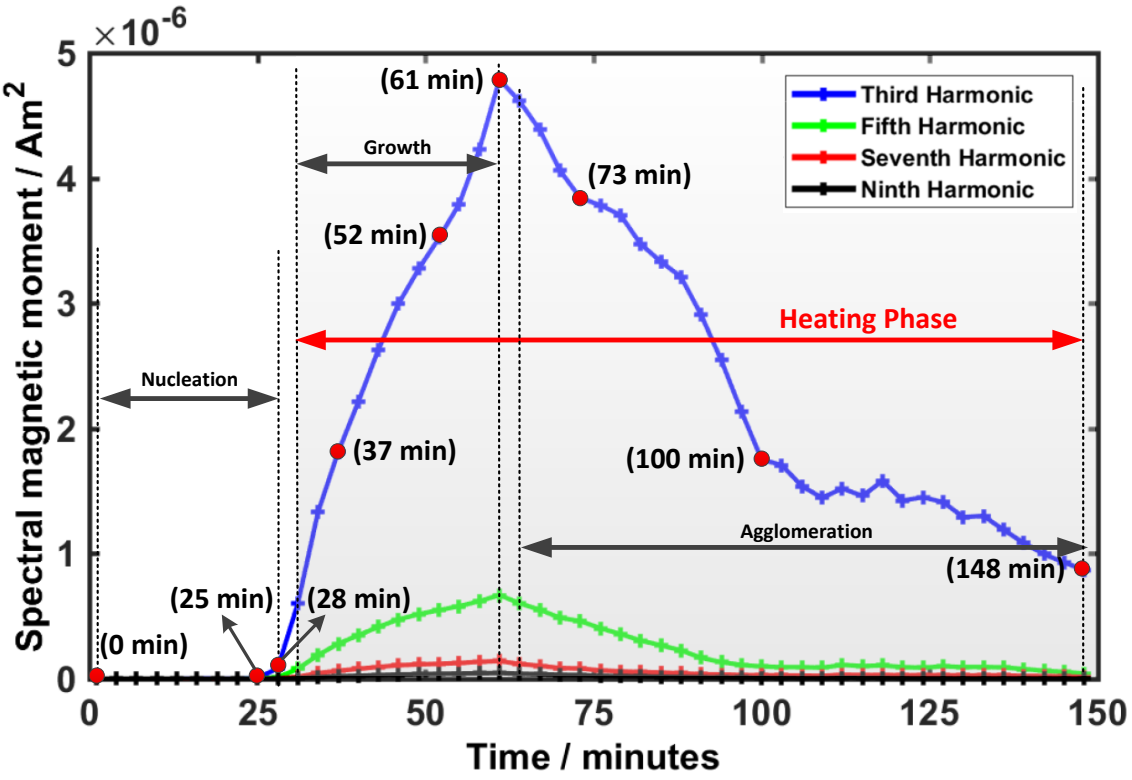


Figure 6.6: The synthesis process can be divided into three different intervals. The first interval is the nucleation phase, the magnetic moment changes very slowly throughout the interval. This is followed by the growth phase, where the magnetic moment changes drastically within a period of approximately 30 minutes. The last interval is the agglomeration phase, where there is a systematic decrease in the magnetic moment due to the agglomeration of the SPIONs. The agglomeration can increase due to lack of coating material such as dextran, therefore, pointing in the direction of uncontrollable growth. This uncontrollable growth leads to an increase in the size of the particles and eventually the SPIONs cannot be excited by the excitation field any more. The measurements marked with the red points will be further discussed in the next section. The heating phase is also indicated in the figure. This is the time point where the addition of the base to the solution is stopped and the solution is further heated to approximately 80 °C.

### 6.5.1 Nucleation phase

Figure 6.7 shows the nucleation phase for the synthesis process undergoing nucleation and growth without the presence of coating material. The measurements consist of the amplitude and the phase spectra as well as the calculated magnetization curves for each

measurement. In the nucleation phase, there is a very slow change in the magnetic moment of the SPIONs as the addition of base takes approximately 25 minutes to reach supersaturation. The first measurement in Figure 6.7 consists of two measurements acquired at the starting of the synthesis process. The first graph is the empty measurement, which would be subtracted from the subsequent measurements for reducing the interference. The second measurement is acquired by placing the glass flask containing a mixture of iron salts and water in the INSPECT. The amplitude spectrum at 0 minute only consists of the first harmonic which is due to the excitation signal produced by the transmit coil. The magnetization curve shows the diamagnetic behaviour of the water as shown in the previous experiment in Figure 6.3. At the timestamp of 25 minutes, the amplitude spectrum shows the third and fifth harmonic signifying that the SPIONs are present in the solution. But the magnitude of the formed SPIONs is still low as supersaturation is localized. But as the addition of the base is completed, the solution becomes supersaturated leading to the formation of more nuclei. In a span of 3 minutes, the magnetic moment changes from $6.27 \times 10^{-9}$ $Am^2$ to $8.19 \times 10^{-8}$ $Am^2$, which is an increase by a factor of 13. At the end of the nucleation phase, the gradual heating of the solution is started.

### 6.5.2 Growth phase

Due to the gradual heating of the solution, the reaction becomes thermodynamically favorable and hence promoting the growth of the nuclei formed in the nucleation phase. Figure 6.8 shows some of the measurements acquired in the growth phase. The measurements are acquired at 37 minutes, 52 minutes, and 61 minutes after initialization of the synthesis process. In this phase, growth takes place leading to an increase in the size of the SPIONs. From the timestamp of 37 minutes to 61 minutes, the magnetic moment increases from $1.81 \times 10^{-6}$ $Am^2$ to $4.78 \times 10^{-6}$ $Am^2$. The difference between the magnetization curves is negligible and the phase keeps on becoming more stable with time. In this phase, the growth is incremental with time. As seen in Figure 6.6, the measurement acquired at 61 minutes has the maximum magnetic moment because after this point agglomeration of the SPIONs starts.

### 6.5.3 Agglomeration phase

After 61 minutes into the synthesis process, a drop in the magnetic moment can be visualized as shown in Figure 6.6. Over time, the magnetic moment keeps on further decreasing until the synthesis process is ended. A sudden decrease in the magnetic moment in the INSPECT can be caused due to two effects. Firstly, the particles may have grown to

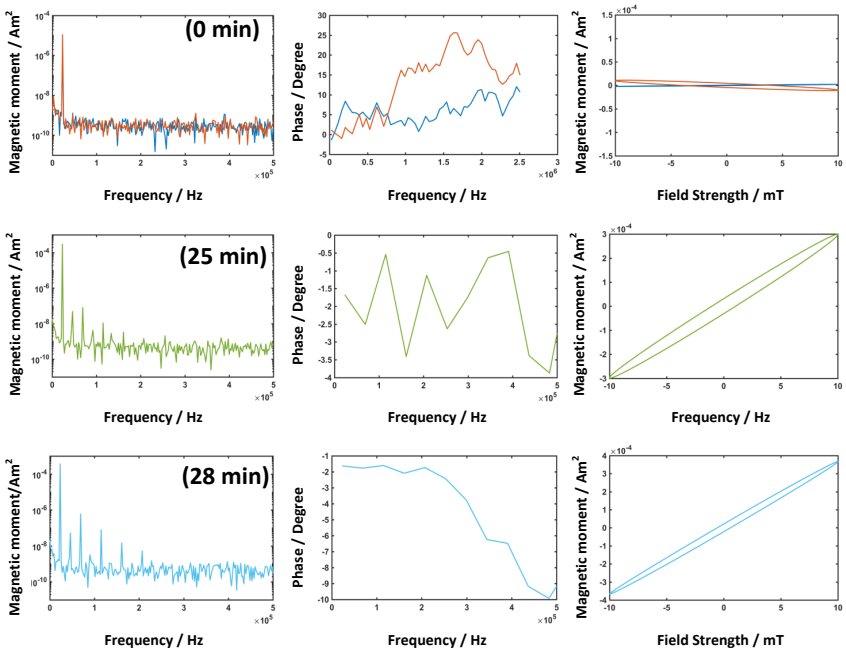


Figure 6.7: Measurements are acquired in nucleation interval. The rows comprise the amplitude and phase spectra, and the magnetization curves at different time intervals. The first row, acquired at timestamp 0 min, includes two measurements, one is the empty measurement (marked in blue color) and the other one with the glass flask containing the iron salts ($Fe^{2+}$ and $Fe^{3+}$) with water inside the synthesis flask (marked in red color). The other measurements are performed at timestamp 25 min and 28 min. As all the above measurements have been acquired in the nucleation phase of the synthesis process, for the amplitude spectrum there are no significant changes. But at 28 min the fourth odd harmonic appears signifying the growth of the previously formed nuclei. There are significant changes in the phase spectra, and, in turn, in the resulting magnetization curves. Due to the absence of the coating material, the SPIONs are growing at a much faster rate and hence till 28 min, there are already the first four odd harmonics visible, which was not the case with the previous experiment.

such a size that they cannot be excited by the excitation field produced by the transmit coil. Secondly, agglomeration is taking place; i.e., the SPIONs form clusters which further lead to an increase in the size of the SPIONs, and hence cannot be excited by the transmit coil. Figure 6.9 shows some of the measurements acquired at different points in the agglomeration phase. These measurements are acquired at 73 min, 100 min, and 148 min and are marked in Figure 6.6. In the complete agglomeration phase the magnetic moment decreases from $4.78 \times 10^{-6}$ $Am^2$ to $8.67 \times 10^{-7}$ $Am^2$ in a span of approximately 90 minutes. Moreover, as the synthesis progresses the phase becomes more unstable for the higher harmonics which is opposite to what happens in the growth phase. This could be seen by comparing the phase spectra from 73 minutes to 148 minutes. The same phe-

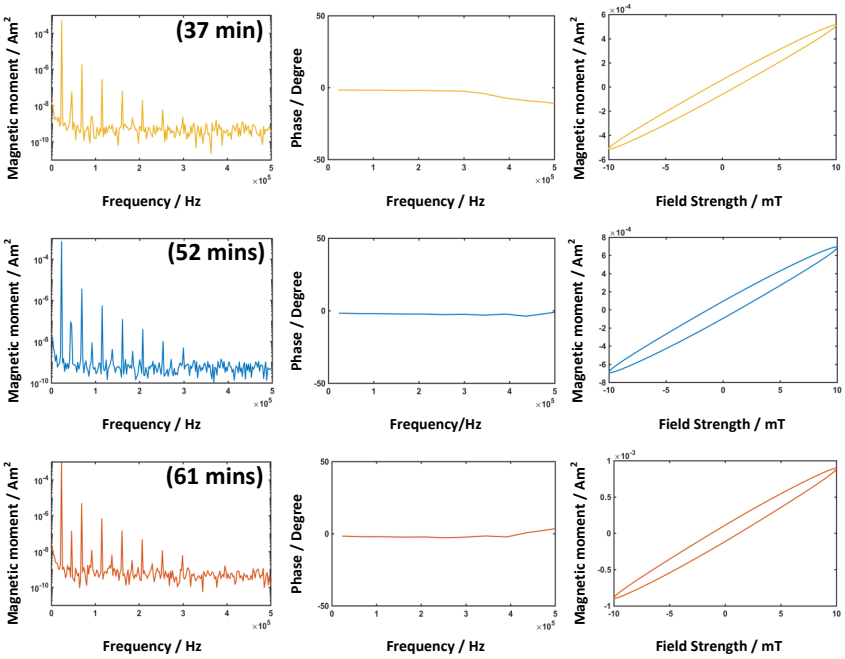


Figure 6.8: Measurements are acquired in the growth phase for a synthesis process without the presence of a coating material such as dextran. The measurements are performed at timestamps 37 min, 52 min, and 61 min. The particles undergo approximately incremental growth in this phase. The phase spectra get stable with time and there is an increase in the magnetic moment from 37 min to 61 min.

nomena can be observed for the amplitude spectra for all the three measurements. For example, for the measurement at 73 minutes, at least first seven odd harmonics can be observed. But with further agglomeration, only first four odd harmonics can be observed at the timestamp of 148 minutes. This experiment is just conducted to understand the effects of coating material on the synthesis of the SPIONs, as these agglomerates lack the properties which could be used for making high-quality images using an MPI scanner.

In the next sections, there will be a comparison of different synthesis parameters which can affect the nucleation and growth of SPIONs. As every synthesis process produces several measurements comprising of both the amplitude and phase spectra in INSPECT. Therefore, it is not feasible to show each and every measurement and hence only the third harmonic versus time curves will be compared for the complete synthesis process followed by the comparison of the amplitude and phase spectra at the end of the synthesis process.

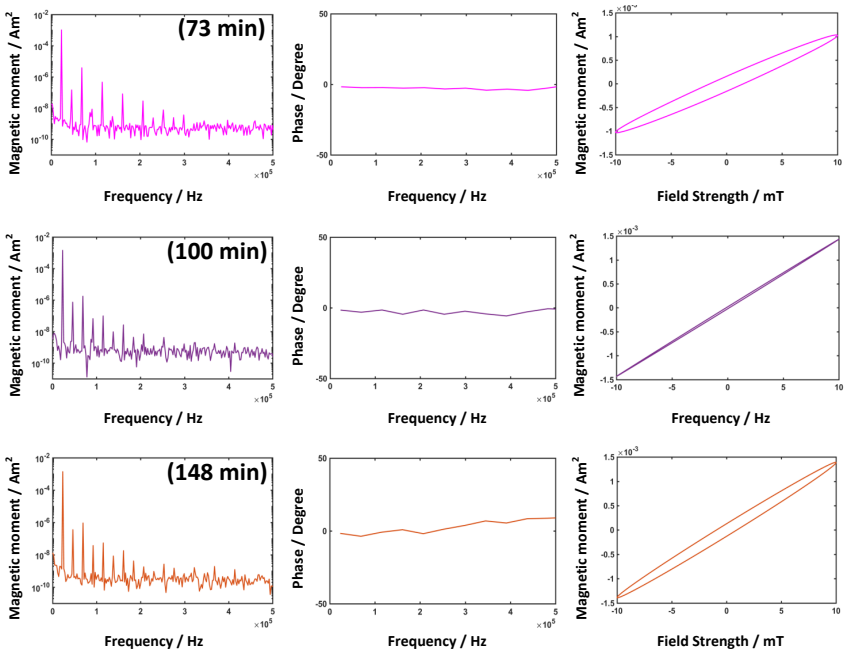


Figure 6.9: Measurements are acquired in the agglomeration phase for a synthesis process without the presence of a coating material such as dextran. In this phase, there is a decrease in the magnetic moment with time. This is because the particles undergo agglomeration due to the absence of the coating material. These newly formed agglomerates are way bigger in size and hence cannot be excited by the excitation field. Therefore with time, the magnetic moment decreases. The synthesis process is stopped after 148 min.

## 6.6 Synthesis of SPIONs subjected to different flow rates of the base

For synthesis, the iron salts and the dextran are dissolved in demineralized water at room temperature inside a flask and placed in an ultrasound bath with a frequency of 45 kHz. The whole synthesis process is carried out in the INSPECT. The measurements are acquired at different time steps and required approximately 1 s. The field strength of the INSPECT is approximately 10 mT which has a negligible effect on the growth and nucleation phase of the SPIONs, as only continuous application of high external magnetic fields has an impact on the nucleation and growth of the SPIONs. To sense the impact of the flow rate, this experiment is further divided into two experiments. The details of the experiments and the different parameters used are shown in Table 6.1 and Table 6.2.

### 6.6.1 Change in flow rate without initial cooling

As mentioned in the previous Section 6.4, the addition of the base takes place in the presence of an ice bath to reduce the dynamics of the chemical reaction in the nucleation phase. For this particular experiment, no initial cooling was applied and only the flow rate is changed. The change in the flow rate is achieved with the help of an infusion pump (PERFUSOR secura FT, B.Braun). Sample 16 has a flow rate of 35 ml/h and Sample 17 has a flow rate of 25 ml/h. Other parameters like the amount of iron salts and dextran are kept constant. Table 6.1 describes the different parameters in detail. For characterization, change in the magnetic properties of the colloidal solution of the entire synthesis process is shown in Figure 6.10 **(A)**. The amplitude and magnetization curve of the final measurement are also compared in Figure 6.10 **(A and B)** respectively.

Table 6.1: Parameters for the synthesis of SPIONs with different flow rates without initial cooling at the starting of the synthesis process. Sample 16 has a flow rate of 35 ml/h and Sample 17 has a flow rate of 25 ml/h respectively, all other parameters are kept constant for the synthesis.

| **Probe** | **Reagents** | **Quantity** (g) | **Temperature** (°C) | **Ultrasound frequency** (kHz) | **Flow rate** (ml/h) |
|---|---|---|---|---|---|
| **Sample 16** | $FeCl_3 \cdot 6H_2O$ | 1.32 ± 0.01 | 24-70 | 45 | 35 |
| | $FeCl_2 \cdot 4H_2O$ | 0.50 ± 0.01 | | | |
| | Dextran T70 | 1.32 ± 0.01 | | | |
| **Sample 17** | $FeCl_3 \cdot 6H_2O$ | 1.32 ± 0.01 | 24-70 | 45 | 25 |
| | $FeCl_2 \cdot 4H_2O$ | 0.50 ± 0.01 | | | |
| | Dextran T70 | 1.32 ± 0.01 | | | |

It can be easily inferred from Figure 6.10 that a higher flow rate leads to more delay in the initialization of the growth phase (as shown in Figure 6.10 **(A)** for Sample 16). But a smaller flow rate leads to a steeper increase in the magnetic moment (as shown in Figure 6.10 **(A)** for the Sample 17 at a flow rate of 25 ml/h). Moreover, it leads to higher saturation magnetization (as shown in magnetization curves for Sample 17 compared to Sample 16). These effects are more evident as there is no initial cooling leading to a faster rate of co-precipitation.

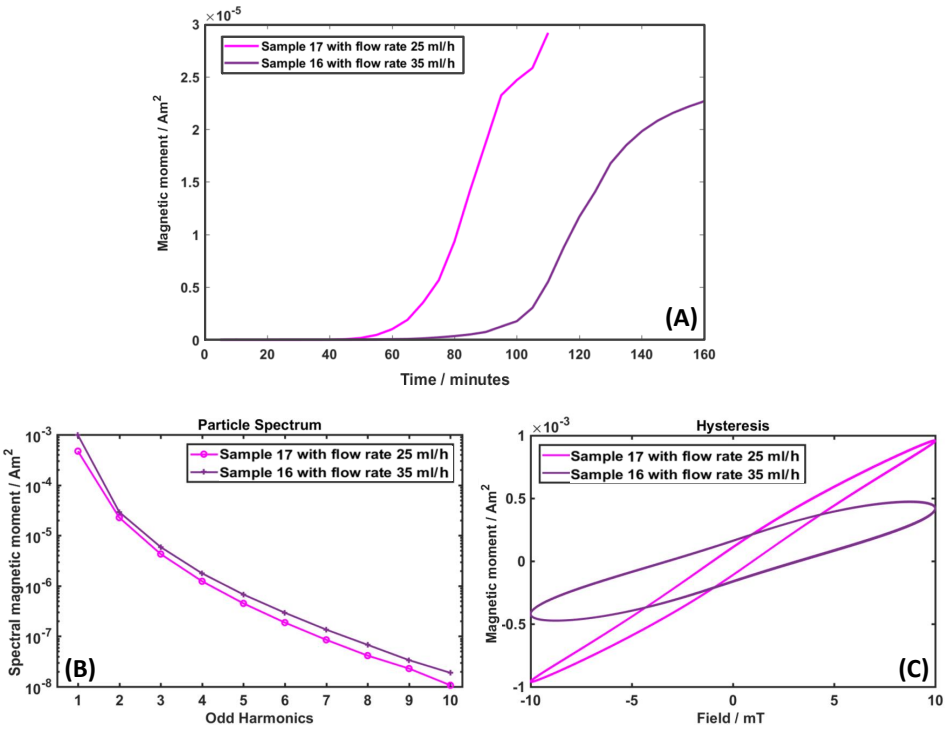


Figure 6.10: Measurements comparing synthesis conducted at different flow rates without initial cooling. The magnetic moment of the third harmonic versus time for the entire synthesis process is shown in **(A)**. The final amplitude spectra and the magnetization curve for the Sample 16 and Sample 17 at the end of the synthesis process are shown in **(B)** and **(C)**, respectively.

### 6.6.2 Change in flow rate with initial cooling

In this experiment, the flow parameter is again changed but with initial cooling. So instead of starting the synthesis process at room temperature, the nucleation phase is started at a temperature ranging from 0 - 4 °C. This initial cooling decreases the kinetic time constants of the reaction and may lead to a uniform formation of nuclei for the growth. For this particular experiment flow rates of 10 ml/h (Sample 18) and 20 ml/h (Sample 19) are compared. All the other parameters are kept constant. The details of the parameters are stated in Table 6.2. The change in the magnetic properties of the colloidal solution of the entire synthesis process is shown in Figure 6.11 **(A)**. The amplitude spectra and magnetization curve of the final measurements are compared in Figure 6.11 **(B and C)**. All the measurements are acquired with the help of INSPECT.

It can be easily inferred from Figure 6.11 that a higher flow rate leads to a delay in the initialization of the growth phase (as shown in Figure 6.11 **(A)** for Sample 19). These are consistent results compared with the previous experiment. But the steeper increase in

Table 6.2: Parameters for the synthesis of SPIONs with different flow rates with initial cooling. For this particular experiment flow rates of 10 ml/h (Sample 18) and 20 ml/h (Sample 19) are compared and other parameters are kept constant.

| **Probe** | **Reagents** | **Quantity (g)** | **Temperature (°C)** | **Ultrasound frequency (kHz)** | **Flow rate (ml/h)** |
|---|---|---|---|---|---|
| **Sample 18** | $FeCl_3 \cdot 6H_2O$ | 1.32 ± 0.01 | 0-70 | 45 | 10 |
| | $FeCl_2 \cdot 4H_2O$ | 0.50 ± 0.01 | | | |
| | Dextran T70 | 1.32 ± 0.01 | | | |
| **Sample 19** | $FeCl_3 \cdot 6H_2O$ | 1.32 ± 0.01 | 0-70 | 45 | 20 |
| | $FeCl_2 \cdot 4H_2O$ | 0.50 ± 0.01 | | | |
| | Dextran T70 | 1.32 ± 0.01 | | | |

the magnetization of Sample 19 is contradictory as compared to the previous experiment. This can be attributed to the initial temperature conditions. Therefore, until and unless the chemical reaction reaches a specific temperature during the nucleation phase, there is no or insignificant growth. This provides favorable conditions for the growth as seen in Sample 19 (In Figure 6.11). The hysteresis curve, as well as magnetic moment of Sample 18, is better for MPI/MFH than that of the Sample 19 as shown in Figure 6.11 **(B and C)**. Hence, the role of initial temperature in the nucleation phase cannot be neglected. Therefore, to obtain SPIONs, which can be used for MPI or MFH, there is a need to maintain a balance between the flow rate and temperature during the reaction.

## 6.7 Effect of the quantity of dextran on the nucleation and growth of the SPIONs

This experiment is also divided into two sub-parts. In the first part, the amount of dextran is varied at lower flow rates (lower than 10 ml/h), so the effect of the dextran could play a vital role. In the second part, the effect of the dextran is compared at higher flow rates of 20 ml/h.

### 6.7.1 Change in quantity of dextran at low flow rates

The amount of different chemical reagents used for the synthesis of SPIONs is shown in Table 6.3. In these synthesis, low flow rate means lower than 10 ml/hr. For these particular experiments, two different quantities of dextran are used (Sample 20 contains

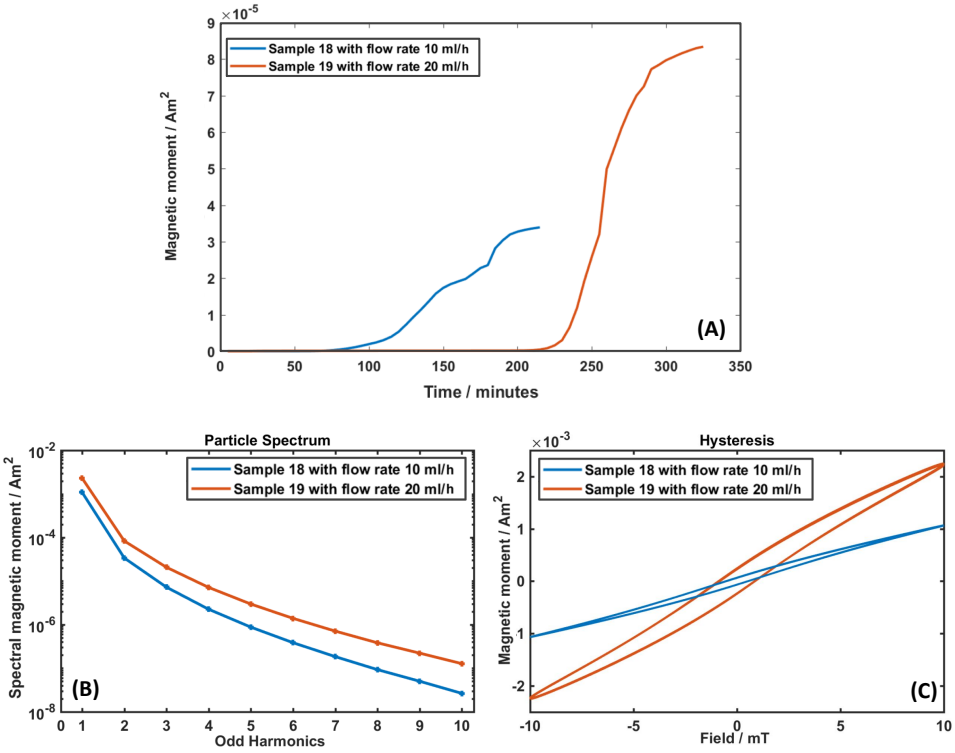


Figure 6.11: Measurements comparing synthesis conducted at different flow rates with initial cooling. The magnetic moment of the third harmonic versus time for the entire synthesis process is shown in **(A)**. The final amplitude spectra and the magnetization curve for the Sample 18 and Sample 19 at the end of the synthesis process are shown in **(B)** and **(C)** respectively. The saturation effect of the SPIONs is quite evident for the final measurement of Sample 19.

1.32 ± 0.01 g and Sample 21 contains 0.33 ± 0.01 g of dextran). All other parameters like the amount of iron salt, flow rate, etc. are kept constant. The results obtained through this particular experiment are displayed in Figure 6.12. For this experiment, the nucleation takes place at a lower temperature of 0-4 °C.

From Figure 6.12 **(A)** it could be inferred the amount of dextran plays a critical role in the growth phase of the SPIONs. The initialization of the growth corresponds to the amount of dextran in chemical synthesis. At low flow rates of less than 10 ml/h, it holds that the smaller the amount of dextran, the earlier the magnetic moment increases. This corresponds to the fact that the core of the SPIONs is growing faster. On the other hand, a higher amount of dextran leads to more rapid and uniform growth and even causes a delay in the saturation effect. This can be seen in Figure 6.12 **(A)** as Sample 20 with dextran T70 = 1.32 ± 0.01 g has a steeper slope as compared to Sample 21 with dextran T70 = 0.33 ± 0.01 g. Figure 6.12 **(B and C)** shows a comparison of the amplitude spectra and the magnetization curve obtained from the final measurements.

Table 6.3: Parameters for the synthesis of SPIONs with different quantities of dextran with initial cooling. Two different quantities of dextran are used (Sample 20 contains 1.32 ± 0.01 g and Sample 21 contains 0.33 ± 0.01 g of dextran) and all other parameters are kept constant

| **Probe** | **Reagents** | **Quantity** (g) | **Temperature** (°C) | **Ultrasound frequency** (kHz) | **Flow rate** (ml/h) |
|---|---|---|---|---|---|
| **Sample 20** | $FeCl_3 \cdot 6H_2O$ | 1.32 ± 0.01 | 0-70 | 45 | <10 |
| | $FeCl_2 \cdot 4H_2O$ | 0.50 ± 0.01 | | | |
| | Dextran T70 | 1.32 ± 0.01 | | | |
| **Sample 21** | $FeCl_3 \cdot 6H_2O$ | 1.32 ± 0.01 | 0-70 | 45 | <10 |
| | $FeCl_2 \cdot 4H_2O$ | 0.50 ± 0.01 | | | |
| | Dextran T70 | 0.331 ± 0.01 | | | |

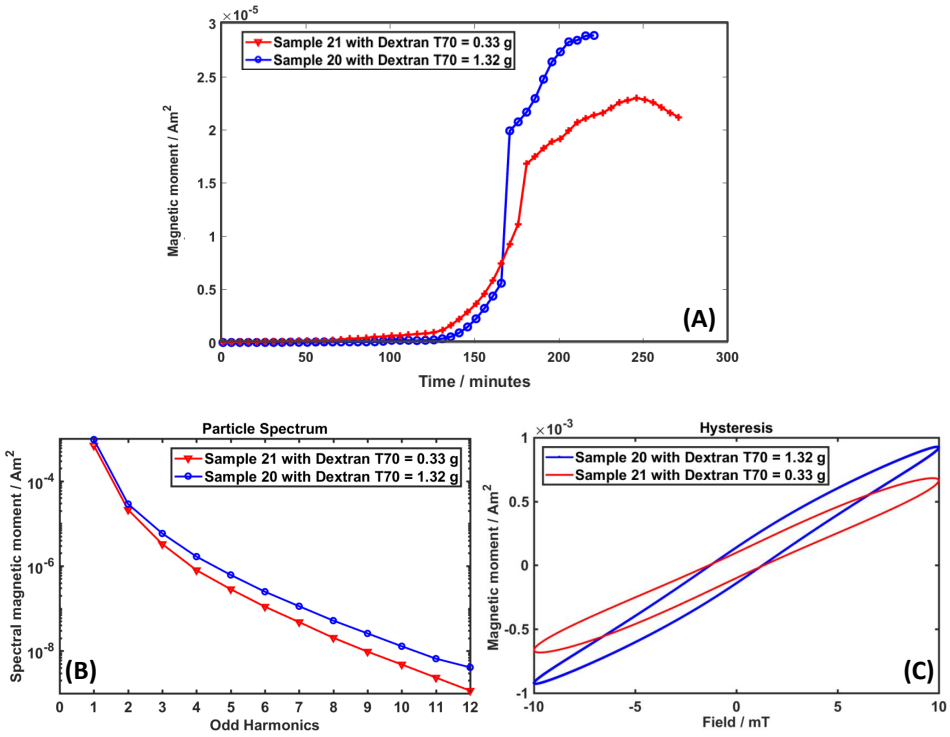


Figure 6.12: Measurements comparing synthesis conducted with different quantities of dextran at a low flow rate of less than 10 ml/h. The magnetic moment of the third harmonic versus time for the entire synthesis process is shown in **(A)**. The final amplitude spectra and the magnetization curve for the Sample 20 and Sample 21 at the end of the synthesis process are shown in **(B)** and **(C)** respectively.

### 6.7.2 Change in quantity of dextran at a flow rate of 20 ml/h

In this experiment, the impact of the quantity of dextran at a higher flow rate is investigated. Three different experiments are analyzed with different quantities of dextran. Sample 22 has 1.50 ± 0.01 g of dextran followed by Sample 23 and Sample 24 has 1.30 ± 0.01 g and 0.99 ± 0.01 g respectively. For these experiments, the flow rate is kept constant at 20 ml/h and all other parameters such as the quantity of iron salts are also kept constant. Detailed parameters are given in Table 6.4 below.

Table 6.4: Parameters for the synthesis of SPIONs with different quantities of dextran at a constant flow rate of 20 ml/h. Sample 22 has 1.50 ± 0.01 g of dextran followed by Sample 23 and Sample 24 has 1.30 ± 0.01 g and 0.99 ± 0.01 g respectively, all other parameters are kept constant.

| **Probe** | **Reagents** | **Quantity (g)** | **Temperature (°C)** | **Ultrasound frequency (kHz)** | **Flow rate (ml/h)** |
|---|---|---|---|---|---|
| **Sample 22** | $FeCl_3 \cdot 6H_2O$ | 1.32 ± 0.01 | 0-80 | 45 | 20 |
| | $FeCl_2 \cdot 4H_2O$ | 0.50 ± 0.01 | | | |
| | Dextran T70 | 1.50 ± 0.01 | | | |
| **Sample 23** | $FeCl_3 \cdot 6H_2O$ | 1.32 ± 0.01 | 0-80 | 45 | 20 |
| | $FeCl_2 \cdot 4H_2O$ | 0.50 ± 0.01 | | | |
| | Dextran T70 | 1.32 ± 0.01 | | | |
| **Sample 24** | $FeCl_3 \cdot 6H_2O$ | 1.32 ± 0.01 | 0-80 | 45 | 20 |
| | $FeCl_2 \cdot 4H_2O$ | 0.50 ± 0.01 | | | |
| | Dextran T70 | 0.99 ± 0.01 | | | |

At higher flow rates the effect of the different quantities of dextran is not very evident, as a higher flow rate leads to an early supersaturation of the solution. At higher flow rates the nucleation of the SPIONs is indecisive, the first batch of nuclei formed do not follow the same pattern as described in the earlier experiment in Section 6.7.1. This is shown in the magnified image of the nucleation phase for all the three samples. Sample 22 and Sample 24 showed almost the same change in the magnetic moment (Figure 6.13 **(A)**, regardless of the quantity of dextran involved in the reaction. The saturation of the SPIONs occurs first in Sample 23 (dextran = 1.32 ± 0.01 g) followed by Sample 24 (dextran = 0.99 ± 0.01 g) and the SPIONs with the maximum quantity of dextran Sample 22 (dextran = 1.50 ± 0.01 g) does not saturates. But if we compare a previous Sample 20 (dextran = 1.32 ± 0.01 g at a flow rate of < 10 ml/h) with the Sample 24 (dextran = 1.32 ± 0.01 g at a flow rate of 20 ml/h), the same inference can be drawn that with the higher the flow rate, more late the SPIONs start growing. In Sample 20 this effect can

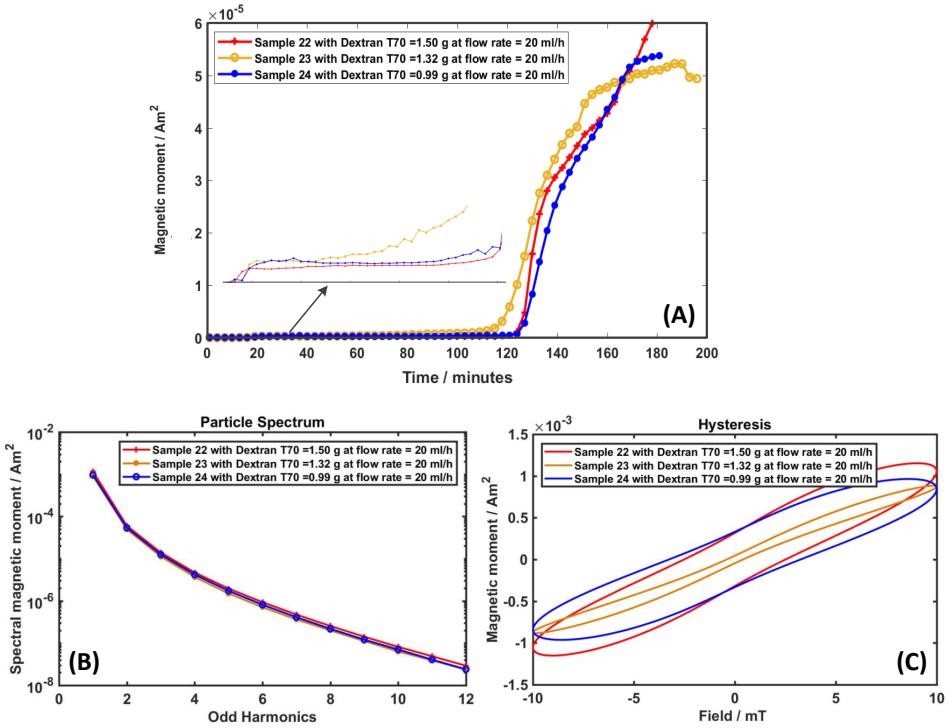


Figure 6.13: Measurements comparing synthesis process conducted with different quantities of dextran at a flow rate of 20 ml/h. The magnetic moment of the third harmonic versus time for the entire synthesis process is shown in **(A)**. The final amplitude spectra and the magnetization curve for the Sample 22 to Sample 24 at the end of the synthesis process are shown in **(B)** and **(C)** respectively.

be seen at a timestamp around 100 minutes. But at a higher flow rate (Sample 24), this occurs around the timestamp at 120 minutes. The amplitude spectra of all the samples are relatively equal in magnitudes. To evaluate this much further there is a necessity to analyse the effects of flow rate as well as the dextran separately. This is achieved through the comparison between Sample 20 and Sample 21, where low flow rates of less than 10 ml/h are used. Furthermore, to confirm the effect of the flow rate, Sample 25 and Sample 26 are synthesized without any dextran, shown in the next experiments.

## 6.8 Effect of flow rate on the nucleation and growth of the SPIONs without the presence of coating material

For this particular experiment, the SPIONs are synthesized without the presence of dextran at different flow rates. The details of the parameters are shown in Table 6.5. Sample 25 is synthesized with a flow rate of 25 ml/h and Sample 26 is synthesized with a

flow rate of 50 ml/h. All other parameters are kept constant. Figure 6.14 **(A)** shows the change in the magnetic moment versus time for both the samples. Figure 6.14 **(B and C)** displays the magnetic spectra and hysteresis of the SPIONs at the maximum magnetic moment while undergoing synthesis.

Table 6.5: Parameters for the synthesis of SPIONs at different flow rates and with absence of coating material. Sample 25 is synthesized with a flow rate of 25 ml/h and Sample 26 is synthesized with a flow rate of 50 ml/h. All other parameters are kept constant.

| **Probe** | **Reagents** | **Quantity (g)** | **Temperature (°C)** | **Ultrasound frequency (kHz)** | **Flow rate (ml/h)** |
|---|---|---|---|---|---|
| **Sample 25** | $FeCl_3 \cdot 6H_2O$ | 1.32 ± 0.01 | 0-80 | 45 | 25 |
| | $FeCl_2 \cdot 4H_2O$ | 0.50 ± 0.01 | | | |
| | Dextran T70 | - | | | |
| **Sample 26** | $FeCl_3 \cdot 6H_2O$ | 1.32 ± 0.01 | 0-80 | 45 | 50 |
| | $FeCl_2 \cdot 4H_2O$ | 0.50 ± 0.01 | | | |
| | Dextran T70 | - | | | |

Before going into the comparison of the two samples, it is crucial to interpret the behaviour of these curves. As it can be seen from the Figure 6.14 **(A)**, the SPIONs show an increase in the magnetic moment until approximately 100 minutes in the synthesis chamber and later on there is a decrease in the magnetic moment. This is caused due to the absence of the coating material such as dextran. When the SPIONs achieve a critical size, the agglomeration between the SPIONs begins and the field strength of the INSPECT is not high enough to excite these SPIONs undergoing nucleation and growth. Hence, with the increase in agglomeration the size of the SPIONs increases and, with time, there is a constant decrease in the magnetic moment. Synthesis without coating material is explained in detail in the previous Section 6.5.

Nevertheless, the same behaviour is observed in the initial nucleation and growth of these SPIONs i.e. the higher the flow rate, more time is required for the growth to begin. This can be easily inferred by comparing Sample 25 (flow rate of 25 ml/h), which starts growth earlier, in comparison to the Sample 26 (flow rate of 50 ml/h). Figure 6.14 **(B and C)** shows the higher spectra as well as higher saturation magnetization for Sample 26 as compared to Sample 25.

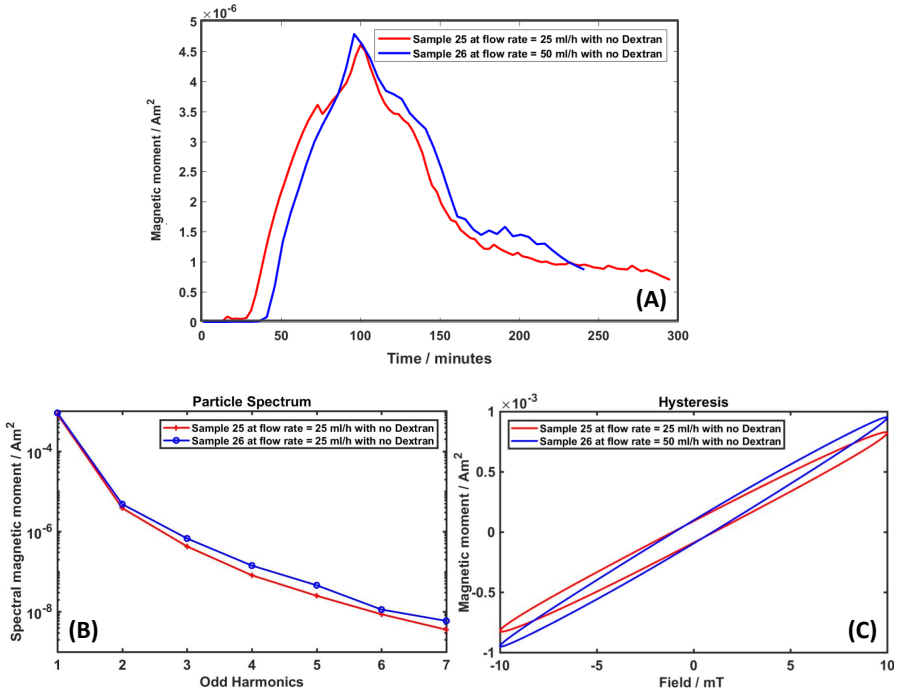


Figure 6.14: Measurements comparing synthesis conducted at two different flow rates (25 ml/h (red) and 50 ml/h (blue)) without the presence of dextran (coating material). The magnetic moment of the third harmonic versus time for the entire synthesis process is shown in **(A)**. The final amplitude spectra and the magnetization curve for the Sample 25 to Sample 26 at the end of the synthesis process are shown in **(B)** and **(C)** respectively.

# 7

# Effects of external parameters on the magnetic properties of SPIONs

## Contents



## 7.1 Introduction

In the previous chapters, we discussed different parameters which could affect the nucleation and growth of the SPIONs by analyzing the real-time changes in the magnetic moment through INSPECT. INSPECT proves to be a very powerful tool for characterizing the complete synthesis process for SPIONs. In this chapter, the focus will be on other parameters which play an essential role for the final magnetic properties of SPIONs. These parameters are analyzed without using INSPECT but with the help of specially

designed setups. In the coming section, a brief idea is given regarding these parameters which could be used for altering the final magnetic properties of SPIONs for specific applications. Section 7.2 deals with the presence of external static magnetic fields on the synthesis process. Section 7.3 describes the effects of an AC homogeneous magnetic field. And the last Section 7.4 deals with the effects of temperature, different types of dextran as well as the effect of ultrasound frequency on the final magnetic properties of the SPIONs. Ultrasonic mediated synthesis process is based on the research work by Lüdtke-Buzug [83].

## 7.2 Synthesis of SPIONs subjected to static magnetic fields

As mentioned earlier, the classical synthesis route for SPIONs is based on the alkaline co-precipitation of iron salts in an aqueous solution in the presence of biocompatible coating material. This method is not only simple but also provides a high yield of SPIONs. One drawback for such a synthesis process is that the SPIONs are not monodisperse i.e having a large core and hydrodynamic size variability leading to a mixed response to excitation fields. There are several techniques to achieve monodispersity such as the addition of surfactants, reducing agents and controlling the temperature when SPIONs are undergoing growth. In this experiment, it is demonstrated that there is one more parameter, which has a significant impact on the final core size of the synthesized SPIONs, a static magnetic field applied during the synthesis of the process. The effects due to the presence of the external magnetic field have been previously shown for nickel nanowires [135] and in the preparation of Co-doped $\alpha-Fe_2O_3$ cubic nanocrystal assemblies [136]. In this work, the effect of the presence of a static magnetic field on an ultrasound-mediated synthesis with dextran as a coating material is shown [O4]. A static magnetic field ranging from approximately 200 mT to 400 mT is applied at the time of synthesis.

### 7.2.1 Material and methods

As stated earlier, the SPIONs are synthesized via alkaline co-precipitation of iron salts ($Fe^{2+}$ and $Fe^{3+}$) in deionized water under ultrasonic control [83]. The synthesis process, as well as the involved chemical equations, are mentioned in Section 6.3. For this particular synthesis the iron salts, iron (III) (1.32 g of $FeCl_3 \cdot 6H_2O$, $\geq$ 99 %, Carl Roth GmbH Karlsruhe, Germany), iron (II) (0.50 g of $FeCl_2 \cdot 4H_2O$, $\geq$ 99 %, Merck kGaA, Darmstadt, Germany) and dextran T70 (from AppliChem GmbH, Darmstadt, Germany) are used. A

pair of permanent magnets is used to generate the required static magnetic field. The distance between the permanent magnets can be adjusted to attain the required field strength. The schematic diagram of the complete setup as well as the 3-D printed holder for permanent magnets is shown in Figure 7.1. The diameter of the magnets used for the synthesis process is approximately 62 mm and are safely secured to prevent any movement of these magnets. To prevent the collapse of the magnets both walls are separated with the help of four rods. **D** is the distance between the two magnets and can be altered to produce different field strengths. Therefore, it is essential to secure the permanent magnets properly as a very high magnetic force is exerted when the two magnets are lying in close proximity. The permanent magnet setup is suspended inside the ultrasound bath with the help of clamps. The field strength between the permanent magnets is measured with a 3-channel gauss meter 460 (Lake Shore Cryotronics, USA). The effective field strength obtained from various positions is shown in Table 7.1.

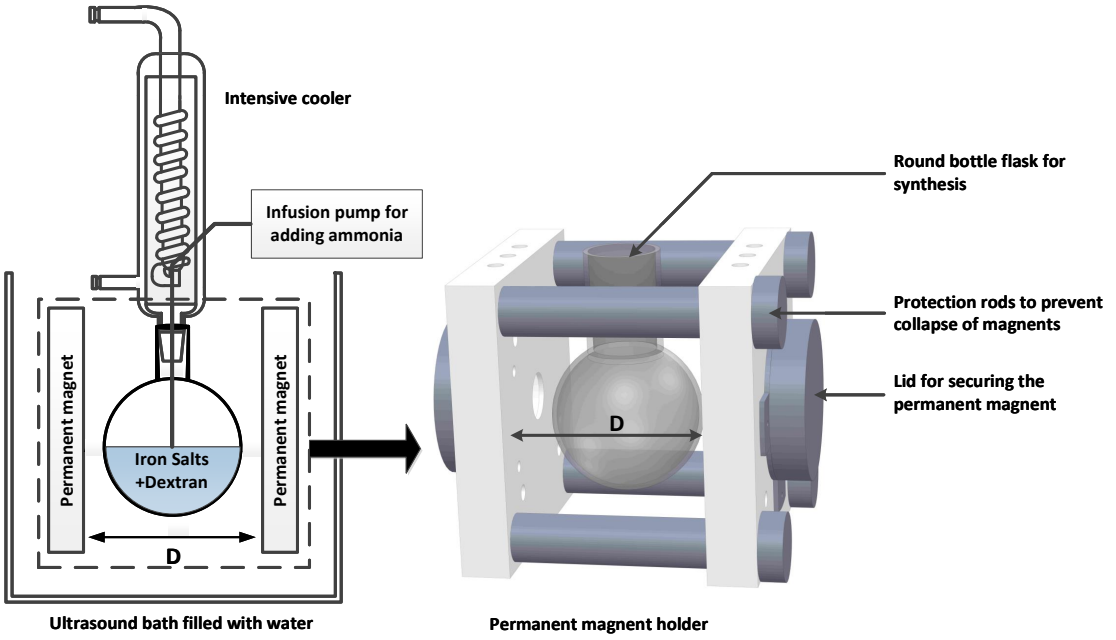


Figure 7.1: Block diagram of the setup for the synthesis of the SPIONs in a static magnetic field and the designed holder for the permanent magnets. The permanent magnet holder is suspended inside the ultrasound bath with the help of clamps. The permanent magnet holder consists of covered spaces to secure the magnets for safety as well as the protection rods to prevent the collapse of the magnets. **D** is the separation distance between the magnets and can be varied to produced static fields with different field strengths.

For synthesis, the iron salts are dissolved in deionized water at room temperature inside a reaction flask. The synthesis is conducted under ultrasonic control with a frequency

Table 7.1: The measured field produced due to different positions of the permanent magnets for synthesis under a permanent static magnetic field. The field is measured with a 3-channel gauss meter.

| D (cm) | X (mT) | Y (mT) | Z (mT) | XYZ (mT) |
|---|---|---|---|---|
| **2.5** | 278.47 | 295.61 | 32.7 | 407.44 |
| **3** | 206.89 | 293.94 | 21.79 | 359.61 |
| **4** | 183.13 | 210.89 | 15.71 | 279.75 |
| **5** | 136.73 | 172.15 | 11.17 | 220.13 |
| **5.5** | 149.48 | 126.45 | 11.38 | 196.23 |

of 45 kHz. For alkaline co-precipitation sodium hydroxide (NaOH) is used. For all the measurements the flow rate of the base is kept constant at 15 ml/h. The quantity of different chemical reagents and the applied external static field for every synthesis is shown in Table 7.2. For Samples 10-14 the static magnetic field is varied from approximately 195 mT to 400 mT. Sample 15 is used as the control experiment i.e. synthesis without the presence of any external magnetic field.

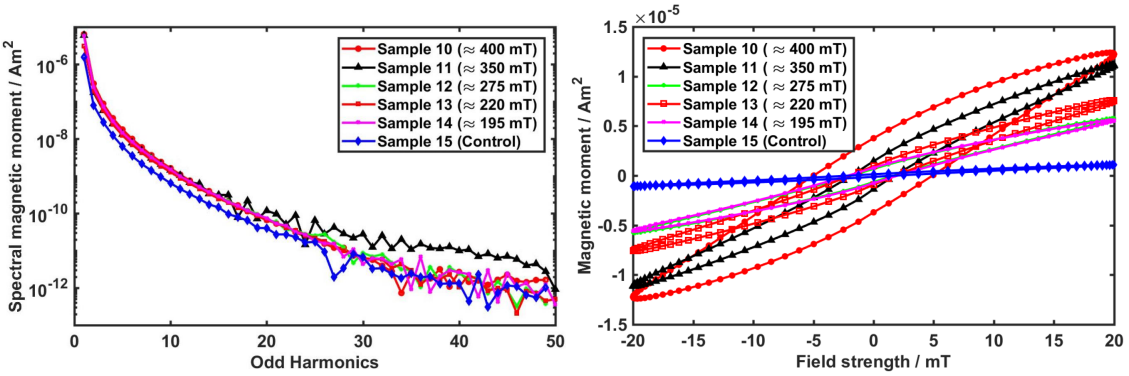


Figure 7.2: The amplitude spectra and the magnetization curves for all the samples obtained through the synthesis in presence of static magnetization fields varied from 0 mT to 400 mT. The measurements are obtained through one dimensional MPS [20] [51]. The amplitude spectra from different samples show negligible change but the area under the magnetization curve changes significantly depending on the applied static magnetic field signifying bigger core size.

### 7.2.2 Results

For characterization of the synthesized SPIONs, a one dimensional MPS operating at an excitation frequency of 25 kHz with a magnetic field strength of 20 mT at room temperature is used [20][51]. For measuring the amplitude spectra and the magnetization

Table 7.2: Parameters for the synthesis of SPIONs in presence of a static magnetic field. The static magnetic field is varied from 195 mT to 400 mT by positioning the permanent magnets around the synthesis flask. Sample 15 corresponds to the control, i.e. absence of any external magnetic fields.

| **Probe** | **Reagents** | **Quantity** (g) | **Temperature** (°C) | **Flow rate** (ml/h) | **Field strength** (mT) |
|---|---|---|---|---|---|
| **Sample 10** | $FeCl_3 \cdot 6H_2O$ | 0.39 ± 0.01 | 0-50 | 15 | ≈ 400 |
| | $FeCl_2 \cdot 4H_2O$ | 0.15 ± 0.01 | | | |
| | Dextran T70 | 0.39 ± 0.01 | | | |
| **Sample 11** | $FeCl_3 \cdot 6H_2O$ | 0.38 ± 0.01 | 0-50 | 15 | ≈ 350 |
| | $FeCl_2 \cdot 4H_2O$ | 0.15 ± 0.01 | | | |
| | Dextran T70 | 0.39 ± 0.01 | | | |
| **Sample 12** | $FeCl_3 \cdot 6H_2O$ | 0.39 ± 0.01 | 0-50 | 15 | ≈ 275 |
| | $FeCl_2 \cdot 4H_2O$ | 0.15 ± 0.01 | | | |
| | Dextran T70 | 0.39 ± 0.01 | | | |
| **Sample 13** | $FeCl_3 \cdot 6H_2O$ | 0.39 ± 0.01 | 0-50 | 15 | ≈ 220 |
| | $FeCl_2 \cdot 4H_2O$ | 0.14 ± 0.01 | | | |
| | Dextran T70 | 0.39 ± 0.01 | | | |
| **Sample 14** | $FeCl_3 \cdot 6H_2O$ | 0.39 ± 0.01 | 0-50 | 15 | ≈ 195 |
| | $FeCl_2 \cdot 4H_2O$ | 0.15 ± 0.01 | | | |
| | Dextran T70 | 0.39 ± 0.01 | | | |
| **Sample 15** | $FeCl_3 \cdot 6H_2O$ | 0.38 ± 0.01 | 0-50 | 15 | 0 |
| | $FeCl_2 \cdot 4H_2O$ | 0.15 ± 0.01 | | | |
| | Dextran T70 | 0.39 ± 0.01 | | | |

curves, 10 µL samples of all the experiments are measured. The amplitude spectra and the calculated magnetization curves for all the Samples 10-14 are shown in Figure 7.2. The amplitude spectra do not significantly change for all the samples except the control synthesis. But there are significant changes in the area of the magnetization curves. This increase in area under the magnetization curve can be attributed to an increase in the core size of the SPIONs. Therefore, the presence of the static magnetic field directly accelerates the growth of the SPIONs. The magnetic moment increases quite linearly with the increase in the applied field strength except for Sample 12 at a field strength of 275 mT. It is observed, static magnetic fields can also be used for influencing the growth of the SPIONs and the changes in the area enclosed by the hysteresis curve is directly proportional to the strength of the static magnetic field. The enclosed area for Sample 14 is $1.207 \times 10^{-6}$ Am$^2$ and for Sample 10 is $2.125 \times 10^{-6}$ Am$^2$, which is an increase by a factor of 1.76. Due to the higher enclosed area under the magnetization curves, these

SPIONs can be suitable for hyperthermia based applications .

## 7.3 Synthesis of SPIONs subjected to AC magnetic fields

In Section 7.2 the effects of the static magnetic field on the magnetic properties of the SPIONs was shown. An AC magnetic field also affects the magnetic properties of the SPIONs under synthesis. The same methodology is used for the synthesis as described in Section 6.3. Instead of using the permanent magnets setup, a solenoid coil is placed around the synthesis flask. The solenoid coil has the same dimensions and turns as the transmit coil of INSPECT shown in Section 5.2.4.1. With the help of the solenoid coil and the power amplifier AE Techron 2105 (AE Techron, USA), a sinusoidal magnetic field is created around the synthesis flask for the complete duration of the synthesis. The field strength can be varied with the help of the power amplifier. For showing the effects of the AC magnetic field on synthesis, a low magnetic field strength of 2.5 mT (Sample 1) and 3.0 mT (Sample 2) at a sinusoidal frequency of 100 Hz are compared. Furthermore, a synthesis process (Sample 3) with a sinusoidal field at 23.6 kHz with a field strength of approximately 15 mT is performed. Sample 3 is also compared with a commercially available SPION suspension. Table 7.3 contains all the parameters used for the three experiments.

Table 7.3: Parameters for the synthesis of SPIONs in presence of an AC magnetic field. Sample 1 (2.5 mT) and Sample 2 (3.0 mT) at a frequency of 100 Hz and Sample 3 (15 mT) are compared for signifying the effects of AC magnetic field on the magnetic properties of the SPIONs.

| **Probe** | **Reagents** | **Quantity (g)** | **Temperature (°C)** | **Frequency (Hz)** | **Field strength (mT)** |
|---|---|---|---|---|---|
| **Sample 1** | $FeCl_3 \cdot 6H_2O$ | 3.98 ± 0.01 | 0-80 | 100 | ≈ 2.5 |
| | $FeCl_2 \cdot 4H_2O$ | 1.54 ± 0.01 | | | |
| | Dextran T70 | 7.12 ± 0.01 | | | |
| **Sample 2** | $FeCl_3 \cdot 6H_2O$ | 4.07 ± 0.01 | 0-80 | 100 | ≈ 3.0 |
| | $FeCl_2 \cdot 4H_2O$ | 1.52 ± 0.01 | | | |
| | Dextran T70 | 6.93 ± 0.01 | | | |
| **Sample 3** | $FeCl_3 \cdot 6H_2O$ | 4.07 ± 0.01 | 0-80 | 23600 | ≈ 15.0 |
| | $FeCl_2 \cdot 4H_2O$ | 1.53 ± 0.01 | | | |
| | Dextran T70 | 4.01 ± 0.01 | | | |

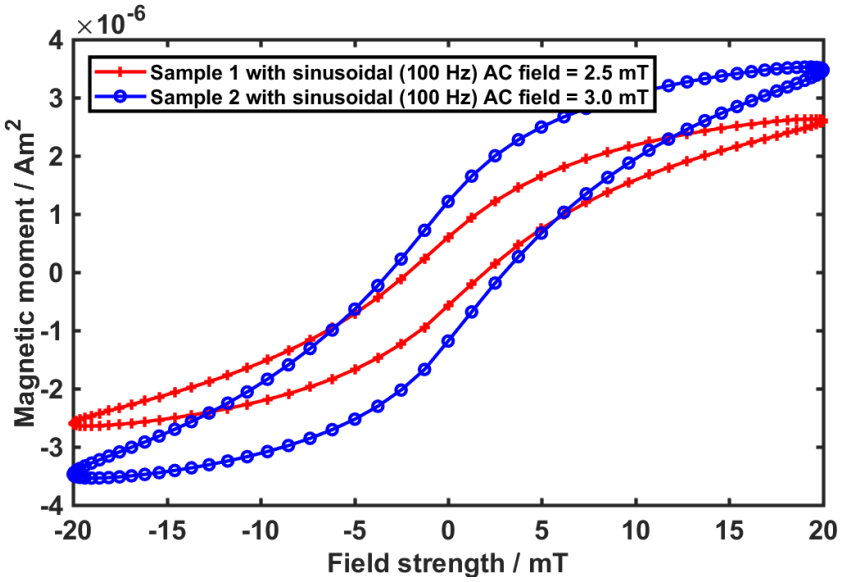


Figure 7.3: The magnetization curves for synthesis under a continuous AC magnetic field with frequency of 100 Hz and a field strength of 2.5 mT (Sample 1) and 3 mT (Sample 2). The area under the magnetization curve for Sample 2 is approximately double in comparison to Sample 1 which marks significant growth of the iron-oxide core when SPIONs are synthesized in the presence of an AC magnetic field.

Figure 7.3 shows the magnetization curves for Sample 1 and Sample 2. Higher magnetic field strengths of the excitation signal lead to bigger core sizes of the SPIONs and hence, these SPIONs are better suited for MFH. The enclosed area under the magnetization curve for Sample 2 is approximately double in comparison to Sample 1 which marks significant growth of the iron-oxide core when SPIONs are synthesized in the presence of an AC magnetic field. Figure 7.4 shows the amplitude spectrum of Sample 3 in comparison to the commercially available nanoparticles (Resovist). In conclusion, higher magnetic field strengths of the excitation signal lead to bigger core sizes of the SPIONs. The amplitude spectrum obtained is higher in comparison to commercially available nanoparticles shown in Figure 7.4. Moreover, the number of visible harmonics goes beyond 1.5 MHz. This proves that the AC magnetic field at the time of synthesis can influence the nucleation and growth of the SPIONs, when administered continuously for the complete duration of the synthesis process. But to conclude, there is a need to do more experimentation with different field strengths at different frequencies, and also different excitation signals like chirps and triangular waves. This experiment proves that there is a potential to manipulate the nucleation and growth of the SPIONs via external AC magnetic fields and can be a potential parameter for synthesizing application based SPIONs.

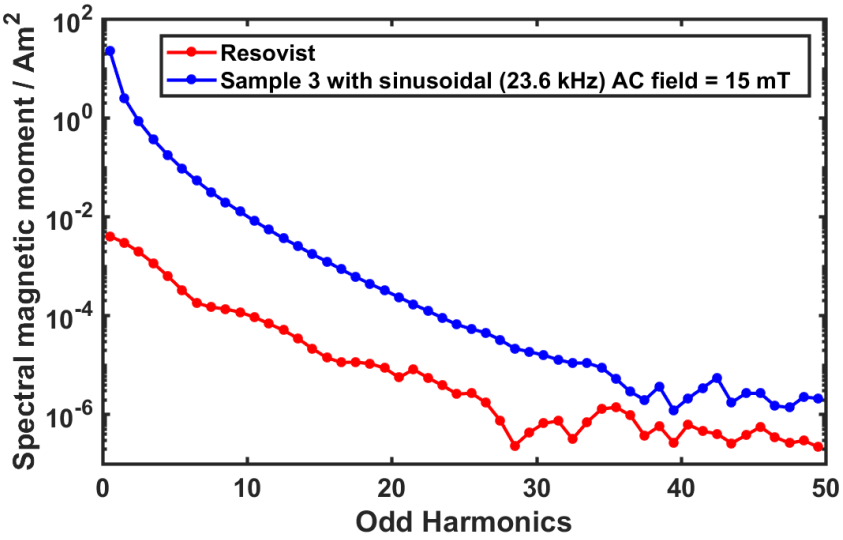


Figure 7.4: The magnetization curves for synthesis under a continuous AC magnetic field with a frequency of 23.6 kHz and field strength of approximately 15 mT. Sample 3 is also compared with commercially available SPIONs widely used in MPI and MRI.

## 7.4 Effect of other parameters on the synthesis of SPIONs

As explained in the previous sections, the continuous presence of a static magnetic field and AC magnetic field can affect the magnetic properties of the SPIONs. These parameters are completely external and the synthesis could be carried out without the presence of an external magnetic field. But there are some parameters which are pretty much part of every synthesis process but are neglected or not given much importance. In this section, we will examine some of these parameters like ultrasound frequency for ultrasonic stirring in Section 7.4.1, effects of different coating materials in Section 7.4.2 and the effect of synthesis temperature in Section 7.4.3 on the final magnetic properties of the SPIONs.

### 7.4.1 Effect of ultrasound frequency on the synthesis of SPIONs

As stated earlier all the synthesis methods explained in this research are done under ultrasonic control [83]. The ultrasound frequency also affects the magnetic properties of the synthesized SPIONs. For analyzing the results, two experiments are shown with two different types of coating materials (dextran T40 and dextran T70) with two different ultrasound frequencies (45 kHz and 135 kHz). The details of the used parameters for this experiment are shown in Table 7.4. For all the syntheses ammonia ($NH_3$) is used as a

base. Moreover, the flow rate of the ammonia is also kept constant for all the syntheses. Ultrasound waves produce cavitation bubbles inside a liquid medium. The size of the cavitation decreases with the increase in the frequency of the ultrasound waves. When these cavitation bubbles reach a critical size then they burst to release energy which leads to a random mixing of the reagents in the synthesis flask. The ultrasound frequency does not have a direct effect on the synthesis process and most of the time it is even not considered. Figure 7.5 shows the amplitude spectra for 10 µL samples measured with the one-dimensional MPS [51].

Table 7.4: Parameters for the synthesis of SPIONs with two different ultrasound frequencies of 45 kHz and 130 kHz. Moreover, the type of dextran is also varied, for example, Sample 4 and Sample 6 are synthesized with dextran T40 and Sample 5 and Sample 7 are synthesized with dextran T70. All these experiments are carried out with initial cooling.

| **Probe** | **Reagents** | **Quantity (g)** | **Temperature (°C)** | **Ultrasound frequency (kHz)** | **Dextran type** |
|---|---|---|---|---|---|
| **Sample 4** | $FeCl_3 \cdot 6H_2O$ | 4.00 ± 0.01 | 0-80 | 45 | T70 |
| | $FeCl_2 \cdot 4H_2O$ | 1.50 ± 0.01 | | | |
| | Dextran | 4.00 ± 0.01 | | | |
| **Sample 5** | $FeCl_3 \cdot 6H_2O$ | 4.01 ± 0.01 | 0-80 | 130 | T70 |
| | $FeCl_2 \cdot 4H_2O$ | 1.50 ± 0.01 | | | |
| | Dextran | 4.00 ± 0.01 | | | |
| **Sample 6** | $FeCl_3 \cdot 6H_2O$ | 4.04 ± 0.01 | 0-80 | 45 | T40 |
| | $FeCl_2 \cdot 4H_2O$ | 1.51 ± 0.01 | | | |
| | Dextran | 4.00 ± 0.01 | | | |
| **Sample 7** | $FeCl_3 \cdot 6H_2O$ | 4.07 ± 0.01 | 0-80 | 130 | T40 |
| | $FeCl_2 \cdot 4H_2O$ | 1.50 ± 0.01 | | | |
| | Dextran | 4.01 ± 0.01 | | | |

In Figure 7.5, Sample 4 and Sample 5 are synthesized with dextran T70 at two different ultrasound frequencies of 45 kHz and 130 kHz and keeping all other parameters constant. Similarly, Sample 6 and Sample 7 are synthesized with dextran T40 and keeping all other parameters constant. Dextran T40 and Dextran T70 have different molecular masses, T70 has a molecular weight of 70000 daltons and T40 has a molecular weight of 40000 daltons. The magnetic moment of Sample 4 and Sample 5 are quite comparable at different ultrasound frequencies. Contrarily, Sample 6 and Sample 7 consisting of T40 dextran have an evident effect on the outcome of the SPIONs. The magnitude of the third harmonic in Sample 6 is $8.159 \times 10^{-8}$ $Am^2$ and for Sample 7 it is $5.009 \times 10^{-9}$ $Am^2$ which is a difference by a factor of approximately 16. So, to visualize the effects of the

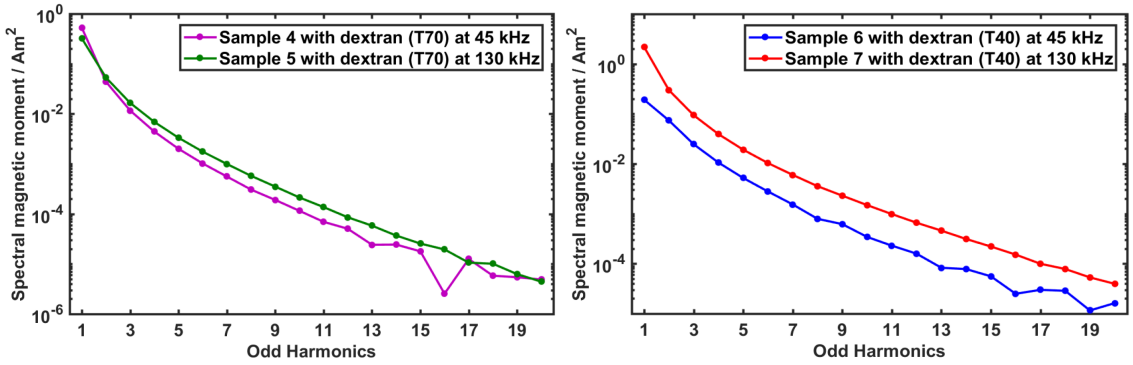


Figure 7.5: The amplitude spectra for all the samples obtained through synthesis under ultrasonic control with different frequencies (45 kHz and 130 kHz) and with two different coating materials (dextran T40 and dextran T70). The measurements are obtained with the help of an MPS.

ultrasound frequency other parameters also play a vital role such as the coating material. The difference between the magnetic moments for samples synthesized with dextran T70 and dextran T40 is due to the length of the polymer chain and the folding mechanism of these polymer chains around the iron-oxide core of the SPIONs. One hypothesis could be that the SPIONs coated with T70 dextran have higher core diameter due to more or less transport of the iron precursors through the dextran shell. But overall the magnetic moment of the SPIONs synthesized at a higher ultrasonic frequency is higher in comparison to synthesis which undergoes nucleation and growth at lower frequencies. This can be seen in both Sample 5 and Sample 7 which are synthesized at a higher ultrasound frequency of 130 kHz. To conclude, the ultrasound frequency is an important parameter which can be used to manipulate the nucleation and growth of SPIONs to tailor them for specific applications.

### 7.4.2 Effect of different types of coating material on the SPION magnetic properties

There are various coating materials available for SPIONs which make them fit for biomed -ical applications. There are three main reasons for using a coating material for SPIONs, foremost is to make the SPIONs biocompatible followed by protection from agglomeration and in last to stabilize the SPIONs in the solution [52]. Therefore, there are various options available for coating such as surfactants, polymers, precious metals, silica, carbon, etc. as shown in Chapter 2 Figure 2.3. The coating material has a direct effect on the magnetic properties of the SPIONs. The coating material can either increase the magnetic moment or further decrease it. In this experiment, we evaluate the effects of

two different polymer coatings (dextran with different molecular weights) on the final magnetic properties of the SPIONs. The synthesis is carried out based on the process by Lüdtke-Buzug [83]. Two types of dextran T40 and T70 with different molecular weights of 40000 daltons and 70000 daltons are used. All other parameters for the synthesis are kept constant. Figure 7.6 shows the amplitude spectrum and the magnetization curve obtained from the two synthesis processes. The measurements are made with the help of MPS [20][51].

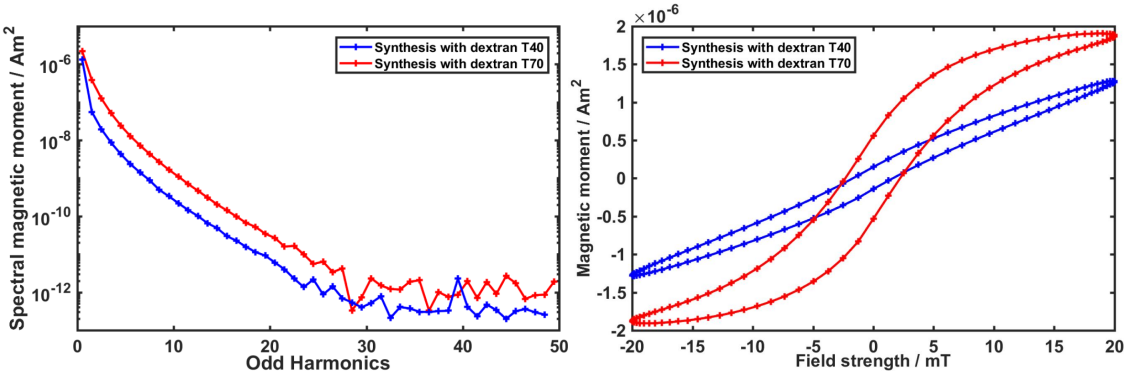


Figure 7.6: The amplitude spectra and the magnetization curves for synthesis with different types of dextran (T40 and T70). Dextran T70 has a molecular weight of 70000 daltons and dextran T40 has a molecular mass of 40000 daltons. The magnitude of the amplitude spectrum and the area under the magnetization curve with dextran T70 is higher in comparison to dextran T40.

As shown in the amplitude spectrum in Figure 7.6, the amplitude spectrum of the synthesis carried out with dextran T70 has a higher magnitude in comparison to the synthesis with dextran T40. Moreover, the area enclosed by the magnetization curve for synthesis with dextran T70 is higher. More area enclosed by the magnetization curves means that the SPIONs would have more energy due to magnetostriction to dissipate when excited with an appropriate magnetic field and hence are better for therapeutic scenarios like hyperthermia. One hypothesis for the difference in the amplitude spectra and magnetization curve could be attributed to the difference of the folding mechanisms of the long chain of dextrans. These folding mechanisms directly affect the hydrodynamic diameter which further affects the transport of the iron precursors to the core of the SPIONs hence directly affecting the composition of the core diameter. This leads to a difference in the magnetic properties of the SPIONs. Therefore quantity and type of coating material is another important parameter for the synthesis of the SPIONs and affects the nucleation and growth of the SPIONs. There are further studies needed to understand the folding mechanisms of the polymer coatings.

### 7.4.3 Effect of co-precipitation temperature on the magnetic properties of SPIONs

As mentioned in Section 2.4.1.1, the synthesis temperature has a direct effect on the response of SPIONs in an MPS/MPI device. This is because the Brownian relaxation time $\tau_B$ and the Néel relaxation time $\tau_N$ are dependent on the thermal energy. Heating of a solution containing SPIONs also leads to change in the viscosity which also affects the Brownian relaxation time $\tau_B$ leading to change in the magnetic moment. As the synthesis of SPIONs is done at different temperature ranges, therefore, there is a change in the magnetic moment of the SPIONs under nucleation and growth. To show the effects of synthesis temperature, the synthesis is carried out based on the process by Lüdtke-Buzug [83]. For this experiment, dextran T70 is used as a coating material and the flow rate of the base ($NH_3$) is kept constant at 99 ml/h. In this experiment, the main focus is on the growth phase therefore different samples of SPIONs undergoing growth are taken out of the synthesis at different temperatures such as 20 °C, 30 °C, 50 °C, 60 °C, 70 °C, and 80 °C. After removal from the synthesis flask, these samples are cooled till they attain room temperature. The amplitude spectra, as well as the magnetization curves, are acquired with the help of the one-dimensional MPS [20][51].

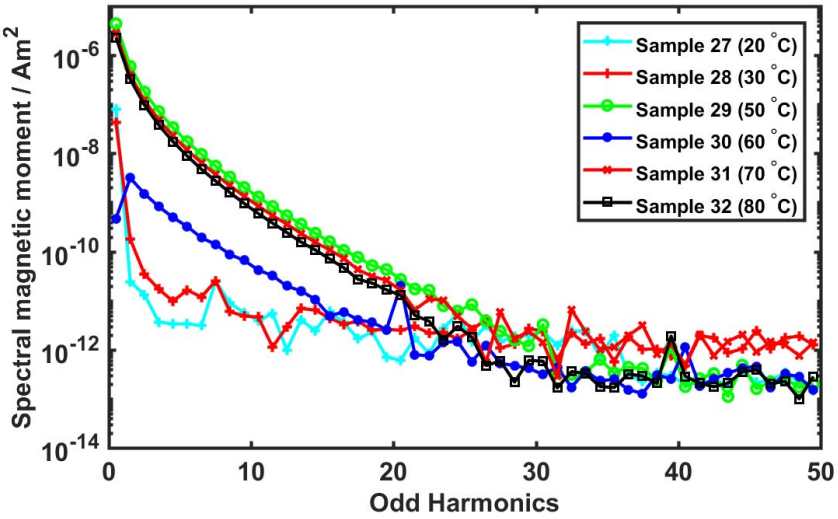


Figure 7.7: The amplitude spectra for all the samples obtained through synthesis under different temperature parameters. In this experiment, different samples of SPIONs undergoing growth are taken out at different temperatures Sample 27 (20 °C), Sample 28 (30 °C), Sample 29 (50 °C), Sample 30 (60 °C), Sample 31 (70 °C) and Sample 32 (80 °C).

The amplitude spectra are shown in Figure 7.7 and the calculated magnetization curve is shown in Figure 7.8 for all the measurements. For synthesis up to 30 °C, there is very

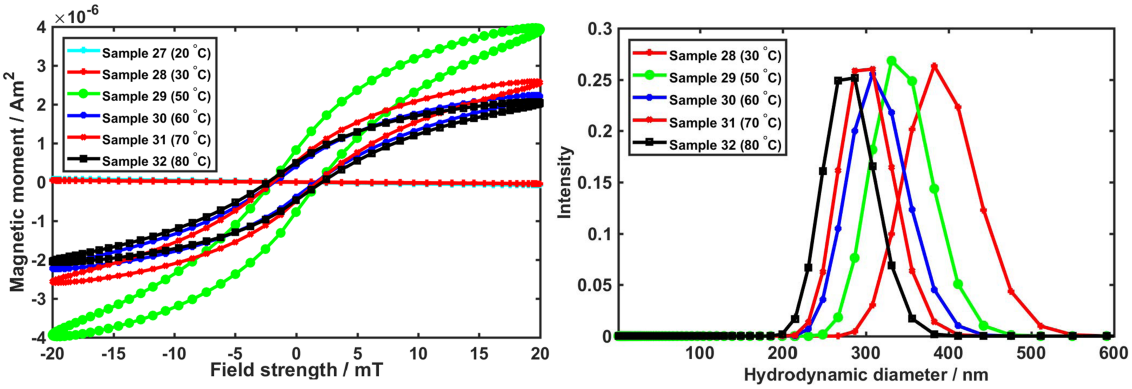


Figure 7.8: The magnetization curves on the left and PCCS measurements on the right for all the samples obtained through synthesis under different temperature parameters. In this experiment, different samples of SPIONs undergoing growth are taken out of the synthesis at different temperatures Sample 27 (20 °C), Sample 28 (30 °C), Sample 29 (50 °C), Sample 30 (60 °C), Sample 31 (70 °C) and Sample 32 (80 °C). The particle size distribution are in range of approximately 200-250 nm with change in the average diameters.

weak or negligible magnetic moment signifying no appropriate growth as shown in Figure 7.7. From 50 °C to 80 °C the magnitude of the amplitude spectra increases to that extent that the SPIONs are usable for MPI imaging. The best amplitude spectrum for MPI is obtained at a temperature of 50 °C. Moreover, there is an exception for Sample 30 acquired at 60 °C, the magnitude of the amplitude spectrum is less than that of the Sample 32 acquired at the highest temperature of 80 °C. Similar results are obtained through the calculated magnetization curves in Figure 7.8. At lower temperatures up to 30 °C, the area of the magnetization curve is negligible and with no saturation effect. Exceeding 30 °C, there is a systematic rise in the area of the magnetization curve with 50 °C showing the maximum enclosed area. Moreover, all the synthesis obtained at higher temperatures from 50 °C to 80 °C show saturation effects making them suitable for MPI and hyperthermia.

Figure 7.8 also shows the hydrodynamic size distribution for all the SPIONs at different co-precipitation temperatures. The measurements are acquired with a photon cross-correlation spectroscopy (PCCS) device (Nanophox, Sympatec GmbH, Germany). PCCS measurements in Figure 7.8 does not show the synthesis obtained at 20 °C as the size of the SPIONs is very small which cannot be precisely measured with the PCCS device. Sample 32 (80 °C) has the lowest mean hydrodynamic diameter and Sample 28 (30 °C) has the highest mean hydrodynamic diameter. One hypothesis is that a lower synthesis temperatures excessive dextran is folding around the magnetite core leading to higher hydrodynamic diameters. With the increase in temperature, dextran can form stronger bonds

with the magnetite core leading to the removal of excessive dextran and hence leading to lower mean hydrodynamic diameters. All the SPION samples have a hydrodynamic size distribution in the range of 200 nm to 250 nm.

# 8

# Conclusion

The presented thesis provides the methodology for the development of a novel tool called INSPECT to track the nucleation and growth of the SPIONs in real-time. The device is fully automated for acquiring the changes in the magnetic moment of the SPIONs undergoing synthesis. Moreover, the device is well suited for the chemistry environment and can easily be integrated into a normal research environment without much effort. There are a handful of devices, which are capable for real-time monitoring of SPIONs, and based on techniques such as X-ray scattering [90] and TEM (transmission electron microscopy) [91], but these devices require the most sophisticated engineering and special conditions for monitoring and analysis. Hence, it comes with great effort using these devices in a normal chemistry environment. On the other hand, INSPECT is a low-cost device with low instrumentation complexity and does not require user expertise in comparison to X-ray scattering and TEM. The minimum time required to acquire one measurement is equal to one period of the excitation frequency which is approximately 42.9 µs. The device is tuned to the excitation frequency of 23 kHz but can easily be tuned to another excitation frequency by changing the impedance matching module. With the help of INSPECT, changes in the magnetic moment of the SPIONs for two complete synthesis processes have been described, i.e. synthesis with and without the coating material in Section 6.4 and Section 6.5, respectively. In these synthesis processes, it has been demonstrated how the diamagnetic behaviour of the reactants involved in the syn-

thesis changes to superparamagnetic SPIONs. Furthermore, the changes in the magnetic moment due to agglomeration are also shown in section 6.5.

Other parameters are also studied which play a vital role in the final magnetic properties of the synthesized SPIONs from Section 6.6 to Section 6.8. In Chapter 7, a brief idea is provided about some external parameters which can also influence the magnetic properties of SPIONs undergoing synthesis and can be used for tailoring the particle response to different application based scenarios in MPI. The major focus is given to the influence caused due to the presence of the external static, AC magnetic field and different ultrasound frequencies.

With the help of all the measurements conducted in this thesis, it was figured there is no specific procedure to synthesize SPIONs. The parameters should be changed according to the application and further research is needed to understand the limits of these parameters. All these parameters play a vital role in the genesis of the SPIONs with desired geometrical properties (size, shape and hydrodynamic diameter) and magnetic properties (amplitude spectrum and magnetization curves). To the best of our knowledge for making ideal SPIONs for MPI, some of the key parameters to consider are stated below with their effects on the properties of SPIONs in Table 8.1. The properties which are marked with a circle do not affect the final nucleation and growth of SPIONs or it is difficult to differentiate the effects caused due to these parameters. For example, an increase in the static magnetic field strength can lead to an increase in the diameter, saturation magnetization, and area enclosed by the magnetization curve but has no significant impact on the magnitude spectrum.

- **Flow Rate:** One of the most significant parameters, as it controls the overall thermodynamics of the reaction. So the ideal flow rate should be between 10 ml/h to 30 ml/h.

- **Quantity of dextran:** For synthesizing smaller SPIONs it is advisable to use large quantities of dextran more than 1.32 ± 0.01 g and then trying to control other parameters through different means. For making bigger SPIONs the quantity of the dextran should be reduced to less than 0.50 ± 0.01 g.

- **External static magnetic field:** Application of an external magnetic field to influence the shape and size of the hysteresis curve of the SPIONs, influences magnetostriction and causes dissipation of heat energy.

- **External AC magnetic field:** External AC magnetic fields effect both the amplitude spectrum as well as the enclosed area of the magnetization curve.

- **Ultrasonic field:** The ultrasound frequency widely influences the amplitude spectrum of the synthesized SPIONs. A lower value of the ultrasound frequency (for example 45 kHz) gives a better magnetic amplitude response of SPIONs in MPS compared to a higher frequency (for example 130 kHz).

Table 8.1: Effect of different parameters on the properties of SPIONs. The direction of the triangle mark an increase (△) or decrease (▽) in the concerned physical properties and circle signifies no observed effect on the particular property.

| **Increase of** | **Magnitude spectrum** | **Core diameter** | **Saturation magnetization** | **Hysteresis area** | **Ratio of 3rd & 5th harmonic** |
|---|---|---|---|---|---|
| **DC magnetic field strength** | ○ | △ | △ | △ | ○ |
| **AC magnetic field strength** | △ | △ | △ | △ | ○ |
| **Flow rate** | ○ | ○ | ▽ | △ | ▽ |
| **Dextran quantity** | ▽ | ▽ | ○ | ○ | ▽ |
| **Ultrasound frequency** | ○ | ○ | △ | ○ | ○ |
| **Synthesis temperature** | △ | ○ | △ | ○ | ○ |

In the end, nucleation and growth of the SPIONs is a very complex process. The final characteristics of the SPIONs widely depend on the mixture of these parameters.

Furthermore, different variations of LNA based on the parallelization of Op-amps to reduce the input noise as well as to achieve better NF were developed. All the LNAs have a wide bandwidth and offer different noise characteristic. A direct comparison between the LNAs is not feasible because of different topology and degree of parallelization, but to get an overview some of the noise characteristics are compared in Table 8.2.

According to Table 8.2, the single-ended LNA based on LT6232 has better noise characteristics in comparison to the single-ended LNA based on LMH6629. But it all depends on the degree of parallelization as the LNA based on LT6232 which consists of 16 Op-amps in parallel as compared to just 4 Op-amps in LNA based on LMH6629. Similarly, the VGA based on AD603 shows good noise characteristics with 8 Op-amps in parallel. But the VGA provides an interesting feature to control the gain by supplying adequate

Table 8.2: A comparison between different prototyped LNAs based on input noise and NF with two different terminations (50 Ω resistor and receiving coil)

| **LNA** | **Termination by 50 Ω** | | **Termination by receive coil** | |
|---|---|---|---|---|
| | **Input noise (nV/ $\sqrt{\text{Hz}}$)** | **NF (dB)** | **Input noise (nV/ $\sqrt{\text{Hz}}$)** | **NF (dB)** |
| **Single-ended (LMH6629)** | 1.10 | 7.87 | 0.561 | 11.57 |
| **Single-ended (LT6232)** | 0.653 | 3.32 | 0.546 | 1.35 |
| **VGA (AD603)** | 0.868 | 1.86 | 0.513 | 1.91 |
| **FDA (LMH6553)** | 1.76 | 11.93 | 0.30 | 14.05 |

voltage to Pin '+' and Pin '-'. This gives an immense advantage to dynamic applications where the iron concentration changes with time as in the case of SPIONs undergoing nucleation and growth. In the future, a feedback loop can be implemented to automatically change the gain by analyzing the input signal to VGA. According to Table 8.2, the NF of the FDA based on LMH6553 is on higher in comparison to other LNAs. But FDA offers other advantages which can make a significant improvement to the receive signal chain. Some of the advantages include extra noise immunity by attenuating the common-mode noise and minimizing even harmonic distortions (Section 2.10). Furthermore, there is no need for an additional protection circuit for the acquisition card as FDA has an in-built clamping circuit. This reduces the noise added due to an external protection circuit and further improves the noise characteristic. Therefore, the usage of the LNA depends on a careful selection of different parameters depending on the application. In the end, the design of the PCB also influences the overall noise characteristic of the LNA. For example in the case of the FDA, an asymmetry in the feedback can lead to worse CMRR leading to higher external interference.

# 9 Outlook

With the advent of MPI, the need for tailoring the SPIONs for a specific application has further risen and there is a need to provide a powerful tool to monitor the changes in the magnetic properties much faster and precisely to develop application based SPIONs. This gap is filled with the help of INSPECT, which is not only fast and precise but also completely automated for acquiring the changes in magnetic moment during synthesis. With INSPECT we opened a new horizon through which we can steer and manipulate the magnetic and physical properties of SPIONs by making real-time changes in the synthesis process and simultaneously tracking the nucleation and growth. With appropriate parameter adjustments at different time spots, the desired physical and magnetic properties of the nanoparticles can be produced. But still, much research is needed to figure out different possibilities which could be achieved and to what extent. To make nucleation and growth studies much easier, it is a necessity to embed INSPECT into a continuous-flow synthesis concept to streamline the research as there are too many parameters with different effects on the magnetic properties of SPIONs. Moreover, this in-synthesis spectrometry combined with the control feedback allows for quality assurance for mass production of SPIONs at industrial level. In this chapter, a brief idea is presented with regards to steering and manipulation of the nucleation and growth to synthesize SPIONs for various applications.

## 9.1 Steering the nucleation and growth of SPIONs

For steering and manipulating the nucleation and growth of the SPIONs during their synthesis, most essential tools are:

- a sensing device, which measures the changes in the properties of the SPIONs in real-time, for example, a device based on the concept of INSPECT.
- a feedback loop, which steers the nucleation and growth process for improving the physical properties, especially the magnetic properties of the SPIONs.

The feedback loop can consist of chemical and biological reagents, which can steer the outcome of the magnetic properties of the SPIONs, or it could be in the form of physical principles such as sound waves or magnetic fields. The feedback loop can adapt chemical, physical and biological parameters (for instance the flow rate of the reagents or energy fields like ultrasound waves, electrical, magnetic and electro-magnetical waves), which can steer the magnetic properties of the nanoparticles. Lüdtke-Buzug *et al.* have already shown that steering of the physical properties of SPIONs by using sound waves in the form of ultrasonic waves and by using static and dynamic magnetic fields is also feasible [O8] [O9].

### 9.1.1 Steering the growth with external magnetic fields

Figure 9.1 shows one of the possible hardware realizations for steering growth of the SPIONs with external magnetic fields. The hardware consists of static and dynamic fields for different directions. Through the information provided by the INSPECT, the growth and nucleation of the SPIONs are steered by different external fields simultaneously or in a stand-alone configuration with different coil topologies. This device works in combination with the INSPECT to provide an appropriate feedback loop. External fields are used for manipulating and steering the nucleation and growth of the SPIONs in the desired direction. Due to the presence of these external fields both the physical and magnetic properties can be manipulated.

The hardware can be located inside INSPECT (as shown in Figure 9.1) or can be located at a distance as a separate unit. The added advantage of having the external magnetic fields at a distant location would be that these external fields could also be used for separating SPIONs according to their desired magnetic and physical properties [137][138]. The various magnetic fields that can be used are:

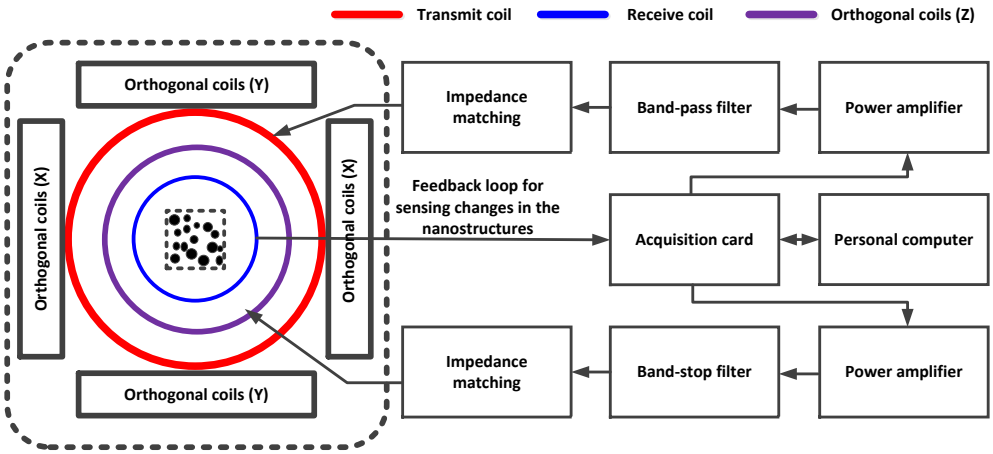


Figure 9.1: The possible realization for steering the growth of SPIONs with external magnetic fields. This device is used in addition to the INSPECT. The device comprises of different coil pairs (orthogonal coils in x, y, and z-directions) for generating the required magnetic field followed by impedance matching units for transmission of maximum power from the power amplifier to the coils, band-pass filter for attenuating the distortions produced by the power amplifier and power amplifiers for generating the required field. The acquisition card generates the excitation signal supplied to the coils as well for acquiring the measurements from the SPIONs under synthesis. A personal computer is used for displaying the data.

- Magnetic fields in the form of homogeneous static fields, generated in such a way that they act on the SPIONs undergoing synthesis process. Such an effect can be achieved with permanent magnets/orthogonal coils in the x-direction, y-direction, and z-direction. As shown with the permanent magnet setup in Section 7.2.

- Magnetic fields in the form of spatially varying static fields, generated in such a way that they act on the SPIONs in a synthesis process.

- Magnetic fields in the form of homogeneous, dynamic (time-varying) fields, generated in such a way that acts on the SPIONs in a synthesis process. As shown with the synthesis in the presence of AC magnetic fields in Section 7.3.

- Magnetic fields in the form of spatially varying, dynamic (time-varying) fields, generated in such a way that it acts on the SPIONs in a synthesis process. This is performed with the help of a pair of orthogonal coils (in and x and y-directions) and a solenoid coil (shown in Figure 9.1 in purple) for the z-direction.

For producing the dynamic fields (homogeneous/spatially varying) in x, y and z-direction there is a need to have additional power amplifiers, band-pass filters and the required

impedance matching for reducing the power losses between the coils and the amplifier. For illustration purpose, only the components for x and y-direction are shown in Figure 9.1, but the z-direction also requires the extra components in the form of power amplifiers, band-stop filters, and the required impedance matching. The function of the acquisition card is to provide the excitation signal to all the electromagnetic coils mentioned in the previous paragraph and to acquire the signals obtained through the receive coil. The personal computer is used for displaying the data obtained from such a synthesis process as well as controlling the different functionalities of the device. The topology of the electromagnetic coils can comprise of saddle coils, solenoids, surface coils, etc.

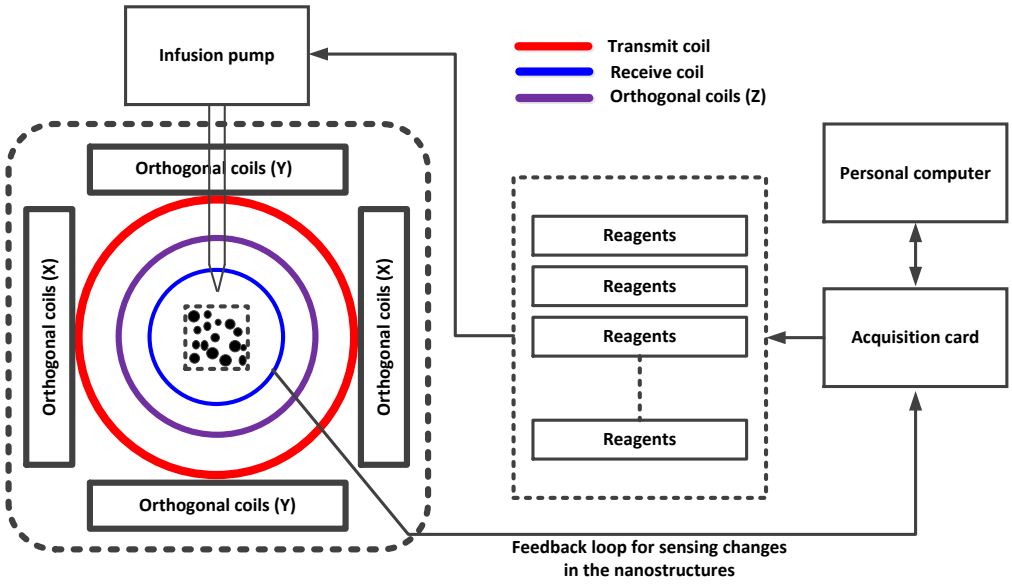


Figure 9.2: The possible realization for steering the growth of SPIONs with chemical/biological reagents. The device comprises of different coil pairs for generating the required magnetic field from the Section 9.1.1. Chemical reagents infusion pumps controlled with the help of an acquisition card are used. The acquisition card senses the changes in the nucleation and growth pattern in the form of a feedback loop, administers the required quantity of the reagents, and keeps on monitoring the growth of the SPIONs.

### 9.1.2 Steering the growth with chemical reagents

The nucleation and growth process can be adapted by the flow rate of chemicals and reagents (as shown in Section 7.4). This method depends on the time constants of the sensing apparatus (INSPECT) as the chemicals and/or biological reagents react fast. This steering method can be used in addition to the method introduced in Section 9.1.1. Figure 9.2 shows one of the possible hardware realizations for such a device consisting

primarily of infusion pumps and a delivery mechanism. The acquisition card is used for controlling the infusion pumps. The acquisition card also senses the change in the magnetic properties of the SPIONs under synthesis and administer the required reagents in the required quantity to steer the nucleation and growth process. For different synthesis processes, the time points for the administration are an important steering parameter.

### 9.1.3 Algorithm to control the feedback loop

As stated earlier, nucleation and growth of the SPIONs is a very complex process. The final characteristics of the SPIONs widely depend on the mixture of parameters described in Chapter 8. Hence, the best steering capabilities can be achieved when the synthesis

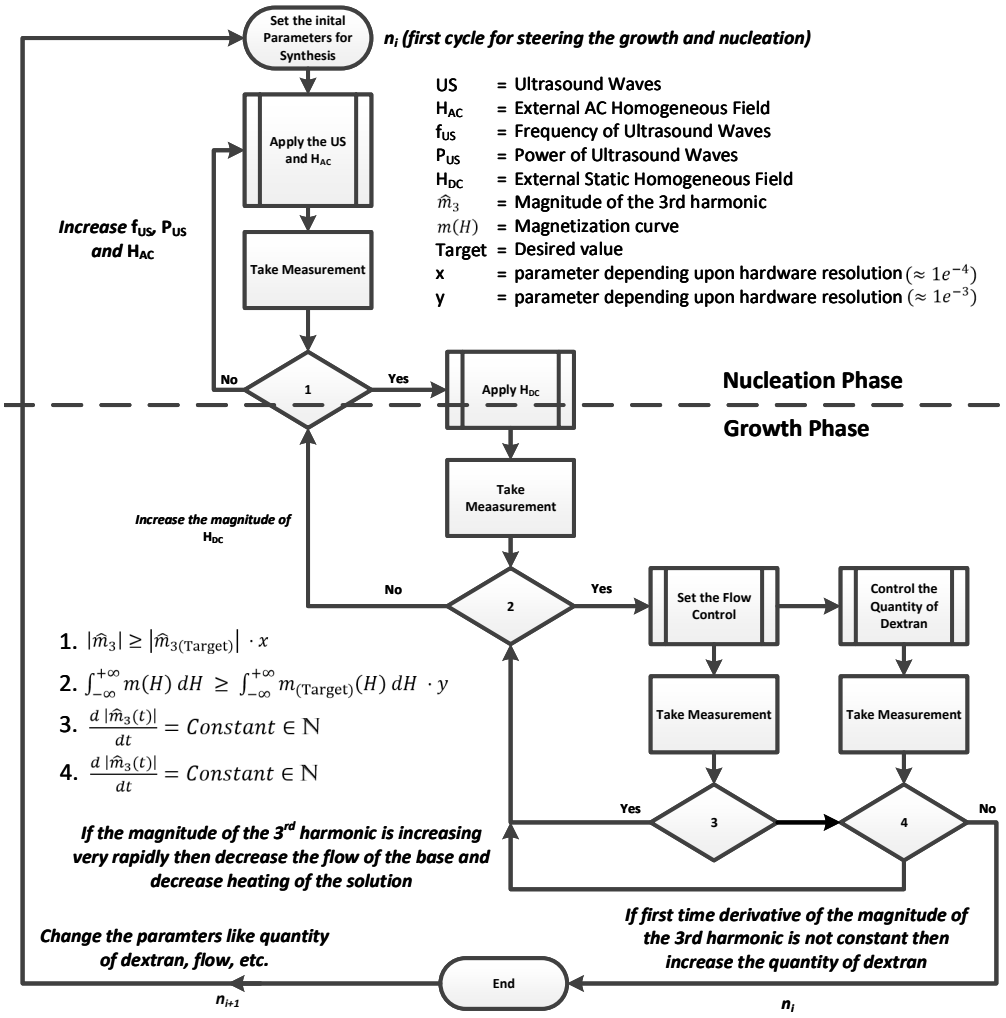


Figure 9.3: An exemplary algorithm to control the nucleation and growth of SPIONs in a continuous cycle.

process undergoes numerous cycles. Figure 9.3 shows a possible algorithm to control the nucleation and growth of the SPIONs in a synthesis process. For the initialization of synthesis, the parameters are chosen according to the chemical synthesis process and then continuous measurements are performed to measure the physical properties (amplitude spectrum, phase spectrum, and magnetization curves). Depending on these measured physical characteristics the parameters are adapted in the discretized control loops. All the decisions in the algorithm are marked with numbers with the underlying equations to take an appropriate decision depending on the various parameters being measured by the sensing device.

This thesis gives a unique insight towards the complexities arising in tracking and manipulating the magnetic properties of the SPIONs undergoing synthesis for various diagnostics and therapeutic applications. General feasibility towards the tracking part is shown by INSPECT with improvements possible in the sensitivity and resolution of the device. Manipulation is difficult as the involved internal and external parameters are interlinked and require in-depth research.

# Bibliography

## Own references


[O1] A. Malhotra and T. Buzug, "Op-amp based low noise amplifier for magnetic particle spectroscopy," *Current Directions in Biomedical Engineering*, vol. 3, no. 2, Sep. 2017. DOI: 10.1515/cdbme-2017-0125.

[O2] A. Malhotra and T. M. Buzug, "A Summing Configuration based Low Noise Amplifier for MPI and MPS," *Current Directions in Biomedical Engineering*, vol. 4, no. 1, pp. 83–86, Sep. 2018. DOI: 10.1515/cdbme-2018-0021.

[O3] A. Malhotra and T. M. Buzug, "A Summing configuration based Low Noise Amplifier for MPI and MPS," in *International Workshop on Magnetic Particle Imaging (IWMPI) Book of Abstracts 2017*, 2018, p. 121, ISBN: 978-3-945954-34-8.

[O4] A. Malhotra, P. Kaiser, T. M. Buzug, and K. Lüdtke-Buzug, "Synthesis of Super-paramagnetic Iron Oxides Nanoparticles Subjected to Magnetic Fields," in *8th International Workshop on Magnetic Particle Imaging IWMPI 2018*, T. Knopp and T. M. Buzug, Eds., 2018, p. 23, ISBN: 978-3-945954-48-5.

[O5] A. Malhotra, F. Spieß, C. Stegelmeier, C. Debbeler, and K. Lüdtke-Buzug, "Effect of key parameters on synthesis of superparamagnetic nanoparticles (SPIONs)," *Current Directions in Biomedical Engineering*, vol. 2, no. 1, Sep. 2016. DOI: 10.1515/cdbme-2016-0117.

[O6] A. Malhotra, C. Stegelmeier, T. Friedrich, K. Lüdtke-Buzug, and T. M. Buzug, "First Results: Phantoms for MPI and Ultrasound Therapy," in *International Workshop on Magnetic Particle Imaging (IWMPI) Book of Abstracts 2016*, 2016, p. 50, ISBN: 978-3-945954-19-5.

[O7] A. Malhotra, A. von Gladiss, A. Behrends, *et al.*, "Tracking the Growth of Superparamagnetic Nanoparticles with an In-Situ Magnetic Particle Spectrometer (INSPECT)," *Scientific Reports*, 2019. DOI: 10.1038/s41598-019-46882-6.

[O8] K. Lüdtke-Buzug and A. Malhotra, "Verfahren und Vorrichtung zur Herstellung von magnetischen Nanopartikeln," 10 2017 108 737 A1, 2018.

[O9] A. Malhotra, A. von Gladiß, K. Lüdtke-Buzug, and T. M. Buzug, "Method and apparatus for in-synthesis sensing and control of magnetic nanostructures," 115665P1013EP, 2019.

[O10] A. von Gladiss, J. Beuke, M. Weber, *et al.*, "Dynamic 2D Imaging with an MPI Scanner Featuring a Mechanically Rotated FFL," in *9th International Workshop on Magnetic Particle Imaging*, 2019, p. 5, ISBN: 978-3945954560.

[O11] J. Beuke, K. Brandt, A. Malhotra, *et al.*, "Combined Active and Passive Cancellation of Receive Chain Direct Feedthrough," in *9th International Workshop on Magnetic Particle Imaging*, 2019, p. 49, ISBN: 978-3945954560.

[O12] C. Stegelmeier, A. Malhotra, and K. Lüdtke-Buzug, "Biocompatible Magnetite Nanoparticles as Tracer Material for Magnetic Particle Imaging," in *International Workshop on Magnetic Particle Imaging (IWMPI) Book of Abstracts 2016*, 2016, p. 99, ISBN: 978-3-945954-19-5.

# Other references

[13] B. Gleich and J. Weizenecker, "Tomographic imaging using the nonlinear response of magnetic particles," *Nature*, vol. 435, no. 7046, pp. 1214–1217, 2005. DOI: 10.1038/nature03808.

[14] J. Weizenecker, B. Gleich, J. Rahmer, H. Dahnke, and J. Borgert, "Three-dimen -sional real-time in vivo magnetic particle imaging," *Physics in medicine and biology*, vol. 54, no. 5, p. L1, 2009. DOI: 10.1088/0031-9155/54/5/L01.

[15] J. Rahmer, J. Weizenecker, B. Gleich, and J. Borgert, "Analysis of a 3-D System Function Measured for Magnetic Particle Imaging," *IEEE Transactions on Medical Imaging*, vol. 31, no. 6, pp. 1289–1299, 2012. DOI: 10.1109/TMI.2012.2188639.

[16] J.-P. Gehrcke, M. A. Rückert, T. Kampf, W. H. Kullmann, P. M. Jakob, and V. C. Behr, "Investigation of the Magnetic Particle Imaging Signal Dependency on Ferrofluid Concentration," in *Magnetic Nanoparticles*, World Scientific, Aug. 2010. DOI: 10.1142/9789814324687_0010.

[17] D. Eberbeck, F. Wiekhorst, S. Wagner, and L. Trahms, "How the size distribution of magnetic nanoparticles determines their magnetic particle imaging performance," *Applied Physics Letters*, vol. 98, no. 18, p. 182 502, May 2011. DOI: 10.1063/1.3586776.

[18] M. Graeser, A. von Gladiss, M. Weber, and T. M. Buzug, "Two dimensional magnetic particle spectrometry," *Physics in Medicine and Biology*, vol. 62, no. 9, pp. 3378–3391, Apr. 2017. DOI: 10.1088/1361-6560/aa5bcd.

[19] M. Graeser, T. Knopp, M. Grüttner, T. F. Sattel, and T. M. Buzug, "Analog receive signal processing for magnetic particle imaging," *Medical Physics*, vol. 40, no. 4, p. 042 303, Apr. 2013. DOI: 10.1118/1.4794482.

[20] S. Biederer, T. Knopp, T. F. Sattel, *et al.*, "Magnetization response spectroscopy of superparamagnetic nanoparticles for magnetic particle imaging," *Journal of Physics D: Applied Physics*, vol. 42, no. 20, p. 205 007, 2009. DOI: 10.1088/0022-3727/42/20/205007.

[21] J. B. Weaver, "Perpendicular Magnetic Particle Imaging, pMPI," *IEEE Transactions on Magnetics*, vol. 51, no. 2, pp. 1–4, Feb. 2015. DOI: 10.1109/tmag.2014.2332292.

[22] N. Panagiotopoulos, F. Vogt, J. Barkhausen, *et al.*, "Magnetic particle imaging: Current developments and future directions," *International Journal of Nanomedicine*, p. 3097, Apr. 2015. DOI: 10.2147/ijn.s70488.

[23] J. Weizenecker, B. Gleich, and J. Borgert, "Magnetic particle imaging using a field free line," *Journal of Physics D: Applied Physics*, vol. 41, no. 10, p. 105 009, 2008. DOI: 10.1088/0022-3727/41/10/105009.

[24] M. Erbe, M. Weber, T. F. Sattel, and T. M. Buzug, "Experimental Validation of an Assembly of Optimized Curved Rectangular Coils for the Use in Dynamic Field Free Line Magnetic Particle Imaging," *Current Medical Imaging Reviews*, vol. 9, no. 2, pp. 89–95, May 2013. DOI: 10.2174/1573405611309020003.

[25] T. Knopp, T. Sattel, S. Biederer, and T. Buzug, "Field-free line formation in a magnetic field," *Journal of Physics A: Mathematical and Theoretical*, vol. 43, no. 1, p. 012 002, 2010. DOI: 10.1088/1751-8113/43/1/012002.

[26] P. Goodwill, G. Scott, P. Stang, G. C. Lee, D. Morris, and S. Conolly, "Direct Imaging of SPIOs in Mice using Magnetic Particle Imaging: Instrument Construction and 3D Imaging," *Proceedings of the International Society for Magnetic Resonance in Medicine (ISMRM)*, vol. 17 (1452), Apr. 2009. DOI: 10.13140/RG.2.1.1609.6889.

[27] P. W. Goodwill, L. R. Croft, J. J. Konkle, *et al.*, "A 7 T/M 3D X-space MPI mouse and rat scanner," in *2013 International Workshop on Magnetic Particle Imaging (IWMPI)*, IEEE, Mar. 2013. DOI: 10.1109/iwmpi.2013.6528387.

[28] P. W. Goodwill, G. C. Scott, P. P. Stang, and S. M. Conolly, "Narrowband Magnetic Particle Imaging," *IEEE Transactions on Medical Imaging*, vol. 28, no. 8, pp. 1231–1237, 2009. DOI: 10.1109/TMI.2009.2013849.

[29] J. J. Konkle, P. W. Goodwill, E. U. Saritas, B. Zheng, K. Lu, and S. M. Conolly, "Twenty-fold acceleration of 3D projection reconstruction MPI," *Biomedizinische Technik/Biomedical Engineering*, vol. 58, no. 6, Jan. 2013. DOI: 10.1515/bmt-2012-0062.

[30] T. Knopp, S. Biederer, T. Sattel, *et al.*, "Trajectory analysis for magnetic particle imaging," *Physics in medicine and biology*, vol. 54, no. 2, p. 385, 2009. DOI: 10.1088/0031-9155/54/2/014.

[31] P. Vogel, M. A. Ruckert, P. Klauer, W. H. Kullmann, P. M. Jakob, and V. C. Behr, "Traveling Wave Magnetic Particle Imaging," *IEEE Transactions on Medical Imaging*, vol. 33, no. 2, pp. 400–407, Feb. 2014. DOI: 10.1109/tmi.2013.2285472.

[32] M. Grüttner, T. Knopp, J. Franke, *et al.*, "On the formulation of the image reconstruction problem in magnetic particle imaging," *Biomedizinische Technik/Biomedical Engineering*, vol. 58, no. 6, Jan. 2013. DOI: 10.1515/bmt-2012-0063.

[33] T. Knopp, J. Rahmer, T. F. Sattel, *et al.*, "Weighted iterative reconstruction for magnetic particle imaging," *Physics in Medicine and Biology*, vol. 55, no. 6, pp. 1577–1589, Feb. 2010. DOI: 10.1088/0031-9155/55/6/003.

[34] P. W. Goodwill and S. M. Conolly, "Multidimensional X-space Magnetic Particle Imaging," *IEEE Transactions on Medical Imaging*, vol. 30, no. 9, pp. 1581–1590, 2011. DOI: 10.1109/TMI.2011.2125982.

[35] J. Rahmer, J. Weizenecker, B. Gleich, and J. Borgert, "Signal encoding in magnetic particle imaging: properties of the system function," *BMC Medical Imaging*, vol. 9, no. 1, p. 4, 2009, ISSN: 1471-2342. DOI: 10.1186/1471-2342-9-4.

[36] T. Knopp, T. F. Sattel, S. Biederer, and T. M. Buzug, "Limitations of measurement-based system functions in magnetic particle imaging," in *Medical Imaging 2010: Biomedical Applications in Molecular, Structural, and Functional Imaging*, R. C. Molthen and J. B. Weaver, Eds., SPIE, Mar. 2010. DOI: 10.1117/12.844181.

[37] T. Knopp, T. Sattel, S. Biederer, *et al.*, "Model-Based Reconstruction for Magnetic Particle Imaging," *IEEE Transactions on Medical Imaging*, vol. 29, no. 1, pp. 12–18, Jan. 2010. DOI: 10.1109/tmi.2009.2021612.

[38] T. Knopp, S. Biederer, T. F. Sattel, *et al.*, "2D model-based reconstruction for magnetic particle imaging," *Medical Physics*, vol. 37, no. 2, pp. 485–491, Jan. 2010. DOI: 10.1118/1.3271258.

[39] J. Rahmer, B. Gleich, J. Weizenecker, and J. Borgert, "3D Real-Time Magnetic Particle Imaging of Cerebral Blood Flow in Living Mice," *Proceedings of the International Society for Magnetic Resonance in Medicine (ISMRM)*, p. 714, May 2010.

[40] J. Haegele, J. Rahmer, B. Gleich, *et al.*, "Magnetic Particle Imaging: Visualization of Instruments for Cardiovascular Intervention," *Radiology*, vol. 265, no. 3, pp. 933–938, Dec. 2012. DOI: 10.1148/radiol.12120424.

[41] J. Rahmer, A. Antonelli, C. Sfara, *et al.*, "Nanoparticle encapsulation in red blood cells enables blood-pool magnetic particle imaging hours after injection," *Physics in Medicine and Biology*, vol. 58, no. 12, pp. 3965–3977, May 2013. DOI: 10.1088/0031-9155/58/12/3965.

[42] X. G. Chen, "First Measurement and SNR Results of a 3D Magnetic Particle Spectrometer," *International Journal on Magnetic Particle Imaging*, 2018. DOI: 10.18416/ijmpi.2018.1810001.

[43] A. von Gladiss, M. Graeser, P. Szwargulski, T. Knopp, and T. M. Buzug, "Hybrid system calibration for multidimensional magnetic particle imaging," *Phys -ics in Medicine and Biology*, vol. 62, no. 9, pp. 3392–3406, Apr. 2017. DOI: 10.1088/1361-6560/aa5340.

[44] M. Graeser, S. Biederer, M. Grüttner, *et al.*, "Determination of System Functions for Magnetic Particle Imaging," in *Springer Proceedings in Physics*, Springer Berlin Heidelberg, 2012, pp. 59–64. DOI: 10.1007/978-3-642-24133-8_10.

[45] M. Graeser, A. von Gladiss, P. Szwargulski, M. Ahlborg, T. Knopp, and T. M. Buzug, "Reconstruction of Experimental 2D MPI Data using a Hybrid System-Matrix," *International Workshop on Magnetic Particle Imaging*, p. 130, 2016.

[46] P. W. Goodwill, K. Lu, B. Zheng, and S. M. Conolly, "An x-space magnetic particle imaging scanner," *Review of Scientific Instruments*, vol. 83, no. 3, pp. 033 708, Mar. 2012. DOI: 10.1063/1.3694534.

[47] T. Wawrzik, M. Schilling, and F. Ludwig, "Debye-based frequency-domain magnetization model for magnetic nanoparticles and its application to viscosity dependent mps measurements," *4th International Workshop on Magnetic Particle Imaging (IWMPI)*, Mar. 2014.

[48] A. M. Rauwerdink, E. W. Hansen, and J. B. Weaver, "Nanoparticle temperature estimation in combined ac and dc magnetic fields," *Physics in Medicine and Biology*, vol. 54, no. 19, pp. L51–L55, Sep. 2009. DOI: 10.1088/0031-9155/54/19/l01.

[49] T. Wawrzik, F. Ludwig, and M. Schilling, "Magnetic Particle Imaging: Exploring Particle Mobility," in *Springer Proceedings in Physics*, Springer Berlin Heidelberg, 2012, pp. 21–25. DOI: 10.1007/978-3-642-24133-8_4.

[50] D. B. Reeves and J. B. Weaver, "Magnetic nanoparticle sensing: decoupling the magnetization from the excitation field," *Journal of Physics D: Applied Physics*, vol. 47, no. 4, p. 045 002, Dec. 2013. DOI: 10.1088/0022-3727/47/4/045002.

[51] S. Biederer, "Magnet-Partikel-Spektrometer: Entwicklung eines Spektrometers zur Analyse superparamagnetischer Eisenoxid-Nanopartikel für Magnetic-Particle -Imaging," Ph.D. dissertation, Universität zu Lübeck, 2011.

[52] A.-H. Lu, E. Salabas, and F. Schüth, "Magnetic Nanoparticles: Synthesis, Protection, Functionalization, and Application," *Angewandte Chemie International Edition*, vol. 46, no. 8, pp. 1222–1244, Feb. 2007. DOI: 10.1002/anie.200602866.

[53] A. Puri, K. Loomis, B. Smith, *et al.*, "Lipid-Based Nanoparticles as Pharmaceutical Drug Carriers: From Concepts to Clinic," *Critical Reviews in Therapeutic Drug Carrier Systems*, vol. 26, no. 6, pp. 523–580, 2009.

[54] U. Häfeli, G. Pauer, S. Failing, and G. Tapolsky, "Radiolabeling of magnetic particles with rhenium-188 for cancer therapy," *Journal of Magnetism and Magnetic Materials*, vol. 225, no. 1-2, pp. 73–78, Jan. 2001. DOI: 10.1016/s0304-8853(00)01230-0.

[55] D. Högemann, L. Jo9hson, R. Weissleder, and J. P. Basilion, "Improvement of MRI Probes To Allow Efficient Detection of Gene Expression," *Bioconjugate Chemistry*, vol. 11, no. 6, pp. 941–946, Nov. 2000. DOI: 10.1021/bc000079x.

[56] P. Oswald, O. Clement, C. Chambon, E. Schouman-Claeys, and G. Frija, "Liver positive enhancement after injection of superparamagnetic nanoparticles: Respective role of circulating and uptaken particles," *Magnetic Resonance Imaging*, vol. 15, no. 9, pp. 1025–1031, Jan. 1997. DOI: 10.1016/s0730-725x(97)00004-0.

[57] Y. R. Chemla, H. L. Grossman, Y. Poon, *et al.*, "Ultrasensitive magnetic biosensor for homogeneous immunoassay," *Proceedings of the National Academy of Sciences*, vol. 97, no. 26, pp. 14 268–14 272, Dec. 2000. DOI: 10.1073/pnas.97.26.14268.

[58] J. Mürbe, A. Rechtenbach, and J. Töpfer, "Synthesis and physical characterization of magnetite nanoparticles for biomedical applications," *Materials Chemistry and Physics*, vol. 110, no. 2-3, pp. 426–433, Aug. 2008. DOI: 10.1016/j.matchemphys.2008.02.037.

[59] Y. Kseoglu, H. Kavas, and B. Aktas, "Surface effects on magnetic properties of superparamagnetic magnetite nanoparticles," *Physica Status Solidi (A)*, vol. 203, no. 7, pp. 1595–1601, May 2006. DOI: 10.1002/pssa.200563104.

[60] X. Duan, Y. Huang, Y. Cui, J. Wang, and C. M. Lieber, "Indium phosphide nanowires as building blocks for nanoscale electronic and optoelectronic devices," *Nature*, vol. 409, no. 6816, pp. 66–69, Jan. 2001. DOI: 10.1038/35051047.

[61] N. Zhu, H. Ji, P. Yu, *et al.*, "Surface Modification of Magnetic Iron Oxide Nanoparticles," *Nanomaterials*, vol. 8, no. 10, p. 810, Oct. 2018. DOI: 10.3390/nano8100810.

[62] A. L. Cortajarena, D. Ortega, S. M. Ocampo, *et al.*, "Engineering Iron Oxide Nanoparticles for Clinical Settings," *Nanobiomedicine*, vol. 1, p. 2, Jan. 2014. DOI: 10.5772/58841.

[63] R. Dhavalikar and C. Rinaldi, "On the effect of finite magnetic relaxation on the magnetic particle imaging performance of magnetic nanoparticles," *Journal of Applied Physics*, vol. 115, no. 7, p. 074 308, Feb. 2014. DOI: 10.1063/1.4866680.

[64] B. Gleich, J. Weizenecker, and J. Borgert, "Experimental results on fast 2D-encoded magnetic particle imaging," *Phys Med Biol.*, vol. 53, no. 6, N81, 2008. DOI: 10.1088/0031-9155/53/6/N01.

[65] S. Laurent, D. Forge, M. Port, *et al.*, "Magnetic Iron Oxide Nanoparticles: Synthesis, Stabilization, Vectorization, Physicochemical Characterizations, and Biological Applications," *Chemical Reviews*, vol. 108, no. 6, pp. 2064–2110, Jun. 2008. DOI: 10.1021/cr068445e.

[66] Y.-X. J. Wang, S. M. Hussain, and G. P. Krestin, "Superparamagnetic iron oxide contrast agents: physicochemical characteristics and applications in MR imaging," *European Radiology*, vol. 11, no. 11, pp. 2319–2331, May 2001. DOI: 10.1007/s003300100908.

[67] X. Mao, J. Xu, and H. Cui, "Functional nanoparticles for magnetic resonance imaging," *Wiley Interdisciplinary Reviews: Nanomedicine and Nanobiotechnology*, vol. 8, no. 6, pp. 814–841, Apr. 2016. DOI: 10.1002/wnan.1400.

[68] R. Toy, P. M. Peiris, K. B. Ghaghada, and E. Karathanasis, "Shaping cancer nanomedicine: the effect of particle shape on the in vivo journey of nanoparticles," *Nanomedicine*, vol. 9, no. 1, pp. 121–134, Jan. 2014. DOI: 10.2217/nnm.13.191.

[69] S. E. Barry, "Challenges in the development of magnetic particles for therapeutic applications," *International Journal of Hyperthermia*, vol. 24, no. 6, pp. 451–466, Jan. 2008. DOI: 10.1080/02656730802093679.

[70] N. T. Thanh, Ed., *Magnetic Nanoparticles: from fabrication to clinical applications*. CRC Press, Feb. 2012. DOI: 10.1201/b11760.

[71] L. Néel, "Some theoretical aspects of rock-magnetism," *Advances in Physics*, vol. 4, no. 14, pp. 191–243, Apr. 1955. DOI: 10.1080/00018735500101204.

[72] W. F. Brown, "Thermal Fluctuations of a Single-Domain Particle," *Journal of Applied Physics*, vol. 34, no. 4, pp. 1319–1320, Apr. 1963. DOI: 10.1063/1.1729489.

[73] K. Lüdtke-Buzug, J. Haegele, S. Biederer, *et al.*, "Comparison of commercial iron oxide-based MRI contrast agents with synthesized high-performance MPI tracers," *Biomedizinische Technik/Biomedical Engineering*, vol. 58, no. 6, Jan. 2013. DOI: 10.1515/bmt-2012-0059.

[74] R. M. Ferguson, A. P. Khandhar, and K. M. Krishnan, "Tracer design for magnetic particle imaging (invited)," *Journal of Applied Physics*, vol. 111, no. 7, 07B318, Apr. 2012. DOI: 10.1063/1.3676053.

[75] A. P. Guimarães, *Principles of Nanomagnetism*. Springer Berlin Heidelberg, 2009. DOI: 10.1007/978-3-642-01482-6.

[76] W. Shi, J. Wang, X. Fan, and H. Gao, "Size and shape effects on diffusion and absorption of colloidal particles near a partially absorbing sphere: implications for uptake of nanoparticles in animal cells," *Physical Review E*, vol. 78, no. 6, Dec. 2008. DOI: 10.1103/physreve.78.061914.

[77] C. Burda, X. Chen, R. Narayanan, and M. A. El-Sayed, "Chemistry and Properties of Nanocrystals of Different Shapes," *Chemical Reviews*, vol. 105, no. 4, pp. 1025–1102, Apr. 2005. DOI: 10.1021/cr030063a.

[78] J. Lodhia, G. Mandarano, N. Ferris, P. Eu, and S. Cowell, "Development and use of iron oxide nanoparticles (Part 1): Synthesis of iron oxide nanoparticles for MRI," *Biomedical Imaging and Intervention Journal*, vol. 6, no. 2, Apr. 2010. DOI: 10.2349/biij.6.2.e12.

[79] C. Corot, P. Robert, J. Idee, and M. Port, "Recent advances in iron oxide nano -crystal technology for medical imaging," *Advanced Drug Delivery Reviews*, vol. 58, no. 14, pp. 1471–1504, Dec. 2006. DOI: 10.1016/j.addr.2006.09.013.

[80] J. P. Jolivet, "Influence of Fe(II) on the Formation of the Spinel Iron Oxide in Alkaline Medium," *Clays and Clay Minerals*, vol. 40, no. 5, pp. 531–539, 1992. DOI: 10.1346/ccmn.1992.0400506.

[81] L. Babes, B. Denizot, G. Tanguy, J. J. L. Jeune, and P. Jallet, "Synthesis of Iron Oxide Nanoparticles Used as MRI Contrast Agents: A Parametric Study," *Journal of Colloid and Interface Science*, vol. 212, no. 2, pp. 474–482, Apr. 1999. DOI: 10.1006/jcis.1998.6053.

[82] W. Jiang, H. Yang, S. Yang, *et al.*, "Preparation and properties of superparamagnetic nanoparticles with narrow size distribution and biocompatible," *Journal of Magnetism and Magnetic Materials*, vol. 283, no. 2-3, pp. 210–214, Dec. 2004. DOI: 10.1016/j.jmmm.2004.05.022.

[83] K. Lüdtke-Buzug, "Magnetische Nanopartikel," *Chemie in unserer Zeit*, vol. 46, no. 1, pp. 32–39, Feb. 2012. DOI: 10.1002/ciuz.201200558.

[84] R. Massart, "Preparation of aqueous magnetic liquids in alkaline and acidic media," *IEEE Transactions on Magnetics*, vol. 17, no. 2, pp. 1247–1248, Mar. 1981. DOI: 10.1109/tmag.1981.1061188.

[85] G. Cao and Y. Wang, *Nanostructures and Nanomaterials: Synthesis, Properties And Applications*. World Scientific, Jan. 2011. DOI: 10.1142/7885.

[86] C. den Ouden and R. Thompson, "Analysis of the formation of monodisperse populations by homogeneous nucleation," *Journal of Colloid and Interface Science*, vol. 143, no. 1, pp. 77–84, Apr. 1991. DOI: 10.1016/0021-9797(91)90438-e.

[87] J. D. Ng, B. Lorber, J. Witz, A. Théobald-Dietrich, D. Kern, and R. Giegé, "The crystallization of biological macromolecules from precipitates: Evidence for Ostwald ripening," *Journal of Crystal Growth*, vol. 168, no. 1-4, pp. 50–62, Oct. 1996. DOI: 10.1016/0022-0248(96)00362-4.

[88] M. Morales, T. González-Carreño, and C. Serna, "The formation of a–fe2o3 monodispersed particles in solution," *Journal of Materials Research*, vol. 7, no. 09, pp. 2538–2545, Sep. 1992. DOI: 10.1557/jmr.1992.2538.

[89] M. Ocaña, R. Rodriguez-Clemente, and C. J. Serna, "Uniform colloidal particles in solution: Formation mechanisms," *Advanced Materials*, vol. 7, no. 2, pp. 212–216, Feb. 1995. DOI: 10.1002/adma.19950070225.

[90] H.-G. Liao, L. Cui, S. Whitelam, and H. Zheng, "Real-Time Imaging of Pt3Fe Nanorod Growth in Solution," *Science*, vol. 336, no. 6084, pp. 1011–1014, May 2012. DOI: 10.1126/science.1219185.

[91] G. Renaud, "Real-Time Monitoring of Growing Nanoparticles," *Science*, vol. 300, no. 5624, pp. 1416–1419, May 2003. DOI: 10.1126/science.1082146.

[92] J. B. Johnson, "Thermal Agitation of Electricity in Conductors," *Physical Review*, vol. 32, no. 1, pp. 97–109, Jul. 1928. DOI: 10.1103/physrev.32.97.

[93] H. W. Ott, *Noise Reduction Techniques in Electronic Systems, 2nd Edition*.

[94] J. Karki, "Fully-Differential Amplifiers," Texas Instruments, Tech. Rep., 2016.

[95] B. Carter, *Op Amps for Everyone*. Newnes, 2009, ISBN: 9780080949482.

[96] M. Gräeser, "Partikeldynamik in Magnet-Partikel-Spektroskopie und -Bildge -bung," Universität zu Lübeck, 2016.

[97] K. Wilson, A. Wilson, W. Rowlands, J. W. Jewett, and R. A. Serway, *Physics For Global Scientists and Engineers, Volume 2*. Cengage Learning Australia, 2016, ISBN: 9780170355520.

[98] E. D. Gates, *Introduction to Basic Electricity and Electronics Technology (Explore Our New Electronic Tech 1st Editions)*. Cengage Learning, 2013, ISBN: 9781133948513.

[99] N. Smith, "Reciprocity principles for magnetic recording theory," *IEEE Transactions on Magnetics*, vol. 23, no. 4, pp. 1995–2002, Jul. 1987. DOI: 10.1109/tmag.1987.1065184.

[100] R. Harrison and C. Charles, "A low-power low-noise CMOS for amplifier neural recording applications," *IEEE Journal of Solid-State Circuits*, vol. 38, no. 6, pp. 958–965, Jun. 2003. DOI: 10.1109/jssc.2003.811979.

[101] C. S. Kim, J.-W. Park, H. K. Yu, and H. Cho, "Gate layout and bonding pad structure of a RF n-MOSFET for low noise performance," *IEEE Electron Device Letters*, vol. 21, no. 12, pp. 607–609, Dec. 2000. DOI: 10.1109/55.887481.

[102] W. Zhang, B. Zheng, P. Goodwill, and S. Conolly, "A custom low-noise preamplifier for Magnetic Particle Imaging," in *2015 5th International Workshop on Magnetic Particle Imaging (IWMPI)*, IEEE, Mar. 2015. DOI: 10.1109/iwmpi.2015.7107027.

[103] M. Weber, J. Beukea, A. von Gladissa, *et al.*, "Novel Field Geometry Using Two Halbach Cylinders for FFL-MPI," *International Journal on Magnetic Particle Imaging*, vol. 4, no. 2, 2018. DOI: 10.18416/ijmpi.2018.1811004.

[104] Texas Instruments, "LMH6629 Ultra-Low Noise, High-Speed Operational Amplifier with Shutdown," Texas Instruments, 2010. [Online]. Available: http://www.ti.com/lit/ds/symlink/lmh6629.pdf.

[105] Linear Technology, "LT6230/LT6230-10/LT6231/LT6232: 215MHz, Rail-to-Rail Output, 1.1 nV/Hz, 3.5 mA Op Amp Family Data Sheet," Linear Technology, 2011. [Online]. Available: https://www.analog.com/media/en/technical-documentation/data-sheets/623012fc.pdf.

[106] Stanford Research Systems (SRS), "MODEL SR560 LOW-NOISE PREAMPLIFIER," 3.0, 2013. [Online]. Available: https://www.thinksrs.com/downloads/pdfs/manuals/SR560m.pdf.

[107] Analog Devices, "AD603: Low Noise, 90 MHz Variable Gain Amplifier Data Sheet (Rev. K)," Analog Devices. [Online]. Available: https://www.analog.com/media/en/technical-documentation/data-sheets/AD603.pdf.

[108] Texas Instruments, "LMH6553 900 MHz Fully Differential Amplifier With Output Limiting Clamp," Texas Instruments, Mar. 2013. [Online]. Available: http://www.ti.com/lit/ds/symlink/lmh6553.pdf.

[109] J. Weizenecker, J. Borgert, and B. Gleich, "A simulation study on the resolution and sensitivity of magnetic particle imaging," *Phys Med Biol.*, vol. 52, no. 21, p. 6363, 2007.

[110] A. Jordan, R. Scholz, P. Wust, H. Fähling, and R. Felix, "Magnetic fluid hyperthermia (MFH): Cancer treatment with AC magnetic field induced excitation of biocompatible superparamagnetic nanoparticles," *Journal of Magnetism and Magnetic Materials*, vol. 201, no. 1-3, pp. 413–419, Jul. 1999. DOI: 10.1016/s0304-8853(99)00088-8.

[111] M. Bañobre-López, A. Teijeiro, and J. Rivas, "Magnetic nanoparticle-based hyperthermia for cancer treatment," *Reports of Practical Oncology & Radiotherapy*, vol. 18, no. 6, pp. 397–400, Nov. 2013. DOI: 10.1016/j.rpor.2013.09.011.

[112] A. K. Gupta and M. Gupta, "Synthesis and surface engineering of iron oxide nanoparticles for biomedical applications," *Biomaterials*, vol. 26, no. 18, pp. 3995–4021, Jun. 2005. DOI: 10.1016/j.biomaterials.2004.10.012.

[113] A. Lindemann, B. M. Fraederich, R. Pries, B. Wollenberg, K. Lüdtke-Buzug, and K. Graefe, "Biological impact of superparamagnetic iron oxide nanoparticles for magnetic particle imaging of head and neck cancer cells," *International Journal of Nanomedicine*, p. 5025, Oct. 2014. DOI: 10.2147/ijn.s63873.

[114] J. Haegele, K. Lüdtke-Buzug, C. Schaecke, *et al.*, "Magnetic particle imaging: Kinetics of the intravascular signal in vivo," *International Journal of Nanomedicine*, p. 4203, Sep. 2014. DOI: 10.2147/ijn.s49976.

[115] C. Alexiou, W. Arnold, R. J. Klein, *et al.*, "Locoregional Cancer Treatment with Magnetic Drug Targeting," *Cancer Research*, vol. 60, pp. 6641–6648, 2000.

[116] R. M. Ferguson, A. P. Khandhar, S. J. Kemp, *et al.*, "Magnetic Particle Imaging with Tailored Iron Oxide Nanoparticle Tracers," *IEEE Transactions on Medical Imaging*, vol. 1, no. 1, p. 1, Jan. 2014. DOI: 10.1109/TMI.2014.2375065.

[117] A. Khandhar, R. M. Ferguson, 7. A. Simon, and K. M. Krishnan, "Tailored Magnetic Nanoparticles for Optimizing Magnetic Fluid Hyperthermia," *J Biomed Mater Res A.*, vol. 100, no. 3, pp. 728–737, Mar. 2012. DOI: 10.1002/jbm.a.34011.

[118] Z. W. Tay, P. W. Goodwill, D. W. Hensley, L. A. Taylor, B. Zheng, and S. M. Conolly, "A High-Throughput, Arbitrary-Waveform, MPI Spectrometer and Relaxometer for Comprehensive Magnetic Particle Optimization and Characterization," *Scientific Reports*, vol. 6, no. 1, Sep. 2016. DOI: 10.1038/srep34180.

[119] A. D. Katsenis, A. Puškarić, V. Štrukil, *et al.*, "In situ X-ray diffraction monitoring of a mechanochemical reaction reveals a unique topology metal-organic framework," *Nature Communications*, vol. 6, no. 1, Mar. 2015. DOI: 10.1038/ncomms7662.

[120] K. Užarević, I. Halasz, and T. Friščić, "Real-Time and In Situ Monitoring of Mechanochemical Reactions: A New Playground for All Chemists," *The Journal of Physical Chemistry Letters*, vol. 6, no. 20, pp. 4129–4140, Oct. 2015. DOI: 10.1021/acs.jpclett.5b01837.

[121] E. A. Stach, "Real-time observations with electron microscopy," *Materials Today*, vol. 11, pp. 50–58, 2008. DOI: 10.1016/s1369-7021(09)70007-0.

[122] D. R. Strachan, D. E. Johnston, B. S. Guiton, *et al.*, "Real-Time TEM Imaging of the Formation of Crystalline Nanoscale Gaps," *Physical Review Letters*, vol. 100, no. 5, Feb. 2008. DOI: 10.1103/physrevlett.100.056805.

[123] E. Longo, W. Avansi, J. Bettini, J. Andrés, and L. Gracia, "In situ Transmission Electron Microscopy observation of Ag nanocrystal evolution by surfactant free electron-driven synthesis," *Scientific Reports*, vol. 6, no. 1, Mar. 2016. DOI: 10.1038/srep21498.

[124] O. Malis, M. Radu, D. Mott, B. Wanjala, J. Luo, and C.-J. Zhong, "An in situ real-time x-ray diffraction study of phase segregation in Au–Pt nanoparticles," *Nanotechnology*, vol. 20, no. 24, p. 245 708, May 2009. DOI: 10.1088/0957-4484/20/24/245708.

[125] P. Nørby, M. Roelsgaard, M. Søndergaard, and B. B. Iversen, "Hydrothermal Synthesis of CoSb2o4: In Situ Powder X-ray Diffraction, Crystal Structure, and Electrochemical Properties," *Crystal Growth & Design*, vol. 16, no. 2, pp. 834–841, Jan. 2016. DOI: 10.1021/acs.cgd.5b01421.

[126] InnovativeIntegration, *X3-25m 2009 users manual. innovative integration*, ed. by InnovativeIntegration, Innovative Integration, 2390-A Ward Ave Simi Valley, California 93065, Jan. 1, 2009.

[127] AE Techron, Ed., *AE Techron 2105 amplifier datasheet*, AE Techron, 507 Warren Street, Elkhart, IN 46516 USA, Feb. 8, 2018.

[128] Formlabs, "FORMLABS MATERIAL PROPERTIES HIGH TEMP: Photopoly -mer resin for form 2 3D Printers," formlabs, Tech. Rep., 2018. [Online]. Available: https://formlabs-media.formlabs.com/datasheets/High_Temp_Technical.pdf.

[129] J. E. Zimmerman and N. V. Frederick, "Miniature Ultrasensitive Superconducting Magnetic Gradiometer and Its Use in Cardiography and Other Applications," *Applied Physics Letters*, vol. 19, no. 1, pp. 16–19, Jul. 1971. DOI: 10.1063/1.1653725.

[130] D. W. Collinson, K. M. Creer, E. Irving, and S. K. Runcorn, "The Measurement of the Permanent Magnetization of Rocks," *Philosophical Transactions of the Royal Society A: Mathematical, Physical and Engineering Sciences*, vol. 250, no. 974, pp. 73–82, Aug. 1957. DOI: 10.1098/rsta.1957.0012.

[131] D. C. Rose and J. N. Bloom, "A SATURATED CORE RECORDING MAGNETOMETER," *Canadian Journal of Research*, vol. 28a, no. 2, pp. 153–163, Mar. 1950. DOI: 10.1139/cjr50a-014.

[132] P. Reimer and T. Balzer, "Ferucarbotran (Resovist): A new clinically approved RES-specific contrast agent for contrast-enhanced MRI of the liver: Properties, clinical development, and applications," *Eur Radiol*, vol. 13, pp. 1266–1276, 2003. DOI: 10.1007/s00330-002-1721-7.

[133] P. A. Petrov, A. Ali, and D. K. Potter, "Diamagnetic Behavior in Nanoparticle Hematite?" *Journal of Modern Physics*, vol. 08, no. 07, pp. 1013–1019, 2017. DOI: 10.4236/jmp.2017.87063.

[134] J. Weizenecker, J. Borgert, and B. Gleich, "A simulation study on the resolution and sensitivity of magnetic particle imaging," *Physics in Medicine and biology*, vol. 52, no. 21, p. 6363, 2007.

[135] W. Sun, J. Cheng, L. Li, S. Chen, and K. Chang, "Preparation and magnetic properties of nickel nanowires by reduction in ethylene glycol medium under the influence of magnetic field," *IOP Conference Series: Materials Science and Engineering*, vol. 167, p. 012 030, Jan. 2017. DOI: 10.1088/1757-899x/167/1/012030.

[136] K. Gandha, J. Mohapatra, N. Poudyal, K. Elkins, and J. P. Liu, "Enhanced coercivity in co-doped Fe2O3 cubic nanocrystal assemblies prepared via a magnetic field-assisted hydrothermal synthesis," *AIP Advances*, vol. 7, no. 5, p. 056 324, May 2017. DOI: 10.1063/1.4978317.

[137] G. D. Moeser, K. A. Roach, W. H. Green, T. A. Hatton, and P. E. Laibinis, "High-gradient magnetic separation of coated magnetic nanoparticles," *AIChE Journal*, vol. 50, no. 11, pp. 2835–2848, Oct. 2004. DOI: 10.1002/aic.10270.

[138] C. T. Yavuz, J. T. Mayo, W. W. Yu, *et al.*, "Low-Field Magnetic Separation of Monodisperse Fe3O4 Nanocrystals," *Science*, vol. 314, no. 5801, pp. 964–967, Nov. 2006. DOI: 10.1126/science.1131475.

# ANKIT MALHOTRA

## *University Education*

09/2011 – 09/2013 **Master of Sciences (M. Sc.) in Biomedical Engineering**
University of Lübeck and Lübeck University of Applied Science
**Thesis title: "***A System for Multimodal Assessment of Cardiovascular Parameters- Design, Test and Measurements".*

07/ 2006 – 08/2010 **Bachelor of Technology (B. Tech., honours) in Biomedical Engineering**
Rajasthan Technical University, India

**Thesis title**: "*Design and development of a low cost calorimeter for blood analysis*"

## *Relevant Internships and Work Experience*

09/2015 – present **Research Assistant** (Tracer Technologies)
Fraunhofer Research Institution for Individualized and Cell-Based Medical Engineering

- Synthesis of SPIONs for different diagnostic and therapeutic applications
- Development of devices for characterizing the magnetic properties of SPIONs
- Development of devices for tracking the nucleation and growth of MNPs
- Automated Continuous Flow Synthesis setup for large scale production of SPIONs

01/2015 – present **Research Assistant**
Institute of Medical Engineering (IMT), University of Lübeck, Lübeck, Germany

- Worked on various projects dealing with hardware construction of MPI (Magnetic particle imaging) and MPS (Magnetic particle spectrometer).
- **Brain guard** (An ambulatory device for stroke detection)
- **LNA** (Low noise amplifiers) based on **VGA** (variable gain amplifiers) and **FDA** (Fully differential amplifiers) and single-ended configuration.

09/2013 – 12/2014 **Graduate Assistant**
Center of Excellence for Technology and Engineering in Medicine (TANDEM), Lübeck

- EIT (Electrical Impedance Tomography) measurement system.
- **Assessment of different current sources for EIT and BMS.**
- A portable In-ear pulse wave measurement system.
- **MS (Bioimpedance Measurement system)** for measuring impedance of skin as well as micro vessels.